Ph.D. Thesis 2023

Ida E. Nielsen

Measurements and manipulation protocols of parafermionic modes

Ida E. Nielsen

KØBENHAVNS UNIVERSITET
NIELS BOHR INSTITUTET

Ida E. Nielsen

Measurements and manipulation protocols of parafermionic modes

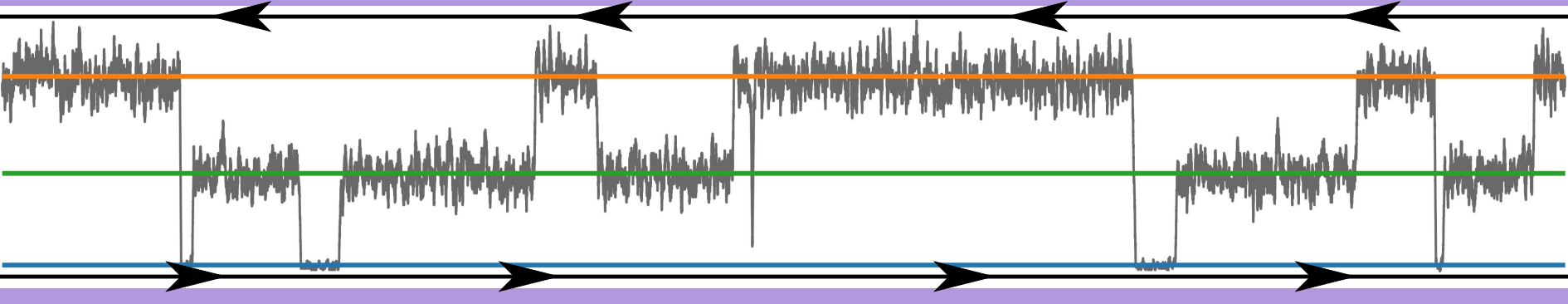

UNIVERSITY OF COPENHAGEN
FACULTY OF SCIENCE

Measurements and manipulation protocols of parafermionic modes

Ida E. Nielsen

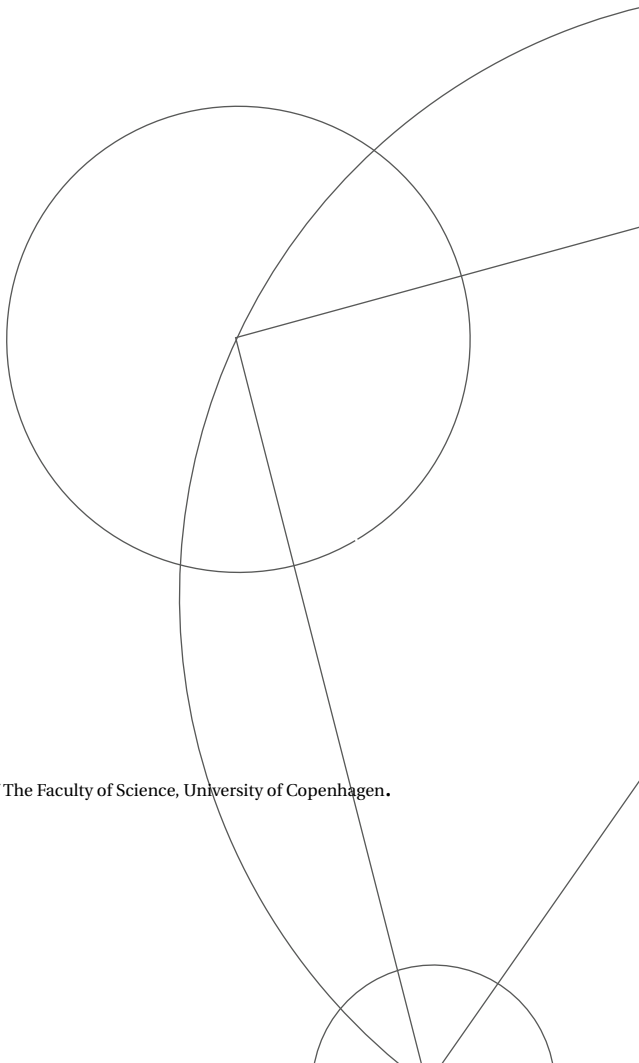

Supervisor:
Assoc. Prof. Michele Burrello

Co-supervisor:
Prof. Karsten Flensberg

Assessment committee:
Assoc. Prof. Jens Paaske
Prof. Ady Stern
Prof. Felix von Oppen

This thesis has been submitted to the PhD School of The Faculty of Science, University of Copenhagen.

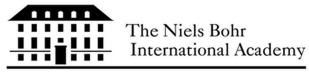

Measurements and manipulation protocols of parafermionic modes

Ida E. Nielsen

Copenhagen, September 2023.

Citation (APA):
Nielsen, I. E. (2023). *Measurements and manipulation protocols of parafermionic modes.* Niels Bohr Institute, Faculty of Science, University of Copenhagen.

Revised: September 29, 2023

Abstract

The experimental search for non-abelian anyons has extended beyond that of Majorana modes with advances in the understanding, manipulation and construction of fractional quantum Hall systems and their combination with elements like superconductors. Further fractionalisation of the electron degrees of freedom leads to parafermionic modes that can share fractions of the elementary charge non-locally. In this thesis we study the $\mathbb{Z}_6$ parafermions through transport spectroscopy and find that their fractional degree of freedom can be observed from a current readout via a standard metallic electrode. By simulating the dynamics of an open quantum system of two parafermions, we show that interaction with a fractional quantum Hall environment, causing fractional quasiparticle poisoning of the parafermion charge, reveals itself in a two or three-level telegraph noise in the current. To this end we use the stochastic quantum jump method and extend the jump operator formalism to describe fractional charges. Finally, we propose and study a protocol to experimentally verify the fusion algebra in a construction with four parafermions. In conclusion, the thesis presents proposals and indications for future experiments to measure compelling signatures of parafermionic modes.

Resumé

Den eksperimentelle søgen efter ikke-abelske anyoner er rakt udover Majoranatilstande med udvikling inden for forståelse, manipulering og konstruktion af fraktionelle kvante-Hall-systemer og deres kombination med for eksempel superledere. Yderligere fraktionering af elektronens frihedsgrader leder til parafermionske tilstande, der kan dele brøkdele af elementarladningen ikke-lokalt. I denne afhandling studerer vi $\mathbb{Z}_6$-parafermioner ved hjælp af transportspektroskopi og finder, at deres fraktionelle frihedsgrad kan observeres ved en strømmåling gennem en standard metallisk elektrode. Ved at simulere dynamikken i et åbent kvantesystem bestående af to parafermioner viser vi, at vekselvirkning med et fraktionelt kvante-Hall-miljø, der leder til forgiftning af parafermionladningen med fraktionelle kvasipartikler, viser sig i en to- eller treniveau telegrafstøj i strømmen. Til dette formål bruger vi den stokastiske kvantespringsmetode og udvider hoppeoperatorformalismen til at beskrive fraktionelle ladninger. Endeligt foreslår og studerer vi en protokol til eksperimentiel bekræftelse af fusionsalgebraen i en konstruktion med fire parafermioner. I alt præsenterer denne afhandling forslag til og indikationer for fremtidige eksperimenter til at måle overbevisende signaturer af parafermioniske tilstande.

Acknowledgements

The work presented in this thesis is a result of great guidance from expert supervisors, fruitful discussions with talented physicists and strong support from friends and family.

First of all, I would like to thank my supervisors Michele Burrello and Karsten Flensberg for giving me the opportunity to explore the research life, experience summer schools and conferences, but most importantly to choose and study for more than three years an area of physics which seems inexhaustible and ever puzzling. I highly value and admire your broad overview and expert knowledge in quantum and many-body physics.

A large thank you to my co-authors Reinhold Egger, Jens Schulenborg, Stavros Athanasiou and Matteo Wauters for enjoyable collaborations in the various projects and for teaching me on each your topic of expertise. A special gratitude to Reinhold and his research group at HHU in Düsseldorf for my very pleasant stay with you in 2022.

I would like to thank the assessment committee for taking their time to read and assess my work. I especially appreciate that Prof. Ady Stern and Prof. Felix von Oppen will travel to Denmark for my defence. Jens Paaske; this is the third (and hopefully last!) thesis of mine that you will be reading. It feels only right to complete more than nine years at the Niels Bohr Institute with you having a final word. Thank you for everything you taught me and for your friendly support all the way through.

A warm thank you to all the good people of the CMT group and QDev. You are good colleagues and friends. A special thank to Andrea Maiani for sharing with me the nice template for this thesis, but most of all for the good times at schools, vacations, on the water and over a beer or just a morning coffee in the office. I look forward to your return to Scandinavia. I am deeply grateful to il Bagai Matto and il Bischero Baffi. You are always ready to help when panic over Python, physics or pasta arises and I highly value our friendship. I greatly appreciate your help improving this thesis by your valuable feedback. Likewise, Morten Munk Kjærgaard thoroughly read and commented on this work, which I very much appreciate. A special mention of my good office mates Hano Sura, Cecilie Hermansen, Clara Breiø and Mercè Server. I am thankful to Brian M. Andersen for your professional guidance and help. You still owe me a bag of licorice though. And of course I want to praise Morten Christensen for being the epitome of good mood.

Thank you Jakob for sharing your life with me. I cannot believe my own luck. Your support is invaluable and, especially during the last six months, I have relied heavily on you to reach this goal.

The greatest gratitude of all, I owe my parents for their unwavering support during my PhD and for the past three decades. Never would I have succeeded with any of this without you.

Contents

Preface

In the second year of physics at the Niels Bohr Institute, we learned that the world can be divided into bosons and fermions – and that is it. However, reality is rarely black or white and likewise, the world offers us more general particle-like modes with exchange statistics that is neither bosonic nor fermionic. Coined in 1982 by F. Wilczek [4], *anyons* interpolate between bosons and fermions in the way that the exchange of two identical anyons results in a phase change of the wave function that can take *any* value between zero and 2π. Even more interesting are the *non-abelian* anyons which, loosely speaking, 'remember' the direction and order in which a collection of them are interchanged in a two-dimensional space. The controlled exchange – or *braiding* – of anyons can therefore be exploited to non-locally store and manipulate information in a non-trivial way [5]. The result is independent of the microscopic details of this process and depends only on the *topology* of the braiding.

An example of a non-abelian anyon that has been proposed for performing *quantum computation* [6] and which has been studied extensively is the *Majorana mode* [7]. Despite its anyonic nature it is often referred to as a Majorana fermion – a terminology I will adopt in this thesis. As far as we know, this is an excitation that emerges from the interaction of many electrons and it can effectively be described as a *quasiparticle* that cannot be isolated or removed from the rest of the system. It takes two Majorana operators to describe one regular fermion (electron) and they can thus be thought of as 'one half of an electron' which is furthermore its own antiparticle.

The fractionalisation can be continued further and one could think of splitting the electron into three, four, ..., etc. modes. In general, all these fractional versions are called *parafermionic modes* or parafermions (PFs) for short [8]. They are localised low-energy excitations that reflect a *topological phase* of the host system and they behave very differently from the known constituent particles. Their physical realisation is thought to require combinations of materials and systems that are already fascinating and complicated on their own. Examples of these are superconductors, topological insulators and quantum Hall systems [9–12].

The struggle to measure convincing signatures of these modes has been ongoing for more than a decade [13–18]. For the Majorana fermions, transport measurements can probe a low-energy state within the energy gap of the host material but at the price of loosing the information stored in the *parity* of a pair of these modes [13, 15, 19]. This thesis investigates how more general PFs, corresponding to smaller fractions of an electron, can be studied through transport spectroscopy which partly conserves their *topologically protected* degree of freedom. Despite recent experimental indications of PFs [20], alternative explanations of the observations as dissipation effects [21] still question their existence. Therefore, much further research within the field is required in order for

us to learn more about the new physics these exotic fractional excitations represent. This could also lead to a better understanding of the constituent electrons and the interaction among these. Our findings serve as useful guides for future experiments and can be implemented in more complex structures than the devices presented here.

In addition, understanding of PFs and their manipulation could in a far-future scenario be employed in the construction of a *topological quantum computer* where pairs of non-abelian anyons constitute *quantum bits* (qubits). A quantum computer could supplement classical supercomputers to solve problems that cannot be answered by a classical computer alone. Importantly, the topological nature of PFs implies that this type of qubit would carry an inherent protection against errors [7, 22].

Outline

This thesis reviews the findings of my research as a PhD student within the field of transport and dynamics in topological phases of matter. The central focus of the thesis is parafermionic modes and after introducing background theory, I will present detailed calculations and analyses of signatures of these modes and discuss the results.

Chapter 1 introduces relevant concepts for understanding the complexity of PFs and the interest in the physics they represent. We lay out the formalism that is used in the later chapters, summarise physical phenomena and systems important for the investigation of PFs and present proposals for the realisation of these modes.

Chapter 2 unfolds our work in Ref. [1] on transport spectroscopy as a method to explore the fractional nature of PFs. With two device proposals inspired by experimental realisations, we present predictions for the conductance signals of these in the presence of PFs. The chapter also explores breaking of the topological protection of the fractional PF degree of freedom.

Chapter 3 analyses the dynamics of sets of PFs under current measurements and studies the effect of quasiparticle poisoning which affects the fractional charge shared by a pair of PFs. The results of these investigations are additionally used to propose and explore a protocol to test the non-abelian character of the PFs through the associativity of fusion. Our work in this chapter is presented in Ref. [2].

Chapter 4 is a reprint of Ref. [3] that investigates another topological phenomenon called *Thouless pumping*. Here we make use of similar techniques as presented in the preceding chapters although the work is outside the central focus of this thesis. My contributions to the work are stated before the manuscript.

Chapter 5 concludes the work on PFs presented in this thesis and discusses possible future directions.

Publications

The thesis presents the results of the two works below in greater detail with extended explanations. Some material (mainly figures) of the original papers are included with minimal or no modification.

Readout of Parafermionic States by Transport Measurements
Ida E. Nielsen, Karsten Flensberg, Reinhold Egger, Michele Burrello
Physical Review Letters, Vol. **129**, Iss. 3 (July 2022), p. 037703, Ref. [1]
Contributor to the development of the theoretical concept and primary contributor to the analytical calculations of transport and the numerical results. Contributor to the main text and sections of the supplemental material.

Dynamics of parafermionic states in transport measurements
Ida E. Nielsen, Jens Schulenborg, Reinhold Egger, Michele Burrello
arXiv:2305.08906 (May 2023), (in voting at the Editorial College of SciPost Physics), Ref. [2]
Contributor to defining the project and identifying the relevant techniques. Primary contributor to the numerical studies and their analysis as well as to the writing of the manuscript.

The thesis also contains the following manuscript:

Thouless pumping in Josephson junction arrays
Stavros Athanasiou, **Ida E. Nielsen**, Matteo M. Wauters, Michele Burrello
arXiv:2308.13597 (August 2023), Ref. [3]
Contributor to the theoretical description of the Harper-Hofstadter model as well as the numerical codes for the pumping scheme and the subsequent data analysis and figures. Contributor to setting up and refining the manuscript.

Although all three works study transport and topological phenomena in mesoscopic superconducting systems, this last one is outside the main focus of the thesis which concentrates on parafermionic modes. Without any further in-depth details or calculations, the manuscript is replicated in Ch. 4.

1

Introduction to parafermionic modes

This chapter provides an introduction for non-expert readers with a background in quantum mechanics to the concepts of parafermionic modes, topological phases and the fractional quantum Hall (FQH) effect. We also review theoretical proposals for the physical realisation of parafermions (PFs) as well as recent experimental signatures of these modes. The subject is vast, so rather than a detailed introduction the chapter provides a broad overview and focuses on the essentials of relevant topics for understanding the work presented later in this thesis. For a more complete introduction the reader is referred to Refs. [8, 24, 26].

1.1 Parafermions, topological phases and the quantum clock model

Explaining my PhD work to family and friends, the most frequently used line has been; 'think of parafermions as one sixth of an electron'. Although not exact, it does convey the core idea. To fellow students from other areas of physics the explanation would contain; 'a generalisation of fermions'. And to colleagues within the same field they are; 'a further fractionalisation of the electron degrees of freedom beyond that of Majorana fermions, exhibiting non-abelian statistics'. Here we review in more detail what defines the PFs and some of their properties.

For readers new to the field we stress that all solid-state systems are made up solely of ions and electrons. Although we will discuss more exotic excitations that can be thought of as fractional versions of the constituents these are merely an effective way to describe the collective behaviour and interplay of the many-body system. The new excitations can have properties that are very different from those of the constituents and cannot be isolated or extracted from the system. In fact, the excitations we will study can only exist in one or two-dimensional (1D or 2D) electron systems [7, 23] such as a wire that is only a few nanometres wide or a 'plate' of similar thickness, typically encapsulated by other layers of materials. Nonetheless, we will often talk about them as individual entities.

We begin by introducing the concept of topological phases after which we present the formalism of PFs and show how the *quantum clock model* can be mapped to a chain of these modes. The concepts are treated in much greater detail for instance in Refs. [8, 24, 26, 28].

Topological phases

Topology is a vast and complex topic from which we here flash only a few properties relevant for the work presented in succeeding chapters. In the context of condensed matter systems, topology is used to classify different physical systems and the corresponding Hamiltonians. It is a way to distinguish phases that do not otherwise differ in their symmetries, long-range order or local order parameters. Instead, different topological phases can be characterised by a non-local *topological invariant* which could be the degeneracy of the ground state, whether the phase has special states existing only on the edges of the system or the statistics of potential quasiparticles [24]. For example, if two Hamiltonians that both have a gapped spectrum can be continuously transformed into each other under smooth variation of some parameter without ever closing the energy gap, they are said to be *topologically equivalent* [26] and thus in the same topological phase. In this case, the topological invariant could be the number of energy levels below the gap. The invariant can change when this gap closes and the system is said to undergo a *topological phase transition*. A phase or system with non-trivial topology - also sometimes simply called a topological system - has a ground state with a degeneracy that is robust against physical perturbations [8, 24]. It is

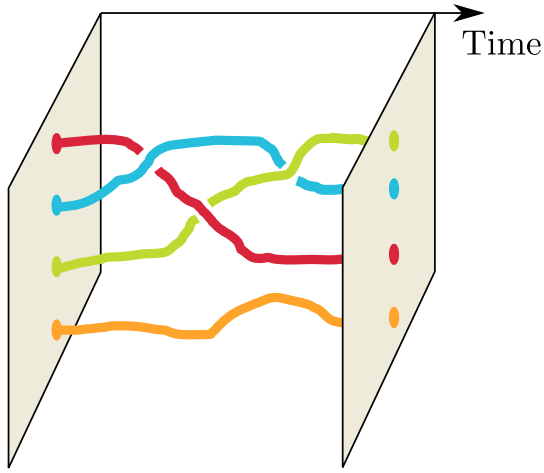

Figure 1.1: Illustration of the braiding of world lines for four non-abelian anyons in two spatial dimensions and time. The irregularities of the lines are to illustrate that the transformation of the quantum state does not rely on the details of the trajectory but only the topology.

not possible to determine the state within the ground state subspace with any measurement of a local operator [11, 23]. Often the ground state is associated with particles of zero excitation energy that appear at the edges of an otherwise gapped bulk system [8]. For instance, in a topological 1D electron system the zero-energy modes will be zero-dimensional and localised at the ends whereas they will be 1D edge modes in a 2D system with non-trivial topology. Criteria on the bulk spectrum and the topological invariant can reveal if these modes are present, a concept referred to as *bulk-edge correspondence*.

The zero-energy excitations are exotic in the way that they neither behave as fermions nor bosons. They are quasiparticles, named anyons, which refers to fact that exchanging two anyons yields a phase that is not necessarily a ± 1 but in general some $e^{i\vartheta}$ [4]. Importantly, this fractional statistics is only possible in two spatial dimensions [24]. In addition to this, the anyons we are to study obey a non-abelian exchange statistics which implies that an adiabatic interchange of e.g. the positions of two modes transforms the quantum state of the system in a non-commutative way [12]. It corresponds to a unitary transformation within the ground state subspace and shifts between those states. Importantly, the transformation depends solely on the topology of the interchange, i.e. the overall characteristics, and not on the exact microscopic details of the trajectory or on noise as long as the degeneracy of the ground state manifold does not change during the operation and the energy gap remains [11]. One talks about *topological braiding* and often draw *world lines* to illustrate the exchange procedure where one of three dimensions is time, see Fig. 1.1. In the ground state manifold, a quantum state of the same dimension as the degeneracy itself can be stored non-locally. The braiding protocol can entangle multiple quantum information registers under topologically protected operations which is the reason why non-abelian anyons are considered potential candidates for quantum computation applications [12].

One example of a topological system is the 1D p-wave superconductor (SC) as described in Kitaev's seminal work (Ref. [7]). In the topological phase the SC supports non-abelian anyons

named Majorana fermions (MFs), localised at each end of the 'wire'. These are described by second quantised operators γ which, despite the name Majorana *fermion*, do not square to zero but rather $\gamma^2 = \mathbb{1}$. Hence, one cannot speak of an occupied or unoccupied Majorana state. One can instead make sense of the parity of a *pair* of MFs; $P_M = i\gamma_2\gamma_1 = \pm 1$. Such a pair can be described as one normal fermion (electron) with annihilation operator $c = (\gamma_1 + i\gamma_2)/2$ [7, 19]. Additionally, the MFs are self-adjoint, $\gamma^\dagger = \gamma$, making them their own anti-particle. A pair of MFs that are well-separated in space encodes a qubit non-locally, and by an ordered exchange of at least two pairs of MFs it is possible to implement a non-universal set of operations or *quantum gates* [5, 22]. These exotic modes are, however, only the most basic type of PFs and there exists more general examples of these localised topological excitations that provide better protection against noise from the environment and have a richer set of fault-tolerant qubit rotations compared to the MFs [23]. Still, however, we note that topological manipulations of PFs cannot realise universal quantum computation [11].

Next we will consider the PFs in general and extend the formalism and notion of parity.

Formalism

PFs bring with them new curious fundamental physics to be understood and tested. Before considering the physical systems where to search for them and how to see signatures of these modes, we review the basic formalism to describe PFs.

As mentioned above, the MF is described by a self-Hermitian operator that squares to $\mathbb{1}$. This is the simplest type of PF and, in general, PFs are non-abelian anyons that come in different $\mathbb{Z}_N$-types. They are represented by an operator α that yields the identity when taken to the N^{th} power [12];

$$\alpha^N = \left(\alpha^\dagger\right)^N = \mathbb{1}\,. \tag{1.1}$$

Furthermore, the PF operator is unitary;

$$\alpha^\dagger = \alpha^{N-1} = \alpha^{-1}\,, \tag{1.2}$$

which, combined with the first equation, means that for even values of N

$$\alpha^{N/2} = \left(\alpha^\dagger\right)^{N/2}\,. \tag{1.3}$$

Indeed, we confirm that for $N = 2$ these operators are self-adjoint and square to identity as the MF operator. For larger N they define the more general PFs. For a collection of PFs, numbered in some order $\alpha_1, \alpha_2, \alpha_3, \ldots$, the following commutation relations apply [11]:

$$\alpha_i \alpha_j = \alpha_j \alpha_i \, e^{i\frac{2\pi}{N}\operatorname{sgn}(j-i)}\,, \tag{1.4}$$

$$\alpha_i^\dagger \alpha_j = \alpha_j \alpha_i^\dagger \, e^{-i\frac{2\pi}{N}\operatorname{sgn}(j-i)}\,, \tag{1.5}$$

where Eq. (1.5) is obtained by combining Eqs. (1.2) and (1.4) and the sign convention follows that of Ref. [25] with $\operatorname{sgn}(0) = 0$. Setting $N = 2$ we see that MF operators anticommute like normal fermions, but in general one obtains a complex phase for PFs. Other useful commutation relations that follow from these are

$$\alpha_i^\dagger \alpha_j \alpha_k = \alpha_k \alpha_i^\dagger \alpha_j \, e^{i\frac{2\pi}{N}(\operatorname{sgn}(k-j)-\operatorname{sgn}(k-i))} \implies [\alpha_i^\dagger \alpha_j, \alpha_k] = 0 \qquad \text{for } k > i, j \text{ or } k < i, j\,, \tag{1.6}$$

and similarly $[\alpha_i^\dagger\alpha_j,\alpha_k^\dagger]=0$. This implies that $[\alpha_i^\dagger\alpha_j,\alpha_k^\dagger\alpha_l]=0$ given that also $l>i,j$ or $l<i,j$. Employing the commutation relation in Eq. (1.5) we make the following rewriting

$$\left(\alpha_i^\dagger\alpha_j\right)^N=\left(\alpha_i^\dagger\right)^N\left(\alpha_j\right)^N\left(\mathrm{e}^{i\frac{2\pi}{N}\mathrm{sgn}(j-i)}\right)^{\sum_{n=1}^{N-1}n}=\left(\mathrm{e}^{i\frac{2\pi}{N}\mathrm{sgn}(j-i)}\right)^{N(N-1)/2}=(-1)^{N-1},\qquad \text{for } i\neq j\,. \tag{1.7}$$

From this point on we will restrict ourselves to consider 'even' PFs where $N=2m$ and $m>0$ is an integer. Therefore, $(\alpha_i^\dagger\alpha_j)^N=-1$ which means we can write the eigenvalues of the operator $\alpha_i^\dagger\alpha_j$ as $\mathrm{e}^{i\frac{2\pi}{N}(q-1/2)}$ where q is an integer.

Let us consider two PFs α_1,α_2 and the operator $\alpha_1^\dagger\alpha_2$ in more detail. We label the eigenstates by $|q\rangle$ such that

$$\alpha_1^\dagger\alpha_2|q\rangle=\mathrm{e}^{i\frac{2\pi}{N}(q-1/2)}|q\rangle\,. \tag{1.8}$$

We see that with this operator there exists N distinguishable values of $q\in\{0,1,\ldots,N-1\}$. With the commutation relations in Eqs. (1.4) and (1.5) we find that

$$(\alpha_1^\dagger\alpha_2)\alpha_j=\mathrm{e}^{-i\frac{2\pi}{N}}\alpha_j(\alpha_1^\dagger\alpha_2),\qquad (\alpha_1^\dagger\alpha_2)\alpha_j^\dagger=\mathrm{e}^{i\frac{2\pi}{N}}\alpha_j^\dagger(\alpha_1^\dagger\alpha_2), \tag{1.9}$$

for $j=1,2$. This means that $\alpha_{1,2}|q\rangle\propto|q-1\rangle$ and $\alpha_{1,2}^\dagger|q\rangle\propto|q+1\rangle$ with proportionality constants of unit magnitude [12]. Furthermore, $\alpha_{1,2}|0\rangle\propto|N-1\rangle$ and $\alpha_{1,2}^\dagger|N-1\rangle\propto|0\rangle$. We choose to fix the relative phases of the states such that

$$\alpha_1|q\rangle=|q-1\rangle\,,\qquad \alpha_1^\dagger|q\rangle=|q+1\rangle\,. \tag{1.10}$$

Since $(\alpha_1^\dagger\alpha_2)\alpha_1|q\rangle=\mathrm{e}^{i\frac{2\pi}{N}(q-1-1/2)}|q-1\rangle$ we can require that

$$\alpha_1^\dagger\alpha_2\alpha_1|q\rangle=\mathrm{e}^{-i\frac{2\pi}{N}}\underbrace{\alpha_1^\dagger\alpha_1}_{\mathbb{1}}\alpha_2|q\rangle\equiv\mathrm{e}^{i\frac{2\pi}{N}(q-1-1/2)}|q-1\rangle\rightarrow\alpha_2|q\rangle=\mathrm{e}^{i\frac{2\pi}{N}(q-1/2)}|q-1\rangle\,, \tag{1.11}$$

and similarly $\alpha_2^\dagger|q\rangle=\mathrm{e}^{-i\frac{2\pi}{N}(q+1/2)}|q+1\rangle$. We can also replace the number q with the corresponding operator $\hat{q}$ and write

$$\mathrm{e}^{i\frac{\pi}{N}}\alpha_1^\dagger\alpha_2=\mathrm{e}^{i\frac{2\pi}{N}\hat{q}},\qquad P_{12}=\mathrm{e}^{-i\frac{\pi}{N}}\alpha_2^\dagger\alpha_1=\mathrm{e}^{-i\frac{2\pi}{N}\hat{q}}\,. \tag{1.12}$$

Here we have introduced the parity operator P_{12}, generalising P_{M} for the MFs to PFs where it has N distinct eigenvalues $\mathrm{e}^{-i\frac{2\pi}{N}q}$ [25]. In conclusion, we can represent the PF pair α_1 and α_2 in an N-dimensional Hilbert space with basis states $|q\rangle$ where $P_{12}|q\rangle=\mathrm{e}^{-i\frac{2\pi}{N}q}|q\rangle$. As we will see below, α_1 and α_2 can describe two localised zero-energy modes in a topological system. The ground state of that system is N-fold degenerate and the states within the ground state manifold can be labelled by the number q.

In this thesis we will focus on $\mathbb{Z}_6$ PFs where

$$\alpha^6=\mathbb{1}\,,\qquad P_{12}=\mathrm{e}^{-i\frac{\pi}{6}}\alpha_2^\dagger\alpha_1=\mathrm{e}^{-i\frac{\pi}{3}\hat{q}}\,,\qquad \alpha^3=\left(\alpha^\dagger\right)^3\,. \tag{1.13}$$

Importantly, the last equality means that the $\mathbb{Z}_6$ PF operator to the third power behaves as a MF operator; $\alpha^3=\tilde{\gamma}=\tilde{\gamma}^\dagger$ which will be exploited for readout protocols later. This concludes the introduction of PF formalism. Next we will see how PFs are connected to the quantum clock model, followed by a brief review of the FQH effect which will prove very useful in the search for physical realisations of PFs.

The quantum clock model

As introduced above, the 1D p-wave SC is an example of a topological system which can host MFs at each end. The Hamiltonian of this system is related to that of a transverse-field Ising model via a non-local mapping, called the Jordan-Wigner transformation [8], between the spin variables of the Ising model and fermions in the model for the SC [7]. Despite being two distinct systems, the paramagnetic phase of the Ising chain maps to a trivial superconducting state whereas the ferromagnetic phase maps to a topologically non-trivial 1D SC with MFs localised at the two ends. In the ferromagnetic phase, the up/down configurations of the spins translate to even/odd fermion parity P_{M} of the SC [12, 23].

Similarly to this connection there exists an analogous non-local transformation, the Fradkin-Kadanoff mapping [27], which maps a generalisation of the Ising model to a chain of PFs. The generalised Ising chain is termed a *clock model* and here each 'spin' can take N different values ($N=2$ corresponds to the usual Ising model) and the system interactions are invariant under a $\mathbb{Z}_N$ symmetry [23]. In this case the symmetry-breaking states of the clock model also map to topological phases with localised zero-energy modes [8]. We label the spin at site j by $s_j = \{1, \omega, \omega^2, \ldots, \omega^{N-1}\}$ where $\omega = \mathrm{e}^{i\frac{2\pi}{N}}$ which reminds us of the eigenvalues of the PF parity operator in Eq. (1.12)! The most general $\mathbb{Z}_N$-invariant coupling between two such (classical) spins is $-J\sum_{m=1}^{N-1} a_m (s_j^* s_k)^m$ with $J>0$ and $a_m^\dagger = a_{N-m}$ to ensure hermiticity[1] [8]. Indeed, sending $s_j \to \omega s_j$ for all j leaves the coupling unchanged. For this generalised Ising chain we can extend the Pauli matrices σ_z and σ_x to an N-dimensional space, σ_j and τ_j, for each site [8];

$$\sigma_j^N = \tau_j^N = \mathbb{1}\,, \qquad \sigma_j^\dagger = \sigma_j^{N-1}\,, \qquad \tau_j^\dagger = \tau_j^{N-1}\,. \tag{1.14}$$

The clock operators are thus unitary and yield the identity when taken to the N^{th} power, similarly to the $\mathbb{Z}_N$ PF operators. Also their commutation relations bear some resemblance;

$$\sigma_j \tau_j = \tau_j \sigma_j \mathrm{e}^{i\frac{2\pi}{N}}\,, \qquad \sigma_j^\dagger \tau_j = \tau_j \sigma_j^\dagger \mathrm{e}^{-i\frac{2\pi}{N}}\,. \tag{1.15}$$

The second relation is obtained by applying $\sigma_j^{-1}(\ldots)\sigma_j^\dagger$ to both sides of the first equality. Operators on different sites commute. In the eigenbasis of σ their representations look like

$$\sigma_j = \begin{pmatrix} 1 & & & & \\ & \mathrm{e}^{i\frac{2\pi}{N}} & & & \\ & & \mathrm{e}^{i\frac{4\pi}{N}} & & \\ & & & \ddots & \\ & & & & \mathrm{e}^{i\frac{2\pi(N-1)}{N}} \end{pmatrix}, \qquad \tau_j = \begin{pmatrix} 0 & 0 & 0 & \ldots & 0 & 1 \\ 1 & 0 & 0 & & 0 & 0 \\ 0 & 1 & 0 & & 0 & 0 \\ \vdots & & & & \vdots & \vdots \\ 0 & 0 & 0 & \ldots & 0 & 0 \\ 0 & 0 & 0 & \ldots & 1 & 0 \end{pmatrix}. \tag{1.16}$$

In this basis, σ_j measures the spin on site j and τ_j shifts or winds the spin by $\mathrm{e}^{i\frac{2\pi}{N}}$. The generalised N-state *quantum clock model* for an open L-site chain is [8, 12]

$$H_{\text{q.clock}} = -J\sum_{j=1}^{L-1}\left(\sigma_j^\dagger \sigma_{j+1} + \sigma_{j+1}^\dagger \sigma_j\right) - \mathcal{H}\sum_{j=1}^{L}\left(\tau_j^\dagger + \tau_j\right). \tag{1.17}$$

[1] With complex coefficients a_m the model is referred to as the *chiral clock model*.

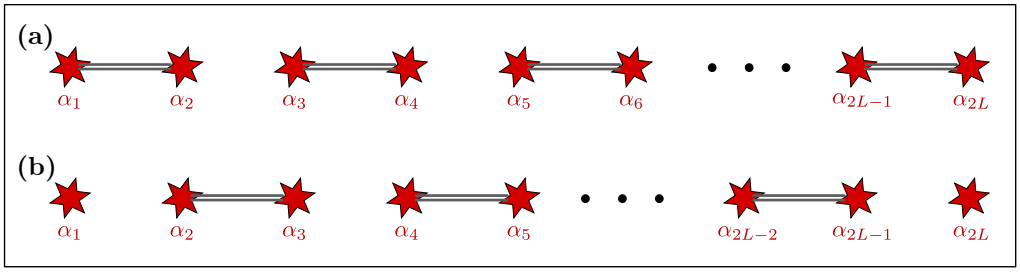

Figure 1.2: Adaptation of Figure 1 from Ref. [12] illustrating the PF chain of Eq. (1.19) in the two special limits: **(a)** $J = 0$ (paramagnetic) and **(b)** $\mathcal{H} = 0$ (ferromagnetic).

Here $J \geq 0$ is a ferromagnetic coupling of neighbouring sites whereas $\mathcal{H} \geq 0$ corresponds to a transverse field [12]. In general, one could include complex phases on e.g. the $\mathcal{H}$ term, but for simplicity we leave it out here. The global $\mathbb{Z}_N$ symmetry corresponds to a uniform shift of all the 'spins', generated by the operator $\prod_{j=1}^{L} \tau_j^\dagger$ which, to the N^{th} power, is the identity operator [8, 23]. Eq. (1.17) reduces to the transverse field Ising model for $N = 2$. For $J = 0$, $\mathcal{H} > 0$, there exists a unique paramagnetic ground state with $\tau_j = +1$. If instead $J > 0$ and $\mathcal{H} = 0$, an N-fold degenerate ferromagnetic ground state emerges with $\sigma_j = \mathrm{e}^{i\frac{2\pi}{N}q}$ and $q \in \{0, \ldots, N-1\}$ [12]. Certainly, the clock operators have features similar to the PFs and, as advertised above, they are related to each other by a non-local transformation [8, 12]

$$\alpha_{2j-1} = \sigma_j \prod_{i<j} \tau_i, \qquad \alpha_{2j} = -\mathrm{e}^{i\frac{\pi}{N}} \tau_j \sigma_j \prod_{i<j} \tau_i \,. \tag{1.18}$$

These expressions for the PF operators are build up of 'strings' of τ operators which wind all the spins up to some point given by j [23]. Combined with the relations in Eqs. (1.14) and (1.15) the above transformation reproduces the PF properties in Eqs. (1.1) to (1.5) (see App. A for explicit calculations), reflecting the non-local nature of the PFs. With the above transformation the quantum clock Hamiltonian becomes

$$H_{\text{q.clock}} = J \sum_{j=1}^{L-1} \left(\mathrm{e}^{i\frac{\pi}{N}} \alpha_{2j}^\dagger \alpha_{2j+1} + \text{H.c.} \right) + \mathcal{H} \sum_{j=1}^{L} \left(\mathrm{e}^{i\frac{\pi}{N}} \alpha_{2j-1}^\dagger \alpha_{2j} + \text{H.c.} \right). \tag{1.19}$$

To show that the two Hamiltonians are equivalent is straightforward and done in App. A. In Fig. 1.2 we reproduce from Ref. [12] a schematic illustration of two specific phases of the above quantum clock Hamiltonian. The first phase is obtained by setting $J = 0$ (paramagnetic phase). The PFs then dimerise as in Fig. 1.2a where each pair $(\alpha_{2j-1}, \alpha_{2j})$ can be diagonalised simultaneously and the ground state is gapped and unique [12]. The other extreme, $\mathcal{H} = 0$ (ferromagnetic phase), has the shifted dimerisation shown in Fig. 1.2b. The bulk system has an energy gap also in this case, but now the ends of the chain support unpaired zero-energy modes α_1 and α_{2L} that do not appear in the Hamiltonian $H_{\text{q.clock}}(\mathcal{H} = 0)$ and thereby commute with it (recall Eq. (1.6)). The combination of the two end modes $\alpha_{2L}^\dagger \alpha_1$ has N distinct eigenvalues $\mathrm{e}^{i\frac{2\pi}{N}q}$, $q \in \{0, 1, \ldots, N-1\}$ and do not affect the energy. The 'ferromagnetic' phase is therefore N-fold degenerate. For $N = 2$ these are the unpaired MFs of Kitaev [7] and for a general $N > 2$ they are parafermionic zero-energy modes.

In more general cases where $\mathcal{H}$ is not precisely zero, the states $\{|q\rangle\}$, corresponding to the eigenvalues of $\alpha_{2L}^\dagger \alpha_1$, are not exactly degenerate and the pair of PFs could likely hybridise in a

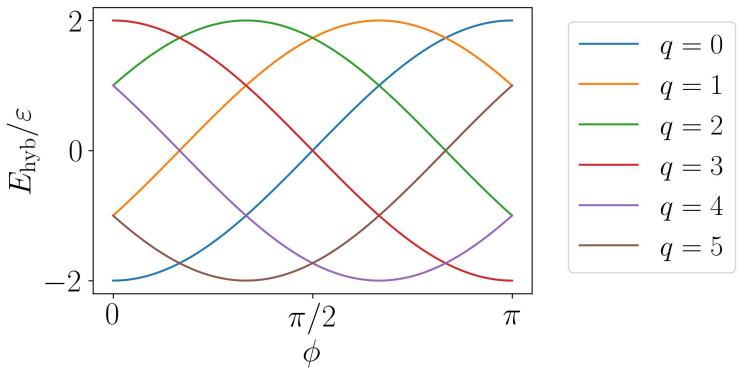

Figure 1.3: Plot of the hybridisation energy between two PFs as a function of the phase ϕ of the coupling. The degeneracy is restored among pairs of $|q\rangle$ states when ϕ takes the specific values $n\pi/6$ with n integer.

realistic physical system. To lowest order the splitting between the different states is given by the Hamiltonian [8, 11, 12]

$$H_{\mathrm{hyb}} = -\varepsilon\, \mathrm{e}^{-i\phi}\, P_{12} + \mathrm{H.c.} = -2\varepsilon \cos(2\pi \hat{q}/N + \phi)\,, \tag{1.20}$$

where P_{12} is the generalised parity operator in Eq. (1.12) and $\varepsilon\, \mathrm{e}^{-i\phi}$ is the coupling of the two modes with $\varepsilon \geq 0$ and a phase ϕ that may be varied depending on the implementation. We will discuss this coupling in later sections. In the case of $\mathbb{Z}_6$ PFs, $\hat{q}$ has six different eigenstates; $\{|0\rangle, |1\rangle, \ldots, |5\rangle\}$. The eigenenergies of these states are plotted in Fig. 1.3 as a function of ϕ and show that the degeneracy is restored pairwise for the special values $\phi = n\pi/6$ with n integer.

The fractional quantum Hall effect

In this section we review some aspects of the quantum Hall effect and in particular the FQH effect which will prove very useful in the search for PFs. The quantum Hall effect appears in 2D electron systems in a strong magnetic field normal to the plane and goes beyond the classical Hall effect. In the classical scenario, the Hall resistivity ρ_{xy} is proportional to the strength B of the magnetic field as long as this is 'weak' and the density of electrons is fixed, whereas the longitudinal resistivity is independent of B. In the low-temperature quantum scenario, $\rho_{xy} = \frac{h}{e^2}\frac{1}{\nu}$ where h is the Planck constant, $-e$ is the electron charge and $\nu \propto B^{-1}$ is the *filling factor* of the Landau levels defined as the ratio between the density of electrons in the 2D electron gas and the density of flux quanta $\Phi_0 = h/e$ [24, 28]. In 1980 experiments by von Klitzing *et al.* (Ref. [29]) showed that in a high magnetic field $B \gtrsim 10$ T and at temperatures $T \sim 1.5$ K the Hall resistance became quantised while the longitudinal resistivity dropped close to zero in certain ranges of the electron density, see Fig. 1.4a. These ranges corresponded to the Fermi energy lying in the gap between two Landau levels (possibly spin- or valley split), equivalent to integer filling factors $\nu = 2, 3, 4, \ldots$. Crucially, the quantised values of the Hall resistance were independent of the device geometry and the direction of the magnetic field. This universality is the awe-inspiring aspect of the quantum Hall effect; integer or fractional, the measured quantised values of $\rho_{xy} = \frac{h}{e^2}\frac{1}{\nu}$ are reproducible and constant

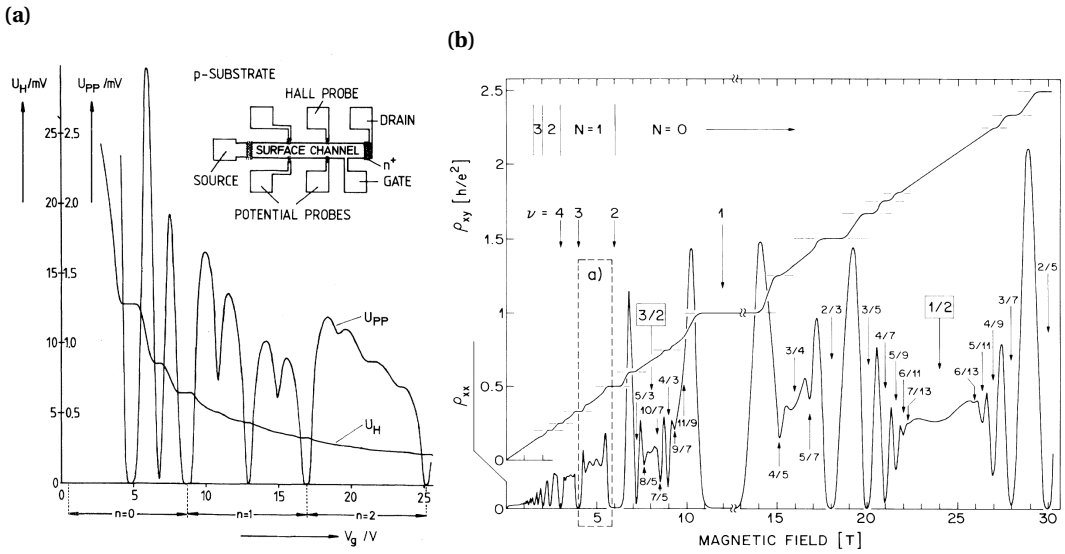

Figure 1.4: Examples of quantum Hall measurements. **(a)** Figure 1 from von Klitzing *et al.* 1980 [29] showing the first measurement of the quantum Hall effect. A metal-oxide-semiconductor field-effect transistor was placed in a constant magnetic field of 18 T and cooled down to 1.5 K. The inset shows a sketch of such a device (dimensions 400 µm × 50 µm) in which a current of 1 µA runs between the source and drain contacts and three probes measure the longitudinal and Hall voltages, U_{PP} and U_{H}, respectively. These are plotted as a function of the gate voltage V_g controlling the density of electrons in the 2D electron gas. In certain ranges of V_g, U_{H} levels out at plateaus while U_{PP} drops close to zero. The $n = \{0,1,2\}$ in the bottom of the plot labels the Landau level corresponding to V_g and plateaus in U_H are observed between these. Additional plateaus are due to breaking of spin and valley degeneracies. **(b)** Figure 1 from Willet *et al.* 1987 [30] displaying the quantisation of ρ_{xy} at both integer and fractional fillings. The figure is a composition of different traces of the magnetic field with temperatures between 85 mK and 150 mK. The majority of the figure shows the FQH effect in the zeroth Landau level ($N = 0$ in the figure) at fractional fillings.

across samples and materials! In fact, the quantisation of the resistivity is so precise that a standard for electrical resistance $\frac{h}{e^2}$ has been introduced from these measurements and is known to an order of 10^{-9} [28]. With the independence on experimental implementation, the quantum Hall effect is a prime example of topology in condensed matter systems where the topological invariant is the filling factor ν.

A shortcut to understanding the *integer quantum Hall effect* is the so-called *Laughlin argument* [26] which regards the effect as an example of *topological pumping* – the topic of Ch. 4. Considering the radial current flow in an annulus geometry with a varying flux through the hole, one can argue that the Hall conductance must be quantised to $\nu e^2/h$. To understand the plateaus of the resistivity we turn to the Pauli exclusion principle; when $\nu = 1$ it means that all the electron states of the lowest Landau level are filled. Charged excitations of effective mass m^* have a finite energy cost

$\hbar\omega_c$ where $\omega_c = eB/m^*$ is the cyclotron frequency and $\hbar = h/2\pi$ is the reduced Planck constant[2]. Because of this energy gap, no low-energy excitations are created in the bulk of the system which is said to form an *incompressible liquid* at these specific values of ν; changes in the chemical potential μ do not change the electron density and hence the Hall resistivity remains at a plateau [24].

Shortly after the first experiments it was found that the Hall conductance is quantised also for some fractional values of the filling factor, for example at $\nu = \frac{1}{3}, \frac{2}{5}, \frac{3}{7}, \frac{4}{7}, \frac{4}{3}$ and $\frac{5}{2}$ [28, 31, 32], see also Fig. 1.4b. Of these, $\nu = 1/3$ is the most frequently observed one and also the state used in later sections to construct $\mathbb{Z}_6$ PFs. To observe the FQH effect requires materials of high mobility $\gtrsim 10^6\,\mathrm{cm}^2/\mathrm{Vs}$ [32]. Whereas the integer quantum Hall effect can be thought of in terms of the Pauli principle, the FQH states only partially fill the Landau levels and there would be a large ground state degeneracy if the electrons were free. The FQH effect must therefore be a result of electron-electron interactions [24]. In 1983 R. B. Laughlin proposed a theory for the FQH effect [33] which included a wave function for the many-body ground state of filling $\nu = 1/m$ where m is an odd integer;

$$\psi_m = \prod_{j<k} (z_j - z_k)^m \, \mathrm{e}^{-\sum_l |z_l|^2/4} \,. \tag{1.21}$$

Here $z_j = x_j + i y_j$ is the position of the j'th electron written in the complex plane and the product and sum run over all the electrons in the system. The factors $(z_j - z_k)$ ensure nodes in the wave function, *vortices*, if the positions of two electrons are the same. m is required to be odd to ensure the sign change of the wave function when two electrons are interchanged.

In both the integer and fractional cases the longitudinal resistivity decays exponentially at low temperatures as $\mathrm{e}^{-1/T}$ when ρ_{xy} is at a plateau [32]. This means that the voltage parallel to the electric field approaches zero at low temperatures and hence there is no dissipation or heating along this direction, reflecting the absence of states at the chemical potential μ in the (gapped) bulk or that the bulk states are localised [28]. The Hall resistivity, however, is finite and thus the current must be carried by dissipationless channels in the edges of the system. The electrons that are pushed out to the edges by the Lorentz force do not dissipate energy as they move perpendicularly to the electric field. Therefore, there has to be available gapless states at μ that the electrons can occupy as they reach the edge. Moving now parallel to the electric field, the electrons absorb energy from the field and run in opposite directions on opposite sides of the sample, i.e. they become chiral [28]. The gapless edge modes is a property of all quantum Hall states. Classically, this can be understood as the Lorentz force-induced cyclotron motion of the electrons being interrupted by the edges of the sample that turns the motion into 'skipping' orbits along the edge.

In a FQH system at filling ν the elementary excitations of the bulk are localised quasiparticles with a charge that is a multiple of $-e\nu$ [11, 32] (meaning they can carry a fraction of the electron charge!). Furthermore, in the case $\nu = 1/3$ the charge of the edge modes is also $-e/3$ [32]. While the edge excitations in the integer quantum Hall case can be described by a chiral 1D Fermi liquid theory, those of the FQH effect are described as a *chiral Luttinger liquid* [24]. This implies a 1D bosonisation of the low-energy excitations as done below. Importantly, we stress again that one cannot remove the fractional charges from the system. They exist only through the interaction of many electrons and the total charge of the whole system must remain an integer times the electron charge.

As noted, the FQH liquid is a great example of a physical system with phases that cannot be distinguished by symmetries and instead are characterised by a topological invariant. The

[2] We will often carelessly set $\hbar = 1$ when its specific value is unimportant.

topological invariant of the bulk (the filling factor ν) determines the charge and structure of the edge modes – an example of the bulk-edge correspondence [24]. At transitions between the different phases, ρ_{xx} becomes finite and the bulk must become either gapless or the states delocalised before the system can enter another phase with a different filling factor [28]. Next we will see how the FQH systems can be exploited to construct PFs.

1.2 Physical realisations

In a work by Fidkowski and Kitaev from 2011 (Ref. [34]) it was proven that MFs are the only non-trivial zero-energy modes that can exist in 1D electron systems. Later work by Lindner *et al.* 2012 [11] and Clarke *et al.* 2013 [12], however, proved that this constraint can be circumvented by forming 1D systems out of the edge states of non-trivial 2D materials, enabling the construction of parafermionic zero-energy modes. Here we review their approach for the physical realisation of such systems which serves as a reference for our work presented in later chapters. Similar proposals are discussed in e.g. Refs. [23, 25]. After this we review an experiment [20] that combines elements of the theoretical proposals and shows resistance data that is compatible with the presence of PFs in the system.

Theoretical proposals

Consider a FQH system at filling factor $\nu = 1/m$ (m is an odd integer) described by the Laughlin wave function in Eq. (1.21). We introduce the edge fields $\phi_{R(L)}(x)$ which satisfy the commutation relations

$$[\phi_{R(L)}(x), \phi_{R(L)}(x')] = \overset{+}{(-)} \frac{i\pi}{m} \operatorname{sgn}(x - x'), \qquad [\phi_L(x), \phi_R(x')] = \frac{i\pi}{m}. \tag{1.22}$$

In terms of these fields the operator $e^{i\phi_{R(L)}(x)}$ annihilates a right(left)-moving low-energy excitation of charge $-e/m$ at position x in the edge. The commutation relation of two such modes is

$$e^{i\phi_{R(L)}(x)} e^{i\phi_{R(L)}(x')} = e^{i\phi_{R(L)}(x')} e^{i\phi_{R(L)}(x)} e^{\overset{+}{(-)} i \frac{\pi}{m} \operatorname{sgn}(x'-x)}, \tag{1.23}$$

which resembles Eq. (1.4) with $2m = N$. This hints at the fact that these edge modes might serve as a viable platform PFs. From the quasiparticle operators we can write the electron operators as $\psi_{R(L)} \sim e^{im\phi_{R(L)}}$ which indeed obey the Fermi statistics:

$$\begin{aligned} \psi_{R(L)}(x)\psi_{R(L)}(x') &\sim e^{im\phi_{R(L)}(x)} e^{im\phi_{R(L)}(x')} = e^{im\phi_{R(L)}(x')} e^{im\phi_{R(L)}(x)} e^{-m^2[\phi_{R(L)}(x), \phi_{R(L)}(x')]} \\ &\sim \psi_{R(L)}(x')\psi_{R(L)}(x) e^{\overset{-}{(+)} i\pi m \operatorname{sgn}(x-x')} = -\psi_{R(L)}(x')\psi_{R(L)}(x). \end{aligned} \tag{1.24}$$

Since m is an odd integer the fields anticommute also when 'mixing' the right and left-moving fields. The same holds true also when one or both of the operators are Hermitian conjugated.

The proposals by Refs. [11, 12] were to combine two FQH systems of the same filling factor but opposite sign Landé g-factors such that the spins of the edge modes would be antiparallel. Aligning two $\nu = 1/m$ FQH 2D electron gasses as in Fig. 1.5, the interface would have counterpropagating gapless states of opposite spins. In order to create a localised mode in this interface they introduced two different mechanisms to induce a gap in the helical edge modes; an insulator with spin-orbit coupling to induce backscattering between the edges and an s-wave SC to couple electrons from

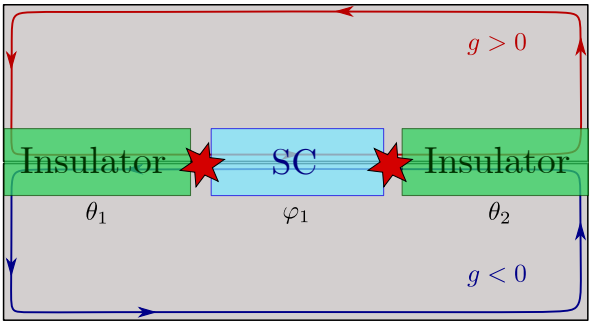

Figure 1.5: Adaptation of Figure 2a of Ref. [12] sketching their proposed heterostructure consisting of two FQH systems (grey) with opposite sign g-factors and same fractional filling factor $\nu = 1/m$. The red and blue lines symbol the edge modes of antiparallel spins. The helical edge modes are gapped by an s-wave SC (blue) and insulators with spin-orbit coupling (green). Under each of the blocks we indicate the pinned values of the bosonic fields. PFs (red stars) are predicted to be localised at the domain walls between the two gapping mechanisms. This is a slightly modified version of the original proposal where the SC is replaced by an insulator and vice versa, but the underlying concept is the same.

each edge into Cooper pairs and induce a superconducting pairing gap via proximity effect [35].[3] This demands a SC that can sustain the high magnetic fields required for the FQH effect. In Fig. 1.5 we show an adaptation of the architecture presented in Clarke *et al.* 2013 [12]. To obtain the PFs it is assumed that backscattering only takes place under the insulators, that Cooper pairs are only formed under the SC and that the chemical potential μ of the edge modes lies within the induced energy gaps. This way the edges of the FQH interface are gapped everywhere except from the domain walls between SC and insulators. This is where PFs are predicted to be localised, which we will now look into.

The fields $\phi_{R(L)}$ are rewritten in terms of two massless *bosonic* fields, φ and θ, as $\phi_{R(L)} = \varphi \overset{+}{(-)} \theta$. We fix the convention of the commutation relation between these new fields to be

$$\left[\varphi(x), \theta(x')\right] = \frac{i\pi}{m}\Theta(x' - x)\,, \tag{1.25}$$

where $\Theta(x)$ is the Heaviside step function. In terms of these fields the charge density of the FQH edges is given by $\rho(x) = -\partial_x\theta/\pi$ and the spin density is $\partial_x\varphi/\pi$ (in units of $\hbar/2$) [11]. As mentioned in the previous section, the gapless counterpropagating edge modes are described as a chiral Luttinger liquid. In terms of the bosonic fields the Hamiltonian of this 1D system reads

$$H_0 = \frac{\nu m}{2\pi}\int \mathrm{d}x \left[K\left(\partial_x\varphi\right)^2 + \frac{1}{K}\left(\partial_x\theta\right)^2\right], \qquad K = 1\,. \tag{1.26}$$

Here $K = 1$ is the Luttinger parameter where we disregard Coulomb interaction between the edge modes. ν is the speed of the edge modes, which we assume to be constant and the same in both directions, and $\nu = 1/m$ is the filling factor of the FQH system. Now we include also the SC and

[3] Alternatively, the insulator could be replaced by a ferromagnet and the FQH systems by a fractional topological insulator, see Refs. [11, 25].

insulators such that the interface is modelled with $H = H_0 + H_1$ where H_1 describes the coupling induced by SC and insulators;

$$H_1 = -\int \mathrm{d}x \left[g_S(x)\psi_R\psi_L + g_I(x)\psi_R^\dagger\psi_L \right] + \text{H.c.} \sim -\int \mathrm{d}x \left[g_S(x)\cos(2m\varphi) + g_I(x)\cos(2m\theta) \right]. \tag{1.27}$$

Here $g_S(x)$ and $g_I(x)$ are the position-dependent couplings of the edge modes, proximity-induced by the SC and insulators, respectively. Consider now the limit where g_S is strong under the SC, compared to the kinetic energy in H_0, and sharply transitions to zero outside this region. With analogous assumptions for g_I under the insulators we can approximate the bosonic fields φ and θ to each being pinned to one of their $2m$ (semiclassical) minima $\varphi_1, \theta_i = \{0, \frac{\pi}{m}, \frac{2\pi}{m}, \ldots, \frac{(2m-1)\pi}{m}\}$ under the corresponding element. Here φ_1 is the pinned value of the φ field under the SC, θ_1 is the θ field under the left insulator and θ_2 that under the right insulator, see Fig. 1.5. In the thin domain walls between the SC and the insulators $g_S(x)$ and $g_I(x)$ vanish and the fields can fluctuate. A low-energy effective description of these domains is then given by H_0 bounded by the conditions on φ and θ under each of the surrounding domains. It can be shown [11, 12] that the operators

$$\alpha_1 = \mathrm{e}^{i(\varphi_1 - \theta_1)}, \qquad \alpha_2 = \mathrm{e}^{i(\varphi_1 - \theta_2)}, \tag{1.28}$$

commute with the effective Hamiltonian when disregarding excitations with a finite energy gap inversely proportional to the domain wall length. Hence, they represent zero-energy modes and are localised in the left and right domain walls, respectively. Since both operators are $\mathrm{e}^{i\phi_L}$ evaluated in the corresponding domain wall they change the charge by $-e/m$. For $m > 1$ these are the PF operators introduced in Sec. 1.1 with $N = 2m$;

$$\alpha_1^{2m} = \mathrm{e}^{i2m(\varphi_1 - \theta_1)} = \mathrm{e}^{i2m\left(\frac{q\pi}{m} - \frac{q'\pi}{m}\right)} = \mathbb{1}, \qquad \alpha_2^{2m} = \mathrm{e}^{i2m(\varphi_1 - \theta_2)} = \mathbb{1}. \tag{1.29}$$

$$\begin{aligned} \alpha_1\alpha_2 &= \mathrm{e}^{i(2\varphi_1 - \theta_1 - \theta_2) + \frac{1}{2}[\varphi_1, \theta_2]} = \mathrm{e}^{i(\varphi_1 - \theta_2) + i(\varphi_1 - \theta_1) + \frac{1}{2}[\theta_2, \varphi_1] + [\varphi_1, \theta_2]} \\ &= \mathrm{e}^{i(\varphi_1 - \theta_2)}\,\mathrm{e}^{i(\varphi_1 - \theta_1)}\,\mathrm{e}^{[\varphi_1, \theta_2]} = \alpha_2\alpha_1\,\mathrm{e}^{i\frac{\pi}{m}}. \end{aligned} \tag{1.30}$$

In the first equations we use that φ_1, θ_1 and θ_2 are each pinned to a minimum $\frac{q\pi}{m}$ with $q = \{0, 1, \ldots, 2m-1\}$, and to show the commutation relation we use Eq. (1.25). The zero-modes yield a 2m-fold degeneracy of the ground state, corresponding to the eigenvalues of the parity operator defined in Eq. (1.12):

$$P_{12} = \mathrm{e}^{-i\frac{\pi}{2m}}\alpha_2^\dagger\alpha_1 = \mathrm{e}^{-i\frac{\pi}{2m}}\mathrm{e}^{-i(\varphi_1 - \theta_2)}\mathrm{e}^{i(\varphi_1 - \theta_1)} = \mathrm{e}^{-i\frac{\pi}{2m}}\mathrm{e}^{-i(\theta_1 - \theta_2) - \frac{1}{2}[\theta_2, \varphi_1]} = \mathrm{e}^{-i(\theta_1 - \theta_2)} = \mathrm{e}^{-i\frac{\pi\hat{q}}{m}}. \tag{1.31}$$

The $2m$ different eigenstates of P_{12} correspond to $2m$ different charge states of the SC: $\int \rho(x)\,\mathrm{d}x = (\theta_1 - \theta_2)/\pi = \frac{q}{m}$, where the integral is from the domain wall edge of the left insulator to that of the right insulator. This means that the SC can host $2m$ different charge states: $0, \frac{e}{m}, \frac{2e}{m}, \ldots, \frac{(2m-1)e}{m}$ modulo $2e$. Indeed, since the charge of the SC is only defined up to one Cooper pair, $\mathrm{e}^{-i\pi\hat{Q}} = \mathrm{e}^{-i\frac{\pi\hat{q}}{m}}$ is an appropriate charge operator [11]. In the Majorana case $m = 1$ it represents the electron parity of the SC. We can write the fusion of the two PFs schematically as $\alpha_1 \otimes \alpha_2 = 0 \oplus 1 \oplus \ldots \oplus 2m-1$, i.e. in terms of the number of fractional charges.

In a realistic scenario, the fields φ and θ will not be ideally pinned as we assumed and, as discussed previously, the two PFs will hybridise like $-\varepsilon\,\mathrm{e}^{i\phi}\,P_{12} + \text{H.c.}$ where the coupling strength ε

is expected to decay exponentially with g_S and the length L of the gapped superconducting region like $e^{-g_S L/v}$ [11]. We will quantify this coupling better in Ch. 2. Hence, the ground state is $2m$-fold degenerate within exponential accuracy.

Alternatively, we could do everything in terms of the analogous PF operators $\tilde{\alpha}_1 = e^{i(\varphi_1+\theta_1)}$ and $\tilde{\alpha}_2 = e^{i(\varphi_1+\theta_2)}$, constructed from the right-moving field, with a similar commutation relation;

$$\tilde{\alpha}_2\tilde{\alpha}_1 = e^{i(2\varphi_1+\theta_1+\theta_2)}\, e^{-\frac{1}{2}[\theta_2,\varphi_1]} = e^{i(\varphi_1+\theta_1)}\, e^{i(\varphi_1+\theta_2)}\, e^{-[\theta_2,\varphi]} = \tilde{\alpha}_1\tilde{\alpha}_2\, e^{i\frac{\pi}{m}}\,, \tag{1.32}$$

and parity operator;

$$e^{i\frac{\pi}{2m}}\,\tilde{\alpha}_2^\dagger\tilde{\alpha}_1 = e^{i\frac{\pi q}{m}}\,. \tag{1.33}$$

Since both types of operators lead to equivalent descriptions of the system in Fig. 1.5, differing only in local operators, we stick to the former definition without loosing any degrees of freedom [36].

If we prolonged the insulator-SC-insulator construction with $n-1$ repeated segments of SC-insulator along the interface we would have in total $2n$ PFs. In terms of the φ and θ fields the operators can be expressed as

$$\alpha_{2n-1} = e^{i(\varphi_n-\theta_n)}, \qquad \alpha_{2n} = e^{i(\varphi_n-\theta_{n+1})}, \tag{1.34}$$

where φ_n is the φ field pinned under the n^{th} SC, and θ_n the θ field pinned under the n^{th} insulator. The charge operator of the n^{th} SC is then $e^{-i(\theta_n-\theta_{n+1})}$, and a spin operator for the insulating regions can be defined analogously as $e^{i(\varphi_n-\varphi_{n-1})}$. Note, however, that this spin operator cannot be exploited to distinguish the $2m$ states characterised by the charge operator since the two do not commute.

Example of experimental signatures

In 2020 a preprint was shared on arXiv containing data that could indicate a successful realisation of induced superconductivity in edge states of quantum Hall systems. The results, published in 2022 by Gül *et al.* [20], displayed signatures of crossed Andreev reflection over a SC placed in a trench of a Hall bar. The 2D electron gas consisted of a single-layer graphene sheet encapsulated by a hexagonal boron nitride dielectric, and to screen remote impurities the whole thing was sandwiched between two layers of graphite. The trench was etched into one end of the Hall bar and extended into the bulk and a thin finger of superconducting niobium nitride (NbN), < 100 nm wide and ~ 1 µm long, was placed therein. A device like this is reprinted in Fig. 1.6a (Figure 1b of Ref. [20]) where the purple Hall bar is the graphene heterostructure and the thin blue stick on the right is the grounded NbN SC. With the gate voltage V they could control the potential of the edge modes and thereby the filling factor of the quantum Hall liquid. In the top, a current bias I_{exc} was inserted and the longitudinal voltage V_{XX} and Hall voltage V_{XY} were measured by normal leads. The voltage V_{CAR} of the edge modes propagating away from the SC was measured as well. A negative V_{CAR} is thought to reflect that electrons are converted to holes in the SC. In the figure, the full and dashed arrows depict electron and hole-like conduction, respectively. It is this setup that has served as a basis construction for the proposals presented in later chapters.

The edge modes of the quantum Hall system are thought to run along each side of the SC, which induces a superconducting pairing between the counterpropagating modes. Despite the fact that the edge modes are polarised by the large magnetic field and that NbN is an s-wave SC, the edge modes are believed to be paired anyway due to the spin-orbit coupling of NbN, effectively

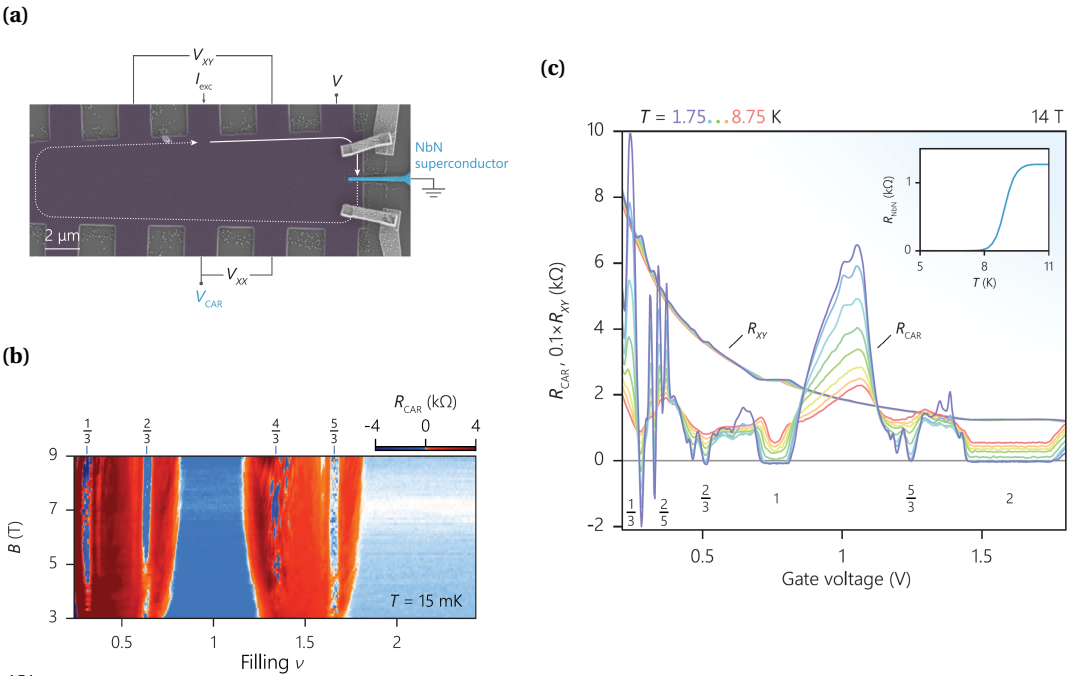

Figure 1.6: Figures 1(b), 1(d) and 1(f) from Gül *et al.* [20]. **(a)** One of the devices used to probe induced superconductivity in quantum Hall edge modes. A magnetic field up to 14 T is applied perpendicularly to the Hall bar (purple). The SC (blue) is placed in a trench of the graphene. The arms of the Hall bar extend and connect to normal leads that are not shown. They supplied the current bias I_{exc} and measured the voltages V_{XY}, V_{XX} and V_{CAR} as well as the potential V of the edge modes that propagate towards the SC and also controls the filling factor ν. **(b)** R_{CAR} colour plot as a function of the filling and the strength B of the magnetic field. An $R_{\text{CAR}} < 0$ is believed to indicate that crossed Andreev reflection takes place over the SC. **(c)** R_{CAR} and R_{XY} as functions of gate voltage for different temperatures in a field of 14 T. The inset shows the superconducting transition of the SC at around 8 K in the 14 T field.

leading to a p-wave-like pairing.[4] The authors of Ref. [20] claimed to have obtained a graphene-SC interface that is transparent enough to allow for this pairing – also helped by the small width (< 100 nm) of the SC which has a coherence length of about 50 nm. The high-quality graphene heterostructure ensures that the magnetic field required to see robust quantum Hall states, both integer and fractional, is low enough that the NbN can remain superconducting due to its large critical field. The idea is that particle-like charges in the edge (e.g. modes with charge $e^* = -e/3$) are drained into the SC by crossed Andreev reflection such that a hole-like charge (e.g. of charge $e^* = +e/3$) propagate further down the edge stream, resulting in an $R_{\mathrm{CAR}} = V_{\mathrm{CAR}}/I_{\mathrm{exc}} < 0$. The effective charge $2e^* = -2e/m$ left on the SC can, with $m-1$ identical processes, form one Cooper pair. The system is gapped to the left of the SC by the bulk quantum Hall incompressible liquid taking over the role of the insulator in the proposals of Refs. [11, 12]. By analogy with the systems described above, the SC should host a localised zero-energy mode at the left end. The other end is not gapped in the same way and the zero-mode of this end is delocalised along the right edge of the Hall bar.

In the experiment, they observed an $R_{\mathrm{CAR}} < 0$ for quantised values of $R_{XY} = V_{XY}/I_{\mathrm{exc}}$ for both integer and fractional fillings, in particular $\nu = 1/3$, see Fig. 1.6b and 1.6c. This implied that the bulk of the quantum Hall system was gapped while the resistance of the edge below the SC became negative, possibly due to Andreev-reflected holes. However, the corresponding probability for crossed Andreev reflection $-V_{\mathrm{CAR}}/V$ was less than 6% even in the most pronounced cases. The authors explained this by dissipation, possibly via vortices in the SC, and by direct tunnelling of edge modes without Andreev reflection, related to disorder in the graphene-SC interface. The probability for crossed Andreev reflection was comparable for integer-filling states and furthermore insensitive to the magnetic field strength for small current bias and low temperature (compared to the induced pairing). This is consistent with a topologically non-trivial induced energy gap. For one of the devices the behaviour of this probability with temperature was found to be consistent with the following interpretation: for integer fillings (or hole-like fractional fillings) the superconducting pairing was between integer charges whereas for the particle-like fractional fillings, the pairing was between fractional charges as opposed to pairing of bunched fractional charges. Another device, however, showed contradicting results. Together with the overall low probability for crossed Andreev reflection and discussion of the interpretation of a $V_{\mathrm{CAR}} < 0$ this means that further investigation of this type of system is needed. The issue is treated for example in Ref. [21].

[4] In fact even for $\nu = 2$, spin-orbit coupling is required due to the mismatch between the Fermi momenta of the opposite-spin modes.

2

Readout of parafermionic states by transport measurements

This chapter is an adaptation of I. E. Nielsen, K. Flensberg, R. Egger and M. Burrello, *Readout of Parafermionic States by Transport Measurements*, Phys. Rev. Lett. **129** (2022) [1] with more elaborate and detailed calculations.

In this chapter we investigate and discuss methods to measure signatures of $\mathbb{Z}_6$ parafermions (PFs) by the use of transport spectroscopy. The underlying idea is to exploit the property that the corresponding operators act as Majorana fermion (MF) operators when taken to the third power α^3 as mentioned in Sec. 1.1. It is thereby possible to couple PFs to normal fermionic electrons which we will introduce through standard metallic leads. While this idea is independent from the concrete system in which the PFs are realised and was conceived before the experimental setup and results of Ref. [20] were published, we have incorporated this type of construction, described in Sec. 1.2, in our work and use it as the basis setup for our proposed measurements. Thus, we consider the graphene fractional quantum Hall (FQH) system in the Laughlin state at filling $\nu = 1/3$ with counterpropagating edge modes coupled through induced superconductivity yielding an effectively topological superconductor (SC) with $\mathbb{Z}_6$ symmetry. We review two complimentary setups to investigate the PFs: in Sec. 2.1 we consider a grounded SC hosting two PFs that interact as described in Ch. 1. We will see that in a low-energy approximation the system conductance can reveal a $\mathbb{Z}_3$ degree of freedom of the $\mathbb{Z}_6$ PFs. Furthermore, we argue that for weak quasiparticle poisoning a three-state telegraph noise in the conductance can be observed – a phenomenon that we will investigate in more detail in the next chapter. In Sec. 2.2 we look into the two-terminal electron conductance of a Coulomb-blockaded SC with PFs, providing additional characteristics of parafermionic modes.

The simplest type of PFs, the MFs, are typically explored in hybrid SC-semiconductor devices where charge transport measurements are used to probe the presence of midgap low-energy excitations in the SC [13, 15–17, 37]. But a zero-bias conductance peak does not imply that the SC is topological or prove the existence of MFs; it only reveals the presence of a zero-energy state. The parity shared by a pair of MFs is the main degree of freedom in proposals for topological quantum computation based on these modes. However, it cannot be read by the transport measurements where electrons with energies below the superconducting gap tunnel into the system and continuously flip the fermionic parity whereby the information encoded in this is lost. The situation is different for $\mathbb{Z}_6$ PFs where the $\mathbb{Z}_3$ part of their shared degree of freedom *can* be detected by transport spectroscopy. As described in Ch. 1 the Hamiltonian for two interacting $\mathbb{Z}_6$ PFs ($\alpha^6 = \mathbb{1}$) with a finite energy splitting ε is [8]

$$H_{2\mathrm{pf}}(q) = -\varepsilon\, \mathrm{e}^{-i\left(\phi+\frac{\pi}{6}\right)}\, \alpha_2^\dagger \alpha_1 + \mathrm{H.c.} = -2\varepsilon \cos(\pi q/3 + \phi)\,, \tag{2.1}$$

where $q = \{0, 1, \ldots, 5\}$ distinguishes the six degenerate ground states by the factional charge $Q = -qe/3$ up to one Cooper pair. We now introduce the *reduced charge* $\tilde{Q} = -\tilde{q}e/3 = (Q \mod 1e)$ counting the charge of the SC up to one electron, i.e. $\tilde{q} = \{0, 1, 2\}$. We can express the parity operator [25] of the two PFs ($P_{12} = \mathrm{e}^{-i\frac{\pi}{3}\hat{q}}$) in terms of an operator for this reduced charge number and the MF-like operators α_1^3 and α_2^3. We first rewrite the corresponding MF parity:

$$P_M = \mathrm{e}^{-i\frac{\pi}{2}}\, \gamma_2\gamma_1 = -i(\alpha_2^\dagger)^3(\alpha_1)^3 = -i\,\mathrm{e}^{i\frac{3\pi}{3}}\,(\alpha_2^\dagger\alpha_1)^3 = i\left(\mathrm{e}^{i\frac{\pi}{3}\left(\frac{1}{2}-\hat{q}\right)}\right)^3 = -\mathrm{e}^{-i\pi\hat{q}}\,, \tag{2.2}$$

where we use that $(\alpha_2^3) = (\alpha_2^\dagger)^3$ and the commutation relation $\alpha_2^\dagger\alpha_1 = \mathrm{e}^{i\frac{\pi}{3}}\,\alpha_1\alpha_2^\dagger$ [12]. We can then state the PF parity operator as

$$P_{12} = \mathrm{e}^{-i\frac{\pi}{3}\hat{q}} = \mathrm{e}^{i\pi\hat{q}}\,\mathrm{e}^{-i\frac{4\pi}{3}\hat{q}} = -\,\mathrm{e}^{i\frac{\pi}{2}}\,\gamma_1\gamma_2\,\mathrm{e}^{-i\frac{4\pi}{3}\hat{q}} = i\gamma_2\gamma_1\,\mathrm{e}^{-i\frac{4\pi}{3}\tilde{q}}\,. \tag{2.3}$$

Here we use that $\exp(-i4\pi q/3)$ is pairwise the same for $q = \{0, 3\}$, $q = \{1, 4\}$ and $q = \{2, 5\}$ to replace the operator $\hat{q}$ with the one corresponding to the reduced charge number $\tilde{q}$. To avoid clumsy

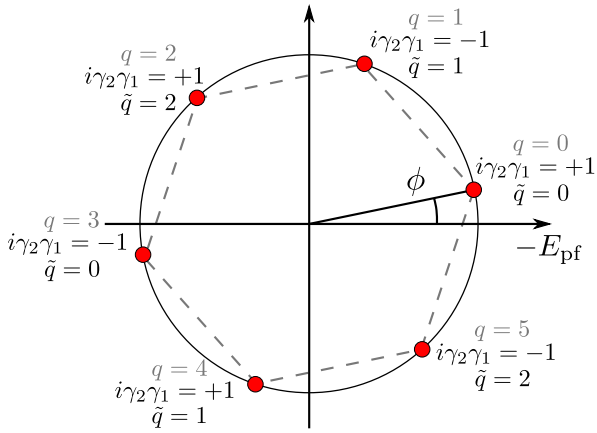

Figure 2.1: Illustration of how the different q and $\tilde{q}$ sectors relate and the corresponding six energy levels. For example, $q = 0$ and $q = 3$ are related by a change in the electron parity. The projection onto the horizontal axis is proportional to the energy of the state. A finite ϕ ($\neq n\pi/6$, $n \in \mathbb{Z}$) split degeneracies in $H_{2\mathrm{pf}}$ (Eq. (2.1)) and with the optimal value $\phi = \arctan(1/\sqrt{27})$ the three energies $|2\varepsilon\cos(4\pi\tilde{q}/3+\phi)|$ for $\tilde{q} = 0,1,2$ are maximally separated.

symbols we leave out a ˆ above this operator, but as long as we consider the eigenstates we are free to shift to eigenvalues. In turn the reduced charge number operator can be expressed in terms of the PF operators, and consequently the operator $\hat{q}$, as

$$e^{i\frac{4\pi}{3}\tilde{q}} = e^{i\frac{2\pi}{3}\hat{q}}\,. \tag{2.4}$$

For the explicit calculation we refer to Eq. (B.2) in App. B.

In total we can now write the Hamiltonian in Eq. (2.1) as

$$H_{2\mathrm{pf}}(\tilde{q}) = -\varepsilon i\gamma_2\gamma_1\left(e^{i\phi}e^{i\frac{4\pi}{3}\tilde{q}} + e^{-i\phi}e^{-i\frac{4\pi}{3}\tilde{q}}\right) = -2\varepsilon i\gamma_2\gamma_1\cos(4\pi\tilde{q}/3+\phi) = -i\frac{\Delta_\varepsilon(\tilde{q})}{2}\gamma_2\gamma_1\,. \tag{2.5}$$

Here we have introduced the energy variable $\Delta_\varepsilon(\tilde{q}) = 4\varepsilon\cos(4\pi\tilde{q}/3+\phi)$. We have separated the two-PF Hamiltonian into a fermionic part and a fractional charge and we can recast the eigenstates $|q\rangle$ into the form $|i\gamma_2\gamma_1, \tilde{q}\rangle$. The relation between q, $\tilde{q}$ and the eigenvalues of $i\gamma_2\gamma_1$ is illustrated in Fig. 2.1. If $\phi = 0$, the two sectors $\tilde{q} = 1$ and $\tilde{q} = 2$ are degenerate while for a finite ϕ this degeneracy is lifted until $\phi = \pi/6$ where the sectors $\tilde{q} = 0$ and $\tilde{q} = 2$ are now degenerate. Our proposal relies on transport spectroscopy and requires that the energies of the different $\tilde{q}$ sectors are distinguishable. To get the most resolved signals we will therefore consider a ϕ such that the energy splittings are equidistant:

$$\begin{aligned} &|\Delta_\varepsilon(0)| - |\Delta_\varepsilon(2)| = |\Delta_\varepsilon(2)| - |\Delta_\varepsilon(1)| = |\Delta_\varepsilon(1)|\,, \qquad \text{for } \phi < \frac{\pi}{6} \\ &|\cos(\phi + 8\pi/3)| = 2|\cos(\phi + 4\pi/3)|\,, \qquad \text{for } \phi < \frac{\pi}{6}\,. \end{aligned} \tag{2.6}$$

This is fulfilled by $\phi = \phi_0 = \arctan(1/\sqrt{27}) \approx 0.19$, as illustrated in Fig. 2.2, or any phase $\phi = \frac{n\pi}{3} \pm \phi_0$ where n is an integer. We stress again that, depending on the implementation, the phase may

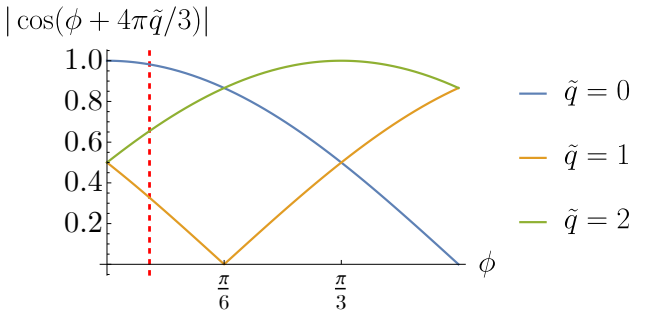

Figure 2.2: Visualisation of the energy splitting in the three sectors $\tilde{q} = 0, 1, 2$ as a function of the phase ϕ.

be tunable or not. In the consider setup, ϕ could possibly be controlled by small changes in the chemical potential of the edge modes [38].

The Hamiltonian in Eq. (2.5) looks similar to that of a pair of overlapping zero-energy MFs [7], but with an energy splitting that depends on the quantum number $\tilde{q}$. It is this $\mathbb{Z}_3$ degree of freedom we claim can be seen by transport spectroscopy.

2.1 Conductance signals of the grounded device

The setup we have in mind to measure signatures of the $\mathbb{Z}_3$ degree of freedom is very similar to that of Ref. [20] shown in Fig. 1.6a, see also Refs. [11, 12, 36, 39–43]. The distinction from the original device is that the trench containing the SC is now placed in the bulk of the Hall bar such that the PFs are localised in both ends, and the SC is not coupled to the outer edge modes of the Hall system. The FQH bulk replaces the insulator in the previously discussed proposals [11, 12], providing the strong electron backscattering. Due to the energy gap Δ_{FQH} of the bulk FQH liquid, the PFs do not exchange fractional charges with the environment at low temperatures $Tk_{\text{B}} \ll \Delta_{\text{FQH}}$ (where k_{B} is the Boltzmann constant). The SC is still grounded, and counterpropagating edge modes of charge $-e/3$ running on either side of the trench inherit by proximity a superconducting pairing and energy gap. As described in Sec. 1.2, the strong spin-orbit coupling of niobium nitride is necessary to induce the pairing between the otherwise polarised edge fields [20, 43]. In Fig. 2.3 we illustrate the setup with the $\nu = 1/3$ FQH liquid in purple, the SC in blue and red stars to symbol the PFs α_1 and α_2. Considering energies below the induced superconducting gap, the Hamiltonian describing the two is indeed that of Eqs. (2.1) and (2.5) where the phase $\phi = \mu\nu L/\hbar v$ [38, 44] depends on the chemical potential of the edge modes μ, their velocity v and the length L of the SC. We introduce a normal metallic lead which couples only to the PFs and *not* the outermost edge modes, isolated from the metallic lead by insulating elements. Furthermore, an insulator is placed between the lead and the SC to minimise the direct coupling between the two. The coupling between lead and PFs allows single electrons to tunnel in and out of the effective topological SC constituted by the combined edge mode + SC system. This means that the integer part of Q is not conserved but only the fractional charge $\tilde{Q} = -\tilde{q}e/3$. The reduced charge number $\tilde{q}$ is then a topologically protected quantity that can be exploited to store quantum information. It is this property that we want to read with transport spectroscopy thanks to the $\tilde{q}$-dependent energy splitting of the interacting PFs.

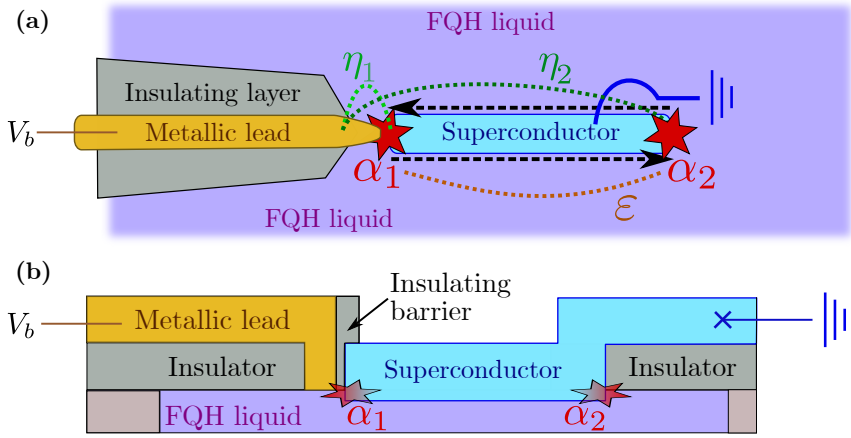

Figure 2.3: A device with two PFs (red stars) emerging from the superconducting pairing of the edge modes (dashed black arrows) along the trench, proximity-induced by the grounded SC (blue). **(a)** and **(b)** provide a top and section view, respectively. The FQH liquid (purple) is in the $\nu = 1/3$ Laughlin state. A metallic lead (gold) couples to the edge modes close to the left PF α_1 and is isolated from the SC and outer edge modes by insulators (grey). The Fermi level of the electrons is controlled by the voltage bias V_b with respect to the grounded SC. The tunnel couplings $\eta_{1,2}$ are illustrated in (a) together with the PF overlap ε.

We introduce the operator $l^{(\dagger)}$ associated with annihilation(creation) of an electron at the tip of the lead and consider only one spin type due to the strong magnetic field. Because of the SC, the coupling between lead and PFs leads to both coherent tunnelling of electrons in and out of the system as well as the formation and destruction of CPs from one electron in the lead and one electron extracted from or inserted into the effective topological SC. As mentioned, α_i^3 behaves as a MF operator and, in analogy with similar Majorana setups [45–49], the coupling is modelled with the Hamiltonian

$$H_c = i \sum_{j=1,2} \eta_j \gamma_j \left(e^{i\chi_j} l + e^{-i\chi_j} l^\dagger \right). \tag{2.7}$$

Here $\eta_{1,2} e^{i\chi_{1,2}}$ is the tunnelling amplitude between the lead and the PF $\alpha_{1,2}$ with real $\{\eta_j, \chi_j\}$. We expect that $\eta_1 \gg \eta_2$ due to the construction. Analogously to Majorana systems, this coupling changes the PF charge by $\pm e$ due to the fact that $\alpha_{1,2}|q\rangle \propto |q-1\rangle$ and $\alpha_{1,2}^\dagger |q\rangle \propto |q+1\rangle$ as shown in Eqs. (1.9)-(1.11) of Ch. 1. Importantly, H_c commutes with the reduced fractional charge number $\tilde{q}$ since it, involving only $\gamma_j = \alpha_j^3$, exclusively changes the fermionic parity $i\gamma_2\gamma_1$. The conductance of the device in Fig. 2.3 between the normal lead and the grounded SC can therefore be calculated in the same way as for a corresponding two-MF device. To this end, we employ the Weidenmüller formula [50] which requires three assumptions of the normal electrode: First, that the lead bandwidth is the largest energy scale in the system. Second, that the lead density of states ν_l is constant in the energy range defined by the voltage bias V_b. And third, that electron-electron interaction in the lead can be neglected.

As mentioned in the previous chapter, a pair of MF operators can be expressed as one electron:

$c^{(\dagger)} = (\gamma_1 \overset{+}{(-)} i\gamma_2)/2$ [7, 19]. We can therefore express the PF Hamiltonian (Eq. (2.5)) for a specific $\tilde{q}$ sector as

$$H_{2\mathrm{pf}}(\tilde{q}) = -i\frac{\Delta_\varepsilon(\tilde{q})}{2} i(c^\dagger - c)(c^\dagger + c) = \Delta_\varepsilon(\tilde{q})\left(c^\dagger c - \frac{1}{2}\right), \tag{2.8}$$

where, as defined above, $\Delta_\varepsilon(\tilde{q}) = 4\varepsilon\cos(4\pi\tilde{q}/3 + \phi)$. Similarly, we can also write the coupling Hamiltonian in terms of these electron operators:

$$\begin{aligned} H_c &= i\eta_1\left(c^\dagger + c\right)\left(l + l^\dagger\right) + i\eta_2 i\left(c^\dagger - c\right)\left(\mathrm{e}^{i(\chi_2-\chi_1)}\, l + \mathrm{e}^{-i(\chi_2-\chi_1)}\, l^\dagger\right) \\ &= c^\dagger l\left(i\eta_1 - \eta_2\,\mathrm{e}^{i\tilde{\chi}}\right) + c^\dagger l^\dagger\left(i\eta_1 - \eta_2\,\mathrm{e}^{-i\tilde{\chi}}\right) + c l\left(i\eta_1 + \eta_2\,\mathrm{e}^{i\tilde{\chi}}\right) + c l^\dagger\left(i\eta_1 + \eta_2\,\mathrm{e}^{-i\tilde{\chi}}\right). \end{aligned} \tag{2.9}$$

Here we made the gauge transformation $l \to l\,\mathrm{e}^{-i\chi_1}$ and put $\chi_2 - \chi_1 = \tilde{\chi}$. We see from this that the coupling indeed only conserves the total fermion parity and not the total number of fermions. We introduce the vectors $\underline{c} = (c, c^\dagger)$ and $\underline{l} = (l, l^\dagger)$ and write H_c as

$$H_c = \underline{c}^\dagger W \underline{l} + \underline{l}^\dagger W^\dagger \underline{c}, \qquad W = \frac{1}{2}\begin{pmatrix} i\eta_1 - \eta_2\,\mathrm{e}^{i\tilde{\chi}} & i\eta_1 - \eta_2\,\mathrm{e}^{-i\tilde{\chi}} \\ i\eta_1 + \eta_2\,\mathrm{e}^{i\tilde{\chi}} & i\eta_1 + \eta_2\,\mathrm{e}^{-i\tilde{\chi}} \end{pmatrix} = \frac{1}{2}\begin{pmatrix} W_{11} & W_{12} \\ W_{21} & W_{22} \end{pmatrix}. \tag{2.10}$$

Note that the *coupling matrix* W does not depend on the energy of the lead electrons. We state also the Bogoliubov-de Gennes Hamiltonian [51] corresponding to the (fermionic part of the) two-PF Hamiltonian in the $\underline{c}$ basis:

$$H_{2\mathrm{pf}}^{\mathrm{BdG}}(\tilde{q}) = \begin{pmatrix} \Delta_\varepsilon(\tilde{q}) & 0 \\ 0 & -\Delta_\varepsilon(\tilde{q}) \end{pmatrix}. \tag{2.11}$$

Here we disregard the constant energy contribution. The scattering matrix, relating in- and outgoing electron mode amplitudes, is by the Weidenmüller formula [50] expressed in terms of this Bogoliubov-de Gennes Hamiltonian and the coupling matrix:

$$S(E) = \mathbb{1}_2 - i2\pi\nu_l W^\dagger \frac{1}{E\mathbb{1}_2 - H_{2\mathrm{pf}}^{\mathrm{BdG}}(\tilde{q}) + i\pi\nu_l W W^\dagger} W = \begin{pmatrix} R_{ee} & R_{eh} \\ R_{he} & R_{hh} \end{pmatrix}. \tag{2.12}$$

Here $\mathbb{1}_2$ is the (2×2) identity matrix, E is the energy of the lead electron and $\nu_l = L_c/h\upsilon_\mathrm{F}$ is the 1D density of states in the lead where L_c is the length of the contact. This expression is valid in the low-energy limit where the induced superconducting gap is a large energy scale such that $H_{2\mathrm{pf}} + H_c$ is a good description of the system. As we can see from the above equation, S is expressed in the $\underline{l}$ basis. The components, R_{ee}, R_{hh} and R_{eh}, R_{he} are named according to the corresponding scattering process, that is, normal electron or hole reflection and Andreev reflection, respectively. Importantly, the expression for the scattering matrix in Eq. (2.12) relies on the system, here described by $H_{2\mathrm{pf}}^{\mathrm{BdG}}(\tilde{q})$, to be effectively non-interacting. The corresponding zero-temperature (differential) conductance $G(E)$ is related to the scattering matrix through the Landauer-Büttiker formalism [52–56]:

$$G(E) = \frac{e^2}{h}\left(1 - R_{ee}^* R_{ee} + R_{he}^* R_{he}\right) = \frac{2e^2}{h}|R_{he}|^2, \tag{2.13}$$

where the last equality follows from the unitarity of the scattering matrix: $SS^\dagger = \mathbb{1}$. In App. B we explicitly calculate the zero-temperature conductance for a given $\tilde{q}$ sector and find

$$G_{\tilde{q}}(E) = \frac{2e^2}{h}\frac{(\pi\nu_l)^2 E^2\left(\eta_1^4 + \eta_2^4 + 2\eta_1^2\eta_2^2\cos 2\tilde{\chi}\right)}{\left(E^2 - \Delta_\varepsilon^2(\tilde{q}) - \left(\pi\nu_l\eta_1\eta_2\sin\tilde{\chi}\right)^2\right)^2 + (\pi\nu_l)^2 E^2\left(\eta_1^2 + \eta_2^2\right)^2}. \tag{2.14}$$

The energy of the incoming electrons with respect to the grounded SC is $E = eV_b$. In the case where only one of the PFs couple to the lead (e.g. $\eta_2 = 0$) and there is no overlap between the PFs ($\varepsilon = 0$), the conductance will display a peak at zero voltage bias $V_b = 0$ for all $\tilde{q}$ sectors. With PF interaction, the conductance will instead show two peaks at $E = eV_b = \pm\Delta_\varepsilon(\tilde{q})$, possibly with three different splittings depending on ϕ. Note that degeneracies in $H_{2\mathrm{pf}}(q)$ leads to degenerate values of $\Delta_\varepsilon(\tilde{q})$ and thereby indistinguishable conductance signals. In general, the conductance peaks are quantised at $2e^2/h$, analogously to two-MF devices [47, 57], when $\tilde{\chi} = 0$ but not for finite $\tilde{\chi} \neq n\pi$, $n \in \mathbb{Z}$. The finite-temperature generalisation of $G_{\tilde{q}}(E)$ is

$$G_{\tilde{q}}(V_b, T) = \int_{-\omega_D}^{\omega_D} \mathrm{d}\omega\, G_{\tilde{q}}(\omega)(-n_{\mathrm{F}}'(\omega)) = \int_{-\omega_D}^{\omega_D} \mathrm{d}\omega\, G_{\tilde{q}}(\omega)\beta n_{\mathrm{F}}(1 - n_{\mathrm{F}}(\omega))\,, \tag{2.15}$$

where $\beta = 1/(k_{\mathrm{B}}T)$ is the inverse of the temperature, $n_{\mathrm{F}}(\omega) = \left(\mathrm{e}^{\beta(\omega - eV_b)} + 1\right)^{-1}$ is the Fermi distribution function in the lead and ω_D an appropriate cut-off energy determined by the temperature. We fix ν_l by assuming gold leads with a Fermi velocity $v_{\mathrm{F}} = 1.4 \times 10^6$ m/s [58] and a length of the metallic contact $L_c = 5\,\mu$m. Note that the conductance is independent of L_c since $\eta_i \propto 1/\sqrt{L_c}$ and $\nu_l \propto L_c$.

In Fig. 2.4 we plot the conductance of Eq. 2.15 at $T = 20$ K for the three different fractional charges $-e\tilde{q}/3$, obtained by numerical integration. In Fig. 2.4a we first show the conductance profile as a function of the voltage bias where the blue, orange and green curves correspond to the signal when the PFs share the fractional charge 0, $-e/3$ and $-2e/3$, respectively (all modulo $1e$). The splitting of the conductance peaks around zero voltage is proportional to the PF overlap, which we here set to $\varepsilon = 0.1$ meV, while the separation between peaks for different charges is optimised by the finite $\phi = \phi_0 = \arctan(1/\sqrt{27}) \approx 0.19$. The peak broadening is controlled by $\eta_{1,2}$ and T. In Figs. 2.4b-2.4b we show the conductance on a colour map, indicated by the scale on the right, for each of the three charge sectors. We plot it as a function of the PF overlap ε and the voltage V_b, still with $\phi = \phi_0$. For vanishing ε, the three charge sectors all display similar conductance signals and become distinguishable only for larger ε. Specifically, it is necessary to have $\varepsilon > T, \eta_1, \eta_2$ for sufficient resolution of the different signals in order to read the topologically protected degree of freedom $\tilde{q}$ from these measurements.

We stress that the conductance measurement cannot assign a specific $\tilde{q}$ to a particular signal. Rather, the PF characteristic is the observation of three different conductance profiles, obtained by repeated measurements with different initialisations. One way in which the initial state can be changed is by poisoning from fractional quasiparticles which we will discuss towards the end of this section and in more detail in the next chapter. The detection of subgap states, like any other spectroscopic technique, is a necessary condition for the PFs, but it is not sufficient to confirm their topological nature. Protocols for exploring the braiding, non-local and thermodynamic properties of MFs have been theoretically proposed [18, 59–62] and similar approaches could be analysed for PFs.

More general coupling Hamiltonian

The coupling in Eq. (2.7) is not the most general coupling, quadratic in the fermionic degrees of freedom. By the condition that all coherent processes caused by the lead-PF coupling must change

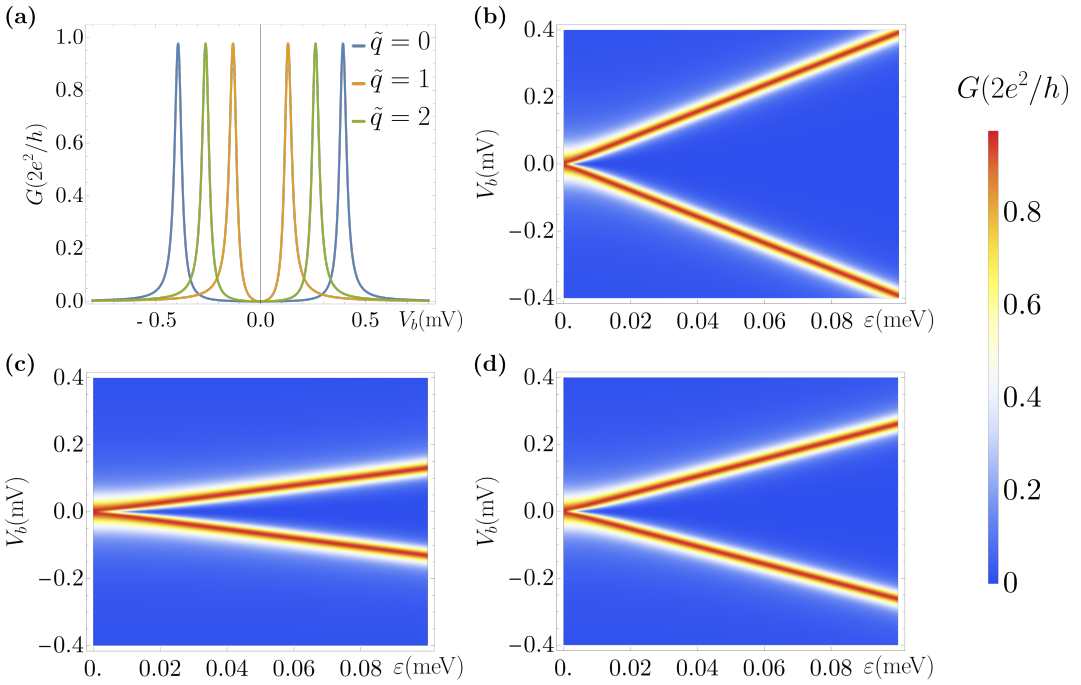

Figure 2.4: The finite-temperature ($T = 20$ K) conductance in Eq. (2.15) of the grounded device in Fig. 2.3 as a function of **(a)** the energy of the lead electron eV_b and **(b)**-**(d)** the PF overlap ε and eV_b for $\nu_l = 1.727\,(\text{meV})^{-1}$, $\eta_1 = 84$ μeV, $\eta_2 = 8.2$ μeV, and $\tilde{\chi} = 0$. Degeneracies in $\Delta_\varepsilon(\tilde{q})$ are split due to the finite $\phi = \arctan(1/\sqrt{27})$. The data in (a) is a cut at $\varepsilon = 0.1$ meV of (b), (c) and (d) that show the conductance in the sectors $\tilde{q} = 0$, 1 and 2, respectively.

the charge of the PFs by $\pm e$, the most general form is

$$H_c = i\sum_{n=0}^{5} \kappa_n \mathrm{e}^{i\chi_n}\, \alpha_1^{3-n}\alpha_2^n l + \text{H.c.}\,, \tag{2.16}$$

where the amplitudes κ_n are considered real. Furthermore, we assume that also the PFs are fully polarised due to the strong magnetic field such that only a single spin type is included in the tunnelling processes. By rewriting

$$i\alpha_1^3\alpha_1^{-n}\alpha_2^n = i\gamma_1\,\mathrm{e}^{-i\frac{\pi}{3}\frac{n(n-1)}{2}}\left(\alpha_1^\dagger\alpha_2\right)^n = i\gamma_1\,\mathrm{e}^{-i\frac{\pi}{3}\frac{n^2}{2}}\,\mathrm{e}^{i\frac{\pi n}{3}q} = i\gamma_1\left(i\gamma_2\gamma_1\right)^n\mathrm{e}^{-i\frac{\pi n^2}{6}}\,\mathrm{e}^{i\frac{4\pi n}{3}\tilde{q}}\,, \tag{2.17}$$

we can express the general coupling Hamiltonian as

$$H_c = \sum_{n\,\text{even}} i\kappa_n\gamma_1\left[l\,\mathrm{e}^{i\left(\chi_n-\frac{\pi n^2}{6}+\frac{4\pi}{3}n\tilde{q}\right)}+\text{H.c.}\right] + \sum_{n\,\text{odd}} i\kappa_n\gamma_2\left[-il\,\mathrm{e}^{i\left(\chi_n-\frac{\pi n^2}{6}+\frac{4\pi}{3}n\tilde{q}\right)}+\text{H.c.}\right]. \tag{2.18}$$

The terms with $n = 0$ and $n = 3$ are independent of the reduced charge number $\tilde{q}$ and match the more simple H_c in Eq. (2.7). The other terms contain $\tilde{q}$-dependent phases and consequently,

the conductance will have a $\tilde{q}$ dependence not only through $\Delta_\varepsilon(\tilde{q})$ but also via the coupling Hamiltonian. Rewriting the MF operators γ_i to electron operators like before, this reads

$$H_c(\tilde{q}) = \sum_{n=0}^{5} i\kappa_n \left(c^\dagger l\, \mathrm{e}^{i\Phi(n,\tilde{q})} + (-1)^n c^\dagger l^\dagger\, \mathrm{e}^{-i\Phi(n,\tilde{q})} + (-1)^n c l\, \mathrm{e}^{i\Phi(n,\tilde{q})} + c l^\dagger\, \mathrm{e}^{-i\Phi(n,\tilde{q})} \right), \tag{2.19}$$

where $\Phi(n,\tilde{q}) = \chi_n - \frac{\pi n^2}{6} + \frac{4\pi n\tilde{q}}{3}$. This leads to a coupling matrix:

$$W_{\tilde{q}} = \sum_n \frac{i\kappa_n}{2} \begin{pmatrix} \mathrm{e}^{i\Phi(n,\tilde{q})} & (-1)^n\, \mathrm{e}^{-i\Phi(n,\tilde{q})} \\ (-1)^n\, \mathrm{e}^{i\Phi(n,\tilde{q})} & \mathrm{e}^{-i\Phi(n,\tilde{q})} \end{pmatrix}. \tag{2.20}$$

We can write up effective couplings $\eta_{1,2}^{\mathrm{eff}} = |\eta_{1,2}^{\mathrm{eff}}|\, \mathrm{e}^{i\chi_{1,2}^{\mathrm{eff}}}$ between $\gamma_{1,2}$ and the lead operators:

$$\eta_1^{\mathrm{eff}}(\tilde{q}) = \kappa_0\, \mathrm{e}^{i\chi_0} + \kappa_2\, \mathrm{e}^{i\Phi(2,\tilde{q})} + \kappa_4\, \mathrm{e}^{i\Phi(4,\tilde{q})}, \qquad \eta_2^{\mathrm{eff}}(\tilde{q}) = -i\left(\kappa_1\, \mathrm{e}^{i\Phi(1,\tilde{q})} + \kappa_3\, \mathrm{e}^{i(\chi_3 - \frac{3\pi}{2})} + \kappa_5\, \mathrm{e}^{i\Phi(5,\tilde{q})} \right), \tag{2.21}$$

such that the coupling matrix in Eq. (2.20) can be expressed as

$$W_{\tilde{q}} = \frac{1}{2} \begin{pmatrix} i\eta_1^{\mathrm{eff}}(\tilde{q}) - \eta_2^{\mathrm{eff}}(\tilde{q}) & i\left(\eta_1^{\mathrm{eff}}(\tilde{q})\right)^* - \left(\eta_2^{\mathrm{eff}}(\tilde{q})\right)^* \\ i\eta_1^{\mathrm{eff}}(\tilde{q}) + \eta_2^{\mathrm{eff}}(\tilde{q}) & i\left(\eta_1^{\mathrm{eff}}(\tilde{q})\right)^* + \left(\eta_2^{\mathrm{eff}}(\tilde{q})\right)^* \end{pmatrix}. \tag{2.22}$$

The scattering matrix is found in the same way as in Eq. (2.12) but now with a $\tilde{q}$-dependent coupling matrix. The resulting zero-temperature conductance is on the exact same form as in Eq. (2.14) but with $\eta_{1,2} \to |\eta_{1,2}^{\mathrm{eff}}(\tilde{q})|$ and $\tilde{\chi} \to \tilde{\chi}^{\mathrm{eff}}(\tilde{q}) = \chi_2^{\mathrm{eff}}(\tilde{q}) - \chi_1^{\mathrm{eff}}(\tilde{q})$. The conductance differs in the three $\tilde{q}$ sectors, not only in the peak position, but also in amplitude due to this $\tilde{q}$-dependence, in particular of the effective phases $\tilde{\chi}^{\mathrm{eff}}(\tilde{q})$, even when all $\chi_i = 0$. We do not expect it will be possible to tune several of these simultaneously. Because of the $\tilde{q}$-dependent displacement of the peaks, setting the phase in the PF overlap energy $\Delta_\varepsilon(\tilde{q})$ to $\phi = \phi_0 = \arctan(1/\sqrt{27})$ no longer guarantees an optimal peak splitting. In the special case where $\eta_1^{\mathrm{eff}}(\tilde{q}) \approx \eta_2^{\mathrm{eff}}(\tilde{q})$ and $\tilde{\chi}^{\mathrm{eff}}(\tilde{q}) \approx \pi/2$ for a particular sector, the conductance for this $\tilde{q}$ is strongly suppressed because of interference effects (see Eq. (2.14)).

Since the real coefficients κ_i depend on the overlap between the PFs and the lead electrons, we assume $\kappa_1 = \kappa_5$ and $\kappa_2 = \kappa_4$ as they correspond to conjugate PF operators in Eq. (2.16). In Fig. 2.5 we plot the zero-temperature conductance with this general H_c and for comparison with the simpler coupling we keep $\phi = \phi_0$. All the phases χ_i are set to 0 for simplicity. The coupling strengths are defined relatively to what we expect to be the strongest for a lead at the left end, namely κ_0, such that: $\kappa_1 = \kappa_5 = \kappa_0/3, \kappa_2 = \kappa_4 = \kappa_0/9$, and $\kappa_3 = \kappa_0/27$. Comparing with the simpler case in Fig. 2.4 we see that, indeed, the conductance in all the charge sectors is suppressed, in particular for $\tilde{q} = 0$. We see in Fig. 2.5b-2.5d that even without PF interaction $\varepsilon = 0$ and all $\chi_n = 0$, the conductance remains peaked at a finite voltage bias V_b, differently from Fig. 2.4. Nevertheless, the signals from the three sectors remain distinguishable at finite $\varepsilon \gtrsim 0.05$ meV for the chosen parameters.

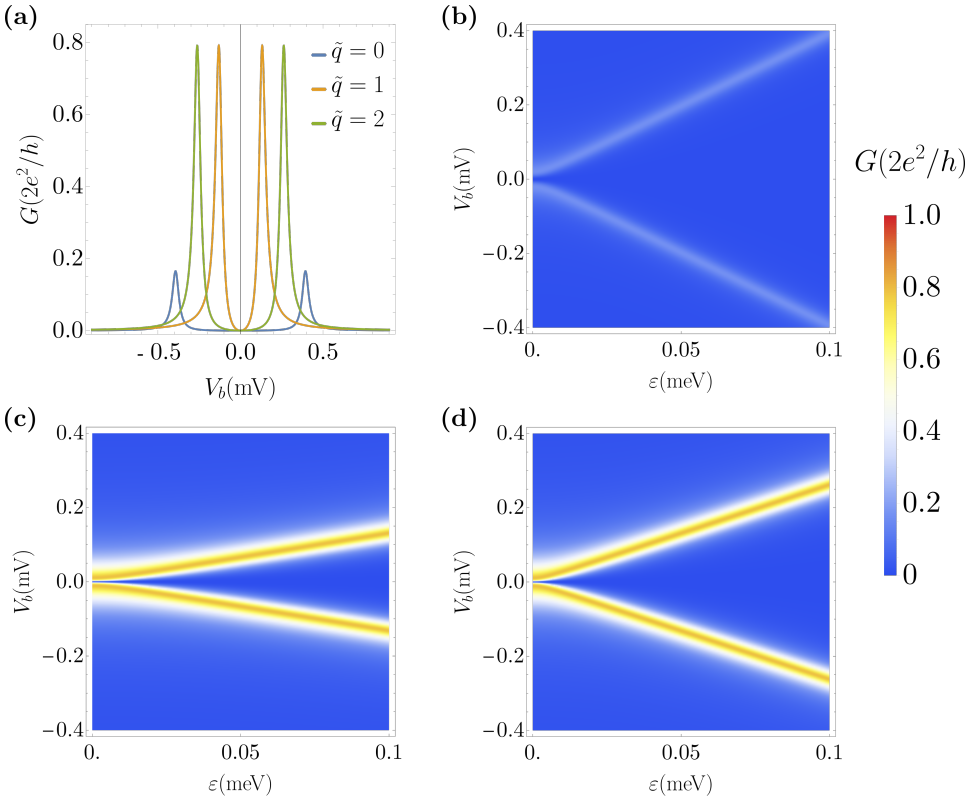

Figure 2.5: Zero-temperature conductance of the grounded device in Fig. 2.3 with the general coupling Hamiltonian in Eq. (2.16) as function of **(a)** the lead electron energy eV_b and **(b)**-**(d)** the PF overlap ε and eV_b. To compare with the results for the simpler coupling, we keep $\nu_l = 1.727\,(\text{meV})^{-1}$, $\phi = 0.19$ and $\kappa_0 = \eta_1 = 84$ μeV. The other couplings are $\kappa_1 = \kappa_0/3$, $\kappa_2 = \kappa_0/9$ and $\kappa_3 = \kappa_0/27$, and all phases χ_n are zero. (a) is a cut at $\varepsilon = 0.1$ meV of (b), (c) and (d) that, by the colour scale on the right, show the conductance in the three charge sectors $\tilde{q} = 0$, 1 and 2, respectively.

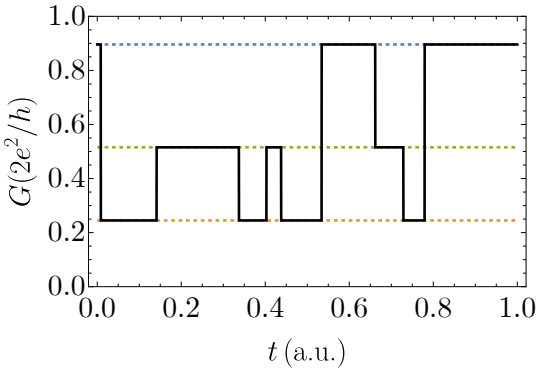

Figure 2.6: Illustration of the three-level telegraph noise in the conductance as a function of time (arbitrary units), expected to show up in the case of weak quasiparticle poisoning. The time it takes to make a conductance measurement must be much shorter than the time between poisoning events to observe the effect.

Effects of quasiparticle poisoning

So far we have considered $\tilde{q}$ to be the topologically protected charge, characterising the state of the two $\mathbb{Z}_6$ PFs, which is left unchanged by the coupling with the lead, simple or general. Other processes, however, could break this protection and thereby change $\tilde{q}$. This would be the case if the two PFs are not sufficiently isolated from other fractional modes in the system, leading to decoherence. For example, a source of poisoning could be fractional quasiparticles in the bulk of the FQH liquid or the external edge modes. Tunnelling of fractional charges in and out of the PF-SC system would shift $\tilde{q}$ by $\pm 1/3$. If this rate of tunnelling is sizeable compared to the time it takes to make the conductance measurement, the readout would display all the three conductance peaks in Fig. 2.4a simultaneously, each with some appropriate weight, reflecting that the stationary state of the PF device is now some statistical mix of the three $\tilde{q}$ sectors. In this case, such a three-peak differential conductance is difficult to distinguish from that of analogous systems hosting three non-topological subgap states, such as Andreev bound states, which could be formed between the SC and the metallic lead. Thus, observation of the specific three-peak conductance pattern in Fig. 2.4a is not sufficient to establish the presence of PFs.

The situation is very different when the poisoning rate is weak compared to the measurement rate; here there is a crucial distinction between the readout signal of trivial bound states and that of PFs. The trivial states can be described by a (non-interacting) scattering matrix, and the transport is determined by a single Landauer-Büttiker out-of-equilibrium steady state that has a well-defined conductance. Here it is not possible to change the fractional charge of the device for energies below the superconducting gap and the FQH bulk gap. Instead, the two-PF system can take three different steady states ($\tilde{q} = \{0, 1, 2\}$) and a weak poisoning rate at a suitable fixed V_b would make the conductance jump between the three levels as fractional quasiparticles enter or leave the PF system. The result would be a three-state telegraph noise of the conductance, similar to that of FQH interferometers [63, 64], like we schematically depict in Fig. 2.6. Such sudden jumps are unlikely to be mimicked by something that is not a fractional subgap state and is therefore a strong signature of quasidegenerate parafermionic states with no counterpart in MF devices.

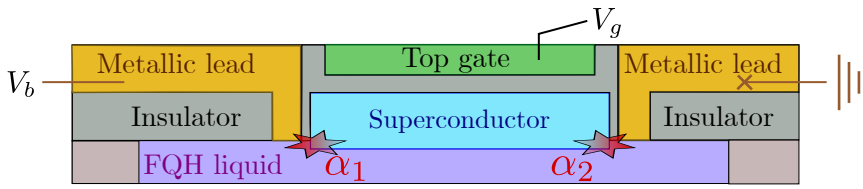

Figure 2.7: Section view of the Coulomb-blockaded device with a floating superconducting island (blue) inside a trench in the bulk of the FQH liquid (purple). Each of the PFs (red stars) are now coupled to a separate metallic lead (gold), still isolated from the SC and outer edge modes by insulator (grey). The voltage difference between the left and right lead is V_b. The induced charge in the SC is controlled through a top gate (green) by a voltage V_g.

It may prove difficult to obtain the correct weak poisoning. Therefore we will next consider a complementary device where the main PF signatures appear at stronger poisoning rates and in the truly topological regime $\varepsilon \to 0$.

2.2 Conductance signals of the Coulomb-blockaded device

In a PF device exposed to fractional quasiparticle poisoning with some intermediate rate with respect to the conductance measurement rate, different signatures of the topological modes can be seen in transport features of a Coulomb-blockaded superconducting island. Analogous devices with MFs have been examined by tunnelling spectroscopy experiments [65–68]. In two-terminal measurements of these devices, the periodicity of zero-bias conductance peaks as a function of a gate-induced charge n_g can distinguish between phases [46, 69, 70]; $2e$ and $1e$-periodic patterns correspond to the trivial and topological phase, respectively, since the presence of a MF allows tunnelling of single electrons rater than Cooper pairs.

Here we analyse the two-terminal conductance of such a type of device with PFs, see the sketch in Fig. 2.7. The SC is now a floating island with a strong charging energy E_C, and the induced charge is controlled by a top gate voltage V_g such that $n_g = -V_g C_g / e$, where C_g is the capacitance between the SC and the top gate. The connection to ground is instead via a second non-interacting metallic lead, placed in close contact to the right PF α_2.

Model for the floating superconductor

We model the floating SC by the Hamiltonian

$$H_{\mathrm{SC}}(N_{\mathrm{CP}}, N_e, N', q, n_g) = H_{2\mathrm{pf}}(q) + H_e(N_e) + H_{e/3}(N') + E_C(2N_{\mathrm{CP}} + N_e + N'/3 + q/3 - n_g)^2 . \quad (2.23)$$

We label the system states by the occupation numbers $|N_{\mathrm{CP}}, N_e, N', q\rangle$ where N_{CP} is the number of Cooper pairs in the SC (with respect to some offset), N_e is the number of quasielectron excitations in the device, N' is the number of *fractional* quasiparticle excitations and, as always, q counts the number of fractional charges shared by the localised PFs. Note that, due to the charging energy term, $q = 0$ and $q = 6$ now become distinguishable states in the way that $|N_{\mathrm{CP}}, N_e, N', q = 6\rangle = |N_{\mathrm{CP}} + 1, N_e, N', q = 0\rangle$. H_e and $H_{e/3}$ are the Hamiltonians for quasielectron

and fractional quasiparticle excitations, respectively. Hence, $H_{\rm SC}$ contains four energy scales: the PF coupling ε, the energy gap for a quasielectron in the paired FQH edge modes Δ_e, the corresponding gap for an $-e/3$ quasiparticle excitation $\Delta_{e/3}$ and the island charging energy E_C. In order to estimate the first three energies, we turn to the usual Luttinger liquid modelling of the counterpropagating fractional edge modes underneath the SC [12].

Like in the previous setup, the Hamiltonian for these modes is, in terms of the dual, bosonic, massless fields φ and θ,

$$H_0 = \frac{3v}{2\pi}\int_0^L \mathrm{d}\,x\left[\left(\partial_x\varphi\right)^2 + \left(\partial_x\theta\right)^2\right], \tag{2.24}$$

where the integral is along the SC with length L, and v still the edge mode velocity. The corresponding vertex operators[1] for left and right-moving quasiparticles of charge $-e$ are, respectively,

$$\psi_{e,L} = \frac{1}{2\pi}\sqrt{\frac{\Delta_{\rm FQH}}{v}}\,\mathrm{e}^{i3(\varphi-\theta)}, \qquad \psi_{e,R} = \frac{1}{2\pi}\sqrt{\frac{\Delta_{\rm FQH}}{v}}\,e^{i3(\varphi+\theta)}, \tag{2.25}$$

where the bulk gap of the FQH liquid $\Delta_{\rm FQH}$ is used as an ultraviolet cutoff. Following the procedure in Ch. 1, we describe the proximity-induced superconducting pairing with a mean-field approach by introducing the crossed Andreev interaction Δ between the chiral edge modes:

$$\begin{aligned} H_\Delta &= -\Delta\int_0^L \mathrm{d}\,x\left[e^{i\phi_{\rm SC}}\psi_{e,R}\psi_{e,L} + \text{H.c.}\right] = -\frac{\Delta_{\rm FQH}\Delta}{(2\pi)^2 v}\int_0^L \mathrm{d}\,x\left[\mathrm{e}^{i\phi_{\rm SC}}\,\mathrm{e}^{i6\varphi+3^2[\varphi,\theta]} + \text{H.c.}\right] \\ &= -\frac{\Delta_{\rm FQH}\Delta}{(2\pi)^2 v}\int_0^L \mathrm{d}\,x\left[-i\,\mathrm{e}^{i(6\varphi+\phi_{\rm SC})} + i\,\mathrm{e}^{-i(6\varphi+\phi_{\rm SC})}\right] = -\frac{\Delta_{\rm FQH}\Delta}{2\pi^2 v}\int_0^L \mathrm{d}\,x\,\sin\left(6\varphi+\phi_{\rm SC}\right), \end{aligned} \tag{2.26}$$

where $\phi_{\rm SC}$ is the phase of the parent SC which we will set to $\pi/2$ for simplicity.[2] In the second line we employed the commutation relation of the fields (see Eq. (1.25)), evaluated in the same position; $[\varphi,\theta] = \frac{i\pi}{3}\Theta(0)$, using the convention $\Theta(0) = 1/2$. The parameter $\Delta \propto \bar{\Delta}\,\mathrm{e}^{-W/\xi}$ is the modulo of the induced superconducting pairing between the left and right chiral modes. It is proportional to the energy gap $\bar{\Delta}$ of the thin parent SC and hence decreases with the magnetic field. Furthermore, the gap decays exponentially with the width W of the SC, compared to a length scale ξ. For a clean SC this ξ coincides with the coherence length whereas it depends on the diffusive length for a disordered SC. The exponential decay is observed in experiments on crossed Andreev reflection over a niobium nitride SC in graphene (see Ref. [43]) where the thin SCs have a typical coherence length $\xi \sim 50$ nm and widths in the range $50-200$ nm, considerably longer than $l_B \lesssim 10$ nm for the relevant fields [71]. The decay is consistent with theoretical analyses on SC-semiconductor heterostructures [72–74]. Since the SC and trench is placed in the bulk of the FQH system, the regions around the SC are FQH states with an energy gap $\Delta_{\rm FQH}$, in particular $x<0$ and $x>L$. This means that any current from the bulk to the edge modes under the SC is blocked.

In terms of the φ field, the total Lagrangian for the edge modes with induced crossed Andreev pairing reads

$$\mathcal{L} = \frac{3}{2\pi}\int_0^L \mathrm{d}\,x\left[\frac{1}{v}\left(\partial_t\varphi\right)^2 - v\left(\partial_x\varphi\right)^2\right] + \frac{\Delta_{\rm FQH}\Delta}{2\pi^2 v}\int_0^L \mathrm{d}\,x\left[\cos\left(6\varphi\right) - 1\right]. \tag{2.27}$$

[1] Here we use a different convention from the paper [1] in order to stay consistent with the left-right orientation defined in Ch. 1.

[2] The phase can be changed with a gauge transformation and does not affect the results.

For a finite induced pairing $\Delta > 0$ this resembles a sine-Gordon model. In such a model excitations are *solitons*, describing an interpolation from one (classical) minimum $\varphi_j = j\pi/3$ of the interaction Hamiltonian (H_Δ) to the next, φ_{j+1}. In a semiclassical description of our system, a *fractional* quasiparticle injected to the system roughly corresponds to the creation of one soliton in the sine-Gordon model [38]. With this comparison we can find the semiclassical energy gap of the fractional quasiparticles (the solitons). We rescale the φ field to $\varphi' = \sqrt{\frac{3v}{\pi}}\varphi$ such that the corresponding static action becomes

$$S' = \int \mathrm{d}\,x \left[\frac{1}{2}\left(\partial_x\varphi'\right)^2 + \frac{\Delta_{\mathrm{FQH}}\Delta}{2\pi^2 v}\cos\left(\frac{6\sqrt{\pi}}{\sqrt{3v}}\varphi'\right)\right] = \int \mathrm{d}\,x \left[\frac{1}{2}\left(\partial_x\varphi'\right)^2 + \frac{6\Delta_{\mathrm{FQH}}\Delta}{\pi v^2 \tilde{g}^2}\cos\left(\tilde{g}\varphi'\right)\right]. \tag{2.28}$$

Here we introduced the coupling constant $\tilde{g} = 2\sqrt{3\pi/v}$. Following Ref. [75] we find the fractional quasiparticle gap to be

$$\Delta_{e/3} = \frac{8}{\tilde{g}^2}\sqrt{\frac{6\Delta_{\mathrm{FQH}}\Delta}{\pi v^2}} = \sqrt{\frac{8\Delta_{\mathrm{FQH}}\Delta}{3\pi^3}}. \tag{2.29}$$

Likewise, a *quasielectron* excitation in the system corresponds to an increase in φ by π. Typically, such an excitation would be unstable since fractional solitons are repulsive [75], and an increase by π would decay into three solitons. We neglect this kind of interaction in our simple model and take instead, as a rough underestimate, the gap of the quasielectron to be $\Delta_e = 3\Delta_{e/3}$. The dispersion of a charge $-e$ excitation is then $\epsilon(k) = \sqrt{\Delta_e^2 + v^2k^2}$ where k is the quasimomentum. Due to the finite length of the SC, we discretise this momentum by $h/(2L)$, corresponding to an energy discretisation of $\delta = hv/(2L)$ (using open boundary conditions). Since our effective 1D model breaks down for excitation energies higher than Δ_{FQH}, we will include only the lowest $\Delta_{\mathrm{FQH}}/\delta \sim 8 \equiv n_{\max}$ excited states with energies

$$\epsilon_n = \sqrt{\Delta_e^2 + \delta^2\,(n+1/2)^2}. \tag{2.30}$$

Typically, however, the temperature and voltage bias considered in our calculations are much lower than the energy gap of the FQH liquid such that any contribution to the current from states with $\epsilon_n > \Delta_{\mathrm{FQH}}$ is negligible.[3] The offset of 1/2 in the above equation is chosen to be consistent with similar MF devices close to the topological phase transition [76], but for different boundary conditions other offsets could be selected. In general, the lowest quasielectron energy level will be $\epsilon_0 \in \left[\Delta_e, \sqrt{\Delta_e^2 + \delta^2/4}\right]$.

In Ref. [38] the PF energy splitting is derived via an instanton calculation based on the Lagrangian in Eq. (2.27). In terms of the bulk gap of the FQH liquid and the induced superconducting pairing, it reads

$$E_q = \frac{-4\sqrt{\Delta_{\mathrm{FQH}}\Delta}}{\pi\sqrt{3}}\exp\left[\frac{-4L\sqrt{\Delta_{\mathrm{FQH}}\Delta}}{3\pi\hbar v}\right]\cos\left(\frac{\pi q}{3} - \frac{\mu L}{3\hbar v}\right). \tag{2.31}$$

As in the previous section, the phase is $\phi = \mu v L/\hbar v$. From Eq. (2.31), we obtain an expression for ε in terms of $\Delta_{e/3}$;

$$\varepsilon = \sqrt{\pi/2}\,\Delta_{e/3}\exp\left[-\sqrt{2\pi/3}\,(L\Delta_{e/3}/\hbar v)\right], \tag{2.32}$$

[3] Jumping a bit ahead, the temperature and FQH gap considered in Figs. 2.8b and 2.10b are, for instance, such that $k_{\mathrm{B}}T/\Delta_{\mathrm{FQH}} \lesssim 10^{-2}$.

which is consistent with the subgap state requirement for well-defined PFs, $\varepsilon < \Delta_{e/3}$ (see also Fig. 2.9). As one could expect, the coupling decays exponentially with the distance between the PFs, i.e. the SC length L. Based on the results in Ref. [20], we make the rough estimate $\Delta \lesssim 1$ meV and take this to be the main parameter to distinguish system regimes in a simplified low-energy description. In addition, we set $\Delta_{\text{FQH}} \sim 0.017 e^2/\epsilon l_B \sim 1.72$ meV [71], where $\epsilon \approx 1$ is the dielectric constant in suspended graphene and $l_B = \sqrt{\hbar/e|B|}$ is the magnetic length, controlled by the strength B of the magnetic field.

Tunnelling processes and zero-bias conductance

In order to study the conductance of the Coulomb-blockaded device, we make the simplification that the left and right leads (see Fig. 2.7) couple only to the left and right ends of the device, respectively. Hence, we describe the coupling by the Hamiltonian

$$H_c' = \sum_{a=L,R} \eta_a l_a^\dagger \psi_e(x_a) + \text{H.c.}, \tag{2.33}$$

where l_L and l_R annihilate an electron at the end of the left and right lead, respectively. $\psi_e(x) = \psi_{e,L}(x) + \psi_{e,R}(x)$ is the electron field at position x (see Eq. (2.25)) which, evaluated in positions $x_L \sim 0$ and $x_R \sim L$, annihilates a charge $-e$ in the coupled FQH edge modes in this region under the SC. Following Ref. [70], we express the coupling strengths η_a in terms of the density of states in the lead and edge modes, ν_l and ν_e, respectively, as well as a dimensionless conductance g_a:

$$\eta_a = \frac{1}{2\pi}\sqrt{\frac{g_a}{\nu_l \nu_e}}. \tag{2.34}$$

Multiplied by $2e^2/h$, this g_a is the conductance of the tunnel junction contact in end a, and we set them to $g_L = g_R = 0.09$. The edge mode density of states is approximated by $\nu_e \approx \delta^{-1} = 2L/(h\upsilon)$ such that the tunnel couplings become $\eta_a = \frac{1}{2\pi}\sqrt{g_a h\upsilon/2\nu_l L}$. We use $\nu_l = 1.727\,(\text{meV})^{-1}$ as before and with an edge mode velocity $\upsilon = 10^5$ m/s and a SC length $L = 1$ µm the coupling strengths are $\eta_L = \eta_R = 52$ µeV.

Analogously to MF devices [66, 70, 77], we model the electron transport across the system by considering two main processes: first, the resonant tunnelling of electrons mediated by the PFs, corresponding to electron teleportation mediated by the effective MFs $\gamma_i = \alpha_i^3$ [46]. Similarly to the grounded system considered in Sec. 2.1, this causes transitions between q and $q \pm 3$ (modulo 6) due to the coupling between neighbouring lead and PF. Second, the incoherent sequential tunnelling of single electrons via quasiparticle states above the induced quasielectron energy gap Δ_e. We assume that electrons jump in and out of the superconducting island causing transitions between $N_e = 0$ and $N_e = 1$ and neglect processes where one quasielectron is scattered into three fractional quasiparticles meaning that N' is conserved. Before concluding, we will also discuss a third process of less practical relevance; sequential Andreev tunnelling of Cooper pairs.

To model all three processes we approximate the electron operator $\psi_e(x)$ in terms of the PF operators and the quasielectrons. The projection of ψ_e on the PFs is

$$\langle N_{\text{CP}}, N_e, N', q-3|\psi_e(x_{L/R})|N_{\text{CP}}, N_e, N', q\rangle = \alpha_{1/2}^3(x_{L/R}) \approx \sqrt{\frac{\nu_e \Delta_e}{2}}, \tag{2.35}$$

where $\alpha_i^3(x)$ is the *amplitude* of the normalised operator α_i^3 in position x. The amplitude decays exponentially into the bulk of the FQH liquid with an approximate decay length $1/v_e\Delta_e$. Regarding the quasielectrons, we describe them as non-interacting particles with a dispersion ϵ_n, as discussed above in Eq. (2.30), and we associate them with annihilation operators $\tilde{\gamma}_n$ such that the corresponding Hamiltoninan is $H_{\rm qe} = \sum_n \epsilon_n \tilde{\gamma}_n^\dagger \tilde{\gamma}_n$. We then obtain the overlap

$$\psi_e(x_a) = \sum_n u_n^*(x_a)\tilde{\gamma}_n + v_n(x_a)\tilde{\gamma}_n^\dagger, \tag{2.36}$$

with coefficients $u_n(x_a)$ and $v_n(x_a)$ given by the Bogoliubov transformation of $H_{\rm qe}$. We let $u_n(x_a)v_n^*(x_a) = \Delta_e/(2\epsilon_n)$ in a rough approximation neglecting the position dependence. Importantly, we exclude the low-energy MF-like modes on the form α^3 in this projection.

We limit the number of quasielectron excitations to $N_e = \{0,1\}$, assuming that states with further excitations are thermally suppressed. Likewise, we limit the number of fractional quasiparticles to $N' = \{0,1,2\}$. Using these truncations we can follow the standard in MF studies [70] and introduce the excess electron number $N = 2N_{\rm CP} + N_e$, where an even-valued N labels a state without quasielectron excitations and an odd value means that a single excitation is present. We can then use the states $|N, N', q\rangle$ as our basis, in which the Hamiltonian of the total SC reads

$$H_{\rm SC}(N, N', q, n_g) = H_{\rm 2pf}(q) + \epsilon_0\left[1-(-1)^N\right]/2 + \epsilon_0' N' + E_C\left(N + N'/3 + q/3 - n_g\right)^2, \tag{2.37}$$

where the quasielectron energy is minimised to $\epsilon_0 = \sqrt{\Delta_e^2 + \delta^2/4}$ and the fractional quasiparticle energy correspondingly to $\epsilon_0' \equiv \sqrt{\Delta_{e/3}^2 + \delta^2/4}$. Now, let us first examine the resonant tunnelling.

Resonant tunnelling

Consider Fig. 2.8a where we plot the energy spectrum of $H_{\rm SC}$ in Eq. (2.37) for states with $N' = 0$ (for simplicity). In the shown low-energy range only the 'even' parabolas with $N = \{-2, 0, 2\}$ are visible, of which $N = 0$ is printed clearly while $N = \{-2, 2\}$ are faded into the background. The three different colours refer to the corresponding $\tilde{q}$, full curves denote $q = 0, 1, 2$ and dashed ones $q = 3, 4, 5$. The black loop highlights crossings between parabolas sharing the same $\tilde{q}$ (but not necessarily the same N). When the voltage bias applied to the device is low compared to the charging energy, resonant electron tunnelling via the PFs requires the involved states to be close in energy (for example $|N = 0, N' = 0, q = 1\rangle$ and $|N = 0, N' = 0, q = 4\rangle$). A current can run through the device at zero voltage bias if the top gate voltage controlling the induced charge on the SC is such that n_g is at one of the crossings. We consider here the limit where such states, differing in PF charge by $\pm 1e$ and with an even N, are energetically isolated from states with an odd N that are excited at an energy $\gtrsim \Delta_e$. Specifically, for energies such that $\varepsilon \ll E_C \ll \Delta_e$ we can use the Weidenmüller formula to find the related conductance like in the previous section but here explicitly ensuring charge conservation.

In the case where the number of Cooper pairs is conserved we can have transitions between states like $|N, N', q\rangle$ and $|N, N', q+3\rangle$ for $q = \{0, 1, 2\}$. In the other case, where six fractional charges of the PFs are converted into one Cooper pair, and vice versa, the involved states are, for example, $|N, N', q\rangle$ and $|N+2, N', q-3\rangle$ for $q = \{3, 4, 5\}$. In both cases, the energy difference $\delta E(n_g)$ between the final and initial states is the same, and we model the two states as a (non-interacting) two-level system described by $H_{\rm 2pf}' = \delta E(n_g)(c^\dagger c - 1/2)$ where $\delta E(n_g) = 2E_C(N + (N'+q)/3 - 1/2 -$

$n_g) - 4\varepsilon\cos(\pi q/3+\phi)$. As before, the operator $c = (\gamma_1 + i\gamma_2)/2$ is the effective electron operator constructed from the two MF-like operators $\alpha_i^3 = \gamma_i$.

By inserting the projection in Eq. (2.35) into the tunnelling Hamiltoninan in Eq. (2.33) we can write the latter as $H_c' = \sum_{a=L,R} c^\dagger W' \underline{f} + \text{H.c.}$ Here the vector $\underline{f} = (l_L, l_R)$ is composed of the annihilation operators for the left and right leads as defined above and

$$W' = \sqrt{\frac{\nu_e \Delta_e}{2}} \begin{pmatrix} \eta_L & i\eta_R \end{pmatrix}, \tag{2.38}$$

where the factor in front is from the localisation of the PFs. The scattering matrix is simple to find from $H_{2\text{pf}}'$ and W':

$$S(E) = \mathbb{1}_2 - i2\pi\nu_l \frac{(\nu_e\Delta_e)/2}{E - \delta E(n_g) + i\pi\nu_l\nu_e\Delta_e(\eta_L^2+\eta_R^2)/2} \begin{pmatrix} \eta_L^2 & i\eta_L\eta_R \\ -i\eta_L\eta_R & \eta_R^2 \end{pmatrix}. \tag{2.39}$$

Here we assume that the density of states ν_l is the same in both leads. Form the scattering matrix we find the differential zero-bias ($E = eV_b = 0$) conductance to be

$$\begin{aligned} \tilde{G}_R(N, N', q, n_g) &= \frac{e^2}{h} \left| \frac{\pi\nu_l\nu_e\Delta_e\eta_L\eta_R}{\delta E(n_g) + i\pi\nu_l\nu_e\Delta_e(\eta_L^2+\eta_R^2)/2} \right|^2 \\ &= \frac{e^2}{h} \frac{g_L g_R}{4(2\pi)^2} \frac{\Delta_e^2}{(\delta E(n_g))^2 + (g_L+g_R)^2\Delta_e^2/(8\pi)^2}, \end{aligned} \tag{2.40}$$

where we apply the rewrting in Eq. (2.34). The above expression is valid as long as the level broadening induced by external leads is much greater than the system temperature $T \ll (g_L + g_R)\Delta_e/8\pi$ [71]. Furthermore, we require $\Delta_e \gg E_C$ such that the states with $N' \neq 0$ and N odd are well-separated in energy from the lowest energy states with $N' = 0$ and N even. In the case we consider with symmetric contacts $g_L = g_R$, the zero-bias conductance has a peak height $\tilde{G}_R = e^2/h$ in agreement with the teleportation peak conductance for MFs [46].

As mentioned in the beginning of this section, we examine the case where the external environment poison the charge of the PFs by allowing quasiparticles to enter and leave the PF-SC system with a rate comparable to that of the conductance measurement. We phenomenologically capture this by considering a thermal equilibrium distribution of the states $|N, N', q\rangle$ at a temperature $T \ll E_C$;

$$G_R = \sum_{N=-6}^{4} \sum_{N'=0}^{2} \sum_{q=0}^{5} Z^{-1} \, \mathrm{e}^{-H_{\text{SC}}(N,N',q,n_g)/T} \, \tilde{G}_R(N, N', q, n_g). \tag{2.41}$$

Here Z is the partition function and we sum over the (integer) charge numbers as indicated. When including these Boltzmann weights the quantisation for symmetric contacts is lost and the magnitude of the conductance becomes very sensitive to the temperature.

In Fig. 2.8b we plot the zero-temperature G_R of Eq. (2.41) as a function of the phenomenological crossed-Andreev interaction Δ and the gate-induced charge n_g. At intermediate pairing, 0.05 meV $\lesssim \Delta \lesssim$ 0.3 meV, it displays six peaks repeating every 2 n_g. We name this the *sixfold regime*. Comparing with Fig. 2.8a, we see indeed six energy crossings corresponding to transitions between states with the same $\tilde{q}$, for every interval where n_g increases by 2. The uneven distance between the conductance peaks for $\Delta \lesssim 0.3$ meV is due to a finite $\varepsilon \ll E_C$ shifting the parabolas depending on q.

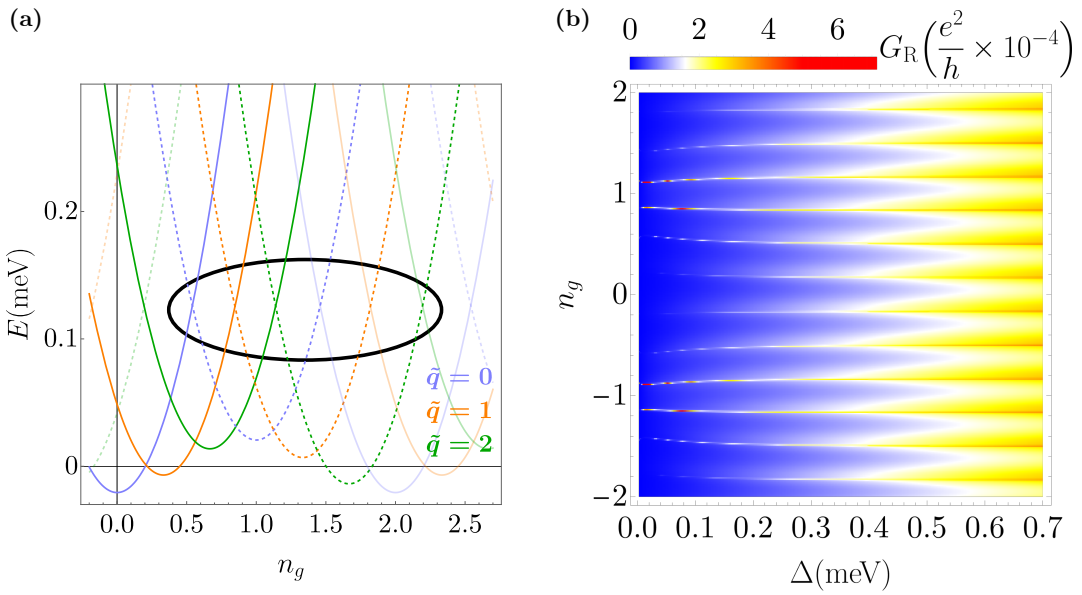

Figure 2.8: Resonant tunnelling process mediated by the PFs of the floating superconducting island (Fig. 2.7). In **(a)** we show the eigenenergies of H_{SC} in Eq. (2.37) as a function of the induced charge number n_g for $N' = 0$. States with $N = 0$ are highlighted in clear colours. Full and dashed curves correspond to states with $q = \{0,1,2\}$ and $q = \{3,4,5\}$, respectively. In the black loop we highlight energy crossings relevant for resonant tunnelling of electrons. We set the induced superconducting pairing to $\Delta = 0.1$ meV and the charging energy to $E_C = 0.5$ meV. As previously fixed, $\Delta_{\mathrm{FQH}} = 1.72$ meV, $v = 10^5$ m/s and $L = 1$ µm. In **(b)** we plot the corresponding contribution to the zero-bias conductance. On the horizontal axis is the interaction Δ determining $\Delta_{e/3}$ and thereby the PF coupling ε. On the vertical axis is the gate-controlled induced charge number n_g. For $0.05\,\mathrm{mev} \lesssim \Delta \lesssim 0.3$ meV we observe that $G_R(\Delta, n_g)$ is periodic in n_g with six peaks every $2e$ period. For larger Δ this evolves into an $e/3$-periodic pattern. The couplings to the metallic leads are $\eta_L = \eta_R = 52$ µeV, $T = 0.15$ K and the remaining parameters are the same as in (a).

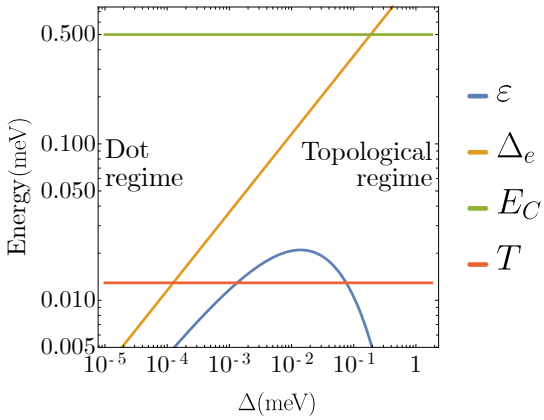

Figure 2.9: Comparison of the energy scales $\varepsilon(\Delta)$ (blue) and $\Delta_e(\Delta)$ (orange) with the charging energy $E_C = 0.5$ meV (green) and the temperature $T = 0.15$ K (red) for realistic parameters $\Delta_{\text{FQH}} = 1.72$ meV, $v = 10^5$ m/s and $L = 1$ µm of the Coulomb-blockaded PF device. The energy gaps $\Delta_{e/3}$, Δ_e and ε vanish when $\Delta \to 0$ and the system act like a quantum dot for fractional charges. We label this the dot regime (left part). In the topological regime, indicated on the right, only the PF energy splitting decays exponentially and the modes are truly topological and localised.

This is seen from Fig. 2.9 where we plot the energy scales $\varepsilon(\Delta)$ (Eq. (2.32)) and $\Delta_e(\Delta)$ (Eq. (2.29)) compared to $T = 15$ K and the charging energy $E_C = 0.5$ meV. For larger $\Delta \gtrsim 0.3$ the PF overlap decays and becomes orders of magnitude smaller than all the other energies. Thus, the vertical shift between energy parabolas with different q becomes negligible and an $e/3$-periodic peak pattern emerges (right part of Fig. 2.8b). Since the PF energy splitting collapses $\varepsilon \ll E_C \ll \Delta_e$ in the limit $\Delta \to \Delta_{\text{FQH}}$ (see Eq. (2.32)), we say that the PF system is deep in the *topological regime* as indicated in the right of Fig. 2.9. This is a characteristic of PFs, analogue to the $1e$ periodicity of MF-mediated electron teleportation [46, 70, 78].

We next derive the conductance associated with the sequential tunnelling of single electrons and compare it to $G_R(\Delta, n_g)$.

Sequential tunnelling of single electrons

In the case where $\Delta_e < E_C$ (see Fig. 2.9), electrons can sequentially tunnel from one lead to the other via a quasielectron excitation in the floating SC. In Fig. 2.10a we plot the energies for states with $N = -1, 0, 1$, $N' = 0$ and $q = 0, \ldots, 5$ where states with $q = 1$ are highlighted to exemplify crossings between states with $|N, N', q\rangle$ and $|N \pm 1, N', q\rangle$. We expect to see a zero-bias peak in the conductance for the corresponding values of n_g. The right circle shows the crossing between states $|N, N', q\rangle$ and $|N+1, N', q\rangle$ where the total electron number N is even. The rate for excitation of a quasielectron by absorption of an electron with momentum p from lead a can to lowest order be approximated by Fermi's golden rule. For a system with initially N electron charges the rate is

$$\Gamma^{a,p}_{N\to N+1,n} = \frac{2\pi}{\hbar} \left| {}_a\langle 0|\, {}_n\langle 1|\, H_c\, |0\rangle_n\, |p\rangle_a \right|^2 \delta(\mathcal{E}_{N+1} - \xi_p + \epsilon_n)\,, \tag{2.42}$$

where ϵ_n is the energy of the quasielectron, excited by the lead electron that enters with energy ξ_p. $|0\rangle_n$ labels the state with N electrons, all paired in the condensate whereas $|1\rangle_n$ is the state with one additional electron charge due to the excited quasielectron. The variable $\mathcal{E}_{N+1}$ is the difference in charging energy between the states $|N+1,N',q\rangle$ and $|N,N',q\rangle$:

$$\mathcal{E}_{N+1} = 2E_C(N+(N'+q)/3+1/2-n_g)\,. \tag{2.43}$$

To calculate the rate $\Gamma^{a,p}_{N\to N+1,n}$ we use the projection in Eq. (2.36) and express the lead operator l_a in momentum space as $l_a = \sum_p \phi_p(x_a) l_p$. Thus, the inner product in Eq. (2.42) becomes

$$\sum_{p',n'} {}_a\langle 0|\,{}_n\langle 1|\left[\eta_a(u_{n'}(x_a)\tilde{\gamma}^\dagger_{n'} + v^*_{n'}(x_a)\tilde{\gamma}_{n'})\phi_{p'}(x_a) l_{p'}\right]|0\rangle_n\,|p\rangle_a = \eta_a u_n(x_a)\phi_p(x_a) \tag{2.44}$$

We follow the normalisation in Ref. [70]; $\eta_a^2|u_n(x_a)|^2|\phi_p(x_a)|^2 = g_a\delta\delta_a/(8\pi^2)$ where δ is the energy discretisation of the excitations in the SC and δ_a is the level spacing in lead a. The rate thereby becomes

$$\Gamma^{a,p}_{N\to N+1,n} = \frac{2\pi}{\hbar}\frac{g_a\delta_a\delta}{8\pi^2}\delta(\mathcal{E}_{N+1}-\xi_p+\epsilon_n)\,. \tag{2.45}$$

We multiply by the Fermi-Dirac distribution function $n_{\rm F}(\xi_p - eV_a)$ of lead a, where $V_L = V_b$ and $V_R = 0$, and sum over the momentum p to obtain the rate

$$\Gamma^{a}_{N\to N+1,n} = \frac{g_a\delta}{4\pi\hbar} n_{\rm F}(\mathcal{E}_{N+1}+\epsilon_n - eV_a)\,. \tag{2.46}$$

The rate for the reverse process is $\Gamma^a_{N+1,n\to N} = \frac{g_a\delta}{4\pi\hbar}(1-n_{\rm F}(\mathcal{E}_{N+1}+\epsilon_n-eV_a))$

Let us next consider the energy crossing in the left circle of Fig. 2.10a which is between the states $|N,N',q\rangle$ and $|N+1,N',q\rangle$, this time with an odd N. Following the same procedure, we find the rate for an electron from lead a with momentum p to scatter into the SC system that hosts initially N charges, one of which is a quasielectron, and change the state to $|N+1,N',q\rangle$, i.e. a state without quasielectron excitations: $\Gamma^a_{N,n\to N+1} = \frac{g_a\delta}{4\pi\hbar} n_{\rm F}(\mathcal{E}_{N+1}-\epsilon_n-eV_a)$. The rate for the reverse process $\Gamma^a_{N+1\to N,n}$ is defined analogously to before. By setting up a simplified set of rate equations and finding the steady state solution, we find the contribution to the current across the SC from sequential tunnelling of single electrons. The simplification implies that when finding an expression for the current we assume that the occupation probabilities of all other states than $|N,N',q\rangle$ and $|N+1,N',q\rangle$ are zero close to the crossing of these two states [70]. The explicit calculation is found in App. B. From the current expression we get the zero-bias differential conductance

$$\mathcal{G}^{\rm o/e}_{1e} = \frac{e^2}{2h}\frac{g_L g_R\frac{\delta}{k_{\rm B}T}}{g_L+g_R}\frac{\sum_n\left(1+{\rm e}^{[\epsilon_n\mp\mathcal{E}_{N+1}]/k_{\rm B}T}\right)^{-1}}{1+\sum_n {\rm e}^{-[\epsilon_n\mp\mathcal{E}_{N+1}]/k_{\rm B}T}}\,. \tag{2.47}$$

Here we have labelled the conductance with an "o/e" referring to whether N is odd or even. Thus, the total contribution to the conductance from sequential tunnelling of single electrons is

$$G_{1e} = \sum_{N=-6}^{4}\sum_{N'=0}^{2}\sum_{q=0}^{5} Z^{-1}\,{\rm e}^{-H_{\rm SC}(N,N',q,n_g)/T}\left(\mathcal{G}_{1e}(N-1,N',q,n_g)+\mathcal{G}_{1e}(N,N',q,n_g)\right). \tag{2.48}$$

In Fig. 2.10b we plot $G_{1e}(\Delta,n_g)$ which displays 12 peaks of varying intensity for every n_g period of 2. The values of n_g where these peaks occur depend on the dot energy level spacing $\delta = vh/2L$.

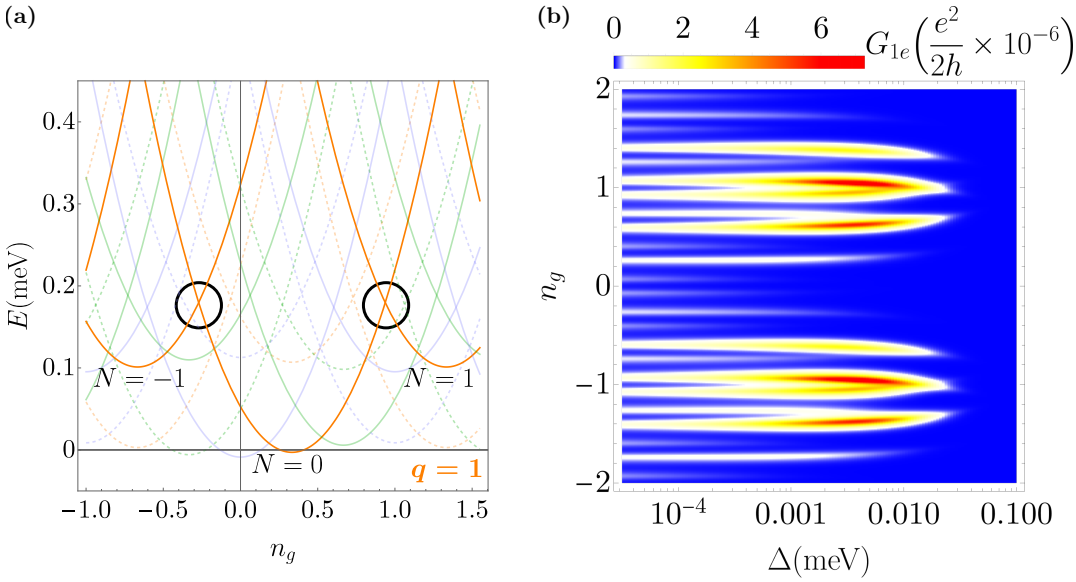

Figure 2.10: Sequential tunnelling of single electrons in the Coulomb-blockaded device. In **(a)** we plot the eigenenergies of $H_{\rm SC}$ as function of n_g. The highlighted energies are states with $q = 1$ and in the two circles we highlight the crossings of states differing by one electron charge. We show only states with $N' = 0$. The pairing is $\Delta = 10^{-4}$ meV and otherwise the parameters are the same as in 2.8. In **(b)** we show the corresponding zero-bias differential conductance of Eq. (2.48) $G_{1e}(\Delta, n_g)$ in the limit $\Delta_e < E_C$, now with Δ on a log scale. For every $2e$ the conductance displays twelve peaks for low pairing $\Delta \lesssim 1$ μeV. The physical parameters are the same as in Fig. 2.8.

In Fig. 2.10 δ is comparable to the charging energy E_C which yields the twelve irregular peaks in each $2e$ period for $\Delta \to 0$. Conversely, a system with $\delta, \Delta_{e/3} \ll E_C$ yields an $e/3$-periodic pattern which we show in App. B where we plot $G_{1e}(\Delta, n_g)$ in Fig. B.1 for a SC ten times longer than the one considered here. All the three energy gaps ε, $\Delta_{e/3}$ and Δ_e vanish for $\Delta \to 0$ and the system therefore behaves as a blockaded *quantum dot* for fractional quasiparticles [79, 80]. We indicate this in the left side of Fig. 2.9. For increasing $\Delta \gg 0.01$ meV, the quasielectron energy gap Δ_e becomes so large that the energy parabolas with odd N are much above those with even N and the resonant tunnelling takes over (Fig. 2.8b).

In Fig. 2.11a we provide a log-scale summary of all the relevant energies. For realistic parameter choices we can distinguish three main conductance patterns as a function of the induced superconducting pairing Δ; the quantum dot, the sixfold and the topological regimes (see the table in Fig. 2.11b). For vanishing $\Delta \to 0$ the electron sequential tunnelling process is the dominating one, and the result is the complex series of up to twelve zero-bias peaks in the conductance in Fig. 2.10b. Instead the resonant tunnelling becomes relevant for intermediate pairing $0.05\,\text{meV} \lesssim \Delta \lesssim 0.3$ meV with a zero-bias conductance pattern of six dominant peaks repeating with $2e$ periodicity, emerging when $\Delta_e > T$ – the regime labelled sixfold. When the induced pairing in sufficiently long islands becomes strong, $\Delta \to \Delta_{\rm FQH}$, the PF system is deep in the topological regime where zero-bias

(a)

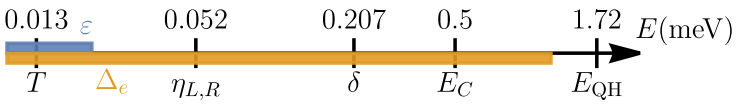

(b)

Δ	Weak	Intermediate	Strong
Regime	Quantum dot	Sixfold	Topological
Condition	$\delta, \Delta_e \ll T, E_C$	$\Delta_e > T$	$\Delta_e > E_C > \varepsilon$
Channel	G_{1e}	G_R	G_R
Pattern	$e/3$	Sixfold	$e/3$

Figure 2.11: Energy scales and regimes for the Coulomb-blockaded PF device. **(a)** Log scale summary of the energies used to produce the conductance plots in Figs. 2.8b and 2.10b, including the dot energy level spacing δ. In blue and orange we indicate the ranges of ε and Δ_e, respectively. **(b)** Summary of the main properties of the discussed transport regimes.

peaks in the dominating G_R are repeating with an $e/3$ periodicity characteristic of PFs.

Sequential tunnelling of Cooper pairs

We finally consider a third process, namely that of Andreev sequential tunnelling of Cooper pairs, relevant for islands with weak charging energy, $E_C \ll \varepsilon$. In Fig. 2.12 we plot a dispersion similar to that of Fig. 2.9, but with an $E_C = 0.04$ meV and a SC length $L = 0.1$ μm (which implies a larger energy discretisation of the quasiparticle excitations (Eq. (2.30)) compared to the previous $L = 1$ μm). The related eigenenergies of $H_{\text{SC}}(\Delta = 0.3\,\text{meV})$ are shown in Fig. 2.13a where we now focus on the states $|N, N' = 0, q = 0\rangle$ with $N = \{0, 1, 2\}$ while other states are in the opaque background. The circle demonstrates the energy crossing of states differing by one Cooper pair and without quasielectron excitations. This crossing should lead to a peak in the conductance at zero voltage bias when n_g is tuned close to an odd integer.

The rates for addition and subtraction of a Cooper pair to the SC-PF system, $\Gamma_{N\to N+2}$ and $\Gamma_{N+2\to N}$, can be found by first finding the amplitudes for the related Andreev reflection processes. For this we neglect the states with one quasielectron excitation which are higher in energy and we consider only even N. To second order in the tunnelling Hamiltonian (Eq. (2.33)), the process where two electrons with momenta p_1 and p_2 are absorbed in the system from lead a therefore has the amplitude

$$A^{a,p_1,p_2}_{N\to N+2} = \eta_a^2 \phi_{p_1}(x_a)\phi_{p_2}(x_a) \sum_n u_n(x_a) v_n^*(x_a) \left(\frac{1}{-\mathcal{E}_{N+1} + \xi_{p_1} - \varepsilon_n} + \frac{1}{-\mathcal{E}_{N+1} + \xi_{p_2} - \varepsilon_n} \right). \tag{2.49}$$

The amplitude for the reverse process $A^{a,p_1,p_2}_{N+2\to N}$ is defined similarly. We follow the approximations done for similar MF setups [70] and set $\xi_{p_1}, \xi_{p_2} \approx 0$ and take the low-temperature limit such that

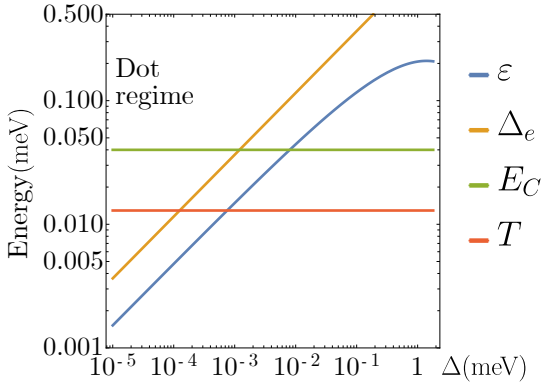

Figure 2.12: Comparison of the energy scales $\varepsilon(\Delta)$, $\Delta_e(\Delta)$, $T = 0.15$ K and E_C for a shorter island, $L = 0.1$ µm, than in Fig. 2.9 which at the same time has a lower charging energy $E_C = 0.04$ meV.

the amplitudes for Cooper pair tunnelling simplify to

$$A^{a,p_1,p_2}_{N\to N+2} = \eta_a^2 \phi_{p_1}(x_a)\phi_{p_2}(x_a) \sum_n \frac{\Delta_e}{2\varepsilon_n} \frac{-2}{\mathcal{E}_{N+1}+\varepsilon_n}\,. \tag{2.50}$$

This process is relevant when the difference in charging energy between the states with and without a quasielectron excitation is lower than the quasiparticle gap: $-\mathcal{E}_{N+1} < \Delta_e$. Considering also the continuum limit of quasiparticle excitations in the SC $n_{\max} \to \infty$ (we refer to Eq. (2.30)), the square amplitude becomes

$$|A^{a,p_1,p_2}_{N\to N+2}|^2 \approx \frac{g_a^2\delta_a^2}{(2\pi)^4} \frac{4\Delta_e^2}{\Delta_e^2-\mathcal{E}_{N+1}^2} \arctan^2\left(\sqrt{\frac{\Delta_e-\mathcal{E}_{N+1}}{\Delta_e+\mathcal{E}_{N+1}}}\right), \tag{2.51}$$

which leads to a scattering rate

$$\Gamma^a_{N\to N+2} = \frac{2\pi}{\hbar}|A^a_{N\to N+2}|^2 \sum_{p_1,p_2} \delta(\xi_{p_1}+\xi_{p_2}-\mathcal{E}_{N+2}) n_{\mathrm{F}}(\xi_{p_1}-eV_a) n_{\mathrm{F}}(\xi_{p_2}-eV_a)\,. \tag{2.52}$$

Again $\Gamma^a_{N+2\to N}$ is defined similarly with $n_{\mathrm{F}} \to 1-n_{\mathrm{F}}$. To find the zero-bias differential conductance we rely on an expression for the $2e$-tunnelling current contribution from Ref. [70] and find:

$$\mathcal{G}_{2e} = \frac{e^2}{2h} \frac{g_L^2 g_R^2}{g_L^2+g_R^2} \frac{1}{\pi^2} \frac{\Delta_e^2}{\Delta_e^2-\mathcal{E}_{N+1}^2} \arctan^2\left(\sqrt{\frac{\Delta_e-\mathcal{E}_{N+1}}{\Delta_e+\mathcal{E}_{N+1}}}\right) \frac{\mathcal{E}_{N+2}/k_{\mathrm{B}}T}{\sinh\left[\mathcal{E}_{N+2}/k_{\mathrm{B}}T\right]}\,. \tag{2.53}$$

Here $\mathcal{E}_{N+2} = 4E_C(N+(N'+q)/3+1-n_g)$ is the difference in charging energy between the states with N and $N+2$ electrons. As for the other processes we include quasiparticle poisoning by taking the weighted sum:

$$G_{2e} = \sum_{N,N',q} \frac{\mathrm{e}^{-H_{\mathrm{SC}}(N,N',q,n_g)/T}}{Z} \left(\mathcal{G}_{2e}(N)+\mathcal{G}_{2e}(N-2)\right)\,. \tag{2.54}$$

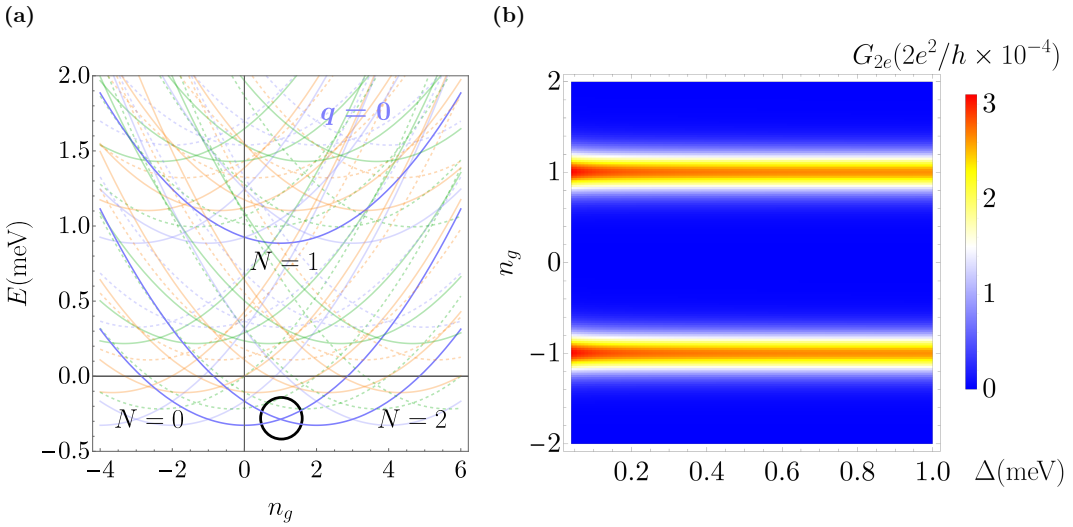

Figure 2.13: Coulomb-blockaded short PF device with low charging energy. **(a)** Energy dispersion as a function of the voltage-controlled induced charge number n_g. The three featured states $|N, N' = 0, q = 0\rangle$ with $N = \{0, 1, 2\}$ display the $2e$ crossing (black circle) and the energy separation Δ_e between states with and without a quasielectron excitation. The SC length is now $L = 0.1$ µm, the charging energy $E_C = 0.04$ meV, $\Delta = 0.3$ meV, $\Delta_{\mathrm{FQH}} = 1.72$ meV and the edge mode velocity $v = 10^5$ m/s. **(b)** Zero-bias differential conductance $G_{2e}(\Delta, n_g)$ with energies as shown in Fig. 2.12. As expected from (a), we see two clear peaks at odd integer values of n_g.

An example of this conductance contribution is plotted in Fig. 2.13b for a SC that is ten times shorter than otherwise assumed in this chapter, $L = 0.1$ µm. We assume that the charging energy is weak, $\Delta_e > \varepsilon \gg E_C \gg T$, such that the Cooper pair tunnelling is relevant. We see that the conductance displays a single peak every $2e$ as opposed to the six peaks in Fig. 2.8b. We expect, however, that for experimentally relevant systems with a thin SC the charging energy will be larger than ε for any pairing Δ. Thus, this Andreev-dominated regime would be hard to observe and, in practice, for all intermediate pairings the $2e$ pattern will be sixfold as for $\Delta \lesssim 0.3$ meV in Fig. 2.8b.

We conclude from this discussion of the three types of tunnelling processes that for typical experimental parameters $L = 1$ µm and $E_C = 0.5$ meV the $e/3$ periodicity signals the onset of a topological phase where the two PFs are strongly localised. Only in devices where the quasielectron excitation energy can be safely neglected, i.e. the quantum dot regime with $\delta, \Delta_e \ll T < E_C$, can a similar $e/3$-periodic pattern appear (see also the table in Fig. 2.11b). We furthermore note that grounding the SC to make a three-terminal device will not provide additional signatures in the conductance due to electron-hole symmetry making the cross conductance between the two normal leads zero.

2.3 Conclusions on the readout of signatures of parafermionic states

In this chapter we have seen that PFs in FQH systems with induced superconductivity [20] can be investigated through transport measurements. For example, low-bias conductance peaks corresponding to energies below the induced superconducting pairing can be observed in two-terminal devices, analogously to MF setups. However, differently from MFs, it is possible to distinguish the GSs of a pair of interacting PFs by a current readout. We have seen that distinct values of the shared fractional charge $-e\tilde{q}/3$ result in distinct low-energy resonances in the conductance between a normal metallic lead, tunnel-coupled to the PFs, and a superconducting background. We note that these proposed setups are different from those characterised by transport of fractional quasiparticles [81–87]. We argued that in the presence of weak fractional quasiparticle poisoning a three-state telegraph noise in the current is expected providing a way to distinguish parafermionic and trivial electronic subgap states.

We analysed complementary signatures of PFs in a Coulomb-blockaded device, in particular predictions for the two-terminal conductance across the floating fractional SC as a function of the induced charge. For intermediate superconducting pairing and at low temperatures the zero-bias conductance shows a six-peak pattern repeating with a $2e$ periodicity in the induced charge. These zero-bias peaks evolve into an $e/3$-periodic pattern for strongly localised PFs (i.e. in the truly topological regime), similar to what is observed in fractional quasiparticle transport [82].

The methods of electronic tunnelling spectroscopy described here can be extended and generalised to devices with more leads or with quantum dots like what was proposed for non-topological $\mathbb{Z}_4$ PFs [88–91]. Furthermore, integration of this spectroscopy method with additional fractional quasiparticle elements could lead to new topological quantum computation platforms based on PFs.

3

Dynamics of parafermionic states

This chapter is an adaptation of I. E. Nielsen, J. Schulenborg, R. Egger and M. Burrello, *Dynamics of parafermionic states in transport measurements*, arXiv:2305.08906 (May 2023) [2] with more elaborate and detailed calculations.

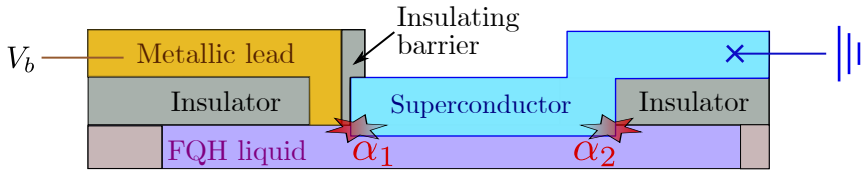

Figure 3.1: Reprint of the grounded device with two PFs (red stars) from Ch. 2.

In the previous chapter we saw how signatures of parafermions (PFs) in a hybrid fractional quantum Hall-superconductor (FQH-SC) device can be obtained with otherwise standard transport spectroscopy. A current readout could, under the right conditions, reflect the $\mathbb{Z}_3$ degree of freedom of $\mathbb{Z}_6$ PFs, namely the reduced charge $-e\tilde{q}/3$ with $\tilde{q} = \{0,1,2\}$, defined up to one electron charge. We also discussed how poisoning from fractional quasiparticles with charge $\pm e/3$, while breaking the conservation of $\tilde{q}$, could be beneficial in this respect. It could reveal itself in a three-level telegraph noise in the conductance provided the poisoning rate is much lower than the other energy scales in the system (up to an $\hbar$). In this chapter we will elaborate on this claim and quantify the required energy and time scales by use of a stochastic quantum jump method [92, 93]. We study the transport *dynamics*, including noise, of such a device out of equilibrium and see how a current can projectively measure the reduced charge number $\tilde{q}$ (Sec. 3.1). We will consider two types of poisoning effects: in Sec. 3.2 we study incoherent poisoning from a bath of fractional quasiparticles which could be the outer edge modes of the FQH system. Sec. 3.3 treats instead the coherent coupling between PFs and a fractional quasiparticle such as an antidot in the bulk of the FQH liquid [80, 94]. In Sec. 3.4 we will extend the system to four PFs – the minimum number of PFs required to investigate their braiding and fusion rules [44, 95]. We show how the associativity of the (anyonic) fusion rules for the $\tilde{q}$ degree of freedom of the PFs could be explored with transport measurements. The analysis and proposals of this chapter are to further advance the investigation of PFs and provide alternative signatures to those experimentally observed for example in Ref. [20]; these measurements could be explained with dissipation from e.g. single-electron tunnelling into vortices in the SC [21] and therefore many further experiments in these hybrid devices are required in the search for PFs.

The setup for studying a pair of $\mathbb{Z}_6$ PFs will be the same as in Fig. 2.3, inspired by the experiments of Refs. [20, 43] and the theoretical proposals in Refs. [8, 11, 12, 23, 36, 39, 40, 42]. With respect to the first chapter, we will assume that only the left PF α_1 is coupled to the lead, i.e. $\eta_2 \to 0$. For convenience we reproduce the proposed setup here (Fig. 3.1). Let us begin by examining the readout dynamics of this device.

Unless explicitly stated otherwise, we will keep $\hbar = k_B = 1$ throughout this chapter.

3.1 Readout dynamics of two parafermions

Recall that the state of the two PFs α_1 and α_2 can be characterised by their shared parity [25] $P_{12} = e^{-i\frac{\pi}{6}}\alpha_2^\dagger\alpha_1 = e^{-i\frac{\pi}{3}\hat{q}}$ where $\hat{q}$ is the operator counting fractional $-e/3$ charges up to one Cooper pair in the gapless edge modes that are coupled by the SC. As before, the corresponding energy splitting of the PFs is $H_{2\text{pf}} = -2\varepsilon\cos(\pi\hat{q}/3+\phi)$ [38, 96]. We take the simple lead coupling $H_c = i\eta_1\alpha_1^3(l+l^\dagger)$ [45–49, 97] where $l = l_{x=0}$ is the electron annihilation operator at the end of the normal electrode. The conductance displays quantised peaks of $2e^2/h$ when the voltage bias V_b

is tuned to the resonances $eV_b = 4\varepsilon\cos(4\pi\tilde{q}/3+\phi) \equiv \Delta_\varepsilon(\tilde{q})$ where $\tilde{q}$ is the topologically protected degree of freedom in absence of poisoning. Like in Ch. 2 we will keep $\phi = \phi_0 = \arctan(1/\sqrt{27})$. From the estimate of ε in Sec. 2.2, which was based on results in Ref. [38] and [20], we introduce the convenient energy scale $\lambda = 2\pi\cdot 2.4$ GHz ≈ 10 μeV which will be our reference energy throughout this chapter. In fact, unless otherwise stated the PF overlap is taken to be $\varepsilon = \lambda$ and the temperature to $T = \lambda/3$.

Electron jump operators for a two-parafermion system

In this chapter we focus on the dynamics of PFs, and we would like to put forward predictions on the electrical current signatures which could be tested in future experiments. To begin with, we analyse the open system consisting of the two PFs that are coupled to the metallic lead (see Fig. 3.1). We assume that the lead electron reservoir acts as a Markovian bath which means that the correlation time of the electrons in the electrode is the shortest timescale in the system dynamics [98]. The (ensemble average) evolution of the two PFs can be expressed in terms of a *Lindblad master equation* for their density operator ρ [93, 98]:

$$\partial_t\rho = -i\left[H_{2\text{pf}}+\Lambda,\rho\right] + \sum_i \left[L_i\rho L_i^\dagger - \frac{1}{2}\left\{L_i^\dagger L_i,\rho\right\}\right]. \tag{3.1}$$

Here Λ is a Hermitian Lamb shift of $H_{2\text{pf}}$ which is renormalised due the coupling with the bath. The operators L_i are known as *jump operators* that describe the dissipative part of the system evolution due to the coupling with an external bath – the lead in our case. The operator L_i introduces a charge $\pm 1e$ in the PF system with a rate that is determined by the coupling strength. The number of jump operators in the sum of Eq. (3.1) depends on properties of the bath(s) and coupling(s). With the above rate equation we can find the steady state solution to the density matrix ρ which will in general describe some mixture of $\tilde{q} = 0, 1, 2$. We are, however, interested in following the evolution of the PF state in order to compare with experimental readouts, and we therefore adopt a different approach which still makes use of the jump operators but allows us to track single realisation trajectories; the stochastic quantum jump method [92, 93, 99–101]. Following Refs. [98, 101], the jump operators corresponding to the coupling Hamiltonian H_c are

$$L_\pm^e = \sum_{q,q'} \sqrt{2\pi\eta_1^2\tilde{J}_\pm(E_{q'}-E_q)}\,\langle q|i\alpha_1^3|q'\rangle\,|q\rangle\langle q'|\,, \tag{3.2}$$

where the operator L_+^e moves an electron charge from the lead to the PFs and vice versa for L_-^e. The states $|q\rangle$ and $|q'\rangle$ ($q, q' \in \{0,\ldots,5\}$) are the eigenstates of $H_{2\text{pf}}$ (and of $\hat{q}$) with corresponding eigenenergies E_q and $E_{q'}$, respectively. The functions $\tilde{J}_+(\omega)$ and $\tilde{J}_-(\omega)$ are the spectral functions of the bath, corresponding to the Fourier transform of the two-point bath correlation functions $\langle l^\dagger(t)l(0)\rangle$ and $\langle l(t)l^\dagger(0)\rangle$, respectively. The Hamiltonian for the simple metallic lead with chemical potential μ_{lead} is $H_{\text{lead}} = \sum_k \xi_k l_k^\dagger l_k$ where $\xi_k + \mu_{\text{lead}} = \frac{k^2}{2m}$ is the kinetic energy of an electron with quasimomentum k. The electron annihilation operator in momentum space is defined such that $l_x = \frac{1}{\sqrt{N_c}}\sum_k l_k e^{ikx}$ where $N_c = L_c/a_c$ with L_c the contact length and a_c the lattice spacing.[1] The

[1] This ensures that $\{l_x^\dagger, l_x\} = \{l_k^\dagger, l_k\} = 1$ in discrete spaces.

bath correlation functions are thus

$$\tilde{J}_+(t-t') = \langle l^\dagger(t) l(t')\rangle = \frac{1}{N_c}\sum_{k,k'} \langle \mathrm{e}^{i\xi_k t}\, l_k^\dagger \mathrm{e}^{-i\xi_{k'} t'}\, l_{k'}\rangle = \frac{1}{N_c}\sum_k \mathrm{e}^{i\xi_k(t-t')}\, n_\mathrm{F}(\xi_k, V_b)\,, \tag{3.3}$$

$$\tilde{J}_-(t-t') = \langle l(t) l^\dagger(t')\rangle = \frac{1}{N_c}\sum_{k,k'} \langle \mathrm{e}^{-i\xi_k t}\, l_k \mathrm{e}^{i\xi_{k'} t'}\, l_{k'}^\dagger\rangle = \frac{1}{N_c}\sum_k \mathrm{e}^{-i\xi_k(t-t')}(1-n_\mathrm{F}(\xi_k, V_b))\,, \tag{3.4}$$

where $n_\mathrm{F}(\xi_k, V_b) = [\exp(\beta(\xi_k - eV_b))+1]^{-1}$ is the Fermi-Dirac distribution function at a voltage bias V_b with respect to the grounded SC and β is the inverse temperature. The corresponding spectral functions become

$$\tilde{J}_+(\omega) = \frac{1}{2\pi N_c}\sum_k \int_{-\infty}^{\infty} \mathrm{d}\, t\, \mathrm{e}^{i(\omega+\xi_k)t}\, n_\mathrm{F}(\xi_k, V_b) = \frac{1}{N_c}\sum_k \delta(\omega+\xi_k) n_\mathrm{F}(\xi_k, V_b) = \nu_l\, n_\mathrm{F}(-\omega, V_b)\,, \tag{3.5}$$

$$\tilde{J}_-(\omega) = \frac{1}{2\pi N_c}\sum_k \int_{-\infty}^{\infty} \mathrm{d}\, t\, \mathrm{e}^{i(\omega-\xi_k)t}(1-n_\mathrm{F}(\xi_k, V_b)) = \nu_l(1-n_\mathrm{F}(\omega, V_b))\,, \tag{3.6}$$

where we again assumed a constant density of states ν_l in the lead. With our chosen phase convention (Ch. 1), $\langle q|\alpha_1^3|q'\rangle = \delta_{q',q+3}$ where all q are still defined modulo 6 such that $|q+3\rangle = |q-3\rangle$. In total the jump operators are thus

$$L_\pm^e = i\sum_{q=0}^{5} \sqrt{\Gamma J_\pm(\Xi_q, V_b)}\, |q\rangle\langle q+3|\,, \quad \Gamma = 2\pi\nu_l\eta_1^2\,, \tag{3.7}$$

where we introduced the coupling rate Γ such that Γ^{-1} characterises the typical time between PF-lead interactions. We rescaled the spectral function to $J_\pm(\omega, V_b) = n_\mathrm{F}(-\omega, \pm V_b)$ and use the shorthand notation $\Xi_q = E_{q+3} - E_q = 4\varepsilon\cos(\pi q/3+\phi)$. We see that application of a jump operator changes the charge of the PFs $q \to q\pm 3$.

The Lamb shift in the Lindblad master equation (3.1) contains two contributions, $\Lambda = \Lambda_+ + \Lambda_-$, where [98]

$$\begin{aligned}\Lambda_\pm &= \sum_{q,q',q''} f_\pm(E_q - E_{q'}, E_{q''} - E_q)\, \langle q'|i\alpha_1^3|q\rangle\langle q|i\alpha_1^3|q''\rangle\, |q'\rangle\langle q''| \\ &= i^2\sum_q f_\pm(E_q - E_{q-3}, E_{q+3} - E_q)\, |q-3\rangle\langle q+3| \\ &= -\sum_q f_\pm(E_q - E_{q+3}, E_{q+3} - E_q)\, |q+3\rangle\langle q+3|\,,\end{aligned} \tag{3.8}$$

and the function $f(-\Xi_q, \Xi_q)$ is

$$f_\pm(-\Xi_q, \Xi_q) \equiv -\nu_l\eta_1^2\, \mathcal{P}\int_{-\infty}^{\infty} d\omega\, \frac{J_\pm(\omega+\Xi_q, V_b)}{\omega}\,. \tag{3.9}$$

Here $\mathcal{P}\int$ denotes the Cauchy principal value of the integral. It is not straight forward to calculate these Lamb shifts analytically, but a part of them can be expressed in terms of the di-gamma function. However, we see from Eq. (3.8) that the shifts are diagonal in the PF Hilbert space and thereby only yield a renormalisation of ε. By numerical calculations we find the elements of $\Lambda_\pm$ to be of the order $\lesssim 3\nu_l\eta_1^2 \approx \Gamma/2$. We will restrict our analysis to a coupling rate that is much smaller

than the energy level spacing of $H_{2\mathrm{pf}}$ which, for a phase ϕ not close to a multiple of $\pi/6$, means $\Gamma \ll \varepsilon$ such that the Lamb shift can be neglected. We fix the coupling rate to $\Gamma = 0.1\lambda$

Note that one could have defined just a single Hermitian bath operator $l + l^\dagger$ and thereby only have one jump operator [98]. For our approach with counting jumps of electrons in and out, keeping the two jump operators separate is more convenient. Importantly, our calculations rely on the assumption that electrons in the lead are immediately projected, i.e. on the shortest time scale of the entire system dynamics. That way we can interpret the application of $L^e_\pm$ as an electron moving either out of or into the lead. We describe now how the single track trajectories are calculated.

The quantum jump method

We would like to know the evolution of the PF state over some time interval. We divide this into small steps δt such that $\delta t \ll 2\pi\Gamma^{-1}$. Specifically, we set $\delta t = 0.1$ ns. In each interval there is a small probability $\propto \delta t \cdot \Gamma \ll 1$ that an electron will scatter into or out of the PF system. We follow the Monte Carlo protocol from Ref. [101] and define the no-jump evolution operator

$$\mathcal{U} = \exp\left[-i\delta t\left(H_{2\mathrm{pf}} - \frac{i}{2}\sum_{s=\pm}\left(L^e_s\right)^\dagger L^e_s\right)\right]. \tag{3.10}$$

Due to coupling between PF α_1 and the lead, the evolution is non-unitary even when no jump takes place. The protocol steps are the following:

Step 0: We initialise the PF state in some superposition of the charge eigenstates of $H_{2\mathrm{pf}}$;

$$|\psi(t=0)\rangle = \sum_q c_q\,|q\rangle\,, \tag{3.11}$$

where the coefficients c_q can in principle all be non-zero.
Step 1: We evolve the state under the no-jump evolution operator $\mathcal{U}$. Due to the dissipative part of the evolution, the state at time $t+\delta t$ must be renormalised:

$$|\psi(t+\delta t)\rangle = \frac{\mathcal{U}\,|\psi(t)\rangle}{\sqrt{\langle\psi(t)|\mathcal{U}^\dagger\mathcal{U}\,|\psi(t)\rangle}}. \tag{3.12}$$

Step 2: We set a random order of L^e_+ and L^e_- and draw two numbers from a uniform distribution, $p_{s=\pm} \in [0,1]$.
Step 3: The probability at time $t+\delta t$ that a jump corresponding to L^e_s has taken place within the time interval δt, is

$$P_s(t+\delta t) = \langle\psi(t+\delta t)|\left(L^e_s\right)^\dagger L^e_s|\psi(t+\delta t)\rangle\,\delta t\,. \tag{3.13}$$

By the order set in step 2, say $(s', -s')$, we first check if $p_{s'} < P_{s'}(t+\delta t)$ in which case the corresponding jump operator is applied to the state, followed by renormalisation:

$$|\psi(t+\delta t)\rangle \to \frac{L^e_{s'}\,|\psi(t+\delta t)\rangle}{\sqrt{\langle\psi(t+\delta t)|(L^e_{s'})^\dagger L^e_{s'}|\psi(t+\delta t)\rangle}} = \frac{L^e_{s'}\,|\psi(t+\delta t)\rangle}{\sqrt{P(t+\delta t)/\delta t}}. \tag{3.14}$$

If not, we check if $p_{-s'} < P_{-s'}(t+\delta t)$ and apply the jump operator corresponding to a jump in the opposite direction. If neither of the conditions are fulfilled we leave the state $|\psi(t+\delta t)\rangle$ unchanged.

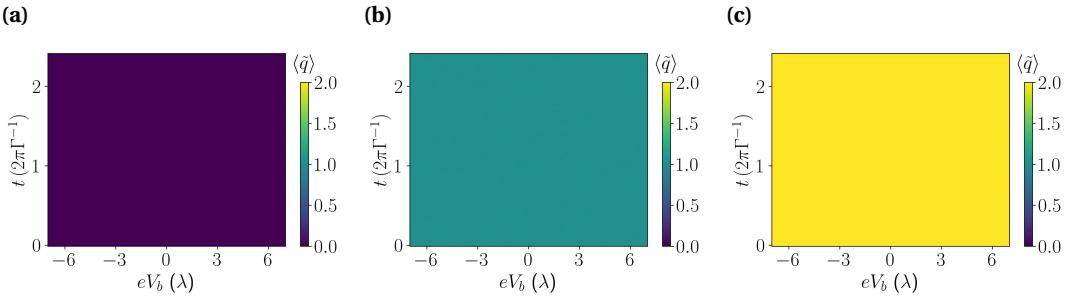

Figure 3.2: Expectation value of $\tilde{q}$ on the timescale $\mathcal{O}(2\pi\Gamma^{-1}) \sim \mathcal{O}(\text{ns})$ for the three initial states: **(a)** $|\tilde{q}=0\rangle$, **(b)** $|\tilde{q}=1\rangle$ and **(c)** $|\tilde{q}=2\rangle$. The trajectories are calculated at 900 equally distributed values of the voltage bias in the interval $[-7\lambda, 7\lambda]$.

The protocol is repeated from step 1 with the state $|\psi(t+\delta t)\rangle$ and the loop is continued until the final simulation time has been reached. Importantly, because of the assumption of Markovianity of the lead, the application of a jump operator does not change the distribution function of the electron bath which remains the equilibrium Fermi-Dirac distribution. We note that this method is very resemblant to the stochastic Schrödinger equation [93] although not identical; in our case the jump operators can, depending on the state, yield an immediate discontinuous state transition from $|\psi(t+\delta t)\rangle$ to $L_s^e|\psi(t+\delta t)\rangle$ whereas the jump operators of the stochastic Schrödinger evolution always act as weak projections making the state transition continuous. We will use the above protocol to calculate both expectation values of the charge on a given trajectory as well as estimates of the current.

Projection of charge sectors

With the Monte Carlo protocol described above we will now study the evolution of an initial state $|\psi(t=0)\rangle = \sum_q c_q|q\rangle$ and in particular the PF charge. We do this by calculating the expectation value of the reduced charge operator $\tilde{q}$ at every time step of the trajectory.

If the initial state is in a well-defined charge sector such that it is an eigenstate of $\tilde{q}$, the time-evolved state remains within this sector, i.e. a superposition of the states $|q\rangle$ and $|q+3\rangle$, as one would expect. An example of this is shown in Fig. 3.2 where we plot the expectation value of $\tilde{q}$ for the three initial states

$$|\tilde{q}=0\rangle = \frac{|q=0\rangle + |q=3\rangle}{\sqrt{2}}, \quad |\tilde{q}=1\rangle = \frac{|q=1\rangle + |q=4\rangle}{\sqrt{2}}, \quad |\tilde{q}=2\rangle = \frac{|q=2\rangle + |q=5\rangle}{\sqrt{2}}, \tag{3.15}$$

by calculating a single stochastic trajectory for every V_b. The charge expectation value is also conserved on the µs timescale.

If we instead initiate the system in a state that is a superposition of states with distinct $\tilde{q}$ the situation is very different. As before, the state will evolve under the no-jump evolution operator $\mathcal{U}$ and occasionally an electron will jump into or out of the system through the lead. These jumps all consist a weakly projective measurement, and for sufficiently long times the current measurement projects to a fixed but random $\tilde{q}$. We test a 'worst-case' scenario initial state $|\text{equal}\rangle = \frac{1}{\sqrt{6}}\sum_{q=0}^{5}|q\rangle$ that is an equal superposition of all charge states with an expectation value of $\tilde{q}$ that is 1. We

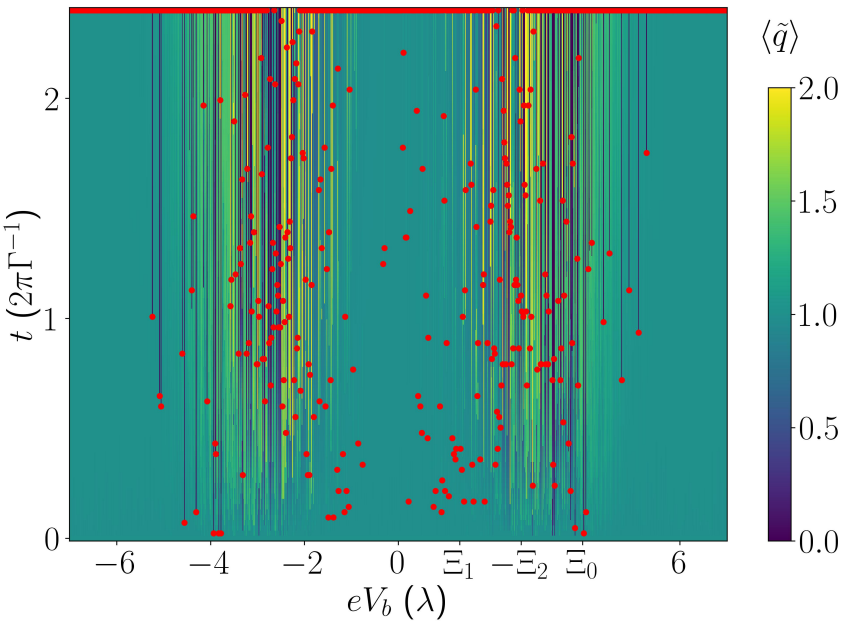

Figure 3.3: Expectation value of $\tilde{q}$ for the initial state $|\text{equal}\rangle = \frac{1}{\sqrt{6}}\sum_{q=0}^{5}|q\rangle$. We would expect to see all three charge sectors realised with equal probability 1/3, but there is a clear overweight of $\langle\tilde{q}\rangle \approx 1$, in particular for voltage biases away from the resonance energies. In round numbers, the part of trajectories with a $\langle\tilde{q}\rangle \in [0, 0.66e[$ after 10 ns is 14%, 68% are within $\langle\tilde{q}\rangle \in [0.66e, 1.33e[$ and 18% within $\langle\tilde{q}\rangle \in]1.33e, 2e]$. The red dots mark when the threshold $\zeta^* = 0.9$ is reached. The many dots in the top of the plot illustrate that this threshold is not reached within 10 ns.

expect that, on average, $\langle\tilde{q}\rangle$ should evolve into 0 or 2 or remain 1 with equal probability 1/3 for all three values. Looking at the results in Fig. 3.3 we see that this is clearly not the case, at least not on the nanosecond timescale. On the colour scale we show as before the evolution of $\langle\tilde{q}\rangle$ in separate random trajectories for different values of V_b. For voltage values around the three resonance energies $|\Xi_0| = 4\varepsilon|\cos(\phi)|$, $|\Xi_1| = 4\varepsilon|\cos(\pi/3+\phi)|$ and $|\Xi_2| = 4\varepsilon|\cos(2\pi/3+\phi)|$, $\langle\tilde{q}\rangle$ seems to distribute somewhat between 0, 1 and 2 but not away from these voltages. We interpret these cases as trajectories where the PF-lead interaction is insufficient to project the state into either of the three sectors on a timescale of order $2\pi\Gamma^{-1} \approx 4$ ns and the state remains in a superposition.

As a quantitative measure of the projection we introduce a measure that is inspired by the inverse participation ratio. We note that for any general superposition $|\psi\rangle = \sum_{q=0}^{5} c_q|q\rangle$ the normalisation enforces $\sum_q |c_q|^2 = 1$ whereas, in general, $\sum_q |c_q|^4 \neq 1$ unless all but one c_q are zero. From this observation we present the measure

$$\zeta = \sum_{\tilde{q}=0,1,2} \left(|c_{\tilde{q}}|^2 + |c_{\tilde{q}+3}|^2\right)^2 . \tag{3.16}$$

This is 1/3 for the state $|\text{equal}\rangle$ and approaches 1 when the state is progressively projected into one of the three charge sectors. In Fig. 3.3 we indicate with a red dot, on top of the $\langle\tilde{q}\rangle$ colour plot, the

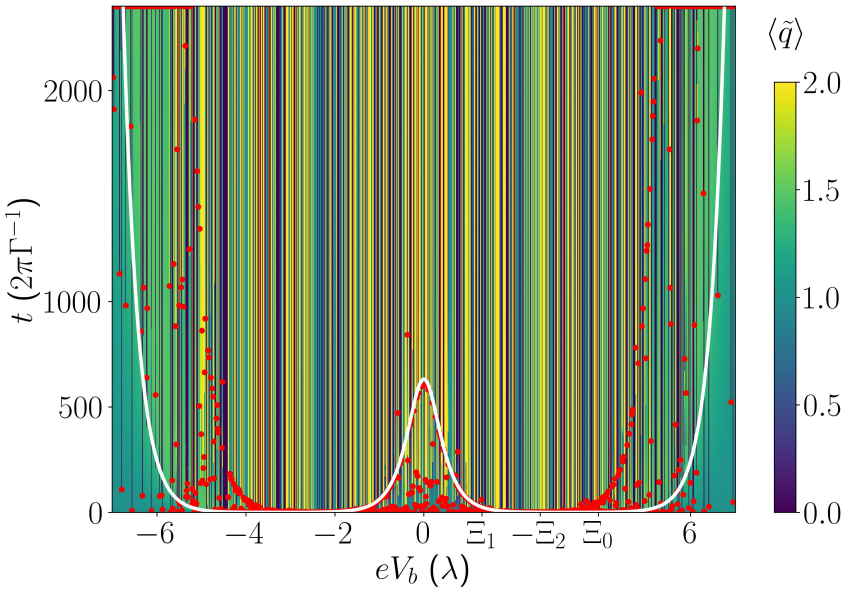

Figure 3.4: Expectation value of $\tilde{q}$ for the initial state $|\text{equal}\rangle = \frac{1}{\sqrt{6}}\sum_{q=0}^{5}|q\rangle$. Red dots mark when the threshold $\zeta^* = 0.9$ is reached. The dots in the top of the plot signal that this threshold is not reached within 10 µs for that particular trajectory. The white curve is the estimate $1.45\cdot 10^{-3}(\tilde{\lambda}(5)-\tilde{\lambda}(0))^{-1}$ for the projection time. We can compare the distribution between the different charge sectors. At 10 µs 29% of the trajectories are within $\langle\tilde{q}\rangle \in [0, 0.66[$, 31% within $\langle\tilde{q}\rangle \in [0.66, 1.33[$ and 40% within $\langle\tilde{q}\rangle \in]1.33, 2]$.

time when ζ of a trajectory reaches $\zeta^* = 0.9$. The many points in the top are to indicate that the projection measure has not reached this threshold within the first 10 ns and hence that the state remains in a superposition of $\tilde{q}$ states, which agrees well with the data on $\langle\tilde{q}\rangle$. From this figure we also see that once the state is almost projected into one of the charge sectors (as indicated by the change in $\langle\tilde{q}\rangle$ and ζ^*) it tends to remain within this in accordance with Fig. 3.2.

In Fig. C.1 of App. C we compare the two estimates of the projection, $\langle q\rangle$ and ζ^*, for three different temperatures and see that an increase in temperature shortens the projection time in general as expected.

On a 10^3 times longer scale of $\mathcal{O}$(µs) we see better the projection of states. In Fig. 3.4 we plot the expectation value of $\tilde{q}$ up to 10 µs together with red dots denoting $\zeta^* = 0.9$. We observe also here that the projection is slow around $V_b = 0$ and at voltage biases larger than the resonant energies $\Xi_{0,1,2}$. For the largest values of $|eV_b|$ the state is not even projected after 10 µs according to our ζ^* measure. Any experiment should therefore be performed at voltages close to the Ξ_q resonances in order to minimise the readout time of the reduced charge.

In Fig. C.2 we show the behaviour of $\langle\tilde{q}\rangle$ and ζ^* for three different temperatures a the time scale of $\mathcal{O}$(µs). Also here we see from both $\langle q\rangle$ and the ζ projection measures that a higher temperature decreases the projection time.

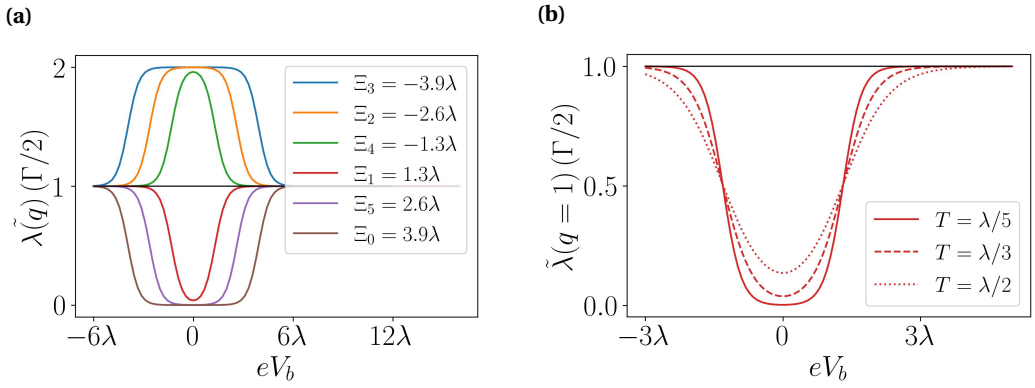

Figure 3.5: The expression for $\tilde{\lambda}(q)$ in Eq. (3.18) for **(a)** fixed temperature $T = \lambda/3$ and different values of q and **(b)** different temperatures and fixed $q = 1$. Increasing temperature 'flattens' the curves.

As a further estimate of the projection time and an attempt to understand its behaviour, we take a closer look at the dissipative no-jump evolution operator

$$\mathcal{U} = \exp\left[-i\delta t\left(H_{2\mathrm{pf}} - \frac{i}{2}\left((L_+^e)^\dagger L_+^e + (L_-^e)^\dagger L_-^e\right)\right)\right]. \tag{3.17}$$

The $H_{2\mathrm{pf}}$ part only changes the phases in the PF state whereas the jump operator part leads to a decay, diagonal in q, which partly compensates for the fact that the jump operators themselves project with different weights into the different states $|q=0\rangle, \ldots, |q=5\rangle$. From Eq. (3.7) we find that, in the basis of $|q\rangle$ states, $(L_\pm^e)^\dagger L_\pm^e$ is diagonal with elements $\Gamma J_\pm(\Xi_{q+3}, V_b)$ in the (q,q) entry. Therefore, the decaying part of the q'th element in the diagonal operator $\mathcal{U}$ is

$$\frac{-\delta t}{2}\Gamma\left[n_\mathrm{F}(-\Xi_{q+3}, V_b) + 1 - n_\mathrm{F}(\Xi_{q+3}, V_b)\right] = \frac{-\delta t}{2}\Gamma\left[\frac{1}{1+\mathrm{e}^{\beta(\Xi_q - eV_b)}} + \frac{1}{1+\mathrm{e}^{\beta(\Xi_q + eV_b)}}\right] = -\delta t\tilde{\lambda}(q), \tag{3.18}$$

where we used that $\Xi_{q+3} = -\Xi_q$. We plot the above expression for $\tilde{\lambda}(q)$ in Fig. 3.5. For $\Xi_q > 0$ this decreases around $V_b = 0$, meaning a slower decay of the $|q\rangle$ component of the state, whereas it increases around $V_b = 0$ for $\Xi_q < 0$. Based on Fig. 3.5a we expect the two states with the highest values of Ξ_q (in this case $|q=0\rangle$ and $|q=5\rangle$) to set the projection time, given that we begin in a superposition of states with different $\tilde{q}$. As an estimate we consider the ratio

$$\left(\frac{\mathrm{e}^{-\tilde{\lambda}(q)\delta t}}{\mathrm{e}^{-\tilde{\lambda}(q')\delta t}}\right)^N = \left(\mathrm{e}^{-(\tilde{\lambda}(q)-\tilde{\lambda}(q'))\delta t}\right)^N \ll 1, \tag{3.19}$$

where N is the number of time steps such that $\delta t \cdot N$ is the projection time and q' and q are the charge sectors with the largest and second to largest Ξ, respectively (meaning the ones that decay most slowly under the operation of $\mathcal{U}$). Thus the projection time is inversely proportional to $\Gamma \propto \eta_1^2$ and the closer the two rates are to each other the longer will be this time. In Fig. 3.6a we plot the inverse of this difference $(\tilde{\lambda}(q=5) - \tilde{\lambda}(q=0))^{-1}$ as function of the bias voltage as a qualitative

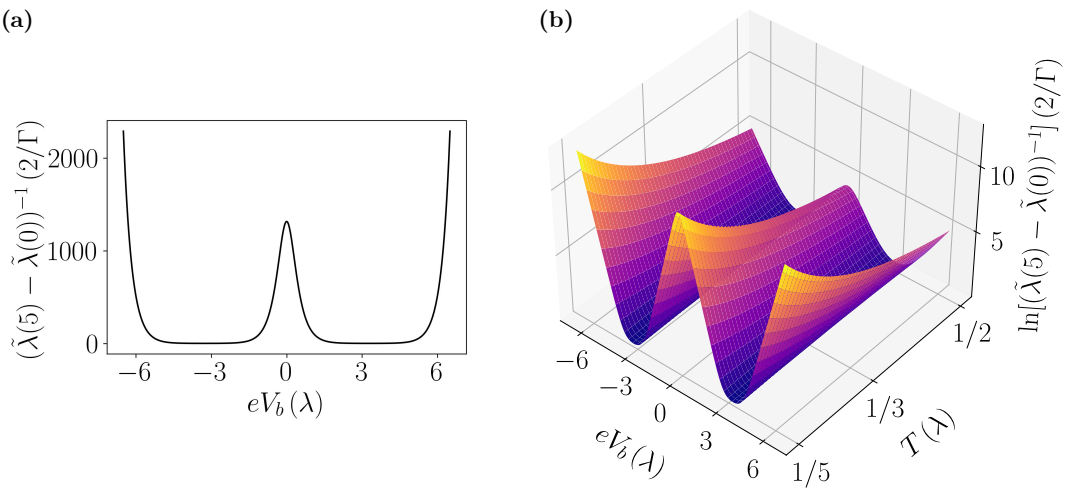

Figure 3.6: Estimate of the qualitative behaviour of the projection time with voltage bias and temperature.

estimate of the projection time for the special trajectory in which no jumps occur. In Fig. 3.4 we plot in white this function scaled by a factor $1.45 \cdot 10^{-3}$. Comparing with the $\langle \tilde{q} \rangle$ and ζ^* measures we find a decent qualitative agreement between these estimates and the analytical expression for voltages corresponding to $|eV_b| \lesssim |\Xi_q|$. Instead, the curve seems to underestimate the projection time at larger voltages. We address this discrepancy to the fact that we did not include in this assessment the random quantum jumps which dephase the state. The temperature behaviour of the analytical expression for the projection time is shown in Fig. 3.6b.

The partly explanation of the projection time by the continuous part of the wave function evolution – and consequently competing decay rates – is supported by the observation that the simpler type of superposition $\frac{1}{\sqrt{3}}(|q=0\rangle + |q=1\rangle + |q=2\rangle)$, still involving all $\tilde{q}$ sectors, has a considerably shorter projection time seen already on the $\mathcal{O}(2\pi\Gamma^{-1}) \sim \mathcal{O}(\text{ns})$ timescale, see Fig. 3.7. Thus we conclude that the projection into one of the reduced charge sectors is highly sensitive to the initial state of the system and |equal⟩ is a worst-case initial state in terms of projection time for the purpose of reading out $\tilde{q}$.

Current behaviour of a two-parafermion system

With the stochastic quantum jump method in place we are ready to calculate trajectories of the current between the metallic lead and the PFs. For now we assume that $\tilde{q}$ is a conserved and protected quantity before extending to more general cases in the subsequent sections. To calculate the current we evolve the system following the Monte Carlo protocol described above and keep track of the times at which the jump operators are applied. As mentioned previously, we associate L_+^e with an electron charge jumping from the lead into the PF system and L_-^e with the reverse process. We introduce the jump-count variable $j_{\text{diff}}(t)$ which increases or decreases by 1 whenever L_+^e or L_-^e, respectively, are applied and $j_{\text{diff}}(0) = 0$. Furthermore, we set an 'average time' t_{avg} which is the interval over which we average this jump-count variable. It corresponds to the integration

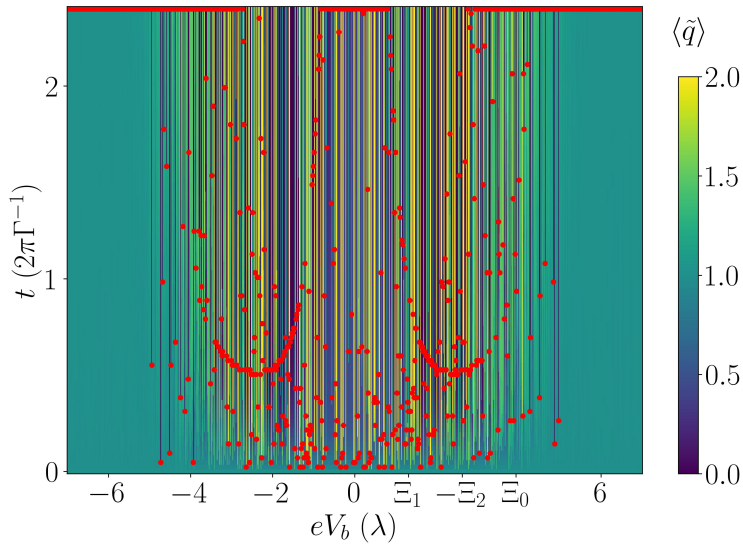

Figure 3.7: Evolution of $\langle\tilde{q}\rangle$ and plot of $\zeta^* = 0.9$, similar to Fig. 3.3 and with the same parameters but for the simpler initial state $\frac{1}{\sqrt{3}}\big(|q=0\rangle + |q=1\rangle + |q=2\rangle\big)$.

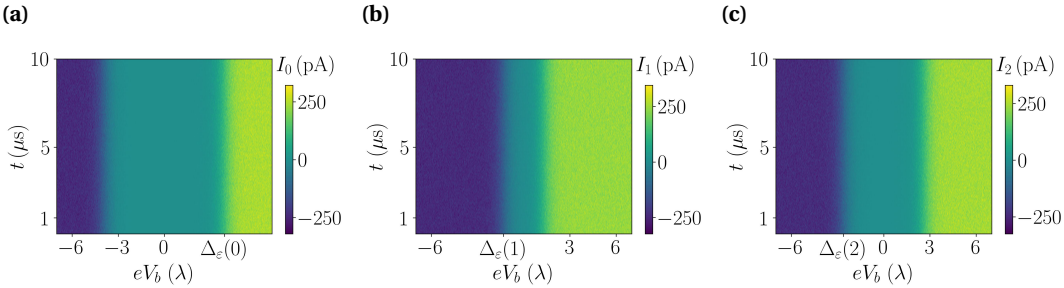

Figure 3.8: Numerical current estimates for the three different initial states: **(a)** $|\tilde{q}=0\rangle$, **(b)** $|\tilde{q}=1\rangle$ and **(c)** $|\tilde{q}=2\rangle$. The integration time is $t_{\text{avg}} = 0.1$ µs. The transitions in $I_{\tilde{q}}(V_b)$ are consistent with the PF level splitting which is indicated at the voltage axis.

time of the current measurement device in a real experiment. From $t \geq t_{\text{avg}}$ we can give estimates of the current:

$$I(t) = e\frac{j_{\text{diff}}(t) - j_{\text{diff}}(t - t_{\text{avg}})}{t_{\text{avg}}}. \tag{3.20}$$

In Fig. 3.8 we show the result of a single random trajectory for each of 900 different voltage values with the three initial states $|\tilde{q}=0\rangle$, $|\tilde{q}=1\rangle$ and $|\tilde{q}=2\rangle$ (see Eq. (3.15)) that are all within a specific charge sector. As we know from Fig. 3.2 the states remain within their respective charge sector under the evolution. We see that the current makes transitions at voltages corresponding to the PF level splitting $\Delta_\varepsilon(\tilde{q})$ of the particular sector. Data that we do not include here show that the transitions are broadened with increasing temperature as we would expect.

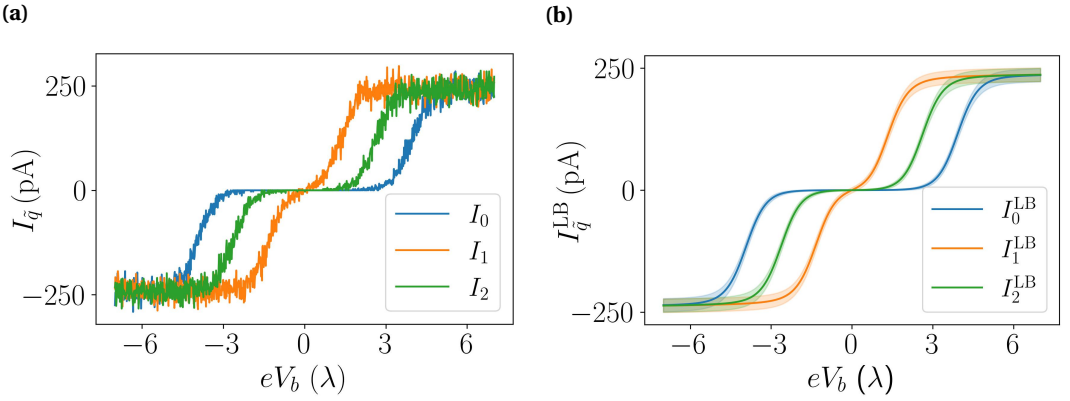

Figure 3.9: Current estimates $I_{\tilde{q}}$ for the three initial states $|\tilde{q}=0\rangle$, $|\tilde{q}=1\rangle$ and $|\tilde{q}=2\rangle$. **(a)** $I_{\tilde{q}}(t=10\,\mu\mathrm{s})$ from Eq. (3.20) calculated with the stochastic quantum jump method with $t_{\mathrm{avg}}=0.1\,\mu\mathrm{s}$. **(b)** Landauer-Büttiker prediction for the currents $I^{\mathrm{LB}}_{\tilde{q}}$ and 1 sigma noise (shaded width). We use $\Omega=20\lambda$ and set $\delta\nu^{-1}=0.1\,\mu\mathrm{s}$ such that it matches t_{avg} in **(a)**.

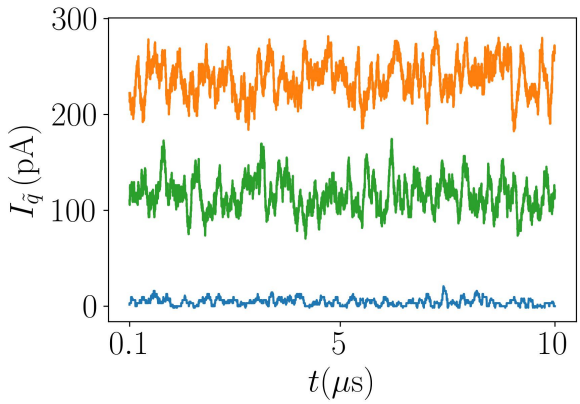

Figure 3.10: $I_{\tilde{q}}(t)$ for the three different initial states $|\tilde{q}=0\rangle$ (blue), $|\tilde{q}=1\rangle$ (orange) and $|\tilde{q}=2\rangle$ (green).

In Fig. 3.9a we show a cut $I_{\tilde{q}}(V_b)$ of the results in Fig. 3.8 at $t=10\,\mu\mathrm{s}>2000(2\pi\Gamma^{-1})$ and from this the current signals of the different charge sectors appear to be distinguishable in a range of $|eV_b|$ comparable to $\varepsilon=\lambda$. Indeed, in Fig. 3.10 we fix the voltage at $eV_b=2.6\lambda$ and plot the evolution of the current in the three cases and we see that they are well separated and distinguishable with respect to the noise.

As a benchmark for our numerical method to obtain the current we compare the results to the average current and current noise as found by the Landauer-Büttiker formalism [52, 53]. The non-perturbative results can be applied to the two-PF device since it is described as an effectively non-interacting system as discussed also in Ch. 2. From the derivation of Eq. (2.14) in that chapter

we write the (differential) zero-temperature conductance in the $\tilde{q}$ sector as

$$G_{\tilde{q}}(E) = \frac{2e^2}{h} \frac{(2\Gamma)^2 E^2}{\left(E^2 - \Delta_\varepsilon^2(\tilde{q})\right)^2 + (2\Gamma)^2 E^2}, \tag{3.21}$$

with peaks centred around $\Delta_\varepsilon(\tilde{q})$. As in Eq. (2.15) the finite temperature conductance is the integral over energy of $G_{\tilde{q}}(E)\beta n_{\mathrm{F}}(1-n_{\mathrm{F}})$. The current in a particular $\tilde{q}$ sector is then

$$I_{\tilde{q}}^{\mathrm{LB}}(V_b) = \int_0^{V_b} \mathrm{d}\, V \int_{-\Omega}^{\Omega} \mathrm{d}\,\omega\, G_{\tilde{q}}(eV) \left(\frac{-\,\mathrm{d}\, n_{\mathrm{F}}(\omega, V)}{\mathrm{d}\,\omega} \right), \tag{3.22}$$

while the zero-frequency noise is

$$\begin{aligned} S(0) = \int_{-\Omega}^{\Omega} \mathrm{d}\,\omega\, \frac{G_{\tilde{q}}(\omega)}{\delta\nu} \Big\{ & (2\omega\Gamma)^2 \left[n_{\mathrm{F}}(\omega, V_b) n_{\mathrm{F}}(-\omega, -V_b) + n_{\mathrm{F}}(\omega, 0) n_{\mathrm{F}}(-\omega, 0) \right] \\ & + (\omega^2 - \Delta_\varepsilon^2(\tilde{q}))^2 \left[n_{\mathrm{F}}(\omega, V_b) + n_{\mathrm{F}}(\omega, 0) - 2 n_{\mathrm{F}}(\omega, V_b) n_{\mathrm{F}}(\omega, 0) \right] \Big\}. \end{aligned} \tag{3.23}$$

Here we introduced an ultraviolet cutoff frequency Ω and $\delta\nu$ is a frequency over which the result is averaged. We plot the analytical predictions of the two in Fig. 3.9b using the same parameters as for the numerical results in Fig. 3.9a and indeed the two agree well. We therefore conclude that for appropriate values of bias voltage the three charge sectors can be distinguished by their current signals. We stress again that it is only possible from this method to detect the presence of three charge sectors and thus the $\mathbb{Z}_3$ degree of freedom of the $\mathbb{Z}_6$ PFs and not to associate a signal with a specific charge.

Next we will lift the restriction of $\tilde{q}$ conservation and consider the situation where the open two-PF system is also affected by fractional quasiparticle poisoning. As we learned from this section the measurement time and thereby the projection time of the PF state can vary greatly depending on the initial state, voltage bias, temperature, coupling etc. In order to measure a useful transport signal of a PF system that is affected by poisoning it is thus required that the projection time is much smaller than any poisoning time.

3.2 Quasiparticle poisoning and a three-level telegraph noise

We turn now to study the effect of fractional quasiparticles. These must originate from either the bulk of the FQH system or from the edges. Considering first the quasiparticle and quasihole excitations in the bulk of the incompressible Hall liquid, these are associated with the energy gap Δ_{FQH}. They are therefore expected to be localised in a glass state by disorder effects at low temperatures [64], consistent with interferometry experiments on gallium arsenide platforms [63, 102, 103]. Since we consider temperatures much lower than the bulk FQH gap we neglect such contributions to the poisoning. The chiral edge modes in the external edge, on the other hand, are gapless. If the PFs are close enough to the edge these two types of modes couple, allowing for fractional charges to move between the two systems. We thus consider the outer edge to be a reservoir of fractional quasiparticles with a weak incoherent coupling to the right PF (α_2) as sketched in Fig. 3.11. Explicitly, we take the coupling to be

$$H_{c,\mathrm{edge}} = \eta_{e/3} \left(\alpha_2 \psi_{e/3}^\dagger + \psi_{e/3} \alpha_2^\dagger \right), \tag{3.24}$$

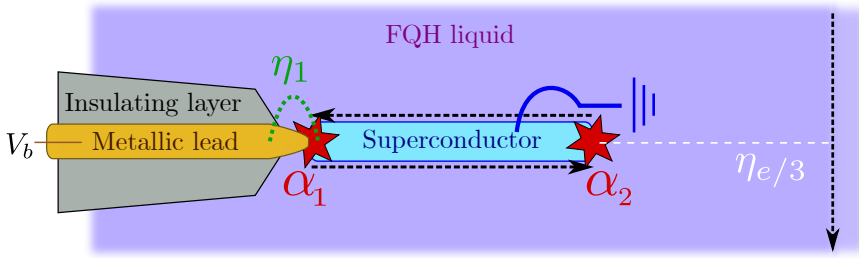

Figure 3.11: Sketch of poisoning due to coupling with external edge modes. The PF at the left end of the SC couples to the metallic lead whereas the right PF couples to the external edge modes of the FQH liquid with a strength $\eta_{e/3}$.

where $\psi_{e/3}$ is the annihilation operator of the charge $-e/3$ edge modes at some position along the edge. One could consider more general interactions where both of the PFs couple to an extended region of the edge, but this does not qualitatively affect the results. The coupling $\eta_{e/3}$ is treated as a phenomenological parameter and is expected to decay with Δ_{FQH} and with the distance between α_2 and the outer edge modes. $H_{c,\mathrm{edge}}$ is an incoherent perturbation to the case where $\tilde{q}$ is conserved and it describes quasiparticle poisoning. We would like to create jump operators for this coupling like we did for the normal lead. For this we need also to assume that the fractional quasiparticle bath is Markovian and relax on a short time scale similar to the relaxation time of the lead modes. This assumption is supported by experimental observations of heat flow in edge states of gallium arsenide-based FQH systems at filling $\nu = 1/3$ [104] with short relaxation times.

Fractional jump operators and the anyonic distribution function

We begin by considering the two-point correlation function in time for the chiral edge modes [105]:

$$\left\langle \psi^\dagger_{e/3}(t)\psi_{e/3}(0)\right\rangle = \frac{\mathrm{e}^{-it\mu_{\mathrm{edge}}}}{\left(2i\Delta_{\mathrm{FQH}}\beta\sinh\frac{\pi t}{\beta}\right)^{1/3}}. \tag{3.25}$$

Here we have assumed that the coupling strength $\eta_{e/3}$ is sufficiently weak that the edge mode properties are left unaffected. μ_{edge} is the chemical potential of the external edge modes which is affected by a current bias on the edge. The exponent 1/3 is a statistical parameter which would be an odd integer for fermions and describe bosons for even integers. We furthermore included also the FQH gap as an ultraviolet cutoff. The Fourier transform is the corresponding spectral function of the edge mode $\psi_{e/3}$:

$$d(E,\mu_{\mathrm{edge}}) = \int_{-\infty}^{+\infty} \mathrm{d}\, t\, \mathrm{e}^{iEt}\left\langle \psi^\dagger_{e/3}(t)\psi_{e/3}(0)\right\rangle, \tag{3.26}$$

whereas the spectral function for $\psi^\dagger_{e/3}$ is $d(E,-\mu_{\mathrm{edge}})$. From the results of Refs. [106, 107] we find the spectral function to be expressed in terms of the finite-temperature Tomonaga-Luttinger equilibrium anyon momentum distribution and, including the cutoff Δ_{FQH}, we obtain

$$d(E,\mu_{\mathrm{edge}}) = \frac{\beta^{2/3}\,\mathrm{e}^{-\beta(E-\mu_{\mathrm{edge}})/2}}{2\pi\boldsymbol{\Gamma}\left(\frac{1}{3}\right)\Delta_{\mathrm{FHQ}}^{1/3}}\boldsymbol{\Gamma}\left(\frac{1}{6}+\frac{i\beta(E-\mu_{\mathrm{edge}})}{2\pi}\right)\boldsymbol{\Gamma}\left(\frac{1}{6}-\frac{i\beta(E-\mu_{\mathrm{edge}})}{2\pi}\right) \equiv \beta\tilde{d}(E,\mu_{\mathrm{edge}}), \tag{3.27}$$

where $\mathbf{\Gamma}$ is the Euler gamma function (see also Ref. [108] for related results). Here we have defined $\tilde{d}$ such that it is dimensionless.

With the anyonic distribution function we can now write up jump operators corresponding to the coupling in Eq. (3.24) by the same procedure [98] as for the lead-PF coupling:

$$L_{\pm}^{e/3} = \sum_{q,q'} \sqrt{2\pi|\eta_{e/3}|^2 d(E_{q'} - E_q, \pm\mu_{\text{edge}})}\, \langle q|\alpha_2^{\mp 1}|q'\rangle\, |q\rangle\langle q'|\,, \tag{3.28}$$

where, as usual, $\alpha_2^{-1} = \alpha_2^\dagger$ (Ch. 1) and the $+(-)$ subscript refers to a fractional charge $-e/3$ from the external edge entering(leaving) the PF system. From Eq. (1.11) in Ch. 1 we have that $\alpha_2|q\rangle = \mathrm{e}^{i\frac{\pi}{3}(q-1/2)}|q-1\rangle$ and $\alpha_2^\dagger|q\rangle = \mathrm{e}^{-i\frac{\pi}{3}(q+1/2)}|q+1\rangle$, thus

$$\langle q|\alpha_2|q'\rangle = \mathrm{e}^{i\frac{\pi}{3}(q'-1/2)}\langle q|q'-1\rangle = \mathrm{e}^{i\frac{\pi}{6}}\,\mathrm{e}^{i\frac{\pi}{3}q}\,\delta_{q,q'-1}\,, \tag{3.29}$$

$$\langle q|\alpha_2^\dagger|q'\rangle = \mathrm{e}^{-i\frac{\pi}{3}(q'+1/2)}\langle q||q'+1\rangle = \mathrm{e}^{i\frac{\pi}{6}}\,\mathrm{e}^{-i\frac{\pi}{3}q}\,\delta_{q,q'+1}\,. \tag{3.30}$$

The fractional jump operators thereby become

$$L_{\pm}^{e/3} = \sum_q \sqrt{\Gamma_{e/3}\tilde{d}(E_{q\mp1} - E_q, \pm\mu_{\text{edge}})}\,\mathrm{e}^{i\frac{\pi}{6}(1\mp 2q)}\,|q\rangle\langle q\mp 1|\,, \tag{3.31}$$

where we introduced the fractional poisoning rate $\Gamma_{e/3} = 2\pi|\eta_{e/3}|^2\beta$. We see from Eq. (3.31) that the average poisoning rate depends on $\tilde{d}$ which we plot in Fig. 3.12. With decreasing temperature β^{-1} the distribution has a sharp peak around $E = \mu_{\text{edge}}$. Analogously to the Bose-Einstein distribution, $d(E,\mu_{\text{edge}}) = \beta\tilde{d}(E,\mu_{\text{edge}})$ diverges in this point as[2] $\Delta_{\text{FQH}}^{-1/3}(\mu_{\text{edge}} - E)^{-2/3}\Theta(\mu_{\text{edge}} - E)$ in the zero-temperature limit $\beta\to\infty$ because of anyonic condensation [106]. As mentioned previously, the poisoning rate must be small compared to the current measurement rate in order for us to use apply the stochastic quantum jump method. The extensive increase in the effective poisoning rate at the resonances $E_{q\mp1} - E_q = \pm\mu_{\text{edge}}$ in the low-temperature limit could therefore potentially be problematic. Let us compare the two rates; from the projection of states investigated in the previous section, we infer an approximate rate $\Gamma/(40\pi)$ around voltages corresponding to the energies $\pm\Xi_q$. The condition for weak poisoning at $\beta\to\infty$ is therefore

$$\Delta_{\text{FQH}}^{-1/3}\delta\mu^{-2/3}|\eta_{e/3}|^2 \ll \frac{\Gamma}{40\pi}\,, \qquad \text{for } T = 0\,, \tag{3.32}$$

where $\delta\mu$ is the minimum of the shifts from the edge chemical potential $E_{q\mp1} - E_q \mp \mu_{\text{edge}}$. Thus with the voltage controlling the edge potential, a divergence can be avoided by only a minor shift in μ_{edge}. For example, with the FQH energy gap $\Delta_{\text{FQH}} = 1.7$ meV, a lead rate $\Gamma = 0.1\lambda$ and an edge-PF coupling $\eta_{e/3} = 3.5\cdot10^{-3}\lambda$, the constraint becomes $\delta\mu \gg 2\cdot10^{-3}\lambda^{3/2}/\Delta_{\text{FQH}}^{1/2} \approx 1.5\cdot10^{-4}\lambda \approx 1.4\cdot10^{-6}$ meV. The peaks at finite temperature are less problematic. Setting $E = \mu_{\text{edge}}$ in Eq. (3.27), the condition for weak fractional quasiparticle poisoning becomes

$$\frac{\mathbf{\Gamma}^2\left(\frac{1}{6}\right)|\eta_{e/3}|^2\beta^{2/3}}{2\pi\mathbf{\Gamma}\left(\frac{1}{3}\right)\Delta_{\text{FQH}}^{1/3}} \approx 1.84\frac{|\eta_{e/3}|^2\beta^{2/3}}{\Delta_{\text{FQH}}^{1/3}} \ll \frac{\Gamma}{40\pi}\,, \qquad \text{at } \delta\mu = 0\,, \tag{3.33}$$

[2] Here Θ is the Heaviside step function.

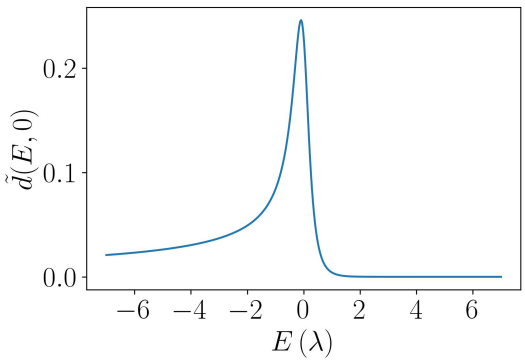

Figure 3.12: The anyonic distribution function for $-e/3$ quasiparticles, $\tilde{d}(E,\mu_{\text{edge}}=0)$, defined in Eq. (3.27). The peak is controlled by the temperature, here set to $T=\lambda/3$ (≈ 40 K).

which, for the same parameters as above, yields a condition $T \gg 0.04$ mK – more than two orders of magnitude smaller than experimentally relevant temperatures $T \geq 10$ K. We thus conclude that the effect of the divergence is negligible. In fact, even when non-universal effects (e.g. interaction among different edge modes) cause a considerable deviation from 1/3 of the scaling exponent of $\Delta_{\text{FQH}}\beta$ (Eq. (3.27)) [109–111], the above equation is always fulfilled for realistic experimental temperatures. Interaction in the edge modes has thus no important consequences for the current readout but only weakly renormalises d.

Current readout with quasiparticle poisoning

With the fractional jump operators defined and the original jump operators associated with the lead from Eq. 3.7, we can use the quantum jump method with all four jump operators to obtain numerical estimates for the current in the normal lead. The protocol is the same as described previously but now with four jump options in every δt cycle. Similarly to Fig. 3.10 we fix the voltage such that $eV_b = 2.6\lambda$ and observe the current evolution. The initial state is now the equal superposition $|\text{equal}\rangle$, and we set the edge coupling to $\eta_{e/3} = 3.5\cdot 10^{-3}\lambda$ such that the poisoning rate is $\Gamma_{e/3} \approx 0.002\Gamma$ ($\beta = 3/\lambda$). In Fig. 3.13 we show an example of a stochastic trajectory of the current as a function of time and compare this to the average values $\langle I_{\tilde{q}}\rangle$ of the current for the states $|\tilde{q}\rangle$ with well-defined $\tilde{q}$ in the absence of poisoning. As advertised, we observe the current jumping between the three current levels which are otherwise well-separated and stable. Moreover, these jumps can be from one level to any of the other two. The time scale of the plot is longer than the poisoning time $2\pi\Gamma_{e/3}^{-1} = 1.8$ µs which is again much longer than the projection time and the projection is not even visible here.

Comparing with two similar trajectories in Fig. 3.14 at voltages $eV_b = 1.6\lambda$ and $eV_b = 3.6\lambda$ we see the necessity of voltage tuning for distinguishing the three charge sectors. This furthermore provides an additional strong signature of PFs in that it is possible to shift between two-level and three-level telegraph noise by changing the voltage bias. This is not expected for a current signal in the absence of PFs, affected instead by the electric potential from a three or two-fold degenerate localised impurity. Notice that the noise of each current level does not change considerably by

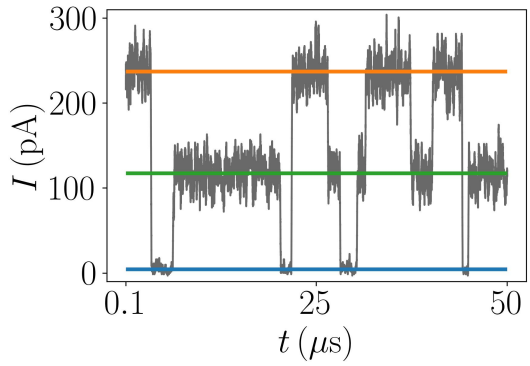

Figure 3.13: Trajectory of the current evolution at fixed $eV_b = 2.6\lambda$ with a coupling $\eta_{e/3} = 3.5 \cdot 10^{-3}\lambda$ between the external edge modes and α_2. The initial state is the equal superposition $|\text{equal}\rangle = \frac{1}{\sqrt{6}}\sum_{q=0}^{5}|q\rangle$ which is projected into one of the $\tilde{q}$ sectors on a time scale of $\mathcal{O}(10\,\text{ns})$ at this voltage and the projection is therefore not visible on the displayed time scale. The horizontal lines correspond to the mean value of the current in absence of poisoning in states with well-defined reduced charge $|\tilde{q}=0\rangle$ (blue), $|\tilde{q}=1\rangle$ (orange) and $|\tilde{q}=2\rangle$ (green), see Eq. (3.15). Every jump from one current level to another is caused by the addition or removal of one $-e/3$ charge via the external edges of the FQH system. As in the former chapter, we set $\Delta_{\text{FQH}} = 1.7$ meV [71, 112], and for simplicity we fix $\mu_{\text{edge}} = 0$.

introducing the new jump operators.

In App. C Fig. C.3 we show three more examples of the current evolution at $eV_b = 2.6\lambda$ where the three sectors can be distinguished. In all four examples of this particular parameter set it seems that the $|\tilde{q}=0\rangle$ state in total is occupied for a shorter time than the $|\tilde{q}=1\rangle$ and $|\tilde{q}=2\rangle$ states. To quantify this, we use the Lindblad master equation in Eq. (3.1) and by use of the QuTiP Python framework [113, 114] we find the steady state to be

$$\rho_0 = \begin{pmatrix} 0.116 & & & & & & \\ & 0.225 & & & & & \\ & & 0.094 & & & & \\ & & & 0.002 & & & \\ & & & & 0.216 & & \\ & & & & & 0.298 & \end{pmatrix}, \tag{3.34}$$

meaning that, in round numbers, the probability for being in the charge sectors $\tilde{q} = 0$, 1 and 2 is 0.17, 0.44 and 0.39, respectively. This confirms our by-eye estimate from Figs. 3.13 and C.3, namely that the sectors $\tilde{q} = 1$ and 2 are approximately twice as frequently occupied as $\tilde{q} = 0$.

Increasing the fractional rate we find $\Gamma_{e/3} \approx 0.02\Gamma$, which corresponds to an $\eta_{e/3}$ three times that of Fig. 3.13, as an approximate upper bound for the poisoning rate in order for the three-level telegraph current signal to remain observable, assuming we keep $t_{\text{avg}} = 0.1$ µs. In Fig. 3.15 we show a trajectory for this stronger coupling. Here it becomes difficult to distinguish the current signals in the different sectors from the noise, in particular in $\tilde{q} = 0$. In addition to a sufficient signal-to-noise ratio, clear observation of the three-level telegraph signal thus also relies on all

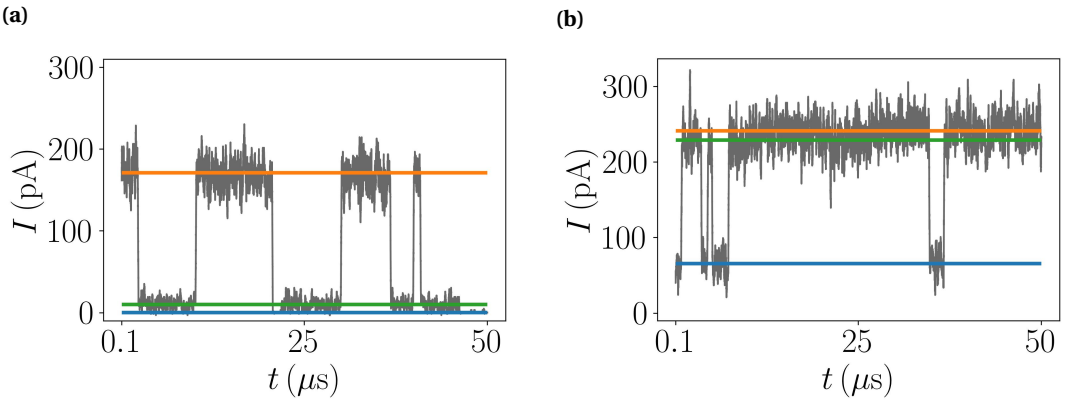

Figure 3.14: Trajectories similar to Fig. 3.13 but at voltage biases **(a)** $eV_b = 1.6\lambda$ and **(b)** $eV_b = 3.6\lambda$. If the voltage bias is not tuned appropriately we cannot distinguish the signals of three different charge states.

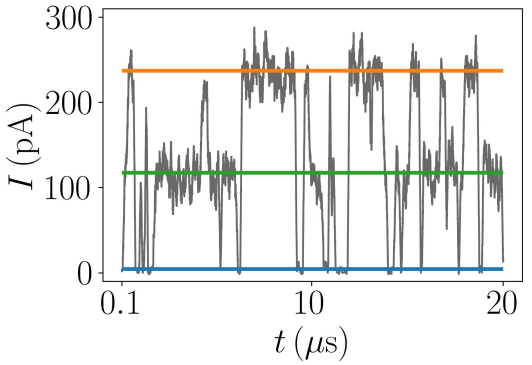

Figure 3.15: Current evolution similar to Fig. 3.13 but with an increased PF-edge coupling $\eta_{e/3} = 10.5 \cdot 10^{-3}\lambda$ – three times that of Fig. 3.13. Apart from this, all parameters are the same in the two simulations. Here the current signal of the $\tilde{q} = 0$ sector becomes difficult to distinguish from noise due to the short occupations of the corresponding states compared with t_{avg}.

three sectors being populated for long enough times compared to the poisoning time. Because of the many physical parameters the effect of these on the system dynamics is far from trivial, but we can state some general qualitative features: an adequate signal-to-noise ratio can be obtained by tuning the voltage bias correctly and choosing appropriate current integration time t_{avg}. The poisoning rate is determined by the temperature, the edge voltage of the FQH system and Δ_{FQH} and, for a low enough rate, all three charge sectors are occupied.

In total we conclude from these numerical estimates that for a weak poisoning rate $\Gamma_{e/3} \lesssim 0.02\Gamma$ the three-level telegraph noise in the current, caused by jumps between the different charge sectors $\tilde{q}$, is observable on long timescales compared to the poisoning time for an appropriately tuned

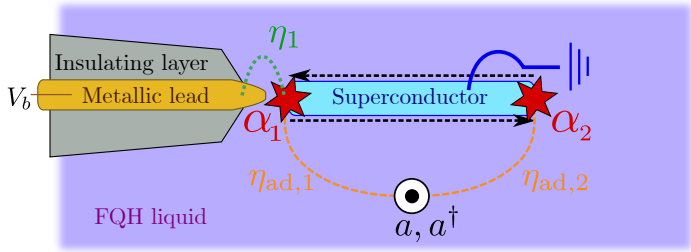

Figure 3.16: Sketch of an antidot in the bulk of the FQH system, coupling to both PFs with strengths $\eta_{\mathrm{ad},1}$ and $\eta_{\mathrm{ad},2}$. The antidot is described by the operators $a, a^\dagger$.

voltage bias. This type of signal is a distinct signature of the $\mathbb{Z}_6$ PFs that is unlikely to be mimicked by trivial states like Andreev bound states. One could imagine an impurity with three degenerate levels in the material around the 2-dimensional electron gas which could change the electric potential around the contact, depending on the state of the impurity, and thereby lead to a three-level noise in the current even in absence of PFs. However, the ability to change between two- and three-level signals with voltage tuning distinguishes the trivial impurity case from that of topological modes.

3.3 Coupling with an antidot

The linear superposition of states with different $\tilde{q}$ that we introduced in Sec. 3.1 can occur when there is another subsystem that can exchange fractional charges with the PFs in a coherent interaction. Such a source of poisoning charges could be impurities or electric potential hills in the bulk of the FQH liquid that trap fractional charges. These are referred to as antidots [115] and we will study the effect on the PF dynamics of one of these. We approximate the antidot to be small such that we can describe it as a two-level system [83] consisting of two almost-degenerate states that are separated in energy from higher excited states by strong interaction. We thus describe the antidot with the operators $(a, a^\dagger)$ fulfilling $a^2 = (a^\dagger)^2 = 0$ and introduce the small energy splitting of the two levels $\delta_{\mathrm{ad}} \ll \Gamma \ll \varepsilon$. The levels correspond to two different charge states of the antidot, Q_{ad} and $Q_{\mathrm{ad}} - e/3$, where the charge Q_{ad} commutes with the PF operators. We introduce the number $q_{\mathrm{ad}} = \{0, 1\}$ that counts the number of excess $-e/3$ charges on this antidot. We furthermore require the commutation relations $a\alpha_i = \mathrm{e}^{i\pi/3}\,\alpha_i a$ and $a^\dagger \alpha_i = \mathrm{e}^{-i\pi/3}\,\alpha_i a^\dagger$, reflecting the interacting nature of the system. We express the coupling between the PFs and the antidot as

$$H_{\text{2pf-ad}} = \sum_{i=1,2} \left(\eta_{\mathrm{ad},i} \alpha_i^\dagger a + \eta_{\mathrm{ad},i}^* a^\dagger \alpha_i \right), \tag{3.35}$$

where $\eta_{\mathrm{ad},i}$ is the coupling strength between PF α_i and the antidot. The PF Hamiltonian is the usual $H_{\mathrm{2pf}} = -2\varepsilon \cos(\pi q/3 + \phi)$ and the antidot Hamiltonian is, in the basis $\{|q_{\mathrm{ad}} = 0\rangle, |q_{\mathrm{ad}} = 1\rangle\}$,

$$H_{\mathrm{ad}} = \begin{pmatrix} 0 & 0 \\ 0 & \delta_{\mathrm{ad}} \end{pmatrix}. \tag{3.36}$$

In Fig. 3.16 we sketch the antidot-PF coupling where we ignore the external edges of the FQH liquid and consider only this coherent quasiparticle poisoning source.

The combined antidot + two-PF system has a common unitary evolution and to describe this we use the basis

$$|q, q_{\text{ad}}\rangle = \left(a^\dagger\right)^{q_{\text{ad}}} \left(\alpha_1^\dagger\right)^q |0,0\rangle = \{|0,0\rangle, |0,1\rangle, |1,0\rangle, \ldots, |5,1\rangle\}. \tag{3.37}$$

The diagonal elements of the total system Hamiltonian $H_{\text{tot}} = H_{2\text{pf}} + H_{\text{ad}} + H_{2\text{pf+ad}}$ are

$$\langle q, q_{\text{ad}}|H_{\text{tot}}|q, q_{\text{ad}}\rangle = -2\varepsilon \cos(\pi q/3 + \phi) + \delta_{\text{ad}}\delta_{q_{\text{ad}},1}, \tag{3.38}$$

and the off-diagonal elements are

$$\begin{aligned}
\langle q', q'_{\text{ad}}|H_{\text{tot}}|q, q_{\text{ad}}\rangle &= \langle q', q'_{\text{ad}}| \sum_{i=1,2} \left(\eta_{\text{ad},i}\alpha_i^\dagger a + \eta^*_{\text{ad},i} a^\dagger \alpha_i\right)|q, q_{\text{ad}}\rangle \\
&= \langle 0,0|\alpha_1^{q'} a^{q'_{\text{ad}}} \left(\eta_{\text{ad},1}\alpha_1^\dagger a + \eta^*_{\text{ad},1} a^\dagger \alpha_1\right)\left(a^\dagger\right)^{q_{\text{ad}}}\left(\alpha_1^\dagger\right)^q |0,0\rangle \\
&\quad + \langle 0,0|\alpha_1^{q'} a^{q'_{\text{ad}}} \left(\eta_{\text{ad},2}\alpha_2^\dagger a + \eta^*_{\text{ad},2} a^\dagger \alpha_2\right)\left(a^\dagger\right)^{q_{\text{ad}}}\left(\alpha_1^\dagger\right)^q |0,0\rangle \\
&= \left(\eta_{\text{ad},1} + \eta_{\text{ad},2}\, \mathrm{e}^{-i\frac{\pi}{6}}\, \mathrm{e}^{-i\frac{\pi}{3}q}\right)\delta_{q',q+1}\delta_{q'_{\text{ad}},0}\delta_{q_{\text{ad}},1} + \left(\eta^*_{\text{ad},1} + \eta^*_{\text{ad},2}\, \mathrm{e}^{i\frac{\pi}{6}}\, \mathrm{e}^{i\frac{\pi}{3}(q-1)}\right)\delta_{q',q-1}\delta_{q'_{\text{ad}},1}\delta_{q_{\text{ad}},0}.
\end{aligned} \tag{3.39}$$

Where we use that $[aa^\dagger, \alpha_i^{(\dagger)}] = [a^\dagger a, \alpha_i^{(\dagger)}] = 0$ and refer to Eqs. (3.29) and (3.30) for the phases.

The left PF (α_1) is still coupled to the normal metallic lead with a simple coupling $H_c = i\eta_1\alpha_1^3(l + l^\dagger)$ and the SC is grounded. The jump operators for electrons tunnelling in or out of the PF system have to account for the extra degree of freedom provided by the antidot. The extended operators are

$$L_\pm = \sum_{\substack{q,q' \\ q_{\text{ad}},q'_{\text{ad}}}} \sqrt{2\pi\eta_1^2 J_\pm(E_{q',q'_{\text{ad}}} - E_{q,q_{\text{ad}}})}\, \langle q, q_{\text{ad}}|i\alpha_1^3|q', q'_{\text{ad}}\rangle\, |q, q_{\text{ad}}\rangle\langle q', q'_{\text{ad}}|. \tag{3.40}$$

The inner products are $\langle q, q_{\text{ad}}|i\alpha_1^3|q', q'_{\text{ad}}\rangle \propto \delta_{q'_{\text{ad}},q_{\text{ad}}}$, meaning that e.g. $\langle 0,0|\alpha_1^3|3,1\rangle = 0$ and thus the current measurement does not change the state of the antidot but still only senses the charge of the two PFs. In general,

$$\begin{aligned}
\langle q, q_{\text{ad}}|\alpha_1^3|q', q'_{\text{ad}}\rangle &= \langle 0,0|a^{q_{\text{ad}}}\alpha_1^q\alpha_1^3(\alpha_1^\dagger)^{q'}(a^\dagger)^{q'_{\text{ad}}}|0,0\rangle = \langle 0,0|\alpha_1^q\alpha_1^3 a^{q_{\text{ad}}}(\alpha_1^\dagger)^{q'}(a^\dagger)^{q'_{\text{ad}}}|0,0\rangle\, \mathrm{e}^{i\frac{\pi}{3}q_{\text{ad}}(q+3)} \\
&= \langle 0,0|\alpha_1^{q+3}(\alpha_1^\dagger)^{q'} a^{q_{\text{ad}}}(a^\dagger)^{q'_{\text{ad}}}|0,0\rangle\, \mathrm{e}^{i\frac{\pi}{3}q_{\text{ad}}(q+3-q')} = \delta_{q+3,q'}\delta_{q_{\text{ad}},q'_{\text{ad}}},
\end{aligned} \tag{3.41}$$

and so we never collect a phase from this product. The jump operators are thereby

$$L_\pm = i\sum_{q,q_{\text{ad}}} \sqrt{\Gamma J_\pm(E_{q+3,q_{\text{ad}}} - E_{q,q_{\text{ad}}}, V_b)}\, |q, q_{\text{ad}}\rangle\langle q+3, q_{\text{ad}}|. \tag{3.42}$$

The coupling with the metallic lead still allows only normal electrons to enter and leave the total system and thus the total charge mod $1e$ is still conserved. The 12 states in Eq. (3.37) are therefore divided into three sets with well-defined total charge $q + q_{\text{ad}} \mod 1e$, each with four states, and the three sets do not couple. Within each set are two different values of $\tilde{q}$ because one – and only one – fractional charge can leak into the antidot.

With the new 12×12 dimensional Hamiltonian and jump operators we obtain current signals like those in Fig. 3.17. Here we compare the current in the three initial states

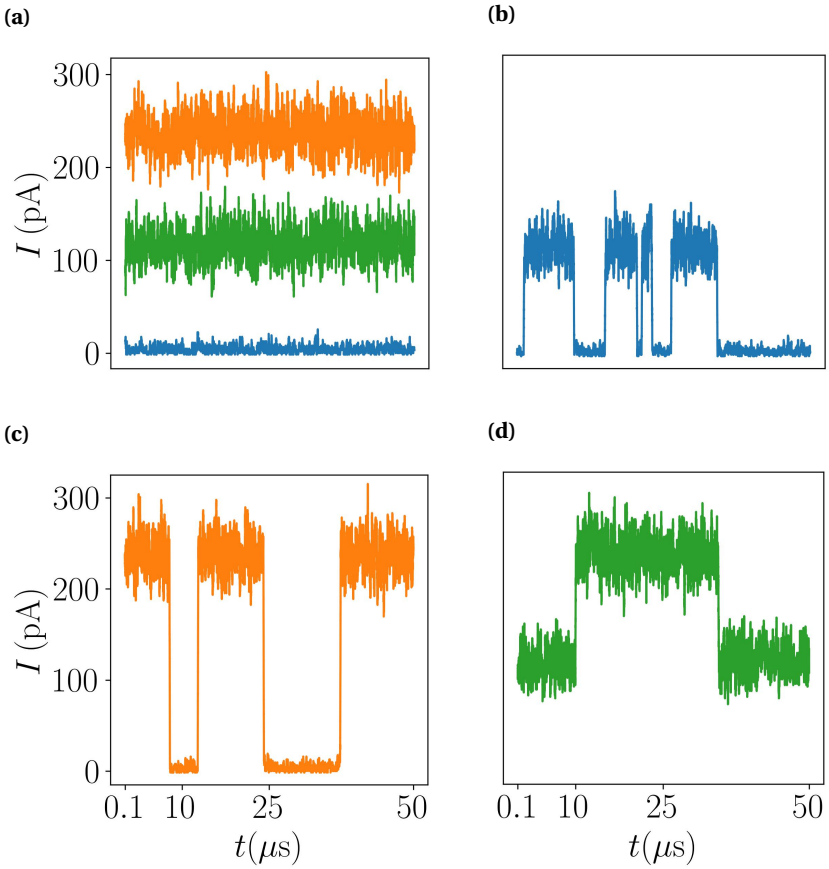

Figure 3.17: Numerical estimates of the current $I(t)$ at $eV_b = 2.6\lambda$ when including an antidot with energy splitting $\delta_{\text{ad}} = 5 \cdot 10^{-4}\lambda$ in the bulk of the FQH liquid. In **(b)**-**(d)** the coupling strength is $\eta_{\text{ad},i} = 5 \cdot 10^{-3}\lambda$ and all initial states are with no additional $-e/3$ charge on the antidot: **(b)** $|\tilde{q} = 0, q_{\text{ad}} = 0\rangle = \frac{1}{\sqrt{2}}(|0,0\rangle + |3,0\rangle)$ (which couples to the states $|5,1\rangle$ and $|2,1\rangle$), **(c)** $|\tilde{q} = 1, q_{\text{ad}} = 0\rangle$ and **(d)** $|\tilde{q} = 2, q_{\text{ad}} = 0\rangle$. Note that the displayed timescale is much longer than $2\pi|\eta_{\text{ad},i}|^{-1} \approx 80$ ns. In **(a)** we compare with the current in the same initial states when $\eta_{\text{ad},i} = 0$. The three colours correspond to the initial states in **(b)**-**(d)**.

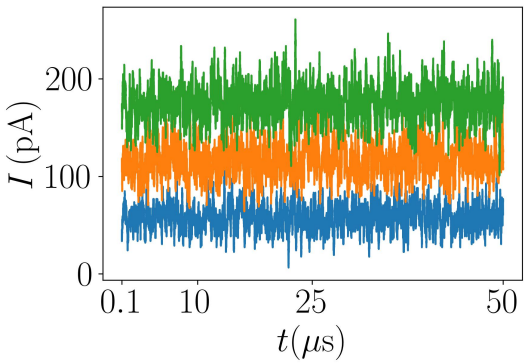

Figure 3.18: Current evolution of the three initial states $|\tilde{q}=0,q_{\rm ad}=0\rangle$ (blue), $|\tilde{q}=1,q_{\rm ad}=0\rangle$ (orange) and $|\tilde{q}=2,q_{\rm ad}=0\rangle$ (green) for a strong coupling to the antidot $\eta_{{\rm ad},1}=\eta_{{\rm ad},2}=10\Gamma$ using otherwise the same parameters as for Fig. 3.17

$$|\tilde{q}=0,q_{\rm ad}=0\rangle=\frac{|0,0\rangle+|3,0\rangle}{\sqrt{2}},\quad |\tilde{q}=1,q_{\rm ad}=0\rangle=\frac{|1,0\rangle+|4,0\rangle}{\sqrt{2}},\quad |\tilde{q}=2,q_{\rm ad}=0\rangle=\frac{|2,0\rangle+|4,0\rangle}{\sqrt{2}}, \tag{3.43}$$

for $\eta_{{\rm ad},i}=0$ (Fig. 3.17a) to the case where $\eta_{{\rm ad},1}=\eta_{{\rm ad},2}=5{\cdot}10^{-3}\lambda$ (Figs. 3.17b-3.17d). All three sectors display telegraph noise but only between two levels because of the limited capacity of the antidot. Take for instance Fig. 3.17c where the initial charge of the antidot is $Q_{\rm ad}$ and the PF system is in a superposition of $|q=1\rangle$ and $|q=4\rangle$. The current is around 250 pA for the first few microseconds as expected for this charge sector $\tilde{q}=1$ of the PF. Due to the coupling with the antidot, however, the state evolves into a superposition of the states $|q=0,q_{\rm ad}=1\rangle$ and $|q=3,q_{\rm ad}=1\rangle$ where one fractional charge is moved from the PFs to the antidot. As a result, the current drops to a few pA consistent with sector $\tilde{q}=0$. In Fig. C.4 in App. C we show that the behaviour is analogous for the initial states $|\tilde{q},q_{\rm ad}=1\rangle$. The two-level telegraph noise that is observed in all the cases is caused by the competition between the weak coherent coupling $\eta_{{\rm ad},i}$ to the antidot and the stronger incoherent coupling rate Γ to the lead.

In Figs. 3.17b-3.17d and C.4 $\eta_{{\rm ad},i}=0.05\Gamma$, but when we increase the coupling, the jumps between current levels become increasingly frequent until $\eta_{{\rm ad},i}\gtrsim\Gamma$ where the current signal return stable as in Fig. 3.17a, only at different values. This we show in Fig. 3.18 and in App. C Fig. C.5 we show the transition from telegraph noise to stable current. The three new emerging levels correspond to the dominating transition within each of the total charge sectors $(\tilde{q}+q_{\rm ad})\mod 3$.

We conclude from this section, that current measurements can be used to distinguish the different charge sectors as long as the coherent coupling to poisoning sources such as an antidot is weaker than the measurement rate (Γ). Despite the fact that $2\pi|\eta_{{\rm ad},i}|^{-1}\lesssim 40\pi\Gamma^{-1}\lesssim t_{\rm avg}$ for the parameters used in this section[3] we find by 200 repetitions of the simulations presented in Figs. 3.17b-3.17d that a jump between current levels within the first $2\pi|\eta_{{\rm ad},i}|^2\approx 80$ ns takes place in less than 2% of the trajectories.

Next we will expand the device in Fig. 3.1 to include in total four PFs and for this we will assume that the current readout is sufficiently fast that the poisoning effects from edge modes or antidots discussed so far can be safely neglected.

[3] Recall that $40\pi\Gamma^{-1}$ is the approximate projection time at this voltage based on Fig. 3.4

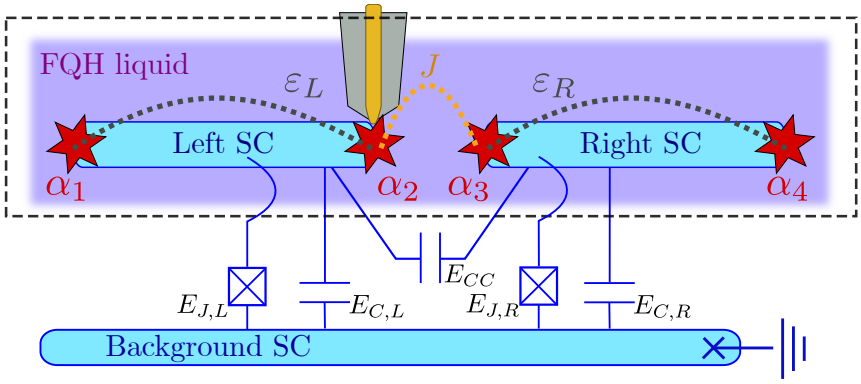

Figure 3.19: Sketch of a device hosting four PFs, $\{\alpha_1,\ldots,\alpha_4\}$, one at each end of two thin SCs (blue) inserted in two trenches in the bulk of the FQH liquid (purple). In the dashed box we highlight the relevant nearest-neighbour couplings between the PFs: ε_L, ε_R and J. A metallic lead (gold) is coupled to α_2. Below the box we sketch elements that could be used for tuning these couplings. The background SC is grounded and couples to both of the small SC islands via a transmon construction with Josephson energies $E_{J,i}$ and charging energies $E_{C,i}$ where $i = L,R$ labels left and right SC. Furthermore, a coupling between all four PFs is generated by a cross capacitance E_{CC}.

3.4 Four-parafermion devices

The analysis so far has been on the simple two-PF device which allows us to measure some signatures of these modes. However, investigation of most of their inherent properties, in particular their non-abelian character, require manipulation of more than two PFs. Therefore we 'double' the device considered so far to two superconducting islands hosting in total four $\mathbb{Z}_6$ PFs; $\alpha_1, \alpha_2, \alpha_3$ and α_4. We neglect any coupling to additional sources of fractional charges.

In Fig. 3.19 we schematically show our proposed setup which is closely related to those of Refs. [83, 116, 117]. We assume that some of the effective couplings can be varied in time, for example through transmon-like constructions, but a more detailed discussion of this will have to wait a few pages. For now we just consider an effective model where α_1 and α_2 are coupled with a strength ε_L and, as usual, the corresponding Hamiltonian is $-2\varepsilon_L \cos(\pi q/3 + \phi_L)$ where the effect of ϕ_L is analogous to that of ϕ defined back in Ch. 1. Similarly, the PFs α_3 and α_4 are coupled with strength ε_R and have the associated phase ϕ_R. The two couplings are of electrostatic origin and we assume that ε_L and ε_R can be tuned. Between the two SCs, a fractional Josephson junction is formed [12, 87, 118] and thus the PFs α_2 and α_3 are coupled with some strength J that we assume to be constant. Lastly, we include a global charging energy interaction ε_{LR} which depends on the total system charge. The total effective low-energy Hamiltonian for the four PFs reads

$$\begin{aligned} H_{4\mathrm{pf}} = \Big\{ & -\varepsilon_L \mathrm{e}^{-i\left(\frac{\pi}{6}+\phi_L\right)} \alpha_2^\dagger \alpha_1 - \varepsilon_R \mathrm{e}^{-i\left(\frac{\pi}{6}+\phi_R\right)} \alpha_4^\dagger \alpha_3 - J \mathrm{e}^{-i\left(\frac{\pi}{6}+\theta\right)} \alpha_3^\dagger \alpha_2 \\ & - \varepsilon_{LR} \mathrm{e}^{-i\left(\frac{\pi}{3}+\phi_L+\phi_R\right)} \alpha_2^\dagger \alpha_1 \alpha_4^\dagger \alpha_3 \Big\} + \mathrm{H.c.} \end{aligned} \tag{3.44}$$

Here the phase[4] θ of the fractional Josephson term is controlled by the magnetic field perpendicular to the Hall bar, and with small variations of the field this phase is tunable. The effect of θ is analogous to that of ϕ in that it controls the splitting of the energy levels associated with the J-term. Fusion of two PFs on the same SC is characterised by the shared fractional charge like before. We label the charge-counting operators corresponding to the left and right SC by $\hat{q}_L$ and $\hat{q}_R$, respectively. The total charge $eQ/3 = e(q_L+q_R)/3$ is conserved up to one Cooper pair in the isolated system. Q thus divides the 36-dimensional Hilbert space of $H_{4\mathrm{pf}}$ into six sectors characterised by $-eQ/3 = \{0, -e/3, \ldots, -5e/3\}$, each with six states, and we can label the eigenstates of $H_{4\mathrm{pf}}$ by this total charge and the energy level $E_n^{(Q)}$ within the sector; $\{|Q,n\rangle\}$, $n = \{1,\ldots,6\}$.

Recall the clock model which was introduced in Ch. 1; our 'chain' of four PFs can be transformed to a two-site quantum clock chain by the non-local Fradkin-Kadanoff mapping [8, 12, 27] as described in Eq. (1.18). Labelling the clock operators by τ_i and σ_i, $i = L, R$, this transformation reads

$$\alpha_1 = \sigma_L\,, \qquad \alpha_2 = \mathrm{e}^{i\frac{\pi}{6}}\,\tau_L\sigma_L\,, \qquad \alpha_3 = \sigma_R\tau_L\,, \qquad \alpha_4 = \mathrm{e}^{i\frac{\pi}{6}}\,\tau_R\sigma_R\tau_L\,. \tag{3.45}$$

The parity operators of the left and right pair of PFs can be expressed in terms of the clock operators as

$$P_L = \mathrm{e}^{-i\frac{\pi}{6}}\,\alpha_2^\dagger\alpha_1 = \mathrm{e}^{-i\frac{2\pi}{6}}\,\sigma_L^\dagger\tau_L^\dagger\sigma_L = \tau_L^\dagger = \mathrm{e}^{-i\frac{\pi}{3}\hat{q}_L}\,, \tag{3.46}$$

$$P_R = \mathrm{e}^{-i\frac{\pi}{6}}\,\alpha_4^\dagger\alpha_3 = \mathrm{e}^{-i\frac{2\pi}{6}}\,\tau_L^\dagger\sigma_R^\dagger\tau_R^\dagger\sigma_R\tau_L = \tau_L^\dagger\tau_R^\dagger\tau_L = \tau_R^\dagger = \mathrm{e}^{-i\frac{\pi}{3}\hat{q}_R}\,. \tag{3.47}$$

Here we exploited the properties listed in Eqs. (1.14) and (1.15). Similarly, we can construct a parity operator corresponding to the fusion of α_2 and α_3:

$$P_J = \mathrm{e}^{-i\frac{\pi}{6}}\,\alpha_3^\dagger\alpha_2 = \tau_L^\dagger\sigma_R^\dagger\tau_L\sigma_L = \sigma_R^\dagger\sigma_L = \mathrm{e}^{-i\frac{\pi}{3}\hat{j}}\,, \tag{3.48}$$

where we introduced j as the dual of the charge numbers. With the transformation in Eq. (3.45) we can write the four-PF Hamiltonian in terms of clock operators:

$$H_{4\mathrm{pf}} = \Big\{-\varepsilon_L\,\mathrm{e}^{-i\phi_L}\,\tau_L^\dagger - \varepsilon_R\,\mathrm{e}^{-i\phi_R}\,\tau_R^\dagger - J\,\mathrm{e}^{-i\theta}\,\sigma_R^\dagger\sigma_L - \varepsilon_{LR}\,\mathrm{e}^{-i(\phi_L+\phi_R)}\,\tau_L^\dagger\tau_R^\dagger\Big\} + \mathrm{H.c.} \tag{3.49}$$

We see form this that the ε_{LR} term shifts the resonance energies (corresponding to $\Delta_\varepsilon(\tilde{q})$ in the two-PF case). In the basis $\{|Q,q_L\rangle\}$, the Josephson term yields

$$\sigma_R^\dagger\sigma_L\,|Q,q_L\rangle = |Q,q_L-1\rangle\,, \qquad \sigma_L^\dagger\sigma_R\,|Q,q_L\rangle = |Q,q_L+1\rangle\,. \tag{3.50}$$

The elements of $H_{4\mathrm{pf}}$ in this basis are therefore

$$\begin{aligned}\langle Q', q_L'|H_{4\mathrm{pf}}|Q,q_L\rangle = &\big\{-2\varepsilon_L\cos(\pi q_L/3+\phi_L) - 2\varepsilon_R\cos(\pi(Q-q_L)/3+\phi_R)\\ &- 2\varepsilon_{LR}\cos(\pi Q/3+\phi_L+\phi_R)\big\}\delta_{Q',Q}\delta_{q_L',q_L}\\ &- J(\mathrm{e}^{i\theta}\,\delta_{q_L',q_L+1} + \mathrm{e}^{-i\theta}\,\delta_{q_L',q_L-1})\delta_{Q',Q}\,.\end{aligned} \tag{3.51}$$

Here we used that the total charge can be expressed as $\tau_L^\dagger\tau_R^\dagger = \mathrm{e}^{-i\frac{\pi}{3}Q}$ such that $\tau_R^\dagger = \mathrm{e}^{-i\frac{\pi}{3}Q}\tau_L$.

As indicated in Fig. 3.19 an external metallic lead is in contact with the PF α_2. Similarly to the previous sections we use the simple coupling Hamiltonian $H_c = i\eta\alpha_2(l+l^\dagger)$. Electrons tunnelling

[4] Not to be confused with the bosonic field variable used in the previous chapters.

back and forth change the *total* charge of the four-PF system by $\pm 1e$ causing transitions between Q and $Q \pm 3$ (still modulo 6). Using the eigenstates $\{|Q,n\rangle\}$ of $H_{4\mathrm{pf}}$, the amplitudes of such transitions are proportional to $\langle Q \pm 3, m|\alpha_2^3|Q,n\rangle$. Because of this coupling the four-PF Hamiltonian is now divided into three rater than six sectors, characterised by a reduced total charge number that is only defined modulo one electron charge. Each sector contains 12 states and between these, in principle 36 transitions are possible. Following the same procedure as in the previous sections we write up the electron jump operators in this basis:

$$\hat{L}^e_{\pm} = \sum_{Q,m,n} \sqrt{\Gamma J_{\pm}(E_n - E_m)}\, \langle Q+3, m|\tau_L^3\sigma_L^3|Q,n\rangle\, |Q+3,m\rangle\langle Q,n|\,. \tag{3.52}$$

Here $\Gamma = 2\pi\nu_l\eta^2$ and $J_{\pm}(\omega, V_b) = n_{\mathrm{F}}(-\omega, \pm V_b)$ as before, and we rewrote $i\alpha_2^3 = i\,\mathrm{e}^{i\frac{3\pi}{6}}(\tau_L\sigma_L)^3 = \mathrm{e}^{i\pi}\,\mathrm{e}^{i\frac{3\pi}{3}}\,\tau_L^3\sigma_L^3 = \tau_L^3\sigma_L^3$. With these jump operators we can numerically calculate current trajectories; this time in a device with four PFs. But before analysing these, let us reflect on different limits of the many couplings introduced above.

Consider first the limit $J \ll \varepsilon_L, \varepsilon_R$: here the two superconducting islands are only weakly coupled to each other and approximately behave as two copies of the single SC considered in Sec. 3.1 with q_L and q_R almost conserved. The basis $\{|q_L, q_R\rangle\}$ thus approximates the eigenstates of $H_{4\mathrm{pf}}$ up to corrections of $\mathcal{O}(J/\min_{q_L}(E_{Q,q_L} - E_{Q,q_L+1}))$ where $E_{Q,q_L}|Q,q_L\rangle = H_{4\mathrm{pf}}(J=0)|Q,q_L\rangle$. If the coupling rate to the lead is $\Gamma \gg J$ the current through this will be similar to that shown in Fig. 3.9a with q_R almost 'frozen'. The measurement dynamics is in this case resemblant to the one discussed in Sec. 3.3 where the lead-PF coupling competes with the coupling to the antidot. Here the fractional Josephson energy J replaces the role of η_{ad} and may cause jumps between current levels that correspond to different values of $\tilde{q}_L = (q_L \mod 3)$. As a result, the current signal would be affected by telegraph noise between two or three levels, depending on the level spacing of the right SC. If instead $\Gamma \ll J$, the tunnelling spectroscopy reflects the complex energy spectrum of $H_{4\mathrm{pf}}$ and does not display telegraph noise.

In the limit $\varepsilon_L, \varepsilon_R \ll J$ the approximate eigenstates of the Hamiltonian are instead the eigenstates of the P_J operator; $\{P_J|Q,j\rangle = \mathrm{e}^{i\frac{\pi}{3}j}|Q,j\rangle\}$. This is again only true up to corrections of $\mathcal{O}(\max(\varepsilon_L,\varepsilon_R)/\min_j(E_{Q,j} - E_{Q,j+1}))$ with $E_{Q,j}|Q,j\rangle = H_{4\mathrm{pf}}(\varepsilon_L = \varepsilon_R = 0)|Q,j\rangle$. Now the charges q_L and q_R are not separately conserved. The eigenenergies of $H_{4\mathrm{pf}}$ are grouped into six sets, each of six almost-degenerate levels with splitting of $\mathcal{O}(\max(\varepsilon_L,\varepsilon_R))$. With a lead-PF coupling such that $\varepsilon_L, \varepsilon_R \ll \Gamma \ll J$ the current is expected to show a three-level telegraph noise just as in Sec. 3.2 where jumps between current levels correspond to changes in $\tilde{j} \to \tilde{j} \pm 1$ where, analogously to $\tilde{q}_i$, $\tilde{j} = (j \mod 3)$ is the $\mathbb{Z}_3$ part of j. When $\varepsilon_L = \varepsilon_R = 0$ the outer PFs α_1 and α_4 are isolated and the Hamiltonian simplifies to that of a two-PF system.

From these considerations we will next present an experimental protocol to test the associativity of the fusion rules for PFs. With the quantum jump operators defined in Eq. (3.52) we will calculate a predicted behaviour of the current that reflects this associativity.

Associativity relations of the anyonic parafermion fusion

A main character of the non-abelian parafermionic modes is the associativity relations of their algebraic fusion rules [119, 120]. Here we describe a protocol to experimentally verify the non-abelian fusion rules of the four PFs in Fig. 3.19. The approach to this is showing that fusion of any pair of the $\mathbb{Z}_6$ PFs is characterised by a degree of freedom that can take six different values and that

when coupling subsequently one of the PFs (say α_2) to two different partners (e.g. α_1 and α_3), the result of the fusions does not only depend on the former (here α_2) but follow specific algebraic rules. In our four-PF setup, α_1 and α_2 are fused due to the interaction ε_L and the outcome is characterised by P_L whereas the J interaction fuses α_2 with α_3 and this result is instead represented by P_J. The associativity relation of these two processes is described by the *F-matrix*; a unitary transformation between the eigenstates of P_L $\{|Q,j\rangle\}$ and the eigenstates of P_J $\{|Q,q_L\rangle\}$.

As we showed back in Ch. 2 the sixfold degree of freedom of a pair of $\mathbb{Z}_6$ PFs can be decomposed into a $\mathbb{Z}_2$ fermionic parity and a $\mathbb{Z}_3$ part which, for PFs on the same island, is the reduced charge number $\tilde{q}_i$. This fusion property is general and holds also for PFs on different islands such as α_2 and α_3. We will now show that also the associativity F-matrix can be split into the tensor product of two associativity matrices related to the two degrees of freedom. The result is new but not surprising since it was already shown in Ref. [11] that the braiding operations of $\mathbb{Z}_{2m}$ PFs can be expressed as a tensor product of a 2×2 Majorana fermion (MF) braiding matrix and a unitary $m\times m$ matrix that affects only the fractional degree of freedom. Recall the rewriting from Ch. 2; $\mathrm{e}^{i\frac{\pi}{3}q_L} = i\alpha_2^3\alpha_1^3\mathrm{e}^{i\frac{4\pi}{3}\tilde{q}_L}$. From this factorisation of the parity we introduce the notation $|q_L\rangle = |p_L,\tilde{q}_L\rangle$ where $p_L = (1-i\alpha_2^3\alpha_1^3)/2$. Likewise, for the fusion of α_2 and α_3 we write $|j\rangle = |p_J,\tilde{j}\rangle = |(1-i\alpha_3^3\alpha_2^3)/2,\tilde{j}\rangle$.

From Ref. [121] we have the 6×6 associativity matrix $F^{(6)}$ for the four PFs:

$$|Q,q_L\rangle = \sum_j F^{(6)}_{q_L,j}|Q,j\rangle = \frac{1}{\sqrt{6}}\sum_{j=0}^{5}\mathrm{e}^{-i\frac{\pi}{3}q_L j}|Q,j\rangle\,. \tag{3.53}$$

The F-matrix acts as a sort of discrete Fourier transformation between the q_L and the j degrees of freedom. We see from the above equation that a state with a well-defined q_L is an equal superposition of the states $|j\rangle$, analogous to the state $|\mathrm{equal}\rangle$ studied in Sec. 3.1. To decompose $F^{(6)}$ into two associativity matrices we first reorder the states in the $|q_L\rangle$ and $|j\rangle$ bases, originally ordered as $\{|0\rangle,|1\rangle,|2\rangle,|3\rangle,|4\rangle,|5\rangle\}$, with the permutation

$$U = \begin{pmatrix} 1 & & & & & \\ & 0 & & & 1 & \\ & & 1 & & & \\ & & & 1 & & \\ & 1 & & & 0 & \\ & & & & & 1 \end{pmatrix}. \tag{3.54}$$

This swaps the states with $q_L = 1$ and $q_L = 4$ such that the first three states in the new ordering all have fermionic parity zero and the last three $p_L = 1$. Likewise, the j basis becomes $\{|p_J,\tilde{j}\rangle\} = \{|0,0\rangle,|0,1\rangle|0,2\rangle,|1,0\rangle,|1,1\rangle,|1,2\rangle\}$. We can then write $F^{(6)} = U\left(F^{(2)}\otimes F^{(3)\dagger}\right)U^\dagger$ where

$$F^{(2)} = \frac{1}{\sqrt{2}}\begin{pmatrix}1 & 1\\ 1 & -1\end{pmatrix}, \qquad F^{(3)\dagger}_{\tilde{q}_L,\tilde{j}} = \frac{\mathrm{e}^{i\frac{2\pi}{3}\tilde{q}_L\tilde{j}}}{\sqrt{3}}\,. \tag{3.55}$$

$F^{(2)}$ is the Majorana F-matrix [120] and relates the fermionic parity degrees of freedom p_L and p_J. $F^{(3)\dagger}$ is the F-matrix for $\mathbb{Z}_3$ PFs and relates the fractional degrees of freedom $\tilde{q}_L$ and j. In absence of poisoning these are robust to the interaction with the normal lead whereas the $\mathbb{Z}_2$ part is scrambled by the constant tunnelling of electrons from and to the lead. We would therefore like to trace out the fermionic parities p_L and p_J to obtain an associativity matrix F_{red} for only the fractional degrees of freedom such that $\tilde{\rho}_L = F_{\mathrm{red}}\tilde{\rho}_J F^\dagger_{\mathrm{red}}$. Here $\tilde{\rho}_L = \mathrm{Tr}_{p_L}[\rho_L]$ and $\tilde{\rho}_J = \mathrm{Tr}_{p_J}[\rho_J]$ are

3×3 reduced density matrices obtained by tracing the full density matrices of the four-PF system in the $|q_L\rangle$ and $|j\rangle$ bases, respectively, over the related fermionic parities. From the definition in Eq. (3.53) this would correspond to

$$\tilde{\rho}_L = \sum_{p_L=0,1} \langle p_L|\rho_L|p_L\rangle = \sum_{p_L=0,1} \langle p_L|F^{(6)}\rho_J F^{(6)\dagger}|p_L\rangle = F_{\text{red}}\left(\sum_{p_J=0,1}\langle p_J|\rho_J|p_J\rangle\right)F_{\text{red}}^\dagger = F_{\text{red}}\tilde{\rho}_J F_{\text{red}}^\dagger . \tag{3.56}$$

Let us find this F_{red} by using the decomposition of $F^{(6)}$:

$$\tilde{\rho}_L = \text{Tr}_{p_L}\left[\rho_L\right] = \text{Tr}_{p_L}\left[U\left(F^{(2)}\otimes F^{(3)\dagger}\right)U^\dagger\rho_J U\left(F^{(2)\dagger}\otimes F^{(3)}\right)U^\dagger\right], \tag{3.57}$$

where we consider ρ_L and ρ_J to be expressed in the $|q_L\rangle$ and $|j\rangle$ bases, respectively. In the trace over p_L we can make a cyclic permutation of U and use that $U^\dagger = U^{-1}$. Furthermore, the reordering of p_L by U (within the $\tilde{q}_L = 1$ sector) does not affect $F^{(3)}$ which can therefore be moved outside the partial trace:

$$\begin{aligned}\tilde{\rho}_L =& F^{(3)\dagger}\left[\sum_{p_L}\langle p_L|\left(F^{(2)}\otimes\mathbb{1}\right)U^\dagger\rho_J U\left(F^{(2)\dagger}\otimes\mathbb{1}\right)|p_L\rangle\right]F^{(3)}\\ =& F^{(3)\dagger}\left[\sum_{p_J}\langle p_J|U^\dagger\rho_J U|p_J\rangle\right]F^{(3)} = F^{(3)\dagger}\tilde{\rho}_J F^{(3)} .\end{aligned} \tag{3.58}$$

In the second line we use that $F^{(2)}$ transforms from the $|p_J\rangle$ states to $|p_L\rangle$. The reduced density matrix $\tilde{\rho}_J$ is thus expressed in the basis $\{|j\rangle\} = \{|0\rangle, |1\rangle, |2\rangle\}$ and the two reduced density matrices are indeed related by a 3×3 reduced associativity matrix $F_{\text{red}} = F^{(3)\dagger}$.

As we discussed on the previous pages the fractional degrees of freedom $\tilde{q}_L$ and $\tilde{j}$ are revealed by the lead current in the two different limits $J \ll \Gamma \ll \varepsilon_L, \varepsilon_R$ and $\varepsilon_L, \varepsilon_R \ll \Gamma \ll J$, respectively. In order to experimentally investigate the associativity matrix $F^{(3)\dagger}$ one could make a series of consecutive fusions of α_1 with α_2 and of α_2 with α_3. The reduced associativity matrix tells us about the probability for a specific outcome $\tilde{j}'$ given that the previous fusion returned $\tilde{q}_L'$, namely $|F^{(3)}_{\tilde{j}',\tilde{q}_L'}|^2$. Looking at Eq. (3.55) we see that all these are 1/3, meaning that for any outcome $\tilde{q}_L'$ the subsequent measurement of $\tilde{j}$ will be 0, 1 or 2 with equal probability 1/3. The same is true the other way around if we were then to measure again $\tilde{q}_L$ afterwards. Similar considerations were made for MFs in Ref. [14]. The fact that alternating measurements of $\tilde{q}_L$ and $\tilde{j}$ yield equal probability for the three possible outcomes is a strong indication that these modes are non-abelian PFs as it reflects the non-trivial commutation relation between the parity operators P_L and P_J (Eqs. (3.46) and (3.48)). This probability distribution is different from what would be observed with a non-topological degree of freedom in proximity to the lead. For example, if we replaced the PFs by a single antidot that could host a localised fractional charge a current readout would always return the same result when disregarding poisoning effects.

We will now propose an experimental protocol for testing the reduced F-matrix in a way that resembles measurement-based topological quantum computation [122]. We propose a quantum quench protocol where the four-PF system is initialised in a state with a well-defined $\tilde{q}_L$ after which $\tilde{j}$ is measured, and the statistics of the outcomes will give insight on the amplitude of $F^{(3)\dagger}$. This requires that the ratios ε_i/J can be tuned. After considering the quench protocol we will discuss how ε_i could be varied over several orders of magnitude.

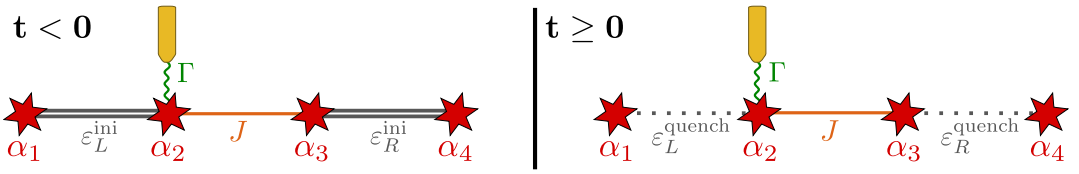

Figure 3.20: Schematic illustration of the quench protocol for four PFs (red stars). The system is initialised such that the outer couplings $\varepsilon_L^{\text{ini}}$ and $\varepsilon_R^{\text{ini}}$ are both much stronger than the fractional Josephson coupling $J \gg \Gamma$ when $t < 0$. At $t = 0$ we quench $\varepsilon_i^{\text{quench}} \ll \Gamma \ll J$. With the lead (gold) coupled to α_2, a current readout can distinguish the three values of $\tilde{j} = 0, 1, 2$ on a timescale of $\mathcal{O}(10 \cdot 2\pi\Gamma^{-1}) \ll 2\pi|\varepsilon_i^{\text{quench}}|^{-1}$.

The protocol does not require tuning of the lead-α_2 coupling rate Γ or the fractional Josephson coupling J and we only assume that $\Gamma \ll J$. In Fig. 3.20 we schematically show the initialisation and readout of the quench protocol that consists of the following steps:

For times $t < 0$**:** The four-PF system is initialised with couplings $\Gamma \ll J \ll \varepsilon_L^{\text{ini}}, \varepsilon_R^{\text{ini}}$ such that the eigenstates of the Hamiltonian $H_{4\text{pf}}$ are approximately $\{|Q, q_L\rangle\}$ and the goundstate is mostly composed of a single $|Q, q_L\rangle$ state. *If* tuning of the rate Γ is possible a current readout can be used to measure $\tilde{q}_L$ and thereby validate the initialisation. However, such a measurement is not required if $\varepsilon_L^{\text{ini}}$ and $\varepsilon_R^{\text{ini}}$ are sufficiently stronger than J and we assume that the four-PF system is in the ground state.

At time $t = 0$**:** The outer couplings are quenched such that $\varepsilon_L^{\text{quench}}, \varepsilon_R^{\text{quench}} \ll \Gamma \ll J$ and the PFs α_1 and α_4 are approximately decoupled from the remaining system. Now the states $\{|Q, j\rangle\}$ are the approximate eigenstates of $H_{4\text{pf}}$

For times $t > 0$**:** On a timescale $\sim 2\pi|\varepsilon_i^{\text{quench}}|^{-1}$, $\tilde{j}$ is conserved within an error of a few percent by analogy with the antidot coupling in Sec. 3.3. In a read out of the current signals we expect that, on average, we will see three levels corresponding to $\tilde{j} = 0, 1$ and 2 with equal probability 1/3.

To calculate the stochastic evolution of the current we once again employ the quantum jump method with the jump operators defined in Eq. 3.52. Since external poisoning sources are disregarded the four-PF system has a well-defined total $Q \mod 3$. The initial state is the ground state of $H_{4\text{pf}}(t < 0)$ and the jump operators, used to describe the readout of $\tilde{j}$, are expressed in the eigenstates of $H_{4\text{pf}}(t > 0)$. Like with the two-PF calculations we consider the current evolution at the fixed voltage $V_b = 2.6\lambda$ with a coupling rate $\Gamma = 0.1\lambda$. The initial outer couplings in $H_{4\text{pf}}(t < 0)$ are $\varepsilon_L^{\text{ini}} = 50\lambda$ and $\varepsilon_R^{\text{ini}} = 45\lambda$, and at $t = 0$ these are both quenched by four orders of magnitude; $\varepsilon_i^{\text{quench}} = 10^{-4}\varepsilon_i^{\text{ini}}$. We set the (assumed constant) Josephson coupling to $J = \lambda$ and take a low global charging energy interaction $\varepsilon_{LR} = 5 \cdot 10^{-4}\lambda$. The phases are fixed at $\phi_L = \arctan(1/\sqrt{27}) \approx \pi/16$, $\phi_R = \pi/14$ and $\theta = \pi/15$.

By the Monte Carlo method described in Sec. 3.1 we calculate and evolve the current in a time t_m from $t = 0.1$ µs to $t = 2$ µs (i.e. $t_m = 456 \cdot 2\pi\Gamma^{-1} \approx 23 \cdot 2\pi|\varepsilon_i^{\text{quench}}|^{-1}$). In Fig. 3.21a we show a histogram of the mean value of the current $\langle I \rangle$ over this time interval for a total 10^4 simulations. We see that they have a tendency to bunch into three pillars around 0 pA, 100 pA and 250 pA. These three values approximately correspond to the mean current obtained when initiating instead the

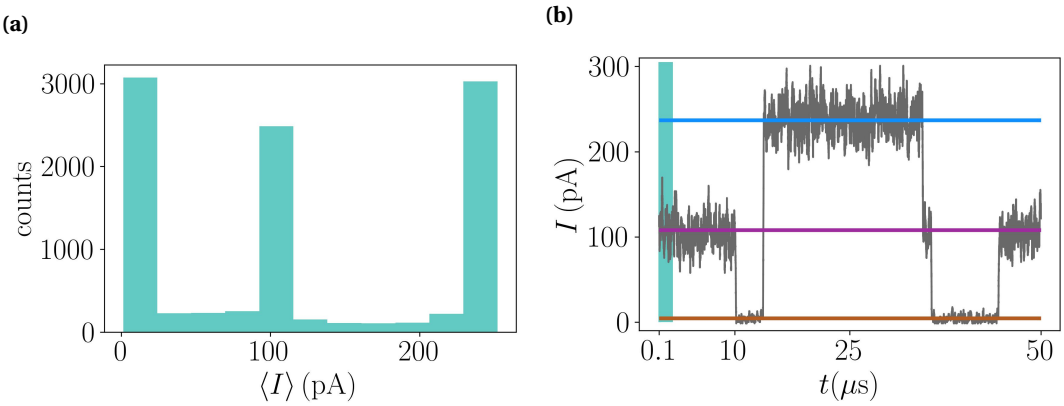

Figure 3.21: Results of the stochastic evolution of the four-PF setup. **(a)** Statistics of 10^4 simulations of the quench protocol. The mean value of the current $\langle I\rangle$ between 0.1 µs and 2 µs after the quench mainly bunches into three values corresponding to $\langle I\rangle_{\tilde{j}}$. The uneven distribution among the three is caused by a finite J prior to the quench. The 'background' counts in between is a result of the finite $\varepsilon_i^{\text{quench}}$ causing jumps between the three $|\tilde{j}\rangle$ states within the first few microseconds. The binning size is 22.8 pA. **(b)** Current trajectory after the quench on a timescale much longer than $2\pi|\varepsilon_i^{\text{quench}}|^{-1} \approx 0.1$ µs. Similarly to the case of incoherent fractional quasiparticle poisoning, the current jumps between three levels this time corresponding to $\langle I\rangle_{\tilde{j}=0}$ (brown horizontal line), $\langle I\rangle_{\tilde{j}=1}$ (blue line) and $\langle I\rangle_{\tilde{j}=2}$ (violet line). On the left we indicate with a shaded turquoise area the time interval t_m over which the mean current in (a) is averaged.

system in one of the eigenstates of $\tilde{j}$, $\{|\tilde{j}=0\rangle, |1\rangle, |2\rangle\}$, (i.e. superpositions of $|\tilde{q}_L\rangle$ states) with a $\varepsilon_i^{\text{quench}} = 0$. An average over 50 µs of these currents yields $\langle I\rangle_{\tilde{j}=0} = 4.5$ pA, $\langle I\rangle_{\tilde{j}=1} = 237$ pA and $\langle I\rangle_{\tilde{j}=2} = 108$ pA, matching well our by-eye estimates from Fig. 3.21a. An ideal protocol would have the fractional Josephson coupling turned off completely for $t < 0$ and only acquire a finite value at $t = 0$ and additionally have $\varepsilon_i^{\text{quench}} = 0$. The distribution is then equal among the three mean values $\langle I\rangle_{\tilde{j}}$ with no $\langle I\rangle$ in between. We explain the deviation from the ideal case with two effects: first, the uneven distribution among $\langle I\rangle_{\tilde{j}=0}$, $\langle I\rangle_{\tilde{j}=1}$ and $\langle I\rangle_{\tilde{j}=2}$, despite the large number of simulations, is due to the finite J at $t < 0$ meaning that the initial state does not have perfectly well-defined q_L. Second, since $\varepsilon_i^{\text{quench}} \neq 0$ in our expectedly more realistic protocol the finite couplings to the outer PFs α_1 and α_4 act as a quasiparticle poisoning source. In some of the simulations this causes a jump between the different states $|\tilde{j}\rangle$ of the two central PFs within the $t_m = 1.9$ µs and thereby also a jump in the current. This then yields an intermediate $\langle I\rangle$ between the $\langle I\rangle_{\tilde{j}}$ and thus the finite background. We conclude from this that within the time interval $t_m = 1.9$ µs the coherent evolution caused by $\varepsilon_i^{\text{quench}} \neq 0$ is a perturbation that cannot be neglected since t_m is considerably larger than $2\pi|\varepsilon_i^{\text{quench}}|^{-1}$ (note that $t_m \neq t_{\text{avg}} = 0.1$ µs). Despite these imperfections we nonetheless do clearly see three well-separated peaks on top of a weak background.

In Fig. 3.21b we show an example of a current trajectory over a long time compared to t_m which

we indicate with the shaded blue area. Indeed we see here a three-level telegraph noise, similar to that of Sec. 3.2, with jumps which typically occur on longer timescales than t_m. Comparing with Sec. 3.1 the projection time into the $\tilde{j}$ sectors is much shorter than 0.1 µs and therefore the current readout displays clear signatures of the three different $\tilde{j}$ sectors.

Physical construction of four-parafermion device

Let us now describe in more detail how to construct a four-PF device where some of the nearest-neighbour couplings are tunable. The proposal is based on transmon technology and inspired by Refs. [25, 87, 116, 117, 123]. In Fig. 3.19 we sketch below the dashed box the elements to obtain the tunability; both the left and right SC are connected via a transmon construction to a background SC that is grounded. Each of the superconducting islands therefore have a charging energy which we label by $E_{C,i}$, $i = \{L, R\}$. In addition to this, the islands also have a cross capacitance leading to a mutual charging energy E_{CC}. The transmon coupling to the background SC is characterised by the Josephson energy $E_{J,i}$ for each of the islands that can be tuned, for example, by a gate-controlled nanowire junction – a *gatemon* [124–126]. Finally, there is the fractional Josephson coupling J between α_2 and α_3 [12, 87, 118] that breaks the conservation of the PF charges $eq_L/3$ and $eq_R/3$. In total the Hamiltonian for this transmon construction reads

$$\begin{aligned} H_{\text{trans}} = \sum_{i=L,R} \Big[E_{C,i} \left(N_i + q_i/3 + q_{\text{ind},i}\right)^2 - E_{J,i} \cos(\vartheta_i) \Big] \\ - J \left(\mathrm{e}^{-i\left(\frac{\pi}{6}+\theta\right)} \mathrm{e}^{i\vartheta_R \delta_{q_R,0}} \, \alpha_3^\dagger \alpha_2 \, \mathrm{e}^{-i\vartheta_L \delta_{q_L,0}} + \text{H.c.} \right) \\ + E_{CC} \left(N_L + q_L/3 + q_{\text{ind},L}\right) \left(N_R + q_R/3 + q_{\text{ind},R}\right) . \end{aligned} \tag{3.59}$$

Here $N_i = -2i\partial_{\vartheta_i}$ is the number operator for Cooper pairs in the island i such that ϑ_i is the superconducting phase operator and $\mathrm{e}^{-i\vartheta_i}$ annihilates one Cooper pair in this SC. The charge induced in the SC i by an external voltage gate is $eq_{\text{ind},i}/3$ and tunable. The phase θ in the fractional Josephson term is proportional to the magnetic flux Φ through the total superconducting circuit consisting of the background SC and the two islands; $\theta = \pi\Phi/\Phi_0$ where Φ_0 is the magnetic flux quantum. This phase can thus be tuned by small variations of the magnetic field as long as the state of the FQH system remains unchanged. The operators $\mathrm{e}^{\pm i\vartheta_i \delta_{q_i,0}}$ are to keep account of the creation and annihilation of Cooper pairs when a fractional charge $-e/3$, through the J-coupling, enters a SC with PF charge number $q_i = 5$ or leaves an island with $q_i = 0$. Analogous architectures for MFs can be found in Refs. [127, 128] and by generalising the results of Refs. [123, 128] in the transmon limit $E_{J,i} \gg E_{C,i}$ we get a semiclassical effective Hamiltonian in the low-energy limit. It is the one of Eq. (3.44) where the couplings are determined by the following relations:

$$\varepsilon_i \propto E_{C,i}^{1/4} E_{J,i}^{3/4} \, \mathrm{e}^{-\sqrt{32 E_{J,i}/E_{C,i}}} , \tag{3.60}$$

$$\varepsilon_{LR} \propto \tilde{E}_C^{1/4} \tilde{E}_J^{3/4} \, \mathrm{e}^{-\sqrt{32 \tilde{E}_J/\tilde{E}_C}} , \tag{3.61}$$

$$\phi_i = \pi q_{\text{ind},i} . \tag{3.62}$$

The estimate of the PF couplings ε_i neglects the charging energy E_{CC} and is calculated from a 2π phase slip of island i, see also Ref. [123] for more detailed results. The expression for the cross capacitance term ε_{LR}, on the other hand, is significant in a device with large E_{CC}. We assume equal Josephson and charging energies; $E_{J,L} = E_{J,R} \equiv E_J$ and $E_{C,L} = E_{C,R} \equiv E_C$ such that the effective

energies in Eq. (3.61) are $\tilde{E}_J \approx 2E_J\cos(\theta)$ and $\tilde{E}_C \approx (E_{CC}+2E_C)/4$. The ε_{LR} term is estimated by imposing $\vartheta_L - \vartheta_R = 0$ and corresponds to a simultaneous phase slip of 2π of both islands [123]. Finally, there is the phase ϕ_i of the SC island i (see Eqs. (3.44) and (3.49)) which is proportional to the charge induced in this SC and thereby controllable by a voltage gate. The estimates in Eqs. (3.60)-(3.62) are found by neglecting the fractional Josephson energy $J \ll E_J$. Eq. (3.60) tells us that the couplings ε_i can be varied exponentially by changing the ratio $E_{J,i}/E_{C,i}$ – something that is commonly controlled in transmon devices by pinching off or opening the Josephson junction with voltage gates. From Refs. [124, 129] we find that the resulting ratio $\varepsilon_i^{\text{quench}}/\varepsilon_i^{\text{ini}}$ can vary over several orders of magnitude when considering aluminium islands of similar size as the niobium nitride in Refs. [20, 43]. This is in line with the factor of 10^{-4} adopted in the simulation shown in Fig. 3.21a.

The quench protocol described in this section could also be employed in similar tunable devices, for example where the four PFs are enclosed in fluxonium circuits [118]. If alternative devices could have a tunable lead rate Γ, one could think of more efficient protocols for testing the associativity rules and perhaps extend the validity of this to a broader parameter range.

3.5 Discussion and conclusions on the dynamics of parafermionic states

In this chapter we have analysed the dynamics of $\mathbb{Z}_6$ PFs in hybrid FQH-SC devices and how signatures of their fractional character show up in transport measurements. Differently from previous works, our study did not rely on transport of fractional charges [81–87] but rather on tunnelling spectroscopy with electrons coupled to one of the PFs via an external electrode. We used the stochastic quantum jump method to calculate single stochastic current trajectories and saw that under realistic conditions, such a measurement becomes a projective measurement of the fractional $\mathbb{Z}_3$ degree of freedom of a pair of PFs. Using the same method we estimated the time required for a PF system to project into a specific fractional charge sector and we furthermore investigated the noise of such measurements. The use of current readouts to distinguish the fractional charge states of PFs thus provides an alternative to interferometry [83, 95].

We extended the jump operator formalism to describe also incoherent coupling to a bath of fractional charges rather than an electron bath. With this we could describe fractional quasiparticle poisoning of pair of PFs and as poisoning source we considered the external edges of the FQH system. When the coupling rate between these and the PFs was weak compared to that of the lead a three-level telegraph noise in the current was observed as anticipated in the previous chapter. These jumps between current levels reflect that fractional charges jump between the outer FQH edges and the PF system. Additionally, we saw that by voltage tuning it is possible to shift this telegraph noise to be either two-level or three-level.

As a coherent poisoning source we considered an antidot in the bulk of the incompressible FQH liquid and saw that for a small antidot with essentially only two levels, weakly coupled to the PFs, a current readout through the normal lead would display a two-level telegraph noise signal. Hence, by deliberately creating an antidot (as demonstrated in Ref. [80]) in proximity to the SC and PFs, possibly of tunable size, one could observe additional PF signatures and obtain another manipulation opportunity [83], extending the results and protocols described in Secs. 3.3 and 3.4. For instance, if the separation of the antidot energy levels (here δ_{ad}) could be dynamically tuned this could be used to control the transitions between the different charge states of the PFs. The protocols for manipulation of states would be similar to those for the topological blockade effect in non-abelian FQH states [130] or for evolution of Majorana modes coupled to a quantum

dot [131–133]. Additionally, the energy level splittings could be lowered by enlarging the antidot and thereby more charge states of the antidot would be involved in the evolution of the PFs. This could lead to a three-level current signal like that of the incoherent poisoning in Sec. 3.2 rather than the two-level observed for smaller antidots.

The conclusion from poisoning considerations is that the PF energy splittings must be such that $|\Xi_{\tilde{q}} - \Xi_{\tilde{q}'}| > \Gamma, T$ and the lead coupling rate much larger than the poisoning rates $\Gamma_{e/3}, |\eta_{\mathrm{ad},i}| \ll \Gamma$ such that the projection time is shorter than or similar to $\Gamma_{e/3}^{-1}, |\eta_{\mathrm{ad},i}|^{-1}$. This is fulfilled for a broad parameter range and ensures a sufficient resolution in the current of different charge sectors and thereby distinguishable current jumps.

Finally, in order to study the anyonic properties of the $\mathbb{Z}_6$ PFs we extended the analysis to a device with four PFs and developed a quench protocol to test the associativity rules of the consecutive fusion of pairs of PFs. For this we could again use the quantum jump method and we obtained statistics of the amplitude of the associativity matrix corresponding to the fractional $\mathbb{Z}_3$ degree of freedom of the PFs. We proposed a physical device where tuning of some of the PF couplings, necessary for the protocol, could be obtained with a transmon-like construction.

A further study of more general noise effects, originating for example from drifting of the system parameters such as the magnetic field, could be made with the simulation techniques presented in this chapter. Future design of hybrid FQH-SC platforms to detect PF can make use of the indications provided in this chapter, also for studying the anyonic properties of these modes. Additionally, more complex devices could be expanded with the readout protocols presented here in order to test the braiding of PFs [25, 95].

4

Thouless pumping in Josephson junction arrays

This chapter is a reprint of the manuscript by Stavros Athanasiou, Ida E. Nielsen, Matteo M. Wauters and Michele Burrello, *Thouless pumping in Josephson junction arrays*, arXiv:2308.13597 [3], submitted to SciPost on the 7th of September 2023 and announced on arXiv in August 2023.

Here we reprint the manuscript *Thouless pumping in Josephson junction arrays* [3] that investigates how the Rice-Mele [134] and Harper-Hofstadter [135] pumping protocols can realise Thouless quantum pumping [136] in a one-dimensional chain of superconducting islands. My contribution to this work mainly lies within the Harper-Hofstadter model. Specifically, I helped to set up the Hamiltonian for the one-dimensional Josephson junction chain (Sec. 2), including the reformulation in terms of hardcore bosons and a periodic modulation of the on-site potential of the superconducting islands, induced by voltage side gates. I contributed to writing the code to simulate the long-time behaviour of six and nine-site chains of islands and I analysed the results. I started an initial draft of the manuscript, produced results and figures for Secs. 2 and 4 and contributed to refining and finishing the manuscript.

We calculate the instantaneous spectrum of the time-periodic Hamiltonian of the Harper-Hofstadter model in Eq. 13 in the thermodynamic limit with many islands. For correct phase tuning between neighbouring voltage gates, the corresponding energy bands in momentum and time space are gapped and topologically non-trivial with non-zero *Chern numbers*. We exploit *Floquet theory* to analyse the dynamics of a small six-site chain over many periods and define a many-body *Floquet operator*, the eigenstates of which are the *many-body Floquet eigenstates* with corresponding *many-body Floquet quasienergies* [137]. We introduce two superconducting leads coupling to the first and last islands of the chain. When the constant part of the on-site chemical potential is between two energy bands (of the corresponding thermodynamic limit) and the system is otherwise insulating, a small adiabatic variation of the potential can pump charge through the system. The time-averaged pumped charge per period of the voltage modulation is found in the infinite-time limit by use of the Floquet eigenstates and quasienergies. When averaging over the phase difference of the leads [138], the pumped charge per cycle is quantised and proportional to the sum of Chern numbers of the filled bands. This requires the coupling to the superconducting leads to be sufficiently strong compared to the Josephson coupling between the islands. By changing the constant chemical potential from one band gap to another, we see that the direction of the pumped current is inverted as expected from the Chern numbers. The quantisation is stable to nearest-neighbour interaction between the islands which even seems to stabilise the topological phases.

Thouless pumping in Josephson junction arrays

Stavros Athanasiou, Ida E. Nielsen, Matteo M. Wauters and Michele Burrello*

Center for Quantum Devices and Niels Bohr International Academy, Niels Bohr Institute, University of Copenhagen, DK–2100 Copenhagen, Denmark
* michele.burrello@nbi.ku.dk

August 29, 2023

Abstract

Recent advancements in fabrication techniques have enabled unprecedented clean interfaces and gate tunability in semiconductor-superconductor heterostructures. Inspired by these developments, we propose protocols to realize Thouless quantum pumping in electrically tunable Josephson junction arrays. We analyze, in particular, the implementation of the Rice-Mele and the Harper-Hofstadter pumping schemes, whose realization would validate these systems as flexible platforms for quantum simulations. We investigate numerically the long-time behavior of chains of controllable superconducting islands in the Coulomb-blockaded regime. Our findings provide new insights into the dynamics of periodically driven interacting systems and highlight the robustness of Thouless pumping with respect to boundary effects typical of superconducting circuits.

Contents

1 Introduction

Josephson junction arrays (JJAs) and their intricate many-body physics have captivated the attention of researchers since ground-breaking experiments in the 1990s (see the review [1]). Due to the possibility of engineering complex networks and their long-range coherence, JJAs have also been one of the leading candidates for quantum simulators in solid-state devices. Their practical application as quantum simulators, however, has been hindered by technological limitations: on one side, difficulties in tuning their physical parameters entailed the necessity of fabricating multiple devices to explore their phases of matter (see, for instance, Refs. [2–6]), thus impeding detailed investigations; on the other, irregularities in the self-capacitance, induced charge, and Josephson coupling of the superconducting elements, resulted in an uncontrolled disorder.

These limitations have been mitigated by recent advancements in epitaxial growth techniques [7] that have paved the way for the realization of clean superconductor-semiconductor (SC-SM) interfaces. These breakthroughs enable an unprecedented tunability of the Josephson couplings through electrostatic gates [8–12], as well as the fabrication of multiple quantum dots on the same hybrid device [13, 14], thereby revolutionizing the potential of JJAs as quantum simulators. Moreover, SC-SM platforms allow for on-chip patterning of arbitrary geometries in one and two dimensions, a precise control of the magnetic fluxes in these systems [11, 12], and a relatively easy scalability. All these elements motivate the theoretical design of novel phases of matter and quantum simulation protocols on controllable JJAs.

In this respect, topological phases of matter are an ideal target for quantum simulations in solid-state platforms due to their intrinsic robustness against disorder, noise, interaction, and possibly dissipation. When combined with a time-periodic driving, one can engineer novel out-of-equilibrium states with no static analogs, known as Floquet topological phases [15–20]. Among these, one of the simplest yet profoundly intriguing examples is Thouless pumping [21–23], a phenomenon arising in one-dimensional (1D) insulators with suitable time-periodic driving of the system parameters. The topology behind this phenomenon leads to quantization of the charge adiabatically pumped during each driving period; in 1D JJAs, this corresponds to a current $I = 2e\Omega\mathcal{C}$, with Ω being the pumping frequency and $\mathcal{C}$ a suitably defined Chern number characterizing the filled energy bands. Although theoretically well understood, experimental implementations of Thouless pumping have so far been confined to systems of ultracold atoms [24–27], optical waveguides [28], magneto-mechanical systems [29], and superconducting quantum processors [30] which fall short in capturing genuine transport phenomena of charged particles.

In this paper, we propose an innovative approach that combines a JJA with the ability to finely tune the induced charge on each SC island and the corresponding Josephson couplings. Through numerical simulations of 1D arrays in the Coulomb-blockaded regime, we focus on the long-time behavior of such systems. To investigate this limit, we connect a Josephson junction chain with superconducting leads that act as Cooper pair (CP) reservoirs. We study the effect of the electrostatic repulsion arising from the cross-capacitance between neighboring islands and show that topological pumping is remarkably robust with respect to both the coupling to the leads and nearest-neighbor interactions. Our proposal is qualitatively different from former experiments based on geometrical pumping which rely on optimal control of the pumping protocol (e.g. Ref. [31] for electron junction systems and Ref. [32, 33] for superconducting transistors). Topological pumping, on the other hand, is predicted to be robust against disorder [34–36] and imperfections in the modulations [22, 37]. Our findings shed new light on the role of interaction and dissipation in topological pumping schemes, which are currently at the core of intense debate [23, 38–40]. Through this research, we expand our understanding of JJAs as versatile platforms for quantum simulations while unveiling new insights into

topological phenomena and the dynamics of interacting systems.

The paper is organized as follows: In Sec. 2 we derive a bosonic model from the Hamiltonian of a 1D JJA. In particular, we specialize on two models characterized by nontrivial topological properties: the Rice-Mele (RM) model [41, 42], which we introduce in Sec. 2.1, and the Harper-Hofstadter (HH) model [43, 44], presented in Sec. 2.2. Our analysis of topological pumping in Josephson junction chains based on the RM model is presented in Sec. 3, where we investigate in detail the role of the coupling with external superconducting leads and the effects of nearest-neighbor interactions. In order to show that the findings are not model-specific, but hold on a wide class of periodically driven systems, we report further numerical analysis on the HH model in Sec. 4. In Sec. 5 we discuss the energy scales and constraints relevant to realistic experimental implementations. Finally, we draw our conclusions and present future outlooks in Sec. 6.

2 Josephson junction arrays in hybrid superconductor - semiconductor platforms

Recent developments in the epitaxial growth techniques of hybrid SC-SM materials [7] allow for the fabrication of 1D and 2D arrays of superconducting islands lithographically patterned in arbitrary geometries [10–12] and contacted to a semiconducting substrate through atomically pristine interfaces [45]. In such devices, the filling of the substrate can be controlled via a global electrostatic gate (a top gate in the experiments in Refs. [10–12]). Additionally, smaller gates can be used to locally change the potential and density of states of the SM [9].

In the following, we consider devices defined by a 1D chain of superconducting islands of sub-micrometer size. For Al islands, the typical critical temperature of such systems is $\sim$ 1.6K [10], and we regard the related superconducting gap as the largest energy scale in the description of these systems. As a consequence, when operating at temperatures of the order of a few tens of milliKelvins, as customary in experiments, we can neglect effects determined by the Bogoliubov quasiparticle excitations of the islands. We can thus describe the low-energy physics of these JJAs by considering solely the dynamics of their CPs.

For a neighboring pair of SC islands, the dynamics can be modeled through the interplay of two kinds of interaction; first, the electrostatic interaction determined by the capacitance matrix which describes not only the potential induced on one island by the charge of the other, but also the charges induced in both islands by the surrounding environment. Second, the tunneling of CPs between the two islands which define an effective SC-SM-SC junction where the coherent hopping of CPs is mediated by Andreev states [46]. These states are induced in the SM layer below the two islands, where superconductivity is induced by proximity [9], and in the in-between region. Both interactions can be affected by neighboring electrostatic gates. Let us consider, for instance, a 1D chain as the one depicted in Fig. 1. In this setup, each superconducting island is addressed by a side gate at potential $V_{g,j}$, controlling the induced charge $2en_{g,j} = V_{g,j}C_j^{\mathrm{g}}$. Additionally, we assume that a cutter gate at potential $V_{c,j}$ can control the filling of the semiconducting region in proximity of each Josephson junction and thereby its transparency. In this way, the effective coherent hopping amplitude of CPs between the islands can be modulated by varying the carrier density in the SM [9] and potentially turned off by totally depleting the substrate.

At low temperature, the JJAs can be modeled through a standard quantum phase model (see, for instance, the review [1]). To describe a chain as the one depicted in Fig. 1, we assign a superconducting phase operator $\hat{\varphi}_j$ and a number operator $\hat{N}_j$ to each superconducting island. $\hat{N}_j$ defines the number of CPs in the island with respect to an arbitrary offset. The two operators obey the standard commutation relation $[\hat{N}_j, \mathrm{e}^{i\hat{\varphi}_j}] = -\mathrm{e}^{i\hat{\varphi}_j}$, and $\mathrm{e}^{i\hat{\varphi}_j}$ annihilates a CP in the

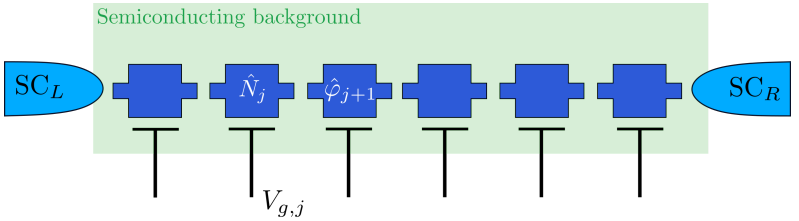

Figure 1: Chain of superconducting islands (dark blue) on top of a semiconducting substrate (green). Next to every island is a T-shaped side gate with tunable voltage $V_{g,j}$. At each end of the chain, there is a superconducting lead.

island j. The Hamiltonian for the chain is written as $\hat{H} = \hat{H}_C + \hat{H}_J$ and describes the interplay between the electrostatic interactions and CP tunneling, respectively. Let us first consider the charging energies of the islands in the chain, defined by

$$\hat{H}_C = 4e^2 \sum_{i,j=1}^{M} C_{ij}^{-1} (\hat{N}_i - n_{g,i})(\hat{N}_j - n_{g,j}) . \tag{1}$$

Here C^{-1} is the inverse capacitance matrix of the islands and M is the number of islands in the chain. However, by assuming that the semiconducting environment and the electrostatic gates in the hybrid device effectively screen the charge of the SCs, we reduce the sum to single-island and nearest-neighbor interactions:

$$\hat{H}_C \approx E_C \sum_{j=1}^{M} (\hat{N}_j - n_{g,j})^2 + E_{CC} \sum_{j=1}^{M-1} (\hat{N}_j - n_{g,j})(\hat{N}_{j+1} - n_{g,j+1}) . \tag{2}$$

In this equation, we introduced two customary energy scales: $E_C = 4e^2/C^{\text{self}}$ sets the charging energy of a single island, with C^{self} being the sum of all capacitances to the other islands and environment elements; $E_{CC} = 4e^2 (C^{-1})_{j,j+1}$ determines the electrostatic energy between neighboring islands. We will assume for simplicity that these quantities are translationally invariant, which is the expected behavior for a strong screening imposed by the environment. Weak variations along the chain, however, do not affect our analysis and can be easily accounted for. $n_{g,j}$ is the charge induced in each superconducting island and can be controlled by the surrounding electrostatic gates (see Fig. 1). In particular, we assume that each induced charge $n_{g,j}$ is primarily controlled by the voltage of the side gate addressing the island j, $n_{g,j} = V_{g,j} C_j^{\text{g}}/2e$. Here C_j^{g} defines the mutual capacitance between the island j and its neighboring side gate. More complex scenarios to account for the charge induced by all electrostatic gates can be easily investigated. The energy scale E_C is determined by the geometry of the islands and their electrostatic environment. We consider, as an example, gated devices with Al islands patterned over an InAs 2D electron gas; for rectangular islands of size $\sim$ 750nm×80nm, the resulting charging energy is approximately $E_C \approx 0.125\text{meV} \approx h30\text{GHz}$ [47].

The coherent tunneling of CPs is modeled by the Hamiltonian

$$\hat{H}_J = -\sum_{j=1}^{M-1} E_{J,j} \cos\left(\hat{\varphi}_{j+1} - \hat{\varphi}_j - \theta_{j,j+1}\right) . \tag{3}$$

Here $E_{J,j}$ is the Josephson coupling between island j and $j+1$ and the Peierls phase $\theta_{j,j+1} = \frac{2e}{\hbar c} \int_j^{j+1} \vec{A}\, \mathrm{d}\vec{x}$ is the line integral of the vector potential $\vec{A}$ along a path between island j and $j+1$,

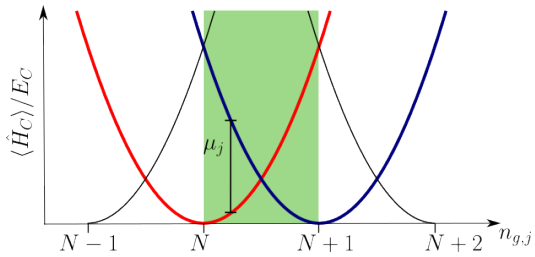

Figure 2: Charging energy of a single island as a function of the induced charge $n_{g,j}$ for states with $N-1$, N, etc. CPs. The thicker red and blue curves mark the two charge states we consider in the hardcore-boson approximation and the shaded area is the maximum region of validity of such an approximation. The effective chemical potential is the energy difference between the $N+1$ (blue) and N (red) parabolas.

which accounts for the role of the magnetic field when embedding the chain in a closed superconducting loop. Eq. (3) corresponds to tunneling of single CPs between neighboring islands. Hence, we are neglecting terms characterized by higher harmonics of the phase difference $\hat{\varphi}_{j+1} - \hat{\varphi}_j$. In SC-SM-SC junctions, such an approximation is justified for cases in which the transmissibilities of the Andreev channels connecting the islands are low [46]. This, in turn, corresponds to a sufficiently depleted semiconducting substrate. Higher-harmonic terms can be considered as well, giving rise to non-quadratic interactions in terms of the annihilation and creation operators of CPs (for instance, coherent tunnelings of charge $4e$ objects). These are, however, considerably weaker than the energy scale $E_{J,j}$ of the single-CP tunneling, and we expect them not to play a crucial role in the implementation of Thouless pumping.

Concerning the Josephson amplitudes $E_{J,j}$, these can be globally controlled by a top gate as in Ref. [10], and the maximal value vastly depends on the width and length of the junction. Additionally, for the implementation of the RM model, we require the ability to separately address them through the voltage $V_{c,j}$ of suitable cutter gates. In general, the function $E_{J,j}(V_{c,j})$ may be complicated (see the experimental data related to gate-tunable devices in Refs. [48, 49]). We consider, however, a regime in which $E_{J,j} = 0$ when $V_{c,j}$ is below a certain threshold $V^*_{c,j}$, such that the substrate is totally depleted, and, for simplicity, we impose that $E_{J,j}$ is approximately linear in $V_{c,j}$ above this threshold [see Fig. 3(a)]. Importantly, the topological character of the RM model makes the pumped current robust against the details of the function $E_{J,j}(V_{c,j})$ as long as it is monotonic and sufficiently regular. Therefore, we consider a device in which the average value of the Josephson coupling $E_{J,j}$ is set by a global gate, whereas an additional periodic time modulation can be imposed by the cutter gate voltages. Experiments on hybrid Josephson junction showed that, for a width of about 0.3μm, the amplitude E_J at zero cutter voltage is of the order of h50GHz [9] and it can be switched off by applying sufficiently strong negative potentials (see, for instance, Ref. [49]).

When the Josephson energy dominates over the electrostatic terms, the system displays global phase coherence and behaves as a SC, allowing for coherent transport of CPs. Instead, the regime in which the electrostatic interaction E_C dominates over the Josephson energies $E_{J,j}$, results in an insulating phase unless all the induced charges $n_{g,j}$ are fine-tuned close to $1/2$. In this scenario, the transport of CPs across the chain is suppressed, as we can consider each island in a Coulomb-blockaded state. In order to devise charge pumping protocols, we consider the regime $E_{C,j} > E_{J,j},\ E_{CC,j}$, and, initially, we neglect the nearest-neighbor electrostatic interactions. We can rewrite the Hamiltonian $\hat{H}$ by introducing the operators $\hat{\Sigma}_j = \mathrm{e}^{i\hat{\varphi}_j}$ and $\hat{\Sigma}^\dagger_j = \mathrm{e}^{-i\hat{\varphi}_j}$ which, respectively, lower and raise the number of CPs in the island j by 1,

such that $[\hat{N}_j, \hat{\Sigma}_j] = -\hat{\Sigma}_j$. We obtain:

$$\hat{H} = \sum_{j=1}^{M} E_C(\hat{N}_j - n_{g,j})^2 - \frac{1}{2}\sum_{j=1}^{M-1} E_{J,j}\left(\hat{\Sigma}_{j+1}^\dagger \hat{\Sigma}_j \, e^{-i\theta_{j,j+1}} + \hat{\Sigma}_j^\dagger \hat{\Sigma}_{j+1} \, e^{i\theta_{j,j+1}}\right). \tag{4}$$

This expression shows explicitly that the quantum phase model corresponds to a tight-binding Hamiltonian for the CPs.

The dispersion of the charging energy of a single island is depicted in Fig. 2 as a function of the induced charge $n_{g,j}$ for different number states. When $n_{g,j}$ is a half-integer, states that differ by one CP are degenerate; let us consider, for instance, the case $n_g \approx 0.5$. If $E_J \ll E_C$, we may assume that only the two lowest-energy states, with charge $N = 0$ and $N = 1$, are significantly occupied. States corresponding to the other parabolas are separated in energy by a gap $\sim 2E_C$ and their population in the many-body ground state is negligible. Therefore, under the assumption $E_C > E_{J,j}, T$, where T is the system temperature, we can further simplify our description of the JJA and map the Hamiltonian $\hat{H}$ into a hardcore boson model. We may then replace $\hat{\Sigma}_j$ by a new hardcore boson operator $\hat{b}_j$, such that $\hat{b}_j^\dagger \hat{b}_j = \{0, 1\}$ and $\hat{b}_j^2 = (\hat{b}_j^\dagger)^2 = 0$. The energy difference between the two lowest charge states is $E_C(1-2n_{g,j})$ for $n_g \approx 0.5$ (Fig. 2). Hence, we can define an on-site potential, resemblant of an effective chemical potential,

$$\mu_j = E_C(1 - 2n_{g,j}), \tag{5}$$

which vanishes for $n_{g,j} = 0.5$. We rewrite the total Hamiltonian (with $E_{CC} = 0$) as a tight-binding model of hardcore bosons:

$$\hat{H} = \hat{H}_C + \hat{H}_J \approx \sum_{j=1}^{M} \mu_j \hat{b}_j^\dagger \hat{b}_j - \frac{1}{2}\sum_{j=1}^{M-1} E_{J,j}\left(\hat{b}_{j+1}^\dagger \hat{b}_j \, e^{i\theta_{j,j+1}} + \text{H.c.}\right). \tag{6}$$

This Hamiltonian shows that, in the hardcore limit $E_C \gg E_{J,j}$, the system can be mapped into a chain of free fermions via a Jordan-Wigner transformation. Any time modulation of the electrostatic gates would translate into a time modulation of the onsite potentials μ_j and the tunneling amplitudes $E_{J,j}$. Hence, by implementing a suitable periodic modulation of these parameters, we expect that the Josephson junction chain is able to reproduce the physics of periodically driven systems of non-interacting fermions.

In the following, we will focus on the two most known schemes for the realization of adiabatic Thouless pumping: the periodically driven RM model and HH model. We restrict our analysis to the hardcore boson description but emphasize that the breakdown of this approximation and the effects of onsite interactions in the RM model have been theoretically investigated in Ref. [39].

Both models rely on a periodic drive of the onsite potential. We consider a generic time modulation of the side gates with

$$V_{g,j}(t) = V_{0,j} + \delta V_{g,j} \cos\left(\omega t + \chi_j\right), \tag{7}$$

where $\omega = 2\pi\Omega$. Such modulation yields:

$$\mu_j(t) = \mu_{0,j} - \delta\mu \cos\left(\omega t + \chi_j\right) \equiv E_C\left(1 - \frac{C_j^g V_{0,j}}{e}\right) - \frac{E_C C_j^g \delta V_{g,j}}{e} \cos\left(\omega t + \chi_j\right). \tag{8}$$

If $\mu_{0,j} \approx \bar{\mu}$ is approximately independent of the position along the chain, it plays the role of an overall chemical potential for the hardcore bosons. The static voltages $V_{0,j}$ can therefore be used to set the average filling of the system. In case of position-dependent variations of the

C_j^g parameters, instead, these voltages can be tuned to reduce the fluctuations of the onsite potentials $\mu_{0,j}$ which, essentially, play the role of onsite disorder in the Hamiltonian (6). Finally, the oscillation amplitudes $\delta V_{g,j}$ determine the modulation of the onsite potential, which is additionally characterized by a position-dependent phase χ_j that we will suitably set to implement the RM and HH models, as described in the next subsections. Throughout this paper, we set $\hbar = 1$.

2.1 Rice-Mele Hamiltonian

The RM model [41] offers the most paradigmatic example of topological pumping in 1D systems. It is a model with a two-site unit cell, and its hardcore boson formulation is defined by a time-periodic Hamiltonian of the form

$$\hat{H}_{RM}(t) = \sum_{j=1}^{M/2} \left(\mu_A(t) \hat{b}^\dagger_{2j-1} \hat{b}_{2j-1} + \mu_B(t) \hat{b}^\dagger_{2j} \hat{b}_{2j} \right) - \frac{E_{J,1}(t)}{2} \sum_{j=1}^{M/2} \left(\hat{b}^\dagger_{2j-1} \hat{b}_{2j} + \text{H.c.} \right) - \frac{E_{J,2}(t)}{2} \sum_{j=1}^{M/2-1} \left(\hat{b}^\dagger_{2j} \hat{b}_{2j+1} + \text{H.c.} \right) . \tag{9}$$

Here we consider a chain with an even number of islands M and open boundary conditions. The instantaneous spectrum of $\hat{H}_{RM}$ in the thermodynamic limit displays two bands with a linear level crossing at $E_{J,1} = E_{J,2}$ and $\mu_A = \mu_B$. For $\mu_A = -\mu_B$ the ground state is found at half-filling, and it is useful to define the two-component parameter vector $\vec{h} = \left(\frac{E_{J,1} - E_{J,2}}{2}, \mu_A - \mu_B \right)$. The time-dependent single-particle gap is given by $|\vec{h}(t)|$, and a topological charge pumping is obtained when $\vec{h}(t)$ winds around the gapless point $\vec{h} = 0$ during one period.

To implement Thouless pumping, we adopt a modulation of the kind in Eq. (8) for the onsite potentials and, in particular, we choose $V_{0,j}$ such that all islands are tuned close to the charge degeneracy point $\mu_{0,j} = 0$ between the lowest energy parabolas (Fig. 2). In order to enforce

$$\mu_A(t) = -\mu_B(t) = \delta\mu \sin(\omega t) , \tag{10}$$

we set $\chi_j = (-1)^{j+1}\pi/2$ and choose modulation amplitudes $\delta V_{g,j}$ such that $\delta\mu$ is approximately constant along the chain. We observe that a residual $\bar{\mu}$ may reduce the energy gap of the system, but in the limit of adiabatic pumping, it does not affect the pumped charge as long as it remains sufficiently smaller than the single-particle gap at all times. The modulation of the Josephson energies $E_{J,j}(V_{c,j})$ is achieved by time-periodic voltages in the cutter gates. In particular, we adopt the following signals:

$$V_{c,j}(t) = V_c + (-1)^{j+1} \delta V_c \cos(\omega t) . \tag{11}$$

We assume that all junctions in the chain are characterized by the same parameters, such that this modulation approximately results in Josephson amplitudes of the kind

$$E_{J,j}(t) = f_{lr}\left[J_0 + (-1)^{j+1} \delta J \cos \omega t \right] , \tag{12}$$

where f_{lr} is a linear rectifier function, with $f_{lr}(x) = x$ if $x > 0$ and $f_{lr}(x) = 0$ otherwise, see Fig. 3(a). V_c is used to control the offset J_0 and the modulation δJ is roughly proportional to δV_c. If $V_c - \delta V_c > V_c^*$, the Josephson amplitudes $E_{J,j}$ are always positive and display a sinusoidal modulation [see the example in Fig. 3(b)]. If instead $V_c - \delta V_c < V_c^*$, $E_{J,j}(t) = 0$ for a fraction of the time period and its modulation is clipped below zero [Fig. 3(c)].

The time-periodic nature of the Hamiltonian H_{RM} allows us to consider the time coordinate as a second dimension for the momentum, such that we can assign a Chern number $\mathcal{C}$ to each

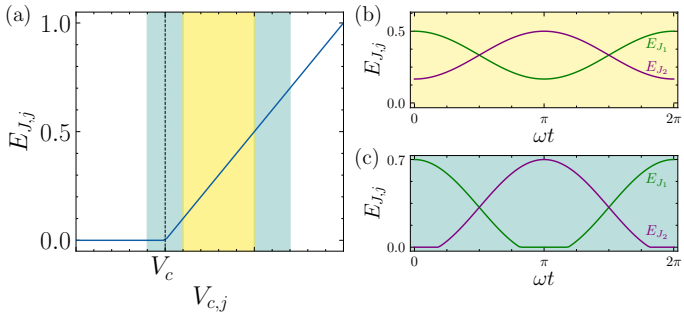

Figure 3: (a) The blue curve displays the approximation considered to model the Josephson energies $E_{J,j}$ as a function of the cutter gate voltage $V_{c,j}$ (arbitrary units). The dashed vertical line indicates the threshold V_c^* below which $E_{J,j}$ is considered zero. Yellow and blue shaded areas schematically indicate the voltage range for the sinusoidal and clipped modulations, respectively. Panels (b) and (c) display the corresponding modulated $E_{J,j}(\omega t)$; green and purple curves refer to odd and even junctions, respectively.

energy band [21]. For the considered modulations, the Chern numbers are $\mathcal{C}_0 = 1$, $\mathcal{C}_1 = -1$, where the index $n = 0, 1$ labels the single-particle bands, resulting in an adiabatic Thouless pumping at half filling with average current $I = 2e\mathcal{C}_0\Omega$.

2.2 Harper-Hofstadter Hamiltonian

The 2D Hofstadter model [43] provides the simplest description of charged particles moving on a square lattice and subject to a uniform out-of-plane magnetic field. The dynamics of the model is determined by the magnetic flux per plaquette and the corresponding Aharonov-Bohm phase Φ acquired by a particle that moves around it. Incommensurate values of the flux result in the celebrated Hofstadter butterfly fractal spectrum, while for commensurate values $\Phi = 2\pi p/q$, the system can be modeled in the Landau gauge by introducing a q-site unit cell, and displays q energy bands with non-trivial Chern numbers.

The equivalent driven 1D Hamiltonian, known as the Harper-Hofstadter model, is obtained by replacing one of the momentum components of the Hofstadter model by the time coordinate and, for hardcore bosons, it reads:

$$\hat{H}_{HH}(t) = \sum_{j=1}^{M} [\bar{\mu} - \delta\mu \cos(\omega t - \Phi j)]\, \hat{b}_j^\dagger \hat{b}_j - \frac{E_J}{2} \sum_{j=1}^{M-1} \left(\hat{b}_{j+1}^\dagger \hat{b}_j + \hat{b}_j^\dagger \hat{b}_{j+1} \right). \tag{13}$$

The realization of this model in the Josephson junction chains requires exclusively the modulation (8) of the onsite potentials and is obtained by setting a position-dependent phase $\chi_j = \Phi j$ in Eq. (7). In particular, setting $\Phi = 2\pi/3$ yields the simplest example of the gapped Hofstadter model. It corresponds to a 3-island periodicity of the phase χ_j and, in the thermodynamic limit, it yields three bands of the instantaneous spectrum (see Fig. 4), characterized by Chern numbers $\mathcal{C}_n = 1, -2, 1$. The band gap is proportional to the minimum between $E_J/2$ and $\delta\mu$.

The realization of the corresponding pumping scheme does not require a modulation of the Josephson amplitudes. Furthermore, the uniform and constant potential $\bar{\mu}$ can be changed by

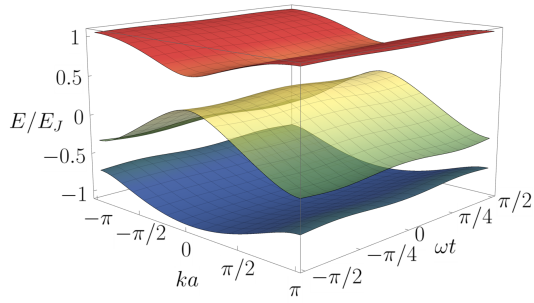

Figure 4: Spectrum of the Harper-Hofstadter model as a function of momentum and time at $\Phi = 2\pi/3$ for $\delta\mu = 0.4E_J$ and $\bar{\mu} = 0$.

regulating the voltage offsets $V_{0,j}$ and be used to set the overall filling of the CPs. The Thouless pumping is achieved when $\bar{\mu}$ lies in either of the band gaps depicted in Fig. 4. In particular, the charge pumped adiabatically in the thermodynamic limit is proportional to the sum of the Chern numbers of the filled bands: this implies that by varying $\bar{\mu}$ from the first to the second gap, we expect the pumped current to change sign from $2e\Omega$ to $-2e\Omega$.

2.3 Coupling with external superconducting leads

So far, we have discussed the modeling of isolated Josephson junction chains. To investigate their transport properties, however, it is necessary to embed these systems in a larger environment. Specifically, our aim is to model the driven transport of CPs across such JJAs. Therefore, the most convenient choice is to include two superconducting leads coupled to the first and last island of the chain (depicted in light blue in Fig. 1 and labeled by SC_L and SC_R). To this purpose, we supplement the Hamiltonian $\hat{H}$ with a boundary term that describes a Josephson junction between the two extreme islands and the related superconducting leads [50]

$$\hat{H}_\mathrm{b} = -E_L\left[\cos(\hat{\varphi}_1 - \hat{\varphi}_L) + \cos(\hat{\varphi}_R - \hat{\varphi}_M)\right], \tag{14}$$

where E_L describes the associated Josephson energy which we consider constant in time. By assuming that both leads are described by standard BCS coherent states, we can replace the related phase operators $\hat{\varphi}_{L/R}$ with classical phases $\varphi_{L/R}$. When embedding the JJA in an external SQUID, the phase difference $\phi = \varphi_R - \varphi_L$ would correspond to the magnetic flux threading it. We observe that such a phase difference can be absorbed in the Peierls phases $\theta_{j,j+1}$ in Eq. (3) by a suitable gauge transformation.

In the hardcore limit, the boundary Hamiltonian $\hat{H}_\mathrm{b}$ becomes

$$\hat{H}_\mathrm{b} = -\frac{E_L}{2}\left[\mathrm{e}^{i\varphi_L}\, b_1^\dagger + \mathrm{e}^{i\varphi_R}\, b_M^\dagger\right] + \mathrm{H.c.}\,. \tag{15}$$

This boundary term violates the conservation of the total number of CPs in the chain, such that, in general, the many-body ground and Floquet states will be superpositions of different particle numbers. Hence, the adiabatic condition no longer involves the single-particle band gap e_g but a *many-body energy gap* E_g that depends on the interplay between the charging energies of the SC islands, the Josephson energies of the junctions, and the coupling with the leads.

3 Results of the Rice-Mele model

In the following, we will investigate Thouless pumping in short chains coupled to external SC leads to identify experimentally relevant regimes where charge quantization can be observed. In particular, we will focus on the role played by the Josephson coupling to the leads, which breaks particle number conservation, and on the effects of the nearest-neighbor interaction E_{CC}. To this end, we adopt a Floquet description of the driven Josephson chain in the hardcore boson limit. We consider the Hamiltonian

$$\hat{H}_{RM,\mathrm{tot}}(t,\phi) = \hat{H}_{RM}(t) + \hat{H}_b(\phi), \tag{16}$$

which describes a RM chain, as defined in Eq. (9), embedded in a superconducting circuit through the contact with the leads in Eq. (15). $\hat{H}_{RM,\mathrm{tot}}(t,\phi)$ is periodic in both t and ϕ, and we can analyze the dynamics of the related system by defining a many-body Floquet operator which, for a generic Hamiltonian $\hat{H}$, reads

$$U(\tau) = \mathcal{T}\, \mathrm{e}^{-i\int_0^\tau \hat{H}(t)\,\mathrm{d}t}\,. \tag{17}$$

Here $\mathcal{T}$ indicates time ordering and $\tau = 1/\Omega$ is the time period such that $\hat{H}(t+\tau) = \hat{H}(t)$. We consider system sizes up to $M = 8$, compatible with realistic devices in which all islands can be independently addressed by gate voltages, and we numerically diagonalize $U(\tau)$ to obtain the many-body Floquet eigenstates $\{|\Phi_\nu(\tau)\rangle\}$:

$$U(\tau)\,|\Phi_\nu(\tau)\rangle = \mathrm{e}^{-i\mathcal{E}_\nu \tau}\,|\Phi_\nu(\tau)\rangle\,, \tag{18}$$

where $\mathcal{E}_\nu$ labels the many-body Floquet quasienergies. In the infinite-time limit, for a given phase difference ϕ, the time-averaged pumped charge per cycle corresponds to [22, 51, 52]

$$Q_\infty \equiv \lim_{m\to\infty} \frac{2e}{m}\int_0^{m\tau} \mathrm{d}\,t'\,\mathrm{tr}\big[\rho(t')\partial_\phi \hat{H}(t',\phi)\big] = 2e\tau \sum_\nu \mathcal{N}_\nu(\phi)\,\partial_\phi \mathcal{E}_\nu\,, \tag{19}$$

with

$$\mathcal{N}_\nu(\phi) = |\langle \Phi_\nu(\tau)|\Psi_0\rangle|^2\,. \tag{20}$$

Here Ψ_0 is the state of the Josephson chain at the beginning of the pumping protocol, which we set to the ground state of $\hat{H}_{\mathrm{RM,tot}}(t=0,\phi)$, $\rho(t)$ is the density matrix of the system at time t, and $2e\partial_\phi \hat{H} = \hat{\mathcal{J}}$ corresponds to the current operator. In the adiabatic limit, the ground state $|\Psi_0\rangle$ of $\hat{H}_{\mathrm{RM,tot}}(t=0,\phi)$ has a large overlap with the Floquet state with the lowest energy expectation value [44], which we denote by $|\Phi_0(\tau)\rangle$, such that $\mathcal{N}_\nu \to \delta_{\nu,0}$. Hence, Q_∞ is carried by a single Floquet state. An equivalent expression for the pumped charge per cycle in the infinite-time limit is [52]

$$Q_\infty = \sum_\nu \mathcal{N}_\nu(\phi)\int_0^\tau \mathrm{d}t\,\langle \Phi_\nu(t)|\hat{\mathcal{J}}(t)|\Phi_\nu(t)\rangle\,, \tag{21}$$

where $\hat{\mathcal{J}}(t)$ is the time-dependent current operator, and $|\Phi_\nu(t)\rangle$ are the time-evolved Floquet states *within one period*. Given the difficulty of accurately differentiating numerically the quasienergies with respect to the external SC phase, due to the many (avoided) level crossings in the Floquet spectrum, we will use Eq. (21) to extract the pumped charge from the time evolution. Our numerical calculations are performed with the QuTiP Python framework [53, 54].

The phase difference between the two external superconducting leads, rescaled by the number of islands in the chain, ϕ/M, can be interpreted as a shift of the quasimomenta of

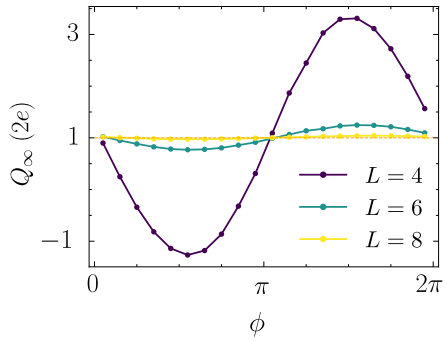

M	$1-\bar{Q}/(2e)$
4	0.0078
6	0.0072
8	0.0071

Figure 5: Pumped charge at infinite time Q_∞ as a function of the phase difference ϕ between the external superconducting leads for $M = 4, 6, 8$ islands. The data correspond to the following parameters: $\delta J = 0.7J_0, \delta\mu = 1.5J_0, E_L = 2J_0, \omega = 0.05J_0$. The table represents the deviations from perfect quantization of the phase averages pumped charge $\bar{Q}$ as a function of the systems size M.

the system CPs via a suitable gauge transformation. For small systems, this shift causes a non-trivial dependence of $\partial_\phi \mathcal{E}_\nu$ on ϕ that yields, in turn, a dependence of Q_∞ on the external phase. This is expected to be relevant only for small systems and vanishes completely in the thermodynamic limit, provided the system is in an insulating phase [55]. To evaluate these finite-size effects for the Hamiltonian $\hat{H}_{RM,\mathrm{tot}}$, we depict in Fig. 5 the time-averaged pumped charge $Q_\infty(\phi)$ for $E_{CC} = 0$, $E_L = 2J_0$ and a ratio $\sim 1/16$ between ω and the *many-body* gap E_g. For $M = 4$ and $M = 6$ islands, the dependence on ϕ is significant, but the oscillation around the average quantized value reduces to $\sim 2\%$ for $M = 8$. We find analogous results for the HH model, see Sec. 4.

To recover an exact quantization in short chains, it is therefore necessary to average the pumped charge over ϕ. By following the Thouless construction [34], we define

$$\bar{Q} = 2e\tau \sum_\nu \int_0^{2\pi} \frac{d\phi}{2\pi}\, \mathcal{N}_\nu(\phi)\, \partial_\phi \mathcal{E}_\nu = \int_0^{2\pi} \frac{\mathrm{d}\phi}{2\pi} Q_\infty(\phi)\,. \tag{22}$$

For systems with periodic boundary conditions conserving the particle number (such that ϕ is a phase twist in the boundary conditions), this quantity is quantized in the adiabatic limit at half-filling and corresponds, when $\mathcal{N}_\nu = \delta_{\nu,0}$, to the Chern number of the lowest energy band. More in general, Eq. (22) implies that only Floquet many-body states whith a quasienergy that winds in the Floquet-Brillouin zone as a function of ϕ contribute to the pumped charge $\bar{Q}$ (see, for instance, Fig. 7). Our results show that $\bar{Q}$ displays a precise quantization towards the adiabatic limit within an error of 1%, even when including the boundary term $\hat{H}_b$. The residual small deviation originates from non-adiabatic effects due to the finite frequency and the choice of the driving protocol [42,44]. Adiabatic perturbation theory gives a leading-order estimate of this correction which scales as $1-\bar{Q} \sim \left(\frac{\omega}{E_g}\right)^2$.

In the following, we will consider small system sizes, for which the phase dependence is sizable, and we will investigate the dependence of the pumped charge on the modulation δJ of the Josephson coupling, the coupling E_L, and the nearest-neighbor interaction E_{CC}.

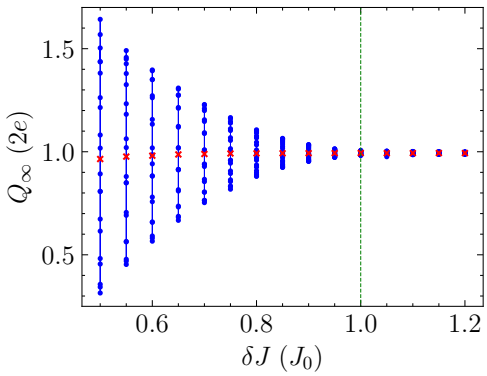

Figure 6: Pumped charge Q_∞ of the RM model for 20 discretized values of ϕ (blue points) as a function of the Josephson energy modulation δJ. The red crosses correspond to $\bar{Q}$. The phase dependence and the charge quantization considerably improve approaching the clipped modulation. The driving frequency is $\omega = 0.05 J_0$.

3.1 Role of the Josephson modulation

The amplitude δV_c of the cutter gate modulation and, consequently, the amplitude δJ in Eq. (12), determine the waveform of $E_{J,j}(t)$ (see the examples in Fig. 3). In this respect, the role of δJ is twofold: on one hand, it determines the minimum single-particle bulk gap $\epsilon_g = \min\left(|\vec{h}(t)|\right)$ over one period, which is given by $\min\left(\delta J, \frac{J_0+\delta J}{2}, 2\delta\mu\right)$. Consequently, δJ plays a major role in determining non-adiabatic corrections to the pumped charge quantization. On the other hand, δJ determines whether the chain dimerizes exactly during the driving protocol. Although this has no effect in the thermodynamic limit, as the topological nature of Thouless pumping makes it insensitive to such details, it becomes important for the short chains we consider in this work.

To estimate these effects, we consider the dependence of Q_∞ on δJ for different values of ϕ (Fig. 6) in an array with $M = 6$ islands. In the sinusoidal regime, where δJ is small, finite-size effects induce a large dispersion of Q_∞ as a function of ϕ, and averaging over the phase is fundamental to obtain the charge quantization. The dispersion rapidly decreases by increasing δJ, until the variation of $Q_\infty(\phi)$ drops below 0.8% when $\delta J \geq J_0$. The weak dependence of $\bar{Q}$ (red crosses) on δJ, instead, originates from non-adiabatic corrections. These are suppressed with δJ since the band gap ϵ_g increases accordingly, bringing the system deeper into the adiabatic regime without changing the driving frequency. In particular, the residual nonadiabatic and finite-size corrections of $\bar{Q}$ are less than 0.6% for $\omega = 0.05 J_0$ in the clipped regime.

This dependence on the Josephson energy modulation can be understood by comparing the behavior of populated Floquet many-body states as a function of ϕ for $\delta J = 0.5 J_0$ (sinusoidal waveform) and $\delta J = 1.2 J_0$ (clipped waveform). They are shown in the left and right panels of Fig. 7, respectively, where we plot the Floquet quasienergies as a function of the phase ϕ, using the corresponding occupation number $\mathcal{N}_\nu$ to set the color of each data point. In both cases, a single low-energy Floquet state $|\Phi_0(\tau)\rangle$ has an almost perfect overlap with the initial ground state, allowing us to follow the winding of $\mathcal{E}_0$ around the Floquet-Brillouin zone and confirming the quantization of $\bar{Q}$, which follows from Eq. (19). In the sinusoidal regime, $\mathcal{E}_0$ is, in general, far from linear in ϕ, leading to a strong dependence of $Q_\infty(\phi)$ on this phase. In the clipped regime, instead, the derivative $\partial_\phi \mathcal{E}_0$ of the most populated state is practically constant,

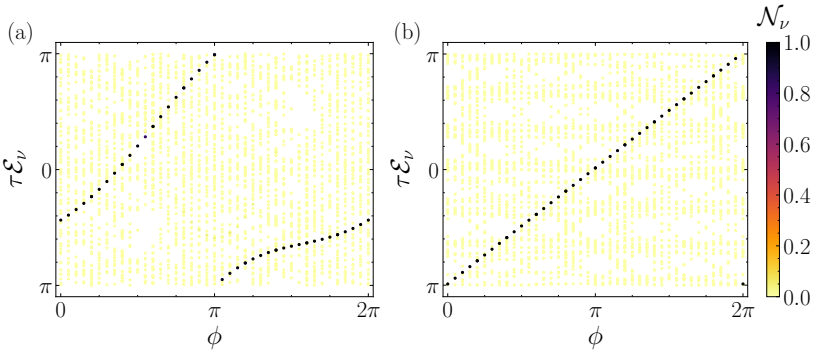

Figure 7: Comparison of the many-body Floquet eigenenergies of the RM model for (a) small sinusoidal modulations $\delta J = 0.5J_0$ (b) and clipped modulation $\delta J = 1.2J_0$ of the Josephson tunnelings. The dot colors represent the overlap $\mathcal{N}_\nu(\phi)$ of the initial ground state with the Floquet states. In the clipped regime $\partial_\phi \mathcal{E}_0$ is almost constant, leading to a pumped charge almost independent on the phase. The data refer to a system with $M = 6$ islands, $\omega = 0.05J_0$, and $E_L = 2J_0$.

and, for the chosen value of ω, $\mathcal{N}_0 \sim 1 - O(\omega^2/E_g^2)$ for all values of ϕ. We conclude that even with small systems ($M = 6$), the phase dependence is very weak in the clipped regime, and a good quantization can be observed without averaging over the SC phase difference.

3.2 Coupling with the leads

Besides the dependence of the pumped charge on the external phase ϕ, it is important to investigate the role of the coupling E_L between the edge islands and the superconducting leads. When E_L dominates over the other energy scales, the first and last islands are effectively merged with the two external leads and, in practice, the system behaves as a shorter chain. If instead E_L is weak compared to J_0, the transport of CPs across the system is hindered, as the pumped current is faster than the rate of charge transferring to or from the leads. Consequently, the system behaves as an open chain. To examine the interpolation between these two limits, it is instructive to consider the behavior of the system for a clipped modulation $\delta J > J_0$. In this situation, the onsite potentials $\mu_{A/B}$ and $E_{J,1}$ vanish in the middle of the pumping period, $t = (n + 1/2)\tau$. Therefore, the ground state of the Hamiltonian $\hat{H}_{RM}(\tau/2)$ corresponds to the extreme topological dimerized state of the Su-Schrieffer-Heeger (SSH) model, and it displays the typical four-fold degeneracy associated with localized zero-energy boundary modes. The boundary Hamiltonian $\hat{H}_b$, however, gaps the SSH edges; the ground states of the first and last islands in this dimerized limit result

$$\left|\psi_{1/M}(\tau/2)\right\rangle = \frac{1}{\sqrt{2}}\left(\left|\hat{N}_{1/M} = 0\right\rangle + e^{i\varphi_{L/R}}\left|\hat{N}_{1/M} = 1\right\rangle\right) \tag{23}$$

and are separated by an energy gap E_L from the localized excited states in the same islands. Therefore, when $E_L < \frac{J_0+\delta J}{2}, 2\delta\mu$, it sets the many-body energy gap E_g. Notably, the limit $E_L \to 0$ corresponds to the isolated RM chain in which the zero-energy SSH edge modes cause transitions between the two energy bands, thereby disrupting the Thouless pumping. Only when E_L is sufficiently larger than ω, this non-adiabatic effect vanishes and the quantized pumping can be restored.

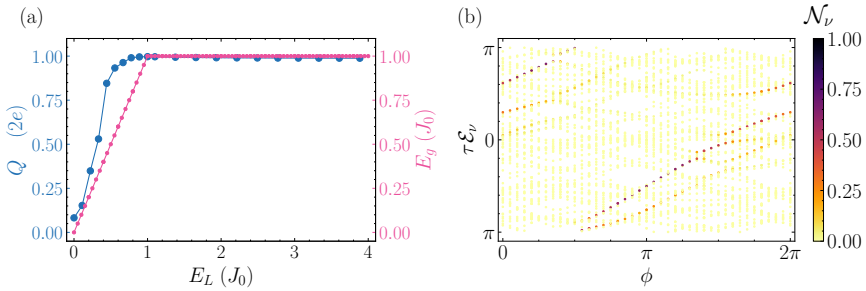

Figure 8: (a) Pumped charge $Q_\infty(\phi = 0)$ and many-body energy gap E_g as a function of E_L for $\delta J = J_0$ (threshold between clipped and sinusoidal modulations). The data are obtained in a system with parameters $\delta\mu = 1.5J_0$, $\omega = 0.05J_0$, and $M = 6$. (b) The many-body Floquet eigenenergies of the Rice-Mele model for $\delta J = J_0$ and $E_L = 0.5J_0$. In this situation, multiple Floquet states overlap significantly with the initial ground state resulting in a non-quantized current. Data are obtained for 6 islands and a driving frequency of $\omega = 0.05J_0$.

Fig. 8(a) displays the pumped charge $Q_\infty(\phi = 0)$ and the many-body gap E_g as a function of E_L/J_0 for a modulation $\delta J = J_0$ and a driving frequency $\omega = 0.05J_0$. The two quantities are clearly correlated; Q_∞ saturates to the quantized value as the gap induced by the coupling with the leads becomes sufficiently large. As expected, E_g eventually saturates as well at the value $E_g = J_0$, when $E_L \geq J_0$. In the case of sinusoidal modulation, instead, the dimerized SSH limit is never reached during the driving period. Therefore the many-body gap saturates at smaller values for large E_L/J_0.

The region $0 < E_L < J_0$ is the most susceptible to non-adiabatic errors since the ratio between the many-body gap and the driving frequency changes continuously between 0 and J_0/ω. Hence, we expect the pumped charge to saturate faster to $Q_\infty = 2e$ for smaller values of ω. In the adiabatic limit $\omega \to 0$, a finite gap opens for any value of $E_L > 0$, leading to the quantization of Q_∞. However, in a realistic scenario, the driving frequency is finite and sets the average magnitude of the current flowing through the array. Thus, E_L needs to be large enough to prevent the CPs from accumulating on one side of the chain, similar to what happens in an open system, suppressing the charge pumping. In the Floquet framework, this can be understood by observing the winding of the quasienergies associated with Floquet states with the highest occupation. When the charge is quantized and the driving is sufficiently slow, there is a clear correspondence between Floquet states and energy eigenstates, leading to an almost perfect fidelity $\mathcal{N}_0 \simeq 1$, for any value of the phase difference ϕ. Instead, when $E_L < J_0$, there are multiple Floquet states that display a large overlap with the initial ground state, as shown in Fig. 8(b), which might interfere destructively. Moreover, large avoided crossings appear in the spectrum as ϕ changes, further suppressing quantized transport.

We conclude that, in order to avoid additional non-adiabatic corrections to the pumped charge, E_L must be larger than the single-particle band gap of the chain.

3.3 Nearest-neighbor interactions

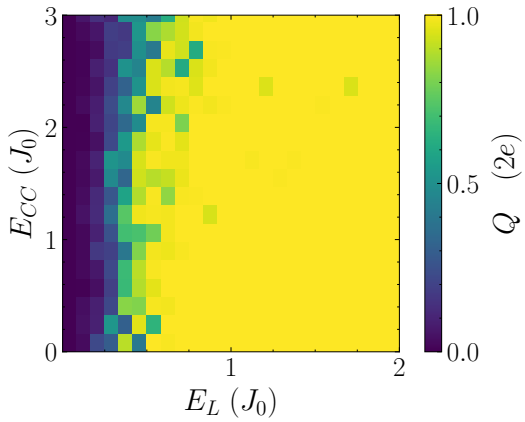

Figure 9: Pumped charge $Q_\infty(\phi = 0)$ as a function of the coupling with the leads E_L and the nearest neighbor interactions E_{CC} for the RM model with 6 islands. The data are obtained with $\delta J = J_0$, $\omega = 0.05 J_0$ and $\delta\mu = 1.5 J_0$.

Differently from the most common trapped ultracold atom systems [23], JJAs can be characterized by sizeable nearest-neighbor interactions. These interactions are bounded by $E_{CC} < E_C$, however, in the hardcore limit, they can be highly relevant because nothing prevents E_{CC} from being of the same order of J_0 or the single-particle gap. For hardcore bosons, the nearest-neighbor interaction reads:

$$\hat{H}_{\text{int}}(t) = E_{CC} \sum_{j=1}^{M-1} \left(\hat{b}_j^\dagger \hat{b}_j - n_{g,j}(t)\right)\left(\hat{b}_{j+1}^\dagger \hat{b}_{j+1} - n_{g,j+1}(t)\right). \tag{24}$$

$\hat{H}_{\text{int}}$ has two effects on the chain: a static repulsion, $E_{CC}\hat{b}_{j+1}^\dagger \hat{b}_j^\dagger \hat{b}_{j+1}\hat{b}_j$, and a shift in the chemical potential, $-E_{CC}(n_{g,j-1} + n_{g,j+1})$, due to the charge of the neighboring islands.

In Fig. 9 we plot the pumped charge $Q_\infty(\phi = 0)$ at the onset of the clipped regime ($\delta J = J_0$), as a function of both E_L and E_{CC}. Q_∞ is remarkably stable against the nearest neighbor interactions and there is a wide region of the phase diagram where the pumped charge is quantized. The role of E_{CC} seems indeed to be negligible for the Rice-Mele pumping: although the Hamiltonian $H_{RM,\text{tot}}$ does not conserve the CP number, its many-body ground states are in good approximation half-filled states where CPs are localized on every other SC island for most of the driving protocol. Therefore, the role of the interaction is marginal. For realistic ranges of E_{CC}, our simulations indicate that the nearest-neighbor interactions do not cause any topological phase transition in the effective 2D Floquet topological insulating state that determines the onset of the quantization of the pumped charge.

4 Results of the Harper-Hofstadter model

The HH model contains two main differences from the RM model. First, its implementation does not require modulation of the tunneling amplitudes but only of the induced charges. This

makes it more suitable for experimental implementations but, at the same time, more susceptible to finite-size effects since this protocol does not rely on any dimerization. Second, when the Aharonov-Bohm phase Φ is set to $2\pi/3$, the model displays two insulating phases with opposite Chern numbers and filling $1/3$ and $2/3$.[1] This implies that by varying the parameter $\bar{\mu}$ in Eq. (13), it is possible to invert the direction of the pumped charge. The two insulating states correspond to intervals in $\bar{\mu}$ with bounds approximately given by the band gaps. These states are separated by a gapless phase in which pumping is not quantized. In addition, since the topological insulating Floquet states of the HH model appear at fillings $1/3$ and $2/3$, the role of nearest-neighbor interaction is less trivial than in the RM model where interactions favor, to a certain extent, the dimerization characterizing the half-filled topological state. In the hardcore boson limit, however, a more careful analysis shows that the two insulating phases of the HH model are related by a particle-hole-like symmetry which is fulfilled also in the presence of the nearest-neighbor interaction in Eq. (24). This symmetry is defined by

$$\hat{b}_r \to \hat{b}_r^\dagger , \tag{25}$$

$$n_{g,j} \to 1 - n_{g,j} . \tag{26}$$

The second equation corresponds to the mapping $\mu_{0,j} \to -\mu_{0,j}$ and $t \to t+\tau/2$. This symmetry relates states with complementary fillings and implies that the pumped charge changes sign when reflecting $n_{g,j}$ around $\frac{1}{2}$. In particular, this holds for any value E_{CC}, implying that the effect of the interaction is insensitive to the average charge density. To control the filling factor and, therefore, the direction of the current, we tune the offset of the chemical potential $\bar{\mu}$ through the average value of the induced charge during one driving period:

$$\bar{n}_g = C^g V_0 = \frac{1}{2} - \frac{\bar{\mu}}{2E_C} . \tag{27}$$

Here we consider, for simplicity, uniform C^g and V_0 across the chain.

To investigate the stability of Thouless pumping in the presence of interactions, we consider the dynamics dictated by the Hamiltonian

$$\hat{H}_{HH,\mathrm{tot}}(t,\phi) = \hat{H}_{HH}(t) + \hat{H}_b(\phi) + \hat{H}_{\mathrm{int}}(t) , \tag{28}$$

defined by the Hamiltonians in Eqs. (13), (15) and (24) with the drive obtained by a modulation of the induced charge with position-dependent phases $\chi_j = 2\pi j/3$. We calculate the charge using Eq. (21): the system is initialized in the ground state of the Hamiltonian in Eq. (28) at $t = 0$ and the time dependence of the Floquet states is computed by solving numerically the Schrödinger equation.

We first examine the pumping for values of $\bar{\mu}$ where the system lies deep in one of the Floquet topological insulator phases. Fig. 10 shows the behavior of $\bar{Q}$ as a function of the lead coupling E_L for different values of the nearest-neighbor interactions, up to half the charging energy, $E_{CC} < E_C/2 = 2E_J$. The behavior is qualitatively analogous to that observed for the RM pumping with clipped modulation (compare Fig. 8(a) and Fig. 10): a good quantization of $\bar{Q}$ is achieved for sufficiently strong $E_L \gtrsim 0.4E_J$. Importantly, even strong interactions ($E_{CC} = 1.9E_J$ in the data) do not significantly alter the behavior of the pumped charge, which appears remarkably stable.

We emphasize that for the HH model, averaging over the phase difference ϕ is necessary to obtain the predicted quantization of the pumped charge since we consider small system sizes ($M = 6, 9$). This is caused by the winding of the eigenenergies of the populated Floquet states, displayed in Fig. 11. For the most occupied state at filling $1/3$ [panel (a)] the quasienergy

[1] The appearance of topological bands with nonzero Chern numbers is not limited to $\Phi = 2\pi/3$ but holds for any rational value of the flux $\Phi = 2\pi p/q$, with $p, q \in \mathbb{N}$, which results in up to q non-overlapping bands.

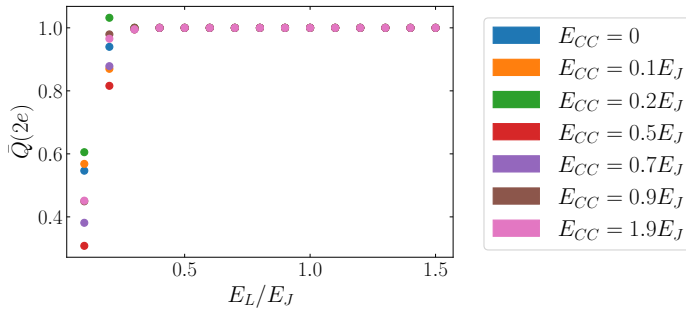

Figure 10: Pumped charge $\bar{Q}$ as a function of the coupling with the leads E_L for different values of the nearest-neighbor interaction. The data are obtained with parameters $M = 6$, $E_C = 4E_J$, $\delta\mu = E_J$, and $\omega = 0.01E_J$, in the gapped topological phase at filling $1/3$.

winds three times in the positive direction and twice in the negative direction, resulting in a total winding number +1. Panel (b) in Fig. 11 shows instead the opposite winding for the gapped phase at filling $2/3$, corresponding to pumping in the opposite direction. In both cases, the current $\partial_\phi \mathcal{E}(\phi)$ strongly depends on ϕ and even changes sign (see Fig. 12(a) for the state at filling $1/3$). Therefore, a quantized pumping can be obtained only by averaging over ϕ. This is a characteristic of small-size systems. By comparing the results for $M = 6$ and $M = 9$ in Fig. 12(a) we see that the phase dependence considerably decreases with the chain length. However, in general, the HH model is considerably more influenced by finite-size effects than the RM model in the clipped regime (see Fig. 5 for comparison).

In an experimental setup, control over the voltage offset V_0 of the side gates provides a possibility of interpolating between the two gapped phases and exploring the phase diagram of the system as a function of $\bar{\mu}$ (Fig. 12(b)): our results clearly show the appearance of the two topological Floquet phases with quantized charge $\bar{Q} = \pm 1 \cdot 2e$ both without interactions, $E_{CC} = 0$, and for strong interactions, $E_{CC} = E_J/2$. A large value of E_{CC} seems indeed to be beneficial for the stability of the topological phases, as it increases the width of the plateaus where the pumped charge is quantized.

In the data of Fig. 12(b), the symmetry in Eqs. (25) and (26) is not exactly reflected. The discrepancy results from the fact that the initial time of the pumping protocol is the same for all values of $\bar{\mu}$. The missing translation $t \to t + \tau/2$ violates the requirement (26), but the effect is only seen when $\bar{\mu}$ is close to the band extrema and the initial conditions strongly affect the pumping outcome. This strong dependence is shown explicitly in the inset of Fig. 12(b), where $\bar{Q}$ fluctuates with $\bar{n}_g$ around the transition between the gapless metallic states ($\bar{n}_g \lesssim 0.35$) and the Floquet topological insulator, ($\bar{n}_g \gtrsim 0.35$). Indeed, when $\bar{\mu}$ lies close to a topological band edge, a small change in the SC phase difference ϕ can change the initial state between being either metallic or insulating. Consequently, $Q_\infty(\phi)$ has discontinuities in ϕ and its phase average $\bar{Q}$ strongly depends on the driving frequency, the precise sampling of ϕ, and the system size, which is reflected in the single-particle level spacing within the bands.

We show this irregular behavior in Fig. 12(a), where we plot the infinite-time-averaged pumped charge Q_∞ as a function of the SC phase ϕ. A comparison of the data obtained at the edge ($\bar{n}_g = 0.35$, orange triangles) and inside ($\bar{n}_g = 0.4$, teal circles) the topological phase clearly shows the different role of ϕ in the two cases. While the amplitude of the variation of Q_∞ is the same, in the topological phase the pumped charge has a smooth dependence on ϕ and it oscillates around the quantized value $\bar{Q} = 1$ marked by the horizontal dashed line.

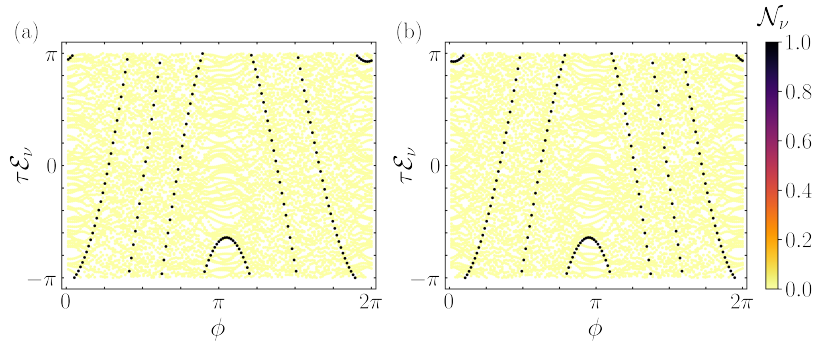

Figure 11: Winding of the quasienergies of the many-body populated state as a function of the lead phase difference ϕ. (a) Winding in the gapped phase at filling $1/3$ ($\bar{n}_g = 0.4$). We observe that the quasienergy winds three times in the positive direction and twice in the negative direction, corresponding to a Chern number $C_1 = 1$ of the lowest band. (b) Winding in the phase at filling $2/3$ ($\bar{n}_g = 0.6$). The winding is opposite with respect to panel (a).

On the edge between the metallic and the insulating phase, on the other hand, Q_∞ has many discontinuities that are reflected in the fluctuations of $\bar{Q}$ in the inset of panel (a).

5 Experimental implementation of the pumping schemes

The analysis presented in the previous sections and the observation of a quantized Thouless pumping rely on several constraints, important in devising an experimental realization of the presented models.

The most fundamental parameter in both driving protocols is the frequency Ω. On one side, Ω determines the ideal pumped current $I = 2e\Omega\mathcal{C}$; therefore, in order to obtain clearly measurable currents ($I \gtrsim 10$pA), we require $\Omega \gtrsim 300$MHz. On the other, the frequency determines the onset of nonadiabatic errors, typically scaling as $(h\Omega/E_g)^2$. Therefore Ω must be sufficiently small compared to the many-body gaps E_g, although the presence of dissipation might mitigate this requirement by suppressing some of the nonadiabatic corrections [56]. For both the RM model with clipped modulation and the HH model at $\Phi = 2\pi/3$, the gap is given by the minimum between $2\delta\mu$ and a Josephson term proportional to E_J (for sufficiently large E_L). $\delta\mu$ is proportional to E_C, and to enter the regime of quantized pumping it is necessary that $E_C \gtrsim E_J$. E_J can be tuned more easily than E_C, for example by applying a suitable voltage to a global gate as in the devices analyzed in Ref. [10]. Therefore, we consider the charging energy as the limiting factor in determining the gap which, for small superconducting islands, is approximately of the order of $h30$ GHz [47]. This poses an upper limit to the frequency, $\Omega \lesssim 10$ GHz, to avoid excessive nonadiabatic errors. The frequency range $\Omega \in (300\,\text{MHz}, 10\,\text{GHz})$ of the voltage drive of the electrostatic gates can be explored with standard waveform generators.

The RM model has the disadvantage of requiring modulation of both the induced charges and the Josephson couplings. This can be particularly challenging as the cutter gates controlling the Josephson energies may additionally induce charge on the neighboring islands. Such an effect can, however, be compensated with suitable corrections of the voltages V_g of the side gates. At the same time, the RM model displays, for $M = 6$ islands, smaller finite-size effects

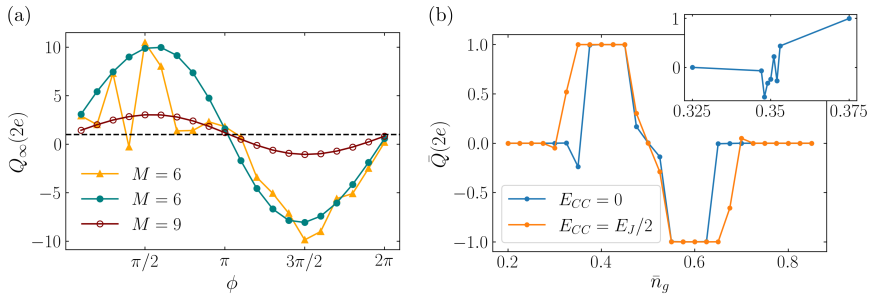

Figure 12: Pumped charge in the hardcore boson HH model. (a) Dependence of the pumped charge on the phase difference ϕ for chains of $M = 6$ and $M = 9$ islands around the transition $\bar{n}_g = 0.35$ (orange) and in the topological insulating phase $\bar{n}_g = 0.4$ (teal and maroon). (b) Averaged pumped charge $\bar{Q}$ for $M = 6$ islands. The blue curve corresponds to vanishing nearest-neighbor interactions. The orange curve is obtained for $E_{CC} = E_J/2$. Interactions extend the Floquet topological phases. Inset: fluctuations of $\bar{Q}$ close to the transition between the metallic and the topological insulating phases for $E_{CC} = 0$.

than the HH model, and, in particular, does not show a strong dependence of the pumped charge Q_∞ on the lead phase ϕ, especially in the clipped regime. For the same number of superconducting islands, the HH model requires control of only half of the electrostatic gates but displays instead a very strong dependence on the phase ϕ for $M = 6$ [Fig. 12(a)]. To avoid this limitation, two strategies can be envisioned: either implementing the pumping in longer chains, or embedding the system in a device that allows for averaging in time over the phase ϕ, similar to the proposals of Refs. [50, 57].

Concerning the scalability of the HH model at flux $2\pi/q$, only q independent voltage signals are needed for SC chains sufficiently uniform, such that the capacitances C_j^g and charging energies present only minor variations along the system. These q signals need then to be distributed across suitable gate structures.

Regarding the averaging over the phase ϕ, several options can be envisioned. The first possibility is based on introducing a suitable voltage bias V_b between the two external SC leads (see Ref. [50]). This yields a linear winding of the phase ϕ with period $\tau_\phi = h/2eV_b$. The number of pumped CPs in this period is given by $Q(\tau_\phi) = \mathcal{C}\Omega\tau_\phi$, and the average over the phase ϕ is suitably implemented if $\Omega\tau_\phi \gg 1$. An alternative method would require instead to embed the HH Josephson junction chain in a superconducting ring, in order to impose a phase bias ϕ that can be varied in time through a driven magnetic flux.

In our analysis of short Josephson junction chains, we did not consider explicitly the role of disorder. For both the RM Hamiltonian (9) and the HH Hamiltonian (13), the onsite disorder corresponds to a position dependence of the time-independent part of μ_j in Eq. (8). This can be caused by non-uniform capacitances C_j^g and a failure in balancing them with the voltages $V_{0,j}$. The effect of this kind of disorder on Thouless pumping has been extensively studied (see, for instance, Refs. [34–37]); in general, the quantization of the pumped charge is robust as long as the random variations of the onsite potential are weaker than the energy gap. In Coulomb-blockaded JJAs, the disorder amplitude of the onsite energy depends on the variance of $E_C\bar{n}_g$, whereas the energy gaps are determined by the Josephson energies. Therefore, to approach an accurate quantization of the pumped charge, we need to consider a balance between the following competing constraints.

On one side, the ratio E_C/E_J cannot be too large. Specifically, the standard deviation of the island-dependent $E_C\tilde{n}_g$ (where $\tilde{n}_g$ represents the targeted n_g average) must be considerably smaller than δJ and E_J in the RM and HH pumping schemes, respectively. Our calculations rely on the CP hardcore assumption $E_C \gg E_J$; however, numerical investigations [39] of the RM model with interactions of the form (2) reveal that the RM Floquet topological insulator phase survives even when the ratio $E_C/\delta J$ decreases to $E_C/\delta J \sim 3$ if $\delta\mu$ is sufficiently strong. Therefore, keeping a moderate value of $E_C/E_J \gtrsim 3$ may be beneficial to reduce onsite disorder and nonadiabatic effects. On the other side, the Josephson energies cannot exceed the threshold corresponding to the insulator-SC transition in the static case. Thouless pumping can indeed be realized only when the instantaneous energy spectrum of the system and the related ground states at each time t correspond to insulating phases.

A different kind of disorder characterizing JJAs are random variations in the Josephson energies and, in the RM model, differences in the functions $E_{J,j}(V_{c,j})$ associated with the junctions along the chain. Also in this case, the related disorder in the hopping terms of Eq. (6) becomes detrimental for an accurate quantization of Thouless pumping when the amplitude becomes comparable with the energy gaps of the systems.

Given the accuracy of the lithographic techniques adopted for the fabrication of hybrid JJAs, however, we expect the typical disorder amplitudes in the Josephson energies to be below 10% (see related experimental estimates in Ref. [58]). A disorder strength in this range is not harmful for the implementation of Thouless pumping as it is way below the necessary threshold to close the many-body gap and suppress quantized transport.

6 Conclusion

Motivated by recent advances in fabrication techniques, we numerically investigated possible driving protocols to implement topological Thouless pumping in short 1D arrays of tunable Josephson junctions. We considered the JJAs to be in a Coulomb-blockaded regime, where the charging energy of each SC island and the SC gap are the dominant energy scales, allowing us to approximate CPs as hardcore bosons. To study quantized transport in the long-time regime, we connected the array to two grounded SC leads, breaking the conservation of particle number. We used Floquet theory to extract the pumped charge at a small but finite driving frequency in the limit of an infinite number of driving cycles.

We focused on two prototypical models for topological quantum pumping, the periodically driven Rice-Mele and Harper-Hofstadter models. For both, we analyzed the role played by the coupling with the SC leads and their phase bias, as well as the effect of nearest-neighbor interactions originating from cross-capacitance between the SC islands. These ingredients are specific to the solid-state implementation of Thouless pumping with JJAs, and they extend the recent analyses of the role of interactions in Floquet topological insulators inspired by ultracold-atom experiments [23, 27, 39]. Furthermore, their understanding is essential for a successful experimental realization of topological quantized transport in hybrid SC-SM devices. Both models display remarkable robustness with respect to nearest-neighbor interaction which does not affect the transport properties, even when it becomes larger than the Josephson tunneling. Moreover, the coupling to the leads helps to stabilize transport as it gaps out the zero-energy edge modes, which would otherwise appear in an open chain, and allows for an adiabatic evolution at sufficiently low driving frequency.

In the RM model, finite-size effects are most easily suppressed in a clipped driving regime where the modulation of the Josephson coupling is tuned such that the SM substrate below the Josephson junctions is depleted at half periods, effectively dimerizing the chain. However, the implementation requires simultaneous tuning of both the Josephson couplings and the charge

induced on each island, resulting in a more complicated experimental protocol.

The HH model, on the other hand, requires fewer control gates as the Josephson couplings are constant in time. The drawback is that for small system sizes ($M = 6, 9$ islands) we find that it is necessary to dynamically average over the phase difference of the external leads to obtain a good quantization of the pumped charge. This behavior appears analogous to previous proposals to achieve quantized pumping in short Josephson junction chains [50]. However, even at constant phase bias, the discrepancies from the ideal quantized case rapidly decrease with the system size. Moreover, the HH model displays a richer topological phase diagram since the number of bands with nontrivial Chern number depends on the effective magnetic flux Φ which in turn is determined by the position-dependence of the on-site energy modulation. In the simplest scenario, where $\Phi = 2\pi/3$, the tuning of the average induced charge $\bar{n}_g$ on the SC islands allows for control of the chemical potential. Tuning this to lie in different band gaps leads to a quantized current flowing in different directions.

Our results suggest that quantized Thouless pumping is experimentally accessible with the recently developed SC-SM JJAs, paving the way for a new generation of experiments investigating topological transport in Floquet systems as an alternative to ultracold-atom approaches. However, there are several further effects worth investigating to improve our analysis. First, one could relax the hardcore boson approximation and allow for a standard onsite repulsion, which has been studied for the RM model with periodic boundaries [38–40, 59]. We expect that an intermediate ratio $E_C/E_J \gtrsim 3$ is beneficial for experimental realizations because it would mitigate the effects of disorder in the induced charges without driving the system away from its insulating phases. In this situation, our estimates indicate that driving frequencies $\Omega \gtrsim 300$MHz result in currents $I \gtrsim 10$pA without introducing excessive non-adiabatic effects. Another important element to consider is the possible presence of longer-range interactions. Indeed, the inverse of the capacitance matrix is approximately tri-diagonal only if the self-capacitance of the SC islands is much larger than their cross-capacitance. While this can be a reasonable approximation, depending on the geometry of the JJA, it is important to examine the pumping robustness when it breaks down. Far from being necessarily a problem, longer-range electrostatic interactions can be exploited to study the transport of fractions of CPs pumped at each cycle [57]. Finally, solid-state devices are subject to many decoherence channels, either due to quasiparticle poisoning, incoherent tunneling, charge noise, or scattering from crystal defects and imperfect interfaces. While precise modeling of these effects is prohibitive, an interesting future perspective is investigating the robustness of quantized transport with respect to simpler decoherence mechanisms, such as local dissipation or dephasing, similarly to Ref. [56], or incoherent coupling between the external (superconducting or normal) leads and the SC islands of the JJA.

Acknowledgements

We thank L. F. Banszerus, C. M. Marcus and S. Vaitiekėnas for useful discussions.

Funding information This project was supported by the Villum Foundation (Research Grant No. 25310) and received funding from the European Union's Horizon 2020 research and innovation program under the Marie Skłodowska-Curie Grant Agreement No. 847523 "INTERACTIONS."

References

[1] R. Fazio and H. van der Zant, *Quantum phase transitions and vortex dynamics in superconducting networks*, Physics Reports **355**(4), 235 (2001), doi:https://doi.org/10.1016/S0370-1573(01)00022-9.

[2] L. J. Geerligs, M. Peters, L. E. M. de Groot, A. Verbruggen and J. E. Mooij, *Charging effects and quantum coherence in regular Josephson junction arrays*, Phys. Rev. Lett. **63**, 326 (1989), doi:10.1103/PhysRevLett.63.326.

[3] H. Van Der Zant, L. Geerligs and J. Mooij, *Superconductor-to-insulator transitions in non and fully frustrated Josephson-junction arrays*, Europhysics Letters **19**(6), 541 (1992), doi:10.1209/0295-5075/19/6/017.

[4] C. D. Chen, P. Delsing, D. B. Haviland and T. Claeson, *Experimental investigation of two-dimensional arrays of ultrasmall Josephson junctions*, Physica Scripta **1992**(T42), 182 (1992), doi:10.1088/0031-8949/1992/T42/031.

[5] C. D. Chen, P. Delsing, D. B. Haviland, Y. Harada and T. Claeson, *Scaling behavior of the magnetic-field-tuned superconductor-insulator transition in two-dimensional Josephson-junction arrays*, Phys. Rev. B **51**, 15645 (1995), doi:10.1103/PhysRevB.51.15645.

[6] H. S. J. van der Zant, W. J. Elion, L. J. Geerligs and J. E. Mooij, *Quantum phase transitions in two dimensions: Experiments in Josephson-junction arrays*, Phys. Rev. B **54**, 10081 (1996), doi:10.1103/PhysRevB.54.10081.

[7] P. Krogstrup, N. L. B. Ziino, W. Chang, S. M. Albrecht, M. H. Madsen, E. Johnson, J. Nygård, C. M. Marcus and T. S. Jespersen, *Epitaxy of semiconductor–superconductor nanowires*, Nat. Mater. **14**, 400 (2015), doi:10.1038/nmat4176.

[8] J. Shabani, M. Kjaergaard, H. J. Suominen, Y. Kim, F. Nichele, K. Pakrouski, T. Stankevic, R. M. Lutchyn, P. Krogstrup, R. Feidenhans'l, S. Kraemer, C. Nayak *et al.*, *Two-dimensional epitaxial superconductor-semiconductor heterostructures: A platform for topological superconducting networks*, Phys. Rev. B **93**, 155402 (2016), doi:10.1103/PhysRevB.93.155402.

[9] L. Casparis, M. R. Connolly, M. Kjaergaard, N. J. Pearson, A. Kringhøj, T. W. Larsen, F. Kuemmeth, T. Wang, C. Thomas, S. Gronin, G. C. Gardner, M. J. Manfra *et al.*, *Superconducting gatemon qubit based on a proximitized two-dimensional electron gas*, Nature Nanotechnology **13**(10), 915 (2018), doi:10.1038/s41565-018-0207-y.

[10] C. G. L. Bøttcher, F. Nichele, M. Kjaergaard, H. J. Suominen, J. Shabani, C. J. Palmstrøm and C. M. Marcus, *Superconducting, insulating and anomalous metallic regimes in a gated two-dimensional semiconductor–superconductor array*, Nature Physics **14**(11), 1138 (2018), doi:10.1038/s41567-018-0259-9.

[11] C. G. L. Bøttcher, F. Nichele, J. Shabani, C. J. Palmstrøm and C. M. Marcus, *Dynamical vortex transitions in a gate-tunable josephson junction array*, doi:10.48550/arXiv.2212.08651 (2022), ArXiv:2212.08651.

[12] C. G. L. Bøttcher, F. Nichele, J. Shabani, C. J. Palmstrøm and C. M. Marcus, *The Berezinskii-Kosterlitz-Thouless transition and anomalous metallic phase in a hybrid Josephson junction array*, doi:10.48550/arXiv.2210.00318 (2022), ArXiv:2210.00318.

[13] G. Wang, T. Dvir, G. P. Mazur, C.-X. Liu, N. van Loo, S. L. D. ten Haaf, A. Bordin, S. Gazibegovic, G. Badawy, E. P. A. M. Bakkers, M. Wimmer and L. P. Kouwenhoven, *Singlet and triplet Cooper pair splitting in hybrid superconducting nanowires*, Nature **612**(7940), 448 (2022), doi:10.1038/s41586-022-05352-2.

[14] A. Danilenko, A. Pöschl, D. Sabonis, V. Vlachodimitropoulos, C. Thomas, M. J. Manfra and C. M. Marcus, *Spin-resolved spectroscopy using a quantum dot defined in InAs 2DEG*, doi:10.48550/arXiv.2212.10175 (2022), ArXiv:2212.10175.

[15] N. H. Lindner, G. Refael and V. Galitski, *Floquet topological insulator in semiconductor quantum wells*, Nature Physics **7**(6), 490 (2011), doi:doi.org/10.1038/nphys1926.

[16] M. C. Rechtsman, J. M. Zeuner, Y. Plotnik, Y. Lumer, D. Podolsky, F. Dreisow, S. Nolte, M. Segev and A. Szameit, *Photonic Floquet topological insulators*, Nature **496**(7444), 196 (2013), doi:10.1038/nature12066.

[17] J. Cayssol, B. Dóra, F. Simon and R. Moessner, *Floquet topological insulators*, Physica status solidi (RRL)-Rapid Research Letters **7**(1-2), 101 (2013).

[18] P. Titum, N. H. Lindner, M. C. Rechtsman and G. Refael, *Disorder-induced floquet topological insulators*, Phys. Rev. Lett. **114**, 056801 (2015), doi:10.1103/PhysRevLett.114.056801.

[19] I. Esin, M. S. Rudner, G. Refael and N. H. Lindner, *Quantized transport and steady states of floquet topological insulators*, Phys. Rev. B **97**, 245401 (2018), doi:10.1103/PhysRevB.97.245401.

[20] M. S. Rudner and N. H. Lindner, *Band structure engineering and non-equilibrium dynamics in Floquet topological insulators*, Nature reviews physics **2**(5), 229 (2020), doi:10.1038/s42254-020-0170-z.

[21] D. J. Thouless, *Quantization of particle transport*, Phys. Rev. B **27**, 6083 (1983), doi:10.1103/PhysRevB.27.6083.

[22] T. Kitagawa, E. Berg, M. Rudner and E. Demler, *Topological characterization of periodically driven quantum systems*, Phys. Rev. B **82**, 235114 (2010), doi:10.1103/PhysRevB.82.235114.

[23] R. Citro and M. Aidelsburger, *Thouless pumping and topology*, Nature Reviews Physics **5**(2), 87 (2023), doi:10.1038/s42254-022-00545-0.

[24] S. Nakajima, T. Tomita, S. Taie, T. Ichinose, H. Ozawa, L. Wang, M. Troyer and Y. Takahashi, *Topological Thouless pumping of ultracold fermions*, Nat. Phys. **12**, 296 (2016), doi:10.1038/nphys3622.

[25] M. Lohse, C. Schweizer, O. Zilberberg, M. Aidelsburger and I. Bloch, *A Thouless quantum pump with ultracold bosonic atoms in an optical superlattice*, Nat. Phys. **12**(4), 350 (2016), doi:10.1038/nphys3584.

[26] M. Lohse, C. Schweizer, H. M. Price, O. Zilberberg and I. Bloch, *Exploring 4D quantum Hall physics with a 2D topological charge pump*, Nature **553**, 55 (2018), doi:10.1038/nature25000.

[27] A.-S. Walter, Z. Zhu, M. Gächter, J. Minguzzi, S. Roschinski, K. Sandholzer, K. Viebahn and T. Esslinger, *Quantisation and its breakdown in a Hubbard-Thouless pump*, doi:10.48550/arXiv.2204.06561 (2022), ArXiv:2204.06561.

[28] A. Cerjan, M. Wang, S. Huang, K. P. Chen and M. C. Rechtsman, *Thouless pumping in disordered photonic systems*, Light Sci. Appl. **9**(178), 1 (2020), doi:10.1038/s41377-020-00408-2.

[29] I. H. Grinberg, M. Lin, C. Harris, W. A. Benalcazar, C. W. Peterson, T. L. Hughes and G. Bahl, *Robust temporal pumping in a magneto-mechanical topological insulator*, Nat. Commun. **11**(974), 1 (2020), doi:10.1038/s41467-020-14804-0.

[30] Z.-C. Xiang, K. Huang, Y.-R. Zhang, T. Liu, Y.-H. Shi, C.-L. Deng, T. Liu, H. Li, G.-H. Liang, Z.-Y. Mei, H. Yu, G. Xue *et al.*, *Simulating quantum Hall effects on a superconducting quantum processor*, doi:10.48550/arXiv.2207.11797 (2022), ArXiv:2207.11797.

[31] M. W. Keller, J. M. Martinis, N. M. Zimmerman and A. H. Steinbach, *Accuracy of electron counting using a 7-junction electron pump*, Applied Physics Letters **69**(12), 1804 (1996), doi:10.1063/1.117492.

[32] M. Möttönen, J. J. Vartiainen and J. P. Pekola, *Experimental determination of the Berry phase in a superconducting charge pump*, Phys. Rev. Lett. **100**, 177201 (2008), doi:10.1103/PhysRevLett.100.177201.

[33] J. J. Vartiainen, M. Möttönen, J. P. Pekola and A. Kemppinen, *Nanoampere pumping of Cooper pairs*, Appl. Phys. Lett. **90**(8) (2007), doi:10.1063/1.2709967.

[34] Q. Niu and D. Thouless, *Quantised adiabatic charge transport in the presence of substrate disorder and many-body interaction*, J. Phys. A-Math. Gen. **17**(12), 2453 (1984), doi:10.1088/0305-4470/17/12/016.

[35] M. M. Wauters, A. Russomanno, R. Citro, G. E. Santoro and L. Privitera, *Localization, topology, and quantized transport in disordered floquet systems*, Phys. Rev. Lett. **123**, 266601 (2019), doi:10.1103/PhysRevLett.123.266601.

[36] A. L. C. Hayward, E. Bertok, U. Schneider and F. Heidrich-Meisner, *Effect of disorder on topological charge pumping in the Rice-Mele model*, Phys. Rev. A **103**, 043310 (2021), doi:10.1103/PhysRevA.103.043310.

[37] R. Wang and Z. Song, *Robustness of the pumping charge to dynamic disorder*, Phys. Rev. B **100**, 184304 (2019), doi:10.1103/PhysRevB.100.184304.

[38] N. H. Lindner, E. Berg and M. S. Rudner, *Universal chiral quasisteady states in periodically driven many-body systems*, Phys. Rev. X **7**, 011018 (2017), doi:10.1103/PhysRevX.7.011018.

[39] A. Hayward, C. Schweizer, M. Lohse, M. Aidelsburger and F. Heidrich-Meisner, *Topological charge pumping in the interacting bosonic Rice-Mele model*, Phys. Rev. B **98**, 245148 (2018), doi:10.1103/PhysRevB.98.245148.

[40] R. Gawatz, A. C. Balram, E. Berg, N. H. Lindner and M. S. Rudner, *Prethermalization and entanglement dynamics in interacting topological pumps*, Phys. Rev. B **105**, 195118 (2022), doi:10.1103/PhysRevB.105.195118.

[41] M. J. Rice and E. J. Mele, *Elementary excitations of a linearly conjugated diatomic polymer*, Phys. Rev. Lett. **49**, 1455 (1982), doi:10.1103/PhysRevLett.49.1455.

[42] L. Privitera, A. Russomanno, R. Citro and G. E. Santoro, *Nonadiabatic breaking of topological pumping*, Phys. Rev. Lett. **120**, 106601 (2018), doi:10.1103/PhysRevLett.120.106601.

[43] D. R. Hofstadter, *Energy levels and wave functions of bloch electrons in rational and irrational magnetic fields*, Phys. Rev. B **14**, 2239 (1976), doi:10.1103/PhysRevB.14.2239.

[44] M. M. Wauters and G. E. Santoro, *Quantization of the Hall conductivity in the Harper-Hofstadter model*, Phys. Rev. B **98**, 205112 (2018), doi:10.1103/PhysRevB.98.205112.

[45] M. Kjaergaard, F. Nichele, H. J. Suominen, M. P. Nowak, M. Wimmer, A. R. Akhmerov, J. A. Folk, K. Flensberg, J. Shabani, C. J. Palmstrøm and C. M. Marcus, *Quantized conductance doubling and hard gap in a two-dimensional semiconductor–superconductor heterostructure*, Nat. Commun. **7**(12841), 1 (2016), doi:10.1038/ncomms12841.

[46] C. W. J. Beenakker, *Universal limit of critical-current fluctuations in mesoscopic Josephson junctions*, Phys. Rev. Lett. **67**, 3836 (1991), doi:10.1103/PhysRevLett.67.3836.

[47] E. C. T. O'Farrell, A. C. C. Drachmann, M. Hell, A. Fornieri, A. M. Whiticar, E. B. Hansen, S. Gronin, G. C. Gardner, C. Thomas, M. J. Manfra, K. Flensberg, C. M. Marcus *et al.*, *Hybridization of subgap states in one-dimensional superconductor-semiconductor coulomb islands*, Phys. Rev. Lett. **121**, 256803 (2018), doi:10.1103/PhysRevLett.121.256803.

[48] M. Kjaergaard, H. J. Suominen, M. P. Nowak, A. R. Akhmerov, J. Shabani, C. J. Palmstrøm, F. Nichele and C. M. Marcus, *Transparent semiconductor-superconductor interface and induced gap in an epitaxial heterostructure Josephson junction*, Phys. Rev. Appl. **7**, 034029 (2017), doi:10.1103/PhysRevApplied.7.034029.

[49] C. Ciaccia, R. Haller, A. C. C. Drachmann, T. Lindemann, M. J. Manfra, C. Schrade and C. Schönenberger, *Gate tunable josephson diode in proximitized inas supercurrent interferometers*, doi:10.48550/arXiv.2304.00484 (2023), ArXiv:2304.00484.

[50] P. A. Erdman, F. Taddei, J. T. Peltonen, R. Fazio and J. P. Pekola, *Fast and accurate Cooper pair pump*, Phys. Rev. B **100**, 235428 (2019), doi:10.1103/PhysRevB.100.235428.

[51] A. Russomanno, S. Pugnetti, V. Brosco and R. Fazio, *Floquet theory of Cooper pair pumping*, Phys. Rev. B **83**(21), 214508 (2011), doi:10.1103/PhysRevB.83.214508.

[52] M. M. Wauters, *Adiabatic approaches to non-equilibrium systems: Topology, optimization, and learning*, PhD Thesis, SISSA (2020).

[53] J. Johansson, P. Nation and F. Nori, *QuTiP: An open-source python framework for the dynamics of open quantum systems*, Computer Physics Communications **183**(8), 1760 (2012), doi:10.1016/j.cpc.2012.02.021.

[54] J. Johansson, P. Nation and F. Nori, *QuTiP 2: A python framework for the dynamics of open quantum systems*, Computer Physics Communications **184**(4), 1234 (2013), doi:10.1016/j.cpc.2012.11.019.

[55] H. Watanabe, *Insensitivity of bulk properties to the twisted boundary condition*, Phys. Rev. B **98**, 155137 (2018), doi:10.1103/PhysRevB.98.155137.

[56] L. Arceci, L. Kohn, A. Russomanno and G. E. Santoro, *Dissipation assisted Thouless pumping in the Rice–Mele model*, Journal of Statistical Mechanics: Theory and Experiment **2020**(4), 043101 (2020), doi:10.1088/1742-5468/ab7a25.

[57] H. Weisbrich, R. L. Klees, O. Zilberberg and W. Belzig, *Fractional transconductance via non-adiabatic topological Cooper pair pumping*, doi:10.48550/arXiv.2212.11757 (2023), ArXiv:2212.11757.

[58] R. Kuzmin, R. Mencia, N. Grabon, N. Mehta, Y.-H. Lin and V. E. Manucharyan, *Quantum electrodynamics of a superconductor–insulator phase transition*, Nature Physics **15**(9), 930 (2019), doi:10.1038/s41567-019-0553-1.

[59] T. Gulden, E. Berg, M. S. Rudner and N. H. Lindner, *Exponentially long lifetime of universal quasi-steady states in topological Floquet pumps*, SciPost Phys. **9**, 015 (2020), doi:10.21468/SciPostPhys.9.1.015.

5

Conclusion and outlook

The central idea and backbone of this thesis on parafermions (PF) is that for $\mathbb{Z}_6$ PFs, it is possible to separate their sixfold degree of freedom into a fermionic parity and a fractional part, allowing for transport spectroscopy with electrons that conserves and even reflects the fractional character. The suggested setups were heavily inspired by theoretical proposals [11, 12] and experimental results [20, 43] on the combination of superconductors and fractional quantum Hall (FQH) systems.

We argued that, unlike the Majorana fermions which are only described by the fermionic parity, the PFs retain a topologically protected charge under a current readout that, for the grounded two-terminal device considered in Sec. 2.1, in part distinguishes the ground states. This relies on a splitting of the PF energy levels set by the interaction strength and the phase ϕ in the PF Hamiltonian. A more detailed analysis could estimate how much this phase can deviate from the optimal value for a given PF interaction strength, coupling to the external lead and temperature. We proposed also a Coulomb-blockaded PF device that could provide complementary signatures of PFs – also through transport measurements. As a function of the induced charge in the superconducting island the zero-bias conductance displays patterns that depend on the induced pairing between the edge modes of the FQH system. For low temperatures we expect that this conductance will display six peaks repeating every $2e$ of the induced charge, and with stronger pairing of the edge modes this will evolve into an $e/3$-periodic pattern that reflects the non-trivial topology of the system. Both the grounded and floating PF devices rely on the ability to couple up to two metallic leads to the PFs while limiting the coupling to the SC by an insulating barrier, which could be challenging to construct.

After this we studied the grounded PF device in greater detail by characterising its dynamics. By the stochastic quantum jump method and the introduction of jump operators, we were able to numerically calculate trajectories of the state evolution as well as the current through the external lead. We saw how a current measurement becomes a projective measurement of the fractional part of the $\mathbb{Z}_6$ PFs and were able to estimate the projection time into the charge sectors. We found that this time was very sensitive to the initial state of the system. We included noise in both numerical and analytical calculations which indicated that the three fractional sectors can be distinguished by current measurements. One could use the same stochastic method to study more general noise effects such as drifting of the physical parameters.

We then extended the formalism to include also jump operators describing a coupling to a bath of fractional quasiparticles. That way we were able to quantify the effect of poisoning, and we considered the external edges of the FQH system to be the source of $-e/3$ charges changing the otherwise protected charge of the PFs. For a weak poisoning rate with respect to the current measurement rate, we found that the jumps of fractional charges in and out of the PF system would show themselves in a three-level telegraph noise in the current. Furthermore, by tuning the voltage bias of the external lead, it is possible to shift the telegraph noise between being three- or two-level.

In order to examine also coherent poisoning sources we modelled an antidot in the bulk of the FQH liquid. We considered the antidot to be small and thus effectively described as a two-level system which would give rise to a two-level telegraph noise in a current readout when coupled weakly to the PFs. We argued that additional signatures of PFs could be obtained by deliberately creating a tunable antidot near the PFs and use this as a manipulation tool to have controlled transitions between the three fractional charge states of the PFs. Furthermore, by tuning the size of the antidot, this type of poisoning as well could lead to both a two-level and three-level current telegraph noise. For both types of poisoning sources we identified conditions on the couplings to the external lead and the poisoning sources as well as on the temperature for the observation of the discussed phenomena. A more rigorous statistical analysis could provider better quantitative

limits on the noise that can be tolerated to still distinguish the three sectors and on the maximum strength of poisoning rates to see the current jumps. One would then also find the time required to say with confidence that the system is in a certain charge sector.

Finally, we enlarged the system and considered four $\mathbb{Z}_6$ PFs and used the developed methods to propose and examine a quench protocol to test the associativity of the PF fusion rules. We obtained statistics of the associativity matrix for the $\mathbb{Z}_3$ degree of freedom of the PFs and proposed a physical device where PF couplings can be tuned in order to realise this protocol. The transmon construction could be challenged by the large magnetic field required for the FQH system, but with a material like niobium nitride, which according to Ref. [20] can sustain the large fields, it could possibly still be realised. Like for the two-PF device, we neglected the Lamb shift which may not be justified for the four PFs that have close-to-degenerate levels. A more rigorous analysis should include this effect.

The results of this thesis provide indications for future experiments on PFs and will hopefully contribute to the discussion and theories of PFs. Although the analyses are not straightforwardly extended to other modes such as e.g. $\mathbb{Z}_{10}$ PFs since we relied on the 'simple' FQH state with filling factor $\nu = 1/3$, the results could be generalised for example to include additional leads or quantum dots. Additionally, one could employ the developed methods in more complex devices to test the braiding properties of PFs.

A

Appendix A: Details of the introduction

In this appendix we show details of the mapping (Eq. (1.18)) between parafermions (PFs) and the clock operators:

$$\alpha_{2j-1} = \sigma_j \prod_{i<j} \tau_i, \qquad \alpha_{2j} = -\mathrm{e}^{i\frac{\pi}{N}} \tau_j \sigma_j \prod_{i<j} \tau_i \,. \tag{A.1}$$

With the above transformation, we can reproduce the PF properties listed in Sec. 1.1. First we show Eq. (1.1), that is $\alpha^N = \mathbb{1}$, exploiting the unitarity of the clock operators (Eq. (1.14)) and their commutation relations (Eq. (1.15)):

$$\alpha_{2j-1}^N = \sigma_j^N \prod_{i<j} \tau_i^N = \mathbb{1}\,, \qquad \left(\alpha_{2j-1}^\dagger\right)^N = \left(\prod_{i<j} \left(\tau_i^\dagger\right)^N\right) \left(\sigma_j^\dagger\right)^N = \mathbb{1}\,. \tag{A.2}$$

$$\begin{aligned} \alpha_{2j}^N &= (-1)^{N+1} (\underbrace{\tau_j\sigma_j}_{1} \tau_j\sigma_j \ldots \underbrace{\tau_j\sigma_j}_{N}) \prod_{i<j} \tau_i^N = (-1)^{N+1} \tau_j^N \sigma_j^N \left(\mathrm{e}^{i\frac{2\pi}{N}}\right)^{\sum_{n=1}^{N-1} n} \\ &= (-1)^{N+1} \left(\mathrm{e}^{i\frac{2\pi}{N}}\right)^{N(N-1)/2} = (-1)^{N+1} (-1)^{2N} = \mathbb{1}\,. \end{aligned} \tag{A.3}$$

$$\left(\alpha_{2j}^\dagger\right)^N = (-1)^{N+1} \left(\prod_{i<j} \left(\tau_i^\dagger\right)^N\right) (\underbrace{\sigma_j^\dagger\tau_j^\dagger}_{1} \sigma_j^\dagger\tau_j^\dagger \ldots \underbrace{\sigma_j^\dagger\tau_j^\dagger}_{N}) = (-1)^{N+1} \left(\mathrm{e}^{-i\frac{2\pi}{N}}\right)^{N(N-1)/2} = \mathbb{1}\,. \tag{A.4}$$

Next, we show the unitarity (Eq. (1.2)):

$$\begin{aligned} \alpha_{2j-1}^\dagger &= \left(\prod_{i<j} \tau_i^\dagger\right) \sigma_j^\dagger, \\ \alpha_{2j-1}^{N-1} &= \sigma_j^{N-1} \prod_{i<j} \tau_i^{N-1} = \sigma_j^\dagger \prod_{i<j} \tau_i^\dagger = \alpha_{2j-1}^\dagger \,. \end{aligned} \tag{A.5}$$

$$\begin{aligned} \alpha_{2j}^\dagger &= -\mathrm{e}^{-i\frac{\pi}{N}} \left(\prod_{i<j} \tau_i^\dagger\right) \sigma_j^\dagger \tau_j^\dagger, \\ \alpha_{2j}^{N-1} &= (-1)^{N-1} \mathrm{e}^{i\pi} \mathrm{e}^{-i\frac{\pi}{N}} (\underbrace{\tau_j\sigma_j}_{1} \ldots \underbrace{\tau_j\sigma_j}_{N-1}) \prod_{i<j} \tau_i^{N-1} = (-1)^N \mathrm{e}^{-i\frac{\pi}{N}} \sigma_j^{N-1} \tau_j^{N-1} \left(\mathrm{e}^{-i\frac{2\pi}{N}}\right)^{\sum_{n=1}^{N-1} n} \prod_{i<j} \tau_i^\dagger \\ &= (-1)^N \mathrm{e}^{-i\frac{\pi}{N}} \mathrm{e}^{-i\pi(N-1)} \sigma_j^\dagger \tau_j^\dagger \prod_{i<j} \tau_i^\dagger = -\mathrm{e}^{-i\frac{\pi}{N}} \sigma_j^\dagger \tau_j^\dagger \prod_{i<j} \tau_i^\dagger = \alpha_{2j}^\dagger \,. \end{aligned} \tag{A.6}$$

And finally, we show the PF commutation relation $\alpha_i\alpha_j = \alpha_j\alpha_i\,\mathrm{e}^{i\frac{2\pi}{N}\operatorname{sgn}(j-i)}$ from clock operators. We check for all three combinations of even and odd site PFs (here $\Theta(x)$ denotes the Heaviside step function):

$$\begin{aligned}\alpha_{2j-1}\alpha_{2k-1} &= \sigma_j\left(\prod_{i<j}\tau_i\right)\sigma_k\left(\prod_{l<k}\tau_l\right) = \sigma_k\sigma_j\left(\prod_{i<j}\tau_i\right)\left(\prod_{l<k}\tau_l\right)\mathrm{e}^{-i\frac{2\pi}{N}\Theta(j-k)}\\ &= \sigma_k\left(\prod_{l<k}\tau_l\right)\sigma_j\left(\prod_{i<j}\tau_i\right)\mathrm{e}^{-i\frac{2\pi}{N}\Theta(j-k)}\,\mathrm{e}^{i\frac{2\pi}{N}\Theta(k-j)} = \alpha_{2k-1}\alpha_{2j-1}\,\mathrm{e}^{i\frac{2\pi}{N}\operatorname{sgn}(k-j)}\,. \end{aligned} \tag{A.7}$$

$$\begin{aligned}\alpha_{2j-1}\alpha_{2k} &= \sigma_j\left(\prod_{i<j}\tau_i\right)\left(-\mathrm{e}^{i\frac{\pi}{N}}\right)\tau_k\sigma_k\left(\prod_{l<k}\tau_l\right) = -\mathrm{e}^{i\frac{\pi}{N}}\,\tau_k\sigma_j\left(\prod_{i<j}\tau_i\right)\sigma_k\left(\prod_{l<k}\tau_l\right)\mathrm{e}^{i\frac{2\pi}{N}\delta_{jk}}\\ &= -\mathrm{e}^{i\frac{\pi}{N}}\,\tau_k\sigma_k\left(\prod_{l<k}\tau_l\right)\sigma_j\left(\prod_{i<j}\tau_i\right)\mathrm{e}^{i\frac{2\pi}{N}\left(\delta_{jk}-\Theta(j-k)+\Theta(k-j)\right)} = \alpha_{2k}\alpha_{2j-1}\,\mathrm{e}^{i\frac{2\pi}{N}\delta_{jk}}\,\mathrm{e}^{i\frac{2\pi}{N}\operatorname{sgn}(k-j)}\,. \end{aligned} \tag{A.8}$$

$$\begin{aligned}\alpha_{2j}\alpha_{2k} &= \mathrm{e}^{i\frac{\pi}{N}}\,\tau_j\sigma_j\left(\prod_{i<j}\tau_i\right)\mathrm{e}^{i\frac{\pi}{N}}\,\tau_k\sigma_k\left(\prod_{l<k}\tau_l\right) = \mathrm{e}^{i\frac{\pi}{N}}\,\tau_k\tau_j\sigma_j\left(\prod_{i<j}\tau_i\right)\mathrm{e}^{i\frac{\pi}{N}}\,\sigma_k\left(\prod_{l<k}\tau_l\right)\mathrm{e}^{i\frac{2\pi}{N}\delta_{jk}}\\ &= \mathrm{e}^{i\frac{\pi}{N}}\,\tau_k\sigma_k\tau_j\sigma_j\left(\prod_{i<j}\tau_i\right)\mathrm{e}^{i\frac{\pi}{N}}\left(\prod_{l<k}\tau_l\right)\mathrm{e}^{i\frac{2\pi}{N}\delta_{jk}}\,\mathrm{e}^{-i\frac{2\pi}{N}\Theta(j-k)}\,\mathrm{e}^{-i\frac{2\pi}{N}\delta_{jk}}\\ &= \alpha_{2k}\alpha_{2j}\,\mathrm{e}^{i\frac{2\pi}{N}\operatorname{sgn}(k-j)}\,. \end{aligned} \tag{A.9}$$

The remaining properties follow from these.

With the transformation in Eq. (1.18), we show here how the quantum clock model Hamiltonian expressed in PF operators is mapped back to clock operators:

$$\begin{aligned}H_{\text{q.clock}} &= J\sum_{j=1}^{L-1}\left(\mathrm{e}^{i\frac{\pi}{N}}\,\alpha_{2j}^\dagger\alpha_{2j+1}+\text{H.c.}\right)+\mathcal{H}\sum_{j=1}^{L}\left(\mathrm{e}^{i\frac{\pi}{N}}\,\alpha_{2j-1}^\dagger\alpha_{2j}+\text{H.c.}\right)\\ &= -J\sum_{j=1}^{L-1}\left(\mathrm{e}^{i\frac{\pi}{N}}\,\mathrm{e}^{-i\frac{\pi}{N}}\left(\prod_{i<j}\tau_i^\dagger\right)\sigma_j^\dagger\tau_j^\dagger\sigma_{j+1}\left(\prod_{i<j+1}\tau_i\right)+\text{H.c.}\right)\\ &\quad -\mathcal{H}\sum_{j=1}^{L}\left(\mathrm{e}^{i\frac{\pi}{N}}\left(\prod_{i<j}\tau_i^\dagger\right)\sigma_j^\dagger\,\mathrm{e}^{i\frac{\pi}{N}}\,\tau_j\sigma_j\left(\prod_{i<j}\tau_i\right)+\text{H.c.}\right)\\ &= -J\sum_{j=1}^{L-1}\left(\sigma_j^\dagger\sigma_{j+1}\left(\prod_{i<j+1}\tau_i^\dagger\right)\left(\prod_{i<j+1}\tau_i\right)+\text{H.c.}\right)\\ &\quad -\mathcal{H}\sum_{j=1}^{L}\left(\mathrm{e}^{i\frac{2\pi}{N}}\,\sigma_j^\dagger\sigma_j\tau_j\,\mathrm{e}^{-i\frac{2\pi}{N}}\left(\prod_{i<j}\tau_i^\dagger\right)\left(\prod_{i<j}\tau_i\right)+\text{H.c.}\right)\\ &= -J\sum_{j=1}^{L-1}\left(\sigma_j^\dagger\sigma_{j+1}+\sigma_{j+1}^\dagger\sigma_j\right)-\mathcal{H}\sum_{j=1}^{L}\left(\tau_j+\tau_j^\dagger\right). \end{aligned} \tag{A.10}$$

B

Appendix B: Details of the readout of parafermionic states

Here we present details of a few calculations and equations from Ch. 2. First, we show explicitly how the reduced charge number operator $\tilde{q}$ can be expressed in terms of the operator $\hat{q}$ as stated in Eq. (2.4). Starting from Eq. (2.3) for the parafermion parity, we have

$$e^{i\frac{4\pi}{3}\tilde{q}} = -i\gamma_1\gamma_2 e^{i\frac{\pi}{3}\hat{q}} = -i\left(\alpha_1^\dagger\right)^3\left(\alpha_2^\dagger\right)^3 e^{i\frac{\pi}{6}}\alpha_1^\dagger\alpha_2 = -i\,e^{-i\frac{\pi}{3}}\left(\alpha_1^\dagger\right)^3\left(\alpha_2^\dagger\right)^2\alpha_1^\dagger e^{i\frac{\pi}{6}}\,. \tag{B.1}$$

In the second equality we used the rewriting $e^{-i\frac{\pi}{6}}\alpha_2^\dagger\alpha_1 = e^{-i\frac{\pi}{3}\hat{q}}$ from Eq. (1.13) and in the third equality the commutation relation of the parafermions and their unitarity (Eqs. (1.2) and (1.5)). Exploiting the same unitarity to write $(\alpha_i^\dagger)^n = (\alpha_i^{-1})^n = \alpha_i^{6-n}$ we obtain

$$\begin{aligned} e^{i\frac{4\pi}{3}\tilde{q}} &= -i\,e^{-i\frac{\pi}{3}}\left(e^{i\frac{2\pi}{3}}\right)^3\left(\alpha_2^\dagger\right)^2\left(\alpha_1^\dagger\right)^4 e^{i\frac{\pi}{6}} = -i\,e^{-i\frac{\pi}{3}}\left(\alpha_2^\dagger\right)^2(\alpha_1)^2 e^{i\frac{\pi}{6}} = -i\left(\alpha_2^\dagger\alpha_1\right)^2 e^{i\frac{\pi}{6}} \\ &= -i\left(e^{i\frac{\pi}{6}}e^{-i\frac{\pi}{3}\hat{q}}\right)^2 e^{i\frac{\pi}{6}} = e^{i\frac{2\pi}{3}\hat{q}}\,. \end{aligned} \tag{B.2}$$

Second, we calculate the zero-temperature differential conductance in Eq. (2.14) from the scattering matrix in Eq. (2.12). As defined in Eq. (2.10), the coupling matrix is

$$W = \frac{1}{2}\begin{pmatrix} W_{11} & W_{12} \\ W_{21} & W_{22}\end{pmatrix}, \qquad W_{11} = -W_{22}^* = i\eta_1 - \eta_2 e^{i\tilde{\chi}}, \quad W_{12} = -W_{21}^* = i\eta_1 - \eta_2 e^{-i\tilde{\chi}}\,. \tag{B.3}$$

Introducing $M^{-1} = E - H_{2\mathrm{pf}}^{\mathrm{BdG}}(\tilde{q}) + i\pi\nu_l WW^\dagger$, the scattering matrix is

$$S(E) = \mathbb{1} - i2\pi\nu_l W^\dagger M W = \begin{pmatrix} R_{ee} & R_{eh} \\ R_{he} & R_{hh}\end{pmatrix}. \tag{B.4}$$

Explicitly,

$$\begin{aligned} M &= \left(E - \begin{pmatrix}\Delta_\varepsilon(\tilde{q}) & 0 \\ 0 & -\Delta_\varepsilon(\tilde{q})\end{pmatrix} + \frac{i\pi\nu_l}{4}\begin{pmatrix}|W_{11}|^2+|W_{12}|^2 & -2W_{11}W_{12} \\ -2W_{11}^*W_{12}^* & |W_{11}|^2+|W_{12}|^2\end{pmatrix}\right)^{-1} \\ &= \left(E - \begin{pmatrix}\Delta_\varepsilon(\tilde{q}) & 0 \\ 0 & -\Delta_\varepsilon(\tilde{q})\end{pmatrix} + \frac{i\pi\nu_l}{2}\begin{pmatrix}\eta_1^2+\eta_2^2 & \eta_1^2-\eta_2^2+i2\eta_1\eta_2\cos(\tilde{\chi}) \\ \eta_1^2-\eta_2^2-i2\eta_1\eta_2\cos(\tilde{\chi}) & \eta_1^2+\eta_2^2\end{pmatrix}\right)^{-1} \\ &= \frac{1}{E^2-\Delta_\varepsilon^2(\tilde{q})+i\pi\nu_l E\left(\eta_1^2+\eta_2^2\right)-\left(\pi\nu_l\eta_1\eta_2\sin(\tilde{\chi})\right)^2}\times \\ &\quad \begin{pmatrix} E+\Delta_\varepsilon(\tilde{q})+\frac{i\pi\nu_l}{2}\left(\eta_1^2+\eta_2^2\right) & \frac{-i\pi\nu_l}{2}\left(\eta_1^2-\eta_2^2+i2\eta_1\eta_2\cos(\tilde{\chi})\right) \\ \frac{-i\pi\nu_l}{2}\left(\eta_1^2-\eta_2^2-i2\eta_1\eta_2\cos(\tilde{\chi})\right) & E-\Delta_\varepsilon(\tilde{q})+\frac{i\pi\nu_l}{2}\left(\eta_1^2+\eta_2^2\right)\end{pmatrix}. \end{aligned} \tag{B.5}$$

The factor in front of the last matrix is $\det(M^{-1})$. The R_{he} element of the scattering matrix is therefore

$$\begin{aligned}
R_{he} = \frac{-i\pi\nu_l}{2\det(M^{-1})}\Big[&-\left(i\eta_1+\eta_2\,\mathrm{e}^{i\tilde{\chi}}\right)\left(i\eta_1-\eta_2\,\mathrm{e}^{i\tilde{\chi}}\right)\left(E+\Delta_\varepsilon(\tilde{q})+\frac{i\pi\nu_l}{2}\left(\eta_1^2+\eta_2^2\right)\right)\\
&+\left(i\eta_1+\eta_2\,\mathrm{e}^{i\tilde{\chi}}\right)\left(i\eta_1+\eta_2\,\mathrm{e}^{i\tilde{\chi}}\right)\frac{i\pi\nu_l}{2}\left(\eta_1^2-\eta_2^2+i2\eta_1\eta_2\cos(\tilde{\chi})\right)\\
&+\left(i\eta_1-\eta_2\,\mathrm{e}^{i\tilde{\chi}}\right)\left(i\eta_1-\eta_2\,\mathrm{e}^{i\tilde{\chi}}\right)\frac{i\pi\nu_l}{2}\left(\eta_1^2-\eta_2^2-i2\eta_1\eta_2\cos(\tilde{\chi})\right)\\
&-\left(i\eta_1-\eta_2\,\mathrm{e}^{i\tilde{\chi}}\right)\left(i\eta_1+\eta_2\,\mathrm{e}^{i\tilde{\chi}}\right)\left(E-\Delta_\varepsilon(\tilde{q})+\frac{i\pi\nu_l}{2}\left(\eta_1^2+\eta_2^2\right)\right)\Big]\\
=\frac{-i\pi\nu_l}{\det(M^{-1})}\Big[&\left(E+\frac{i\pi\nu_l}{2}\left(\eta_1^2+\eta_2^2\right)\right)\left(\eta_1^2+\eta_2^2\,\mathrm{e}^{i2\tilde{\chi}}\right)-\frac{i\pi\nu_l}{2}\left(\left(\eta_1^2-\eta_2^2\right)\left(\eta_1^2-\eta_2^2\,\mathrm{e}^{i2\tilde{\chi}}\right)+4\eta_1^2\eta_2^2\cos(\tilde{\chi})\,\mathrm{e}^{i\tilde{\chi}}\right)\Big]\\
=\frac{-i\pi\nu_l}{\det(M^{-1})}\Big[&E\,\mathrm{e}^{i\tilde{\chi}}\left(\eta_1^2\,\mathrm{e}^{-i\tilde{\chi}}+\eta_2^2\,\mathrm{e}^{i\tilde{\chi}}\right)\\
&+\frac{i\pi\nu_l}{2}\,\mathrm{e}^{i\tilde{\chi}}\left(\left(\eta_1^2+\eta_2^2\right)\left(\eta_1^2\,\mathrm{e}^{-i\tilde{\chi}}+\eta_2^2\,\mathrm{e}^{i\tilde{\chi}}\right)-\left(\eta_1^2-\eta_2^2\right)\left(\eta_1^2\,\mathrm{e}^{-i\tilde{\chi}}-\eta_2^2\,\mathrm{e}^{i\tilde{\chi}}\right)-4\eta_1^2\eta_2^2\cos(\tilde{\chi})\right)\Big]\\
=\frac{-i\pi\nu_l}{\det(M^{-1})}\Big[&E\,\mathrm{e}^{i\tilde{\chi}}\left(\eta_1^2\,\mathrm{e}^{-i\tilde{\chi}}+\eta_2^2\,\mathrm{e}^{i\tilde{\chi}}\right)+\frac{i\pi\nu_l}{2}\,\mathrm{e}^{i\tilde{\chi}}\left(\eta_1^2\eta_2^2 2\left(\mathrm{e}^{i\tilde{\chi}}+\mathrm{e}^{-i\tilde{\chi}}\right)-4\eta_1^2\eta_2^2\cos(\tilde{\chi})\right)\Big]\\
=\frac{-i\pi\nu_l}{\det(M^{-1})}&E\left(\eta_1^2+\eta_2^2\,\mathrm{e}^{i2\tilde{\chi}}\right). \qquad \text{(B.6)}
\end{aligned}$$

This yields a conductance

$$\begin{aligned}
G_{\tilde{q}}(E) &= \frac{2e^2}{h}\frac{(\pi\nu_l)^2}{\left|\det(M^{-1})\right|^2}E^2\left(\eta_1^4+\eta_2^4+2\eta_1^2\eta_2^2\cos(2\tilde{\chi})\right)\\
&= \frac{2e^2}{h}\frac{(\pi\nu_l E)^2\left(\eta_1^4+\eta_2^4+2\eta_1^2\eta_2^2\cos(2\tilde{\chi})\right)}{\left(E^2-\Delta_\varepsilon^2(\tilde{q})-\left(\pi\nu_l\eta_1\eta_2\sin(\tilde{\chi})\right)^2\right)^2+\left(\pi\nu_l E\left(\eta_1^2+\eta_2^2\right)\right)^2}. \qquad \text{(B.7)}
\end{aligned}$$

Here we show how to obtain the zero-bias conductance $\mathcal{G}^{\mathrm{o}}_{1e}(N,N',q,n_g)$ due to sequential tunnelling of single electrons in the case where N is odd by considering only transitions between states $|N,N',q\rangle$ and $|N+1,N',q\rangle$. We follow Ref. [70] and assume that the occupation probabilities of all other states are zero. The steady state is described by the set of rate equations:

$$\dot{P}_{N+1} = 0 = -\sum_n \Gamma_{N+1\to N,n}P_2 + \sum_n \Gamma_{N,n\to N+1}P_{N,n}\,, \qquad \text{(B.8)}$$

$$\dot{P}_{N,n} = 0 = -\Gamma_{N,n\to N+1}P_{N,n} + \Gamma_{N+1\to N,n}P_{N+1}\,, \qquad \text{(B.9)}$$

$$1 = P_{N+1} + \sum_n P_{N,n}\,, \qquad \text{(B.10)}$$

where the rates are defined in Eq. (2.46) and the text after. $\Gamma_{N+1\to N,n} = \Gamma^L_{N+1\to N,n} + \Gamma^R_{N+1\to N,n}$ etc. Combining Eq. (B.8) and the normalisation (B.10) we obtain

$$\sum_n \Gamma_{N+1\to N,n}\left(1-\sum_{n'}P_{N,n'}\right) = \sum_n \Gamma_{N,n\to N+1}P_{N,n} \to \qquad \text{(B.11)}$$

$$\sum_n \Gamma_{N+1\to N,n} = \sum_n P_{N,n}\left(\Gamma_{N,n\to N+1} + \sum_{n'}\Gamma_{N+1\to N,n'}\right)$$
$$= \sum_n \frac{\Gamma_{N+1\to N,n}}{\Gamma_{N,n\to N+1}} P_{N+1}\left(\Gamma_{N,n\to N+1} + \sum_{n'}\Gamma_{N+1\to N,n'}\right). \tag{B.12}$$

Here we inserted Eq. (B.9) for $P_{N,n}$. The occupation probabilities are then

$$P_{N+1} = \sum_n \Gamma_{N+1\to N,n}\left(\sum_{n'}\frac{\Gamma_{N+1\to N,n'}}{\Gamma_{N,n'\to N+1}}\left(\Gamma_{N,n'\to N+1} + \sum_{n''}\Gamma_{N+1\to N,n''}\right)\right)^{-1} = \left(1+\sum_n \frac{\Gamma_{N+1\to N,n}}{\Gamma_{N,n\to N+1}}\right)^{-1}, \tag{B.13}$$

and

$$P_{N,n} = \frac{\Gamma_{N+1\to N,n}}{\Gamma_{N,n\to N+1}}\left(1+\sum_{n'}\frac{\Gamma_{N+1\to N,n'}}{\Gamma_{N,n'\to N+1}}\right)^{-1}. \tag{B.14}$$

Indeed, the normalisation is fulfilled:

$$P_{N+1} + \sum_n P_{N,n} = \left(1+\sum_n \frac{\Gamma_{N+1\to N,n}}{\Gamma_{N,n\to N+1}}\right)\left(1+\sum_{n'}\frac{\Gamma_{N+1\to N,n'}}{\Gamma_{N,n'\to N+1}}\right)^{-1} = 1. \tag{B.15}$$

We can now write the current as

$$I_{1e}^{\mathrm{o}\to\mathrm{e}} = -e\sum_n P_{N+1}\Gamma^L_{N+1\to N,n} + e\sum_n P_{N,n}\Gamma^L_{N,n\to N+1}$$
$$= -e\left(1+\sum_{n'}\frac{\Gamma_{N+1\to N,n'}}{\Gamma_{N,n'\to N+1}}\right)^{-1}\sum_n\left[\Gamma^L_{N+1\to N,n} - \frac{\Gamma_{N+1\to N,n}\Gamma^L_{N,n\to N+1}}{\Gamma_{N,n\to N+1}}\right]. \tag{B.16}$$

We insert the rate expressions from the main text; $\Gamma^a_{N,n\to N+1} = \frac{g_a\delta}{4\pi\hbar} n_{\mathrm{F}}(\mathcal{E}_{N+1} - \epsilon_n - eV_a)$ and $\Gamma^a_{N+1\to N,n} = \frac{g_a\delta}{4\pi\hbar}(1 - n_{\mathrm{F}}(\mathcal{E}_{N+1} - \epsilon_n - eV_a))$. We take the derivative of the result with respect to the voltage bias $V_b = V_L$ and then take the limit $V_b \to 0$:

$$\left.\frac{dI_{1e}^{\mathrm{o}\to\mathrm{e}}}{dV_b}\right|_{V_b=0} = \frac{-eg_l\delta}{2h}\left(1+\sum_{n'}\frac{1-n_{\mathrm{F}}(\mathcal{E}_{N+1}-\epsilon_{n'})}{n_{\mathrm{F}}(\mathcal{E}_{N+1}-\epsilon_{n'})}\right)^{-1}(-e\beta)\sum_n(1-n_{\mathrm{F}}(\mathcal{E}_{N+1}-\epsilon_n))\frac{g_r}{g_l+g_r}. \tag{B.17}$$

We thereby finally obtain the expression for the current:

$$\mathcal{G}^{\mathrm{o}}_{\mathrm{seq}}(n_g) = \frac{e^2\beta\delta}{2h}\frac{g_l g_r}{g_l+g_r}\frac{\sum_n(1-n_{\mathrm{F}}(\mathcal{E}_{N+1}-\epsilon_n))}{1+\sum_n\frac{1-n_{\mathrm{F}}(\mathcal{E}_{N+1}-\epsilon_n)}{n_{\mathrm{F}}(\mathcal{E}_{N+1}-\epsilon_n)}} = \frac{e^2\beta\delta}{2h}\frac{g_l g_r}{g_l+g_r}\frac{\sum_n\left(1+\mathrm{e}^{-\beta(\mathcal{E}_{N+1}-\epsilon_n)}\right)^{-1}}{1+\sum_n \mathrm{e}^{\beta(\mathcal{E}_{N+1}-\epsilon_n)}}. \tag{B.18}$$

The expression for an even N is derived in the same way and reads the same except from $\mathcal{E}_{N+1} \to -\mathcal{E}_{N+1}$. The total conductance contribution from sequential $1e$ tunnelling is thus $\mathcal{G}_{1e} = \sum_{N\mathrm{even}}\mathcal{G}^{\mathrm{e}}_{1e}(n_g) + \sum_{N\mathrm{odd}}\mathcal{G}^{\mathrm{o}}_{1e}(n_g)$. The $1e$ conductance G_{1e} near the crossing points can then be found by multiplying the conductance by the appropriate weights $w(N) = Z^{-1}\,\mathrm{e}^{-\beta H_{\mathrm{SC}}(N,N',q,n_g)}$: $w(N)(\mathcal{G}_{1e}(N) + \mathcal{G}_{1e}(N-1))$ or equivalently $\mathcal{G}_{1e}(N)(w(N)+w(N+1))$ where $\mathcal{G}^{\mathrm{o/e}}_{1e}$ is inserted for $\mathcal{G}_{1e}$ depending on whether N is odd or even.

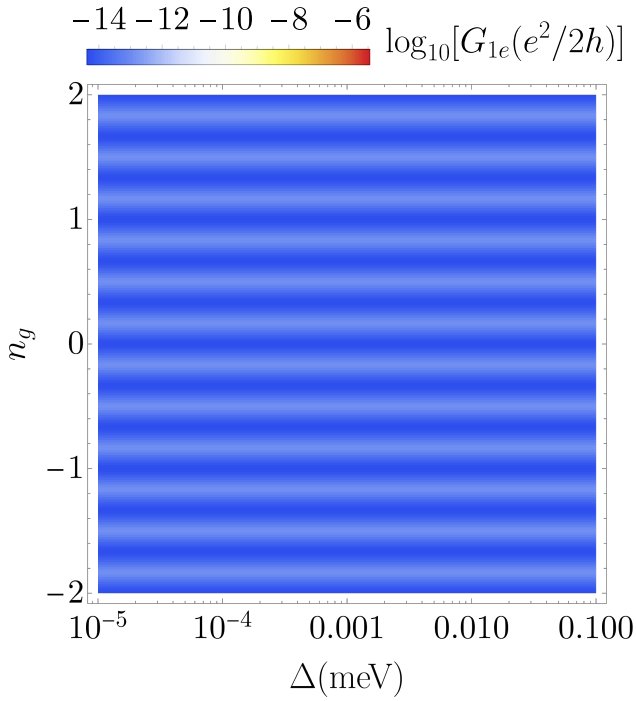

Figure B.1: Zero-bias differential conductance $G_{1e}(\Delta, n_g)$ of the Coulomb-blockaded device due to sequential tunnelling of single electrons. Except from the SC length $L = 10$ µm, all parameters are the same as in Fig. 2.10. The longer SC implies a smaller energy level spacing $\delta = vh/2L \ll E_C$ and the conductance no longer shows twelve irregular peaks per 2 n_g but six peaks evenly-spaced by 1/3. The PF+SC system thus behaves as a Coulomb-blockaded fractional quantum dot for $\delta, \Delta_e \ll T, E_C$ but with a very low conductance signal.

C

Appendix C: Extra figures showing the dynamics of parafermionic states

This appendix includes figures supporting statements of Ch. 3.

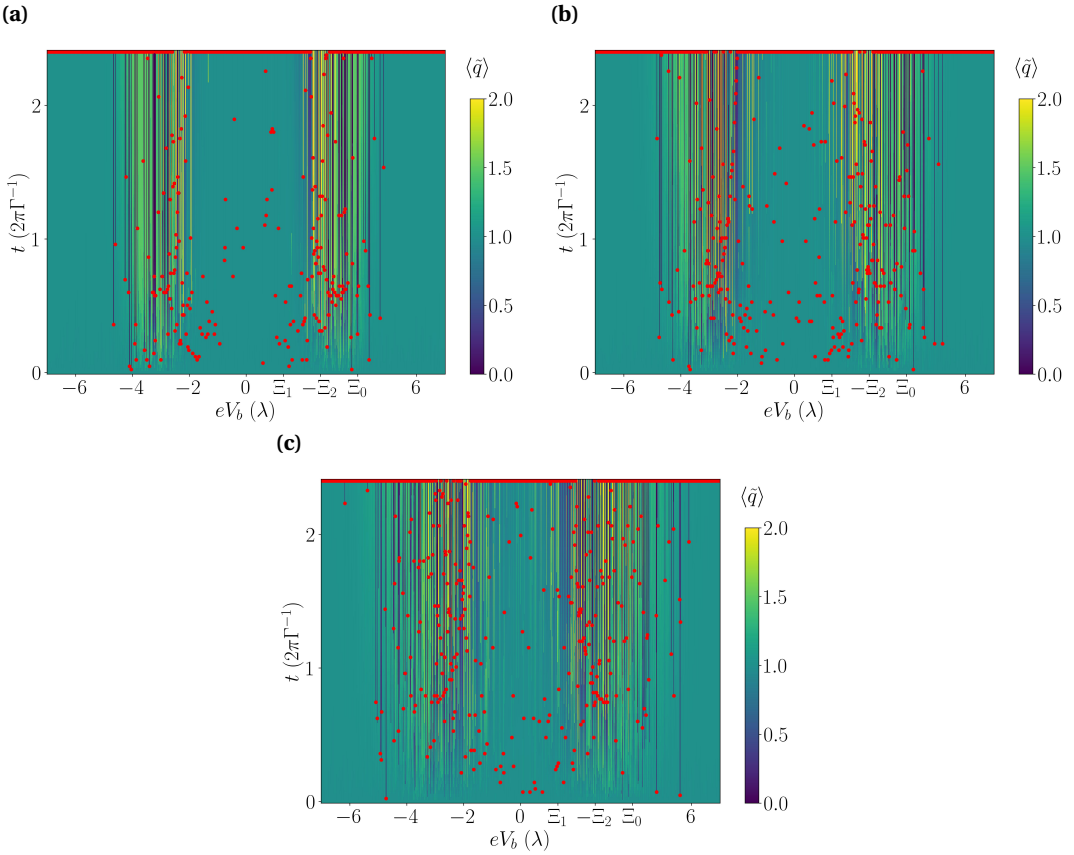

Figure C.1: Projection time on the nanosecond timescale for three different temperatures: **(a)** $T = \lambda/5$, **(b)** $T = \lambda/3$ and **(c)** $T = \lambda/2$. A red dot marks $\zeta^* = 0.8$ unless it is at the top of the figure where it indicates that this threshold is not reached within the first 10 ns.

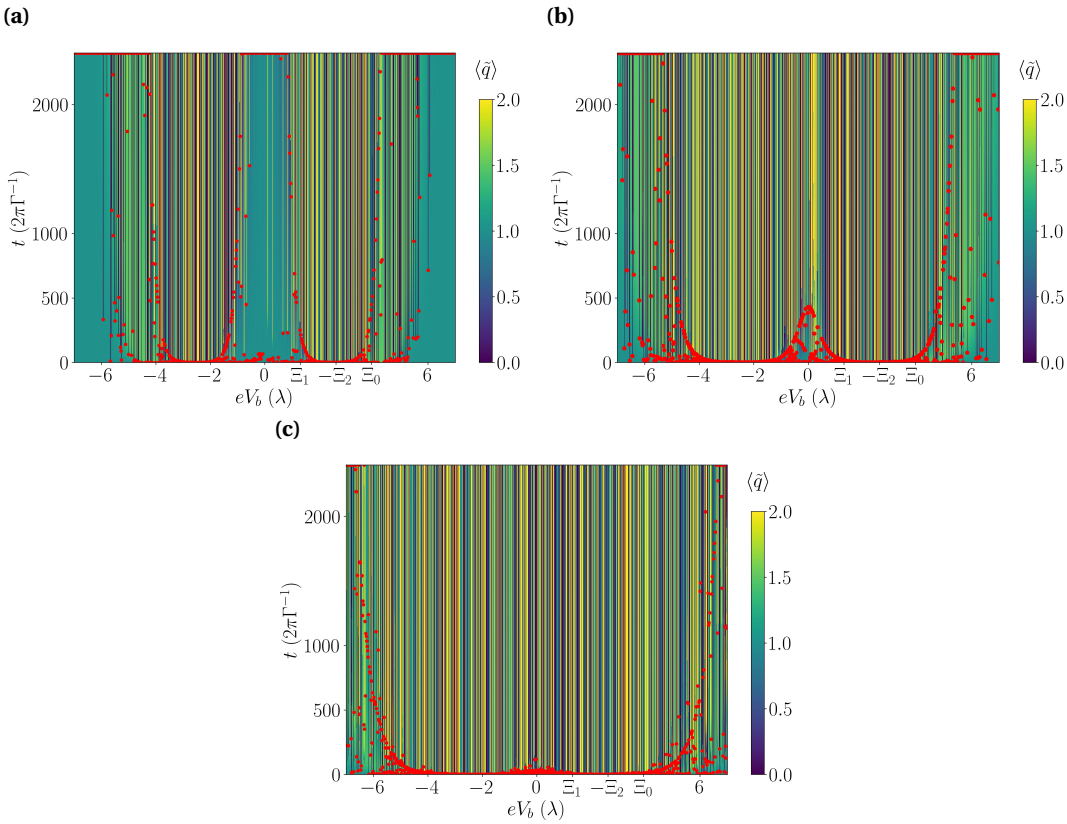

Figure C.2: Projection time on the microsecond scale for three different temperatures: **(a)** $T = \lambda/5$, **(b)** $T = \lambda/3$ and **(c)** $T = \lambda/2$. A red dot marks $\zeta^* = 0.8$ unless it is at the top of the figure where it indicates that this threshold is not reached within 10 µs.

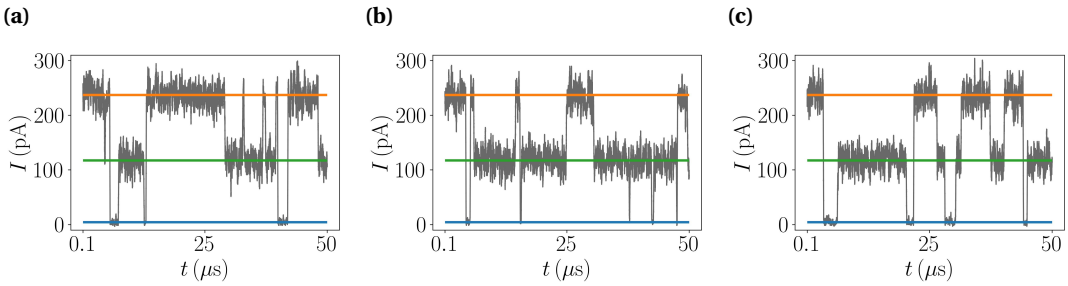

Figure C.3: Samples of numerical estimates of current $I(t)$ at $eV_b = 2.6\lambda$ when including quasiparticle poisoning with coupling strength $\eta_{e/3} = 3.5 \cdot 10^{-3}\lambda$ between the external edge modes of the fractional quantum Hall system and the right parafermion α_2. The initial state is an equal superposition of all six charge eigenstates. Parameters are the same as stated in Fig. 3.13.

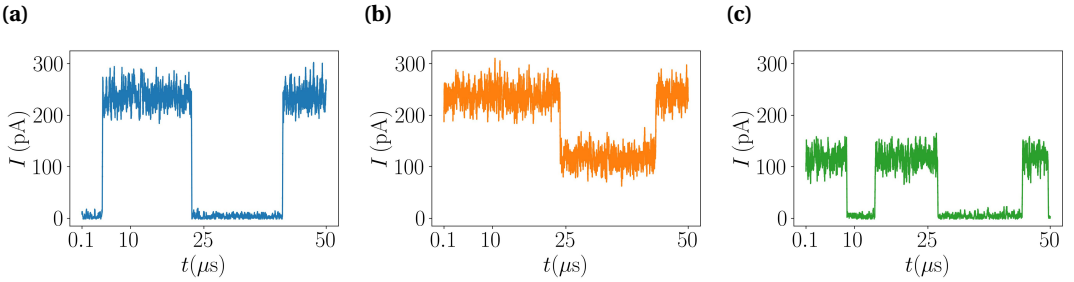

Figure C.4: Numerical estimates of the current evolution at $eV_b = 2.6\lambda$ similar to Fig. 3.17, but with initial states that include a charge $e/3$ on the antidot: **(a)** $|\tilde{q}=0, q_{\text{ad}}=1\rangle = \frac{1}{\sqrt{2}}(|0,1\rangle+|3,1\rangle)$ which couples to the states $|1,0\rangle$ and $|4,0\rangle$, **(b)** $|\tilde{q}=1, q_{\text{ad}}=1\rangle = \frac{1}{\sqrt{2}}(|1,1\rangle+|4,1\rangle)$ and **(c)** $|\tilde{q}=2, q_{\text{ad}}=1\rangle = \frac{1}{\sqrt{2}}(|2,1\rangle+|5,1\rangle)$. Due to the different initial charge on the antidot the current now jumps to the other level with respect to Fig. 3.17.

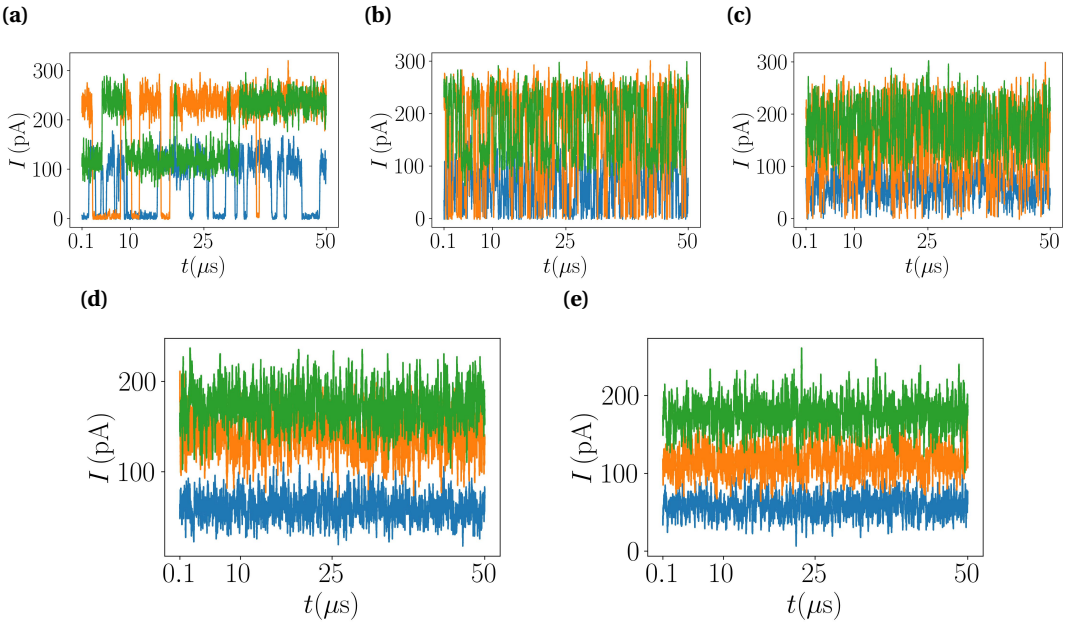

Figure C.5: Current of the three different initial states $|\tilde{q}=0, q_{\text{ad}}=0\rangle$ (blue), $|\tilde{q}=1, q_{\text{ad}}=0\rangle$ (orange) and $|\tilde{q}=1, q_{\text{ad}}=0\rangle$ (green). We keep $\Gamma = 0.1\lambda$ as usual, but increase $\eta_{\text{ad},i}$ from 0.01λ to 1λ, from left to right: $\eta_{\text{ad},i}$, is 0.01λ, 0.05λ, $0.1\lambda(=\Gamma)$, 0.5λ and 1λ. During this change, the current signals become in practice indistinguishable whereas when $\eta_{\text{ad},i} \gg \Gamma$, we see again three current levels, although not as clearly separated with respect to noise as for low $\eta_{\text{ad},i} \ll \Gamma$.

Bibliography

[1] I. E. Nielsen, K. Flensberg, R. Egger, and M. Burrello, "Readout of Parafermionic States by Transport Measurements," *Phys. Rev. Lett.*, vol. 129, p. 037703, Jul 2022.

[2] I. E. Nielsen, J. Schulenborg, R. Egger, and M. Burrello, "Dynamics of parafermionic states in transport measurements," *arXiv*, May 2023.

[3] S. Athanasiou, I. E. Nielsen, M. M. Wauters, and M. Burrello, "Thouless pumping in Josephson junction arrays," *arXiv*, Aug. 2023.

[4] F. Wilczek, "Quantum Mechanics of Fractional-Spin Particles," *Phys. Rev. Lett.*, vol. 49, pp. 957–959, Oct 1982.

[5] A. Y. Kitaev, "Fault-tolerant quantum computation by anyons," *Ann. Phys.*, vol. 303, pp. 2–30, Jan. 2003.

[6] R. P. Feynman, "Simulating physics with computers," *Int. J. Theor. Phys.*, vol. 21, pp. 467–488, June 1982.

[7] A. Y. Kitaev, "Unpaired Majorana fermions in quantum wires," *Phys.-Usp.*, vol. 44, p. 131, Oct 2001.

[8] P. Fendley, "Parafermionic edge zero modes in Z_n-invariant spin chains," *J. Stat. Mech.: Theory Exp.*, vol. 2012, p. 11020, Nov 2012.

[9] R. M. Lutchyn, J. D. Sau, and S. Das Sarma, "Majorana Fermions and a Topological Phase Transition in Semiconductor-Superconductor Heterostructures," *Phys. Rev. Lett.*, vol. 105, p. 077001, Aug 2010.

[10] Y. Oreg, G. Refael, and F. von Oppen, "Helical Liquids and Majorana Bound States in Quantum Wires," *Phys. Rev. Lett.*, vol. 105, p. 177002, Oct 2010.

[11] N. H. Lindner, E. Berg, G. Refael, and A. Stern, "Fractionalizing Majorana Fermions: Non-Abelian Statistics on the Edges of Abelian Quantum Hall States," *Phys. Rev. X*, vol. 2, p. 041002, Oct 2012.

[12] D. J. Clarke, J. Alicea, and K. Shtengel, "Exotic non-Abelian anyons from conventional fractional quantum Hall states," *Nat. Commun.*, vol. 4, pp. 1–9, Jan 2013.

[13] V. Mourik, K. Zuo, S. M. Frolov, S. R. Plissard, E. P. A. M. Bakkers, and L. P. Kouwenhoven, "Signatures of Majorana Fermions in Hybrid Superconductor-Semiconductor Nanowire Devices," *Science*, vol. 336, pp. 1003–1007, May 2012.

[14] D. Aasen, M. Hell, R. V. Mishmash, A. Higginbotham, J. Danon, M. Leijnse, T. S. Jespersen, J. A. Folk, C. M. Marcus, K. Flensberg, and J. Alicea, "Milestones Toward Majorana-Based Quantum Computing," *Phys. Rev. X*, vol. 6, p. 031016, Aug 2016.

[15] M. T. Deng, S. Vaitiekėnas, E. B. Hansen, J. Danon, M. Leijnse, K. Flensberg, J. Nygård, P. Krogstrup, and C. M. Marcus, "Majorana bound state in a coupled quantum-dot hybrid-nanowire system," *Science*, vol. 354, pp. 1557–1562, Dec 2016.

[16] F. Nichele, A. C. C. Drachmann, A. M. Whiticar, E. C. T. O'Farrell, H. J. Suominen, A. Fornieri, T. Wang, G. C. Gardner, C. Thomas, A. T. Hatke, P. Krogstrup, M. J. Manfra, K. Flensberg, and C. M. Marcus, "Scaling of Majorana Zero-Bias Conductance Peaks," *Phys. Rev. Lett.*, vol. 119, p. 136803, Sep 2017.

[17] O. Gül, H. Zhang, J. D. S. Bommer, M. W. A. de Moor, D. Car, S. R. Plissard, E. P. A. M. Bakkers, A. Geresdi, K. Watanabe, T. Taniguchi, and L. P. Kouwenhoven, "Ballistic Majorana nanowire devices," *Nat. Nanotechnol.*, vol. 13, pp. 192–197, Mar 2018.

[18] K. Flensberg, F. von Oppen, and A. Stern, "Engineered platforms for topological superconductivity and Majorana zero modes," *Nat. Rev. Mater.*, vol. 6, pp. 944–958, Oct 2021.

[19] M. Leijnse and K. Flensberg, "Introduction to topological superconductivity and Majorana fermions," *Semicond. Sci. Technol.*, vol. 27, p. 124003, Nov. 2012.

[20] O. Gül, Y. Ronen, S. Y. Lee, H. Shapourian, J. Zauberman, Y. H. Lee, K. Watanabe, T. Taniguchi, A. Vishwanath, A. Yacoby, and P. Kim, "Andreev Reflection in the Fractional Quantum Hall State," *Phys. Rev. X*, vol. 12, p. 021057, Jun 2022.

[21] N. Schiller, B. A. Katzir, A. Stern, E. Berg, N. H. Lindner, and Y. Oreg, "Superconductivity and fermionic dissipation in quantum Hall edges," *Phys. Rev. B*, vol. 107, p. L161105, Apr 2023.

[22] C. Nayak, S. H. Simon, A. Stern, M. Freedman, and S. Das Sarma, "Non-Abelian anyons and topological quantum computation," *Rev. Mod. Phys.*, vol. 80, pp. 1083–1159, Sep 2008.

[23] J. Alicea and P. Fendley, "Topological Phases with Parafermions: Theory and Blueprints," *Annu. Rev. Condens. Matter Phys.*, vol. 7, pp. 119–139, Mar. 2016.

[24] X.-G. Wen, *Quantum Field Theory of Many-Body Systems*. Oxford, England, UK: Oxford University Press, 2004.

[25] M. Burrello, B. van Heck, and E. Cobanera, "Topological phases in two-dimensional arrays of parafermionic zero modes," *Phys. Rev. B*, vol. 87, p. 195422, May 2013.

[26] A. Akhmerov, J. Sau, B. van Heck, S. Rubbert, R. Skolasiński, B. Nijholt, I. Muhammad, and T. Ö. Rosdahl, *Topology in condensed matter: tying quantum knots*. TU Delft, 2021. Online course.

[27] E. Fradkin and L. Kadanoff, "Disorder variables and para-fermions in two-dimensional statistical mechanics," *Nucl. Phys. B*, vol. 170, pp. 1–15, 1980.

[28] A. Stern, B. Yan, E. Berg, H. Beidenkopf, M. Heiblum, N. Avraham, R. Queiroz, R. Ilan, S. Ilani, T. Gao, Y. Oreg, and Y. Ronen, *Topological quantum matter*. Weizmann Institute, 2022. Online course.

[29] K. von Klitzing, G. Dorda, and M. Pepper, "New Method for High-Accuracy Determination of the Fine-Structure Constant Based on Quantized Hall Resistance," *Phys. Rev. Lett.*, vol. 45, pp. 494–497, Aug 1980.

[30] R. Willett, J. P. Eisenstein, H. L. Störmer, D. C. Tsui, A. C. Gossard, and J. H. English, "Observation of an even-denominator quantum number in the fractional quantum Hall effect," *Phys. Rev. Lett.*, vol. 59, pp. 1776–1779, Oct 1987.

[31] D. C. Tsui, H. L. Stormer, and A. C. Gossard, "Two-Dimensional Magnetotransport in the Extreme Quantum Limit," *Phys. Rev. Lett.*, vol. 48, pp. 1559–1562, May 1982.

[32] T. Ihn, *Semiconductor Nanostructures*. Oxford, England, UK: Oxford University Press, Dec. 2009.

[33] R. B. Laughlin, "Anomalous Quantum Hall Effect: An Incompressible Quantum Fluid with Fractionally Charged Excitations," *Phys. Rev. Lett.*, vol. 50, pp. 1395–1398, May 1983.

[34] L. Fidkowski and A. Kitaev, "Topological phases of fermions in one dimension," *Phys. Rev. B*, vol. 83, p. 075103, Feb 2011.

[35] T. D. Stanescu, R. M. Lutchyn, and S. Das Sarma, "Majorana fermions in semiconductor nanowires," *Phys. Rev. B*, vol. 84, p. 144522, Oct 2011.

[36] R. S. K. Mong, D. J. Clarke, J. Alicea, N. H. Lindner, P. Fendley, C. Nayak, Y. Oreg, A. Stern, E. Berg, K. Shtengel, and M. P. A. Fisher, "Universal Topological Quantum Computation from a Superconductor-Abelian Quantum Hall Heterostructure," *Phys. Rev. X*, vol. 4, p. 011036, Mar 2014.

[37] M.-T. Deng, S. Vaitiekėnas, E. Prada, P. San-Jose, J. Nygård, P. Krogstrup, R. Aguado, and C. M. Marcus, "Nonlocality of Majorana modes in hybrid nanowires," *Phys. Rev. B*, vol. 98, p. 085125, Aug 2018.

[38] C. Chen and F. J. Burnell, "Tunable Splitting of the Ground-State Degeneracy in Quasi-One-Dimensional Parafermion Systems," *Phys. Rev. Lett.*, vol. 116, p. 106405, Mar 2016.

[39] M. Cheng, "Superconducting proximity effect on the edge of fractional topological insulators," *Phys. Rev. B*, vol. 86, p. 195126, Nov 2012.

[40] A. Vaezi, "Fractional topological superconductor with fractionalized Majorana fermions," *Phys. Rev. B*, vol. 87, p. 035132, Jan 2013.

[41] M. Barkeshli and X.-L. Qi, "Synthetic Topological Qubits in Conventional Bilayer Quantum Hall Systems," *Phys. Rev. X*, vol. 4, p. 041035, Nov 2014.

[42] D. J. Clarke, J. Alicea, and K. Shtengel, "Exotic circuit elements from zero-modes in hybrid superconductor–quantum-Hall systems," *Nat. Phys.*, vol. 10, pp. 877–882, Nov. 2014.

[43] G.-H. Lee, K.-F. Huang, D. K. Efetov, D. S. Wei, S. Hart, T. Taniguchi, K. Watanabe, A. Yacoby, and P. Kim, "Inducing superconducting correlation in quantum Hall edge states," *Nat. Phys.*, vol. 13, pp. 693–698, July 2017.

[44] S. Groenendijk, A. Calzona, H. Tschirhart, E. G. Idrisov, and T. L. Schmidt, "Parafermion braiding in fractional quantum Hall edge states with a finite chemical potential," *Phys. Rev. B*, vol. 100, p. 205424, Nov 2019.

[45] J. Nilsson, A. R. Akhmerov, and C. W. J. Beenakker, "Splitting of a Cooper Pair by a Pair of Majorana Bound States," *Phys. Rev. Lett.*, vol. 101, p. 120403, Sep 2008.

[46] L. Fu, "Electron Teleportation via Majorana Bound States in a Mesoscopic Superconductor," *Phys. Rev. Lett.*, vol. 104, p. 056402, Feb 2010.

[47] K. Flensberg, "Tunneling characteristics of a chain of Majorana bound states," *Phys. Rev. B*, vol. 82, p. 180516, Nov 2010.

[48] A. Zazunov, A. L. Yeyati, and R. Egger, "Coulomb blockade of Majorana-fermion-induced transport," *Phys. Rev. B*, vol. 84, p. 165440, Oct 2011.

[49] L. Fidkowski, J. Alicea, N. H. Lindner, R. M. Lutchyn, and M. P. A. Fisher, "Universal transport signatures of Majorana fermions in superconductor-Luttinger liquid junctions," *Phys. Rev. B*, vol. 85, p. 245121, Jun 2012.

[50] I. L. Aleiner, P. W. Brouwer, and L. I. Glazman, "Quantum effects in Coulomb blockade," *Phys. Rep.*, vol. 358, pp. 309–440, Mar. 2002.

[51] J. Danon, A. B. Hellenes, E. B. Hansen, L. Casparis, A. P. Higginbotham, and K. Flensberg, "Nonlocal Conductance Spectroscopy of Andreev Bound States: Symmetry Relations and BCS Charges," *Phys. Rev. Lett.*, vol. 124, p. 036801, Jan 2020.

[52] R. Landauer, "Electrical resistance of disordered one-dimensional lattices," *Philosophical Magazine: A Journal of Theoretical Experimental and Applied Physics*, vol. 21, pp. 863–867, Apr. 1970.

[53] M. Büttiker, "Scattering theory of current and intensity noise correlations in conductors and wave guides," *Phys. Rev. B*, vol. 46, pp. 12485–12507, Nov 1992.

[54] H. Bruus and K. Flensberg, *Many-body Quantum Theory in Condensed Matter Physics - an introduction*. United States: Oxford University Press, 2004.

[55] Y. V. Nazarov and Y. M. Blanter, *Quantum Transport: Introduction to Nanoscience*. Cambridge, England, UK: Cambridge University Press, 2009.

[56] E. B. Hansen, *Majorana Bound States in Semiconductor-Superconductor Hybrid Devices*. PhD thesis, Center for Quantum Devices, Niels Bohr Institute, University of Copenhagen, 2018. Chapter 3.

[57] K. T. Law, P. A. Lee, and T. K. Ng, "Majorana Fermion Induced Resonant Andreev Reflection," *Phys. Rev. Lett.*, vol. 103, p. 237001, Dec 2009.

[58] N. W. Ashcroft and N. D. Mermin, *Solid State Physics*. Philadelphia, USA: W. B. Saunders Company, Jan 1976. Chapter 2.

[59] Y. Kasahara, T. Ohnishi, Y. Mizukami, O. Tanaka, S. Ma, K. Sugii, N. Kurita, H. Tanaka, J. Nasu, Y. Motome, T. Shibauchi, and Y. Matsuda, "Majorana quantization and half-integer thermal quantum Hall effect in a Kitaev spin liquid," *Nature*, vol. 559, pp. 227–231, July 2018.

[60] V. Crépel, B. Estienne, and N. Regnault, "Variational Ansatz for an Abelian to Non-Abelian Topological Phase Transition in $\nu = 1/2 + 1/2$ Bilayers," *Phys. Rev. Lett.*, vol. 123, p. 126804, Sep 2019.

[61] E. Sela, Y. Oreg, S. Plugge, N. Hartman, S. Lüscher, and J. Folk, "Detecting the Universal Fractional Entropy of Majorana Zero Modes," *Phys. Rev. Lett.*, vol. 123, p. 147702, Oct 2019.

[62] C. W. J. Beenakker, "Search for non-Abelian Majorana braiding statistics in superconductors," *SciPost Phys. Lect. Notes*, p. 15, 2020.

[63] S. An, P. Jiang, H. Choi, W. Kang, S. H. Simon, L. N. Pfeiffer, K. W. West, and K. W. Baldwin, "Braiding of Abelian and Non-Abelian Anyons in the Fractional Quantum Hall Effect," *arXiv*, Dec 2011.

[64] B. Rosenow and S. H. Simon, "Telegraph noise and the Fabry-Perot quantum Hall interferometer," *Phys. Rev. B*, vol. 85, p. 201302, May 2012.

[65] S. M. Albrecht, A. P. Higginbotham, M. Madsen, F. Kuemmeth, T. S. Jespersen, J. Nygård, P. Krogstrup, and C. M. Marcus, "Exponential protection of zero modes in Majorana islands," *Nature*, vol. 531, pp. 206–209, Mar. 2016.

[66] S. M. Albrecht, E. B. Hansen, A. P. Higginbotham, F. Kuemmeth, T. S. Jespersen, J. Nygård, P. Krogstrup, J. Danon, K. Flensberg, and C. M. Marcus, "Transport Signatures of Quasiparticle Poisoning in a Majorana Island," *Phys. Rev. Lett.*, vol. 118, p. 137701, Mar 2017.

[67] T. Kanne, M. Marnauza, D. Olsteins, D. J. Carrad, J. E. Sestoft, J. de Bruijckere, L. Zeng, E. Johnson, E. Olsson, K. Grove-Rasmussen, and J. Nygård, "Epitaxial Pb on InAs nanowires for quantum devices," *Nat. Nanotechnol.*, vol. 16, pp. 776–781, July 2021.

[68] S. Vaitiekėnas, G. W. Winkler, B. van Heck, T. Karzig, M.-T. Deng, K. Flensberg, L. I. Glazman, C. Nayak, P. Krogstrup, R. M. Lutchyn, and C. M. Marcus, "Flux-induced topological superconductivity in full-shell nanowires," *Science*, vol. 367, Mar. 2020.

[69] Hützen, R. and Zazunov, A. and Braunecker, B. and Yeyati, A. Levy and Egger, R., "Majorana single-charge transistor," *Phys. Rev. Lett.*, vol. 109, p. 166403, Oct 2012.

[70] B. van Heck, R. M. Lutchyn, and L. I. Glazman, "Conductance of a proximitized nanowire in the Coulomb blockade regime," *Phys. Rev. B*, vol. 93, p. 235431, Jun 2016.

[71] K. I. Bolotin, F. Ghahari, M. D. Shulman, H. L. Stormer, and P. Kim, "Observation of the fractional quantum Hall effect in graphene," *Nature*, vol. 462, pp. 196–199, Nov. 2009.

[72] D. Feinberg, "Andreev scattering and cotunneling between two superconductor-normal metal interfaces: the dirty limit," *Eur. Phys. J. B*, vol. 36, pp. 419–422, Dec. 2003.

[73] J. Danon and K. Flensberg, "Interaction effects on proximity-induced superconductivity in semiconducting nanowires," *Phys. Rev. B*, vol. 91, p. 165425, Apr 2015.

[74] C. Reeg, J. Klinovaja, and D. Loss, "Destructive interference of direct and crossed Andreev pairing in a system of two nanowires coupled via an s-wave superconductor," *Phys. Rev. B*, vol. 96, p. 081301, Aug 2017.

[75] G. Mussardo, *Statistical Field Theory: An Introduction to Exactly Solved Models in Statistical Physics*. New York: Oxford University Press, 2nd ed., 2020. Chapter 16.

[76] R. V. Mishmash, D. Aasen, A. P. Higginbotham, and J. Alicea, "Approaching a topological phase transition in Majorana nanowires," *Phys. Rev. B*, vol. 93, p. 245404, Jun 2016.

[77] E. B. Hansen, J. Danon, and K. Flensberg, "Probing electron-hole components of subgap states in Coulomb blockaded Majorana islands," *Phys. Rev. B*, vol. 97, p. 041411, Jan 2018.

[78] M. Thamm and B. Rosenow, "Transmission amplitude through a Coulomb blockaded Majorana wire," *Phys. Rev. Res.*, vol. 3, p. 023221, Jun 2021.

[79] V. J. Goldman and B. Su, "Resonant Tunneling in the Quantum Hall Regime: Measurement of Fractional Charge," *Science*, vol. 267, pp. 1010–1012, Feb. 1995.

[80] S. M. Mills, D. V. Averin, and X. Du, "Localizing Fractional Quasiparticles on Graphene Quantum Hall Antidots," *Phys. Rev. Lett.*, vol. 125, p. 227701, Nov 2020.

[81] M. Barkeshli, Y. Oreg, and X.-L. Qi, "Experimental Proposal to Detect Topological Ground State Degeneracy," *arXiv*, Jan. 2014.

[82] Y. Kim, D. J. Clarke, and R. M. Lutchyn, "Coulomb blockade in fractional topological superconductors," *Phys. Rev. B*, vol. 96, p. 041123, Jul 2017.

[83] K. Snizhko, R. Egger, and Y. Gefen, "Measurement and control of a Coulomb-blockaded parafermion box," *Phys. Rev. B*, vol. 97, p. 081405, Feb 2018.

[84] K. Snizhko, F. Buccheri, R. Egger, and Y. Gefen, "Parafermionic generalization of the topological Kondo effect," *Phys. Rev. B*, vol. 97, p. 235139, Jun 2018.

[85] L. Mazza, J. Viti, M. Carrega, D. Rossini, and A. De Luca, "Energy transport in an integrable parafermionic chain via generalized hydrodynamics," *Phys. Rev. B*, vol. 98, p. 075421, Aug 2018.

[86] N. Schiller, E. Cornfeld, E. Berg, and Y. Oreg, "Predicted signatures of topological superconductivity and parafermion zero modes in fractional quantum Hall edges," *Phys. Rev. Res.*, vol. 2, p. 023296, Jun 2020.

[87] A. E. Svetogorov, D. Loss, and J. Klinovaja, "Insulating regime of an underdamped current-biased Josephson junction supporting $\mathbb{Z}_3$ and $\mathbb{Z}_4$ parafermions," *Phys. Rev. B*, vol. 103, p. L180505, May 2021.

[88] A. Chew, D. F. Mross, and J. Alicea, "Fermionized parafermions and symmetry-enriched Majorana modes," *Phys. Rev. B*, vol. 98, p. 085143, Aug 2018.

[89] A. Calzona, T. Meng, M. Sassetti, and T. L. Schmidt, "$\mathbb{Z}_4$ parafermions in one-dimensional fermionic lattices," *Phys. Rev. B*, vol. 98, p. 201110, Nov 2018.

[90] L. Mazza, F. Iemini, M. Dalmonte, and C. Mora, "Nontopological parafermions in a one-dimensional fermionic model with even multiplet pairing," *Phys. Rev. B*, vol. 98, p. 201109, Nov 2018.

[91] R. L. R. C. Teixeira and L. G. G. V. Dias da Silva, "Quantum dots as parafermion detectors," *Phys. Rev. Res.*, vol. 3, p. 033014, Jul 2021.

[92] K. Mølmer, Y. Castin, and J. Dalibard, "Monte Carlo wave-function method in quantum optics," *J. Opt. Soc. Am. B*, vol. 10, pp. 524–538, Mar. 1993.

[93] H.-P. Breuer and F. Petruccione, *The Theory of Open Quantum Systems*. Oxford, England, UK: Oxford University Press, 2007.

[94] N. Moreau, B. Brun, S. Somanchi, K. Watanabe, T. Taniguchi, C. Stampfer, and B. Hackens, "Upstream modes and antidots poison graphene quantum Hall effect," *Nat. Commun.*, vol. 12, pp. 1–7, July 2021.

[95] U. Khanna, M. Goldstein, and Y. Gefen, "Parafermions in a multilegged geometry: Towards a scalable parafermionic network," *Phys. Rev. B*, vol. 105, p. L161101, Apr 2022.

[96] R. L. R. C. Teixeira, A. Haller, R. Singh, A. Mathew, E. G. Idrisov, L. G. G. V. Dias da Silva, and T. L. Schmidt, "Overlap of parafermionic zero modes at a finite distance," *Phys. Rev. Res.*, vol. 4, p. 043094, Nov 2022.

[97] E. Cobanera, "Modeling electron fractionalization with unconventional Fock spaces," *J. Phys.: Condens. Matter*, vol. 29, p. 305602, June 2017.

[98] F. Nathan and M. S. Rudner, "Universal Lindblad equation for open quantum systems," *Phys. Rev. B*, vol. 102, p. 115109, Sep 2020.

[99] M. B. Plenio and P. L. Knight, "The quantum-jump approach to dissipative dynamics in quantum optics," *Rev. Mod. Phys.*, vol. 70, pp. 101–144, Jan 1998.

[100] A. J. Daley, "Quantum trajectories and open many-body quantum systems," *Adv. Phys.*, vol. 63, pp. 77–149, Mar. 2014.

[101] J. Schulenborg, S. Krøjer, M. Burrello, M. Leijnse, and K. Flensberg, "Detecting Majorana modes by readout of poisoning-induced parity flips," *Phys. Rev. B*, vol. 107, p. L121401, Mar 2023.

[102] J. Nakamura, S. Liang, G. C. Gardner, and M. J. Manfra, "Direct observation of anyonic braiding statistics," *Nat. Phys.*, vol. 16, pp. 931–936, Sept. 2020.

[103] J. Nakamura, S. Liang, G. C. Gardner, and M. J. Manfra, "Impact of bulk-edge coupling on observation of anyonic braiding statistics in quantum Hall interferometers," *Nat. Commun.*, vol. 13, pp. 1–9, Jan. 2022.

[104] M. Banerjee, M. Heiblum, A. Rosenblatt, Y. Oreg, D. E. Feldman, A. Stern, and V. Umansky, "Observed quantization of anyonic heat flow," *Nature*, vol. 545, pp. 75–79, May 2017.

[105] E. Fradkin, *Field Theories of Condensed Matter Physics*. Cambridge University Press, 2 ed., 2013.

[106] A. Liguori, M. Mintchev, and L. Pilo, "Bosonization at finite temperature and anyon condensation," *Nucl. Phys. B*, vol. 569, pp. 577–605, Mar. 2000.

[107] M. Mintchev and P. Sorba, "Luttinger liquid in a non-equilibrium steady state," *J. Phys. A: Math. Theor.*, vol. 46, p. 095006, Feb. 2013.

[108] D. Ferraro, J. Rech, T. Jonckheere, and T. Martin, "Single quasiparticle and electron emitter in the fractional quantum Hall regime," *Phys. Rev. B*, vol. 91, p. 205409, May 2015.

[109] E. Papa and A. H. MacDonald, "Interactions Suppress Quasiparticle Tunneling at Hall Bar Constrictions," *Phys. Rev. Lett.*, vol. 93, p. 126801, Sep 2004.

[110] N. Schiller, Y. Oreg, and K. Snizhko, "Extracting the scaling dimension of quantum Hall quasiparticles from current correlations," *Phys. Rev. B*, vol. 105, p. 165150, Apr 2022.

[111] N. Schiller, Y. Shapira, A. Stern, and Y. Oreg, "Anyon statistics through conductance measurements of time-domain interferometry," *arXiv*, Dec. 2022.

[112] H. Polshyn, H. Zhou, E. M. Spanton, T. Taniguchi, K. Watanabe, and A. F. Young, "Quantitative Transport Measurements of Fractional Quantum Hall Energy Gaps in Edgeless Graphene Devices," *Phys. Rev. Lett.*, vol. 121, p. 226801, Nov 2018.

[113] J. R. Johansson, P. D. Nation, and F. Nori, "QuTiP: An open-source Python framework for the dynamics of open quantum systems," *Comput. Phys. Commun.*, vol. 183, pp. 1760–1772, Aug. 2012.

[114] J. R. Johansson, P. D. Nation, and F. Nori, "QuTiP 2: A Python framework for the dynamics of open quantum systems," *Comput. Phys. Commun.*, vol. 184, pp. 1234–1240, Apr. 2013.

[115] M. Kataoka, C. J. B. Ford, G. Faini, D. Mailly, M. Y. Simmons, D. R. Mace, C.-T. Liang, and D. A. Ritchie, "Detection of Coulomb Charging around an Antidot in the Quantum Hall Regime," *Phys. Rev. Lett.*, vol. 83, pp. 160–163, Jul 1999.

[116] A. Milsted, E. Cobanera, M. Burrello, and G. Ortiz, "Commensurate and incommensurate states of topological quantum matter," *Phys. Rev. B*, vol. 90, p. 195101, Nov 2014.

[117] J. Wouters, F. Hassler, H. Katsura, and D. Schuricht, "Phase diagram of an extended parafermion chain," *SciPost Phys. Core*, vol. 5, p. 008, Feb. 2022.

[118] A. Calzona, M. Carrega, and L. Chirolli, "Anomalous periodicity and parafermion hybridization in superconducting qubits," *Phys. Rev. B*, vol. 107, p. 045105, Jan 2023.

[119] J. Preskill, "Lecture notes for Physics 219: Quantum Computation," *Caltech Lecture Notes*, p. 7, 1999.

[120] A. Kitaev, "Anyons in an exactly solved model and beyond," *Ann. Phys.*, vol. 321, pp. 2–111, Jan. 2006.

[121] G. Ortiz, E. Cobanera, and Z. Nussinov, "Dualities and the phase diagram of the p-clock model," *Nucl. Phys. B*, vol. 854, pp. 780–814, Jan. 2012.

[122] P. Bonderson, M. Freedman, and C. Nayak, "Measurement-Only Topological Quantum Computation," *Phys. Rev. Lett.*, vol. 101, p. 010501, Jun 2008.

[123] F. Hassler and D. Schuricht, "Strongly interacting Majorana modes in an array of Josephson junctions," *New J. Phys.*, vol. 14, p. 125018, Dec. 2012.

[124] L. Casparis, M. R. Connolly, M. Kjaergaard, N. J. Pearson, A. Kringhøj, T. W. Larsen, F. Kuemmeth, T. Wang, C. Thomas, S. Gronin, G. C. Gardner, M. J. Manfra, C. M. Marcus, and K. D. Petersson, "Superconducting gatemon qubit based on a proximitized two-dimensional electron gas," *Nat. Nanotechnol.*, vol. 13, pp. 915–919, Oct. 2018.

[125] L. Casparis, N. J. Pearson, A. Kringhøj, T. W. Larsen, F. Kuemmeth, J. Nygård, P. Krogstrup, K. D. Petersson, and C. M. Marcus, "Voltage-controlled superconducting quantum bus," *Phys. Rev. B*, vol. 99, p. 085434, Feb 2019.

[126] A. Kringhøj, T. W. Larsen, B. van Heck, D. Sabonis, O. Erlandsson, I. Petkovic, D. I. Pikulin, P. Krogstrup, K. D. Petersson, and C. M. Marcus, "Controlled dc Monitoring of a Superconducting Qubit," *Phys. Rev. Lett.*, vol. 124, p. 056801, Feb 2020.

[127] B. van Heck, F. Hassler, A. R. Akhmerov, and C. W. J. Beenakker, "Coulomb stability of the 4π-periodic Josephson effect of Majorana fermions," *Phys. Rev. B*, vol. 84, p. 180502, Nov 2011.

[128] B. van Heck, A. R. Akhmerov, F. Hassler, M. Burrello, and C. W. J. Beenakker, "Coulomb-assisted braiding of Majorana fermions in a Josephson junction array," *New J. Phys.*, vol. 14, p. 035019, Mar. 2012.

[129] E. C. T. O'Farrell, A. C. C. Drachmann, M. Hell, A. Fornieri, A. M. Whiticar, E. B. Hansen, S. Gronin, G. C. Gardner, C. Thomas, M. J. Manfra, K. Flensberg, C. M. Marcus, and F. Nichele, "Hybridization of Subgap States in One-Dimensional Superconductor-Semiconductor Coulomb Islands," *Phys. Rev. Lett.*, vol. 121, p. 256803, Dec 2018.

[130] B. van Heck, M. Burrello, A. Yacoby, and A. R. Akhmerov, "Topological Blockade and Measurement of Topological Charge," *Phys. Rev. Lett.*, vol. 110, p. 086803, Feb 2013.

[131] K. Flensberg, "Non-Abelian Operations on Majorana Fermions via Single-Charge Control," *Phys. Rev. Lett.*, vol. 106, p. 090503, Mar 2011.

[132] S. Hoffman, C. Schrade, J. Klinovaja, and D. Loss, "Universal quantum computation with hybrid spin-Majorana qubits," *Phys. Rev. B*, vol. 94, p. 045316, Jul 2016.

[133] S. Krøjer, R. Seoane Souto, and K. Flensberg, "Demonstrating Majorana non-Abelian properties using fast adiabatic charge transfer," *Phys. Rev. B*, vol. 105, p. 045425, Jan 2022.

[134] M. J. Rice and E. J. Mele, "Elementary Excitations of a Linearly Conjugated Diatomic Polymer," *Phys. Rev. Lett.*, vol. 49, pp. 1455–1459, Nov 1982.

[135] D. R. Hofstadter, "Energy levels and wave functions of Bloch electrons in rational and irrational magnetic fields," *Phys. Rev. B*, vol. 14, pp. 2239–2249, Sep 1976.

[136] D. J. Thouless, "Quantization of particle transport," *Phys. Rev. B*, vol. 27, pp. 6083–6087, May 1983.

[137] M. M. Wauters, *Adiabatic approaches to non-equilibrium systems: Topology, Optimization, and Learning*. PhD thesis, SISSA, Sept. 2020.

[138] M. M. Wauters, A. Russomanno, R. Citro, G. E. Santoro, and L. Privitera, "Localization, Topology, and Quantized Transport in Disordered Floquet Systems," *Phys. Rev. Lett.*, vol. 123, p. 266601, Dec 2019.